Radiogenic isotopes and geochemistry of mafic dykes and plutons in the Bakhuis belt, Western Suriname and their relationship to UHT metamorphism

Bertram Uunk

Master thesis in Earth Sciences: Solid Earth, VU University Amsterdam

Supervised by:
Dr. Emond de Roever
Prof. Gareth Davies
Dr. Fraukje Brouwer

VU VRIJE UNIVERSITEIT AMSTERDAM

Radiogenic isotopes and geochemistry of mafic dykes and plutons in the Bakhuis belt, Western Suriname and their relationship to UHT metamorphism

B. A. Uunk

Master Thesis Solid Earth (AM_450199, 27 ECTS)
Extension Master Thesis Earth Sciences (AM_450149, 12 ECTS)

Supervised by:
Dr. E.W.F. de Roever
Prof. Dr. G.R. Davies
Dr. F.M. Brouwer

Deep earth and planetary science cluster
Earth Science department
Faculty of Earth and Life Sciences
VU University Amsterdam

2nd version: August 8th 2015

Cover photograph: The Bakhuis mountains as seen from the air.

This page is intentionally left blank

Abstract

Within the Guiana shield, the Bakhuis belt forms a ~30 x 100 km horst-shaped geologic anomaly of UHT granulites and plutonic rocks oblique to the older TTG-greenstone in the north and the younger arc-related CSID-belt to the south. Consequently, the belt has the potential to provide important information on the history of the Guiana shield. The belt consists of a ~2.07 Ga metamorphic suite, which was intruded by ~1.97 – 1.99 Ga charnockitic and mafic bodies (de Roever et al., 2003b; Klaver et al., 2015; Klaver et al., *in press;* Nanne, 2013; Thijssen, 2015). Together with Thijssen (2015), this thesis forms a comprehensive study of the possible relationship between these mafic bodies and UHT metamorphism. Specifically, this thesis investigates: 1) the petrogenesis of cm-sized hornblende in metagabbroic bodies, 2) the petrography and geochemistry of a 3 x 4 km sized anorthosite body 3) the geochemistry and age of metadolerite dykes and xenoliths in plutonic bodies and 4) strontium, neodymium and hafnium isotope compositions of all presently discovered mafic magmatic bodies in the Bakhuis belt. The age and geochemistry of two types of gabbroic bodies (the Moi-Moi metagabbro and the Charlie gabbro) is described in Thijssen (2015).

Based on petrographic indications and mineral chemistry, poikilitic hornblende in the Moi-Moi metagabbro was shown to be formed either as a primary intercumulus phase or as the result of a reaction between olivine and pyroxenes with an evolved hydrous melt. The presence of primary hornblende in the Moi-Moi metagabbro provides evidence for a hydrous magmatic origin, which is consistent with the subduction signature shown for the samples by Thijssen (2015).
Based on similar metamorphic textures, overlapping geochemistry, a common ~1980 Ma age and the presence of water in the magma as indicated by poikilitic hornblende, the Mozeskreek anorthosite is interpreted to have a common parental magma to the Moi-Moi metagabbro. Strontium, neodymium and hafnium isotope compositions for one sample did not confirm or deny a common mantle source with the Moi-Moi metagabbro. The Mozeskreek anorthosite is interpreted to have formed following the model the for Proterozoic massif-type complexes, where the relative scarcity of anorthosites in the Bakhuis belt is explained by the presence of water, which suppressed plagioclase crystallisation, in the parental magma.
In neodymium and hafnium isotopes, the Moi-Moi metagabbro shows a steeply positive trend which can be explained by up to 11-12% of magma mixing with the Kabalebo charnockites. When the data of the Moi-Moi metagabbro is corrected for mixing, the data forms a cluster around $\varepsilon Nd_{1980} \sim 1$ and $\varepsilon Hf_{1980} \sim 8$ which differs significantly from the cluster for the Charlie gabbro at εNd_{1980} of ~ 1.2 and εHf_{1980} of ~ 5. This indicates a change in mantle source and tectonic regime between the intrusion of the bodies, despite the relatively close U-Pb zircon ages of 1984 ± 5 Ma and 1970 ± 17 Ma respectively (Thijssen, 2015).

Metadolerites in the Kabalebo charnockites are pyroxene-amphibolites and occur as thin (dm-sized), continuous segments of several meters in length and as dm-sized xenoliths. Their geochemistry and hafnium and neodymium isotope compositions overlap with the Moi-Moi metagabbro, indicating a common subduction-metasomatised mantle source. This is consistent with the interpretation that the Moi-Moi magmatic event provided the heat source for melting of the granulites to produce the Kabalebo charnockites (Klaver et al., 2015; Klaver et al., *in press*).
Metadolerites in the UHT granulites occur as foliated and weakly folded pyroxene-amphibolite dykes of up to ~1 m thickness. Dyke geochemistry shows a typical subduction-metasomatised mantle signature, similar to the Moi-Moi metagabbro. Due to contamination with the hosting granulites, the strontium, neodymium and hafnium isotopes could not be used to infer a different or similar mantle source as the Moi-Moi metagabbro. Zircon crystals in one dyke were interpreted to be xenocrysts derived from the hosting granulites, leaving the age of the dykes unconstrained. Based on their similar subduction-metasomatised geochemistry, an age and relationship to the ~1.97 – 1.99 Ga magmatic event is considered to be more likely.
(Meta)dolerite dykes in the Charlie gabbro and the Mozeskreek anorthosite show a similar geochemistry to their hosting mafic bodies and are interpreted to reflect a late phase of their respective parental magmas.
A U-Pb zircon protolith age of 2098 ± 15 Ma was obtained for a single gabbroic granulite body in the center of the Bakhuis. The body shows a typical MORB-type geochemistry and radiogenic isotopes indicate a depleted mantle origin, which have presently not been described for the surrounding belts in the Guiana shield. The body is interpreted to indicate the Bakhuis belt formed a separated tectonic entity since at least 2.10, possible a narrow rift basin or a narrow developing oceanic basin.

None of the presently analyzed magmatic bodies in the Bakhuis belt show evidence for a relationship with ~2.07 Ga UHT metamorphism, making the scenario that the UHT metamorphic event did not see coeval

mafic magmatism becomes quite plausible. Consequently, the exact tectonic setting and the heat source for ~2.07 Ga UHT metamorphism remain unconstrained.

The ~1.97 – 1.99 Ga magmatic event is separated in two phases. The first phase constitutes a period of major hydrous magmatic underplating, resulting in the intrusion of the hydrous Moi-Moi metagabbro, the Mozeskreek anorthosite and melting of intermediate granulites to form the Kabalebo charnockites. The Moi-Moi metagabbro is interpreted to reflect an Alaskan-type cumulate complex, commonly associated with the root zone of an arc. The first phase is associated with regional amphibolite facies metamorphism in the Bakhuis belt and the surrounding CSID and Cauarane – Coeroeni belts, which provide further indications for the regional scale of this magmatic phase. The second phase of magmatism is formed by the intrusion of the anhydrous Charlie gabbro, which shows a HAB-type geochemistry. The body is presently only discovered in the Bakhuis belt, but can be correlated to collisional I-type and S-type granitic plutons in the CSID-belt to the south. Consequently, the transition to anhydrous melting below the Bakhuis belt is interpreted to reflect slab detachment and associated asthenospheric upwelling, as the result of collision to the south.

Table of Contents

1. Introduction

1.1 General introduction

The Bakhuis belt forms a ~30 x 100 km horst-shaped geologic anomaly of UHT granulites and plutons lying oblique to the surrounding older TTG-greenstone and younger arc-related plutonic belts of the Guiana shield (fig. 2.2). Its deviating geology provides a unique opportunity to study the events that have affected the shield during the Transamazonian orogeny (de Roever et al., 2003b; Delor et al., 2003b).

UHT metamorphic conditions of up to 950°C, at ~2.07 Ga and in a counter-clockwise P-T path were first proven for the northeast of the Bakhuis belt by de Roever et al. (2003b). Recent work of master students at the VU University Amsterdam has shown that UHT metamorphism extends over the entire belt and reaches peak temperatures up to 1050°C (de Groot, 2008; Nanne, 2013). UHT metamorphism is interpreted to reflect asthenospheric upwelling during crustal extension (Delor et al., 2003b) and the widespread occurrence of mafic and charnockitic plutons and dykes was considered to be coeval to metamorphism based on a 2.07 Ga U-Pb zircon age for a charnockite body and two of many metadolerite dykes in the belt (de Roever et al., 2003b; Delor et al., 2003b).
However, recent work on the charnockitic plutons in the southwest of the Bakhuis belt, named Kabalebo charnockite, has shown that this generation of plutonism was ≥60 Myr younger than UHT metamorphism (Klaver, 2011). Two distinct generations of (meta)gabbroic bodies occurring throughout the Bakhuis belt were recently dated to a similar age ~1.98 Ga as the Kabalebo charnockite, and their intrusion is interpreted as the heat source of melting of the UHT granulites to produce charnockite magma (Klaver et al., 2015; Thijssen, 2015).
In these recent studies, the occurrence of metadolerite xenoliths and deformed dykes in the charnockites is associated with the younger ~1.97-1.99 Ma mafic plutonic event. Contrasting with the previously obtained age of ~2.07 Ga, this could indicate that there are multiple generations of metadolerite dykes. However, the geochemistry of the various metadolerite dykes occurring throughout the Bakhuis belt is hitherto uninvestigated. Consequently, the tectonic setting and heat sources for UHT metamorphism at ~2.07 Ga are still enigmatic.

In this master thesis, which is a coupled investigation with that of Thijssen (2015), the relationship between different mafic plutonic bodies, abundant metadolerite dykes and UHT metamorphism in the Bakhuis Belt is investigated. This project is divided in several components: 1) the petrogenesis of cm-sized hornblende in metagabbroic bodies, 2) the petrography and geochemistry of a 3 x 4 km sized anorthosite body 3) the geochemistry and age of metadolerite dykes and xenoliths in plutonic bodies and 4) strontium, neodymium and hafnium isotope compositions of all presently discovered mafic magmatic bodies in the Bakhuis belt. All results are interpreted in relationship to UHT metamorphism and the geologic history of the Guiana Shield. Together with Thijssen (2015), this thesis forms a comprehensive study of the geochemistry of mafic magmatism in the Bakhuis Belt and its geologic significance.

1.2 UHT metamorphism

This section briefly describes the present knowledge on UHT metamorphism, the typical assemblages and the tectonic settings it is interpreted to occur in. For a more extensive description, see review papers such as Harley (2008), Kelsey (2008), Kelsey and Hand (2015). Much of the following section has been adopted from those papers and references therein.

1.2.1 Definition and characteristics

UHT metamorphism (fig. 1.1) is defined as

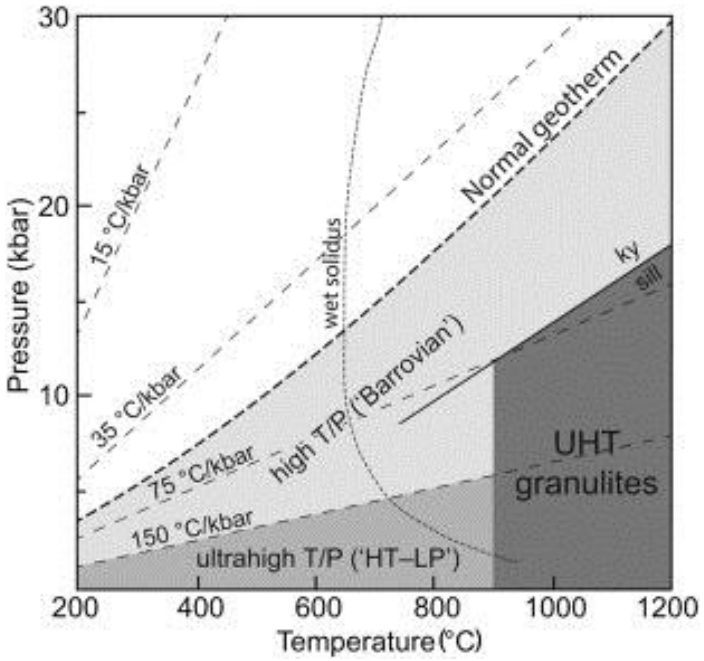

Figure 1.1. P-T diagram with the field of UHT metamorphism shaded as dark grey. Taken from Kelsey and Hand (2015).

crustal metamorphism with temperatures in excess of 900^{0}C at moderate pressures (7–13 kbar) and on a regional (>1000 km^2) scale (Harley, 1998). While most petrologists initially believed regional metamorphism could not exceed 850^{0}C, the occurrence of UHT conditions is now widely accepted as normal rather than anomalous (Kelsey and Hand, 2015). The upper boundary of UHT metamorphism is defined by the liquidus of the crustal rocks and thus dependent on the crustal rock composition, including water and CO_2 contents (Brown, 2007; Harley, 1998).
Part of the slow acceptance of UHT metamorphism by the petrologic community is due to the scarcity of diagnostic assemblages, which only occur in rather uncommon magnesium-rich pelitic gneisses (Kelsey and Hand, 2015). Diagnostic UHT metamorphic assemblages include (Harley, 2008; Kelsey, 2008):

1) Coexistence of sapphirine and quartz in a reduced setting
2) Coexistence of aluminous (>8% wt% Al_2O_3) orthopyroxene and sillimanite or other aluminous minerals such as garnet and sapphirine in a reduced setting
3) Coexistence of osumilite with garnet, orthopyroxe + sillimanite or sapphirine + orthopyroxene + quartz

Indicative but not diagnostic mineral assemblages include (Harley, 2008; Kelsey, 2008):

4) The assemblage of spinel + quartz occurs in both UHT and non-UHT granulites facies rocks
5) The assemblages of corundum + quartz is most commonly found in UHT granulites, but has also been reported in lower-grade rocks.
6) Ternary feldspar in non-magmatic protolith
7) Inverted pigeonite and quadrilateral pyroxene in non-magmatic protolith.

The significance of UHT metamorphism lies in its representation of extreme thermal crustal conditions. Understanding UHT metamorphism and where it occurs in the tectonic cycle allows us to better understand tectonic processes leading up to extreme conditions, crust-mantle interactions at the base of the lithosphere and the rheology of lithosphere.

1.2.2 Spatial and temporal distribution of UHT metamorphism

Spatially, UHT granulites are distributed over all of the continents (fig. 1.2a), occurring both in ancient Proterozoic cratons and in more recent mobile belts. Investigations in the temporal distribution of UHT metamorphism has shown that it is dominantly a Proterozoic phenomenon (fig. 1.2b), closely associated with supercontinent assembly (Brown, 2006; Kelsey, 2008). This suggests a causal relationship between crustal accretion and increased geothermal gradients.
The discovery of UHT conditions in pelitic xenoliths from lava flows in Tibet (Hacker et al., 2000) and the recent discovery of exhumed 16 Ma UHT granulites in Indonesia (Pownall et al., 2014) indicate that UHT metamorphism is still an active process in the recent geologic history.
The timescales for UHT metamorphism show a strong variation and can be classified as short (<5-40 Myr) or long (>40 Myr). The duration of UHT metamorphism is dependent on geological setting, but also the longevity of the heat source (Kelsey and Hand, 2015).

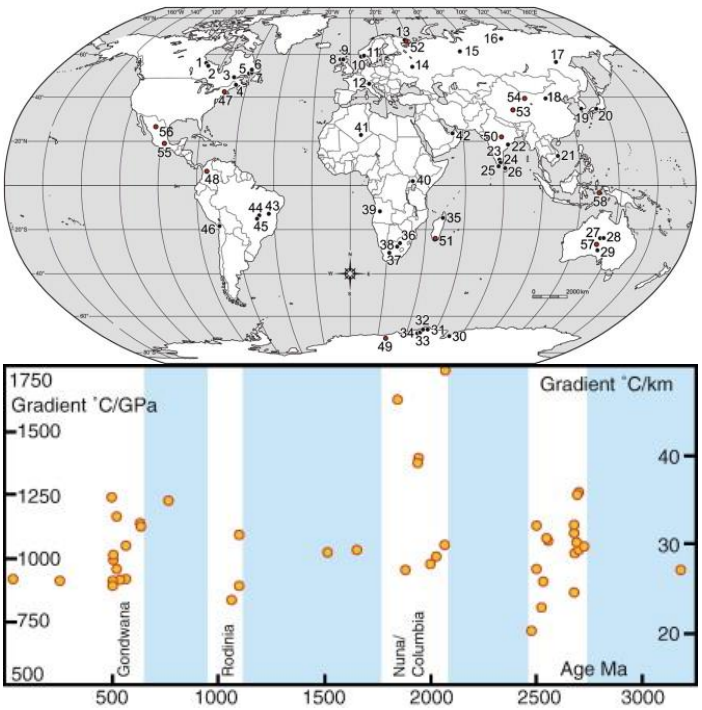

Figure 1.2. Above: All presently known areas that have experienced UHT metamorphism, taken from Kelsey and Hand (2015). The Bakhuis belt is missing in this compilation. Below: Temporal distribution of UHT metamorphic events, broadly coinciding with supercontinent assembly, taken from Kelsey (2008).

1.2.3 Heat sources

Processes providing the heat for UHT conditions are grouped in three categories: 1) Advective heating by mantle derived sources 2) Crustal radiogenic heat production and 3) conductive mantle heat flow. The processes most likely occur simultaneously, rather than in isolation (Kelsey and Hand, 2015).

Advective mantle heating

The most commonly invoked heat source for UHT metamorphism is advective heating from the mantle (e.g. (Bohlen and Mezger, 1989; Brandt et al., 2007; Collins, 2002; Ellis, 1980; Harley, 1989; Wells, 1980). However, the problem with advective mantle heating model is that the potential advective bodies derived from the mantle (mafic-ultramafic intrusive bodies) are absent from many UHT metamorphic terrains (Kelsey and Hand, 2015). In some cases intrusion of co-metamorphic mafic bodies could be directly linked to UHT metamorphism (e.g. Kemp et al., 2007; Maidment et al., 2013; Pownall et al., 2014). Extensive assimilation with lower crust producing more felsic magma's could be an explanation to solve this problem, but it has to be a rule rather than exception (Kelsey and Hand, 2015; Smithies et al., 2011).

Crustal heat production

Crustal heat production has also been invoked as a heat source for UHT metamorphism (Andreoli et al., 2006; Bea, 2012; Chamberlain and Sonder, 1990; Clark et al., 2011; England and Thompson, 1984; Kramers et al., 2001). Recent modelling of radiogenic heat production as a source for UHT metamorphism resulted in the following requirements: 1) (very) elevated (≥3.5 μW m−3) upper-crustal radiogenic heat production; 2) slow (≤0.05 mm y−1) erosion rates; 3) suppression of partial melting and 4) a suitable and volumetrically large enough (tectonic) setting that allows for incubation of the lower crust for long periods of time (Clark et al., 2011).

Elevated mantle heat flow

Lastly, elevated conductive heat flow from a hot mantle due to upwelling of the asthenosphere is proposed as a heat source for UHT metamorphism (Collins, 2002; Currie and Hyndman, 2006; England and Thompson, 1984; Hyndman et al., 2005). Elevated mantle heat flow, especially in and around back-arc basins, is indicated by elevated surface heat flow in thin lithospheric basin settings and high seismic wave velocities. Such elevated heat flow is also found for crustal areas surrounding back-arc settings (Currie and Hyndman, 2006)

1.2.4 Tectonic settings

From a tectonic perspective, UHT metamorphism requires elevated geothermal gradients. The tectonic settings where UHT metamorphism has been interpreted to occur are described in this section, in the context of the possible heat sources described in the previous section.

As UHT terrains are often very old, extensive erosion and tectonic deformation have commonly removed a full tectonic framework in which an UHT metamorphic terrain can be interpreted (Kelsey and Hand, 2015). To assess which heat sources that provide the heat of UHT metamorphism have been active, the shape of the P-T path is commonly used as an indicator of the temperature and pressure changes leading up to and following UHT metamorphism (Brown, 1993; Harley, 1989; Sandiford, 1985; Wells, 1980). The P-T paths are broadly grouped in clockwise and counter-clockwise paths (Kelsey and Hand, 2015).

Clockwise P-T paths

A characteristic feature for clockwise P-T paths is a retrograde path of isothermal decompression. This requires exhumation of the UHT terrain or thinning of the overlying crust faster than the cooling rate following UHT metamorphism.

Two main models are proposed to explain such P-T paths (Kelsey and Hand, 2015). One model is crustal thickening to Tibetan-style crust, followed by extensional collapse and/or delamination, where radiogenic heat production in the crust coupled with upwelling of mantle asthenosphere during extension provide the heat sources (Ellis, 1980; Ellis, 1987; Harley, 1989; Houseman et al., 1981; Platt and England, 1994; Sandiford, 1989). An alternative model for clockwise P-T paths is in back-arc basins, where extension thins the lithosphere and brings up the asthenosphere, elevating the mantle heat flow as a source for UHT metamorphism (Brown, 2007; Collins, 2002; Currie and Hyndman, 2006; Dasgupta et al., 2013; Hyndman et al., 2005).

Counter-clockwise P-T paths

Counter-clockwise P-T paths are characterised by near-isobaric cooling retrograde paths. This requires a relatively short-lived heat source followed by fast cooling, without substantial vertical movements or crustal thickness variations during the retrograde path.

The most popular model for counter-clockwise P-T paths is of mantle-derived magmatic underplating (fig. 1.4b), which can be caused by a mantle plume or through lithospheric extension (Bohlen, 1987; Bohlen, 1991; Brandt et al., 2007; Ellis, 1980; Ellis, 1987; Harley, 1989; Sandiford, 1989; Sandiford and Powell, 1986; Wan et al., 2013b; Wells, 1980). In this model, underplating causes the advective heat source for UHT metamorphism in the overlying crust. Alternatively, the model of thickened back-arc basins has been proposed. The back-arc basin model for UHT metamorphism would normally lead to clockwise P-T paths as described in the previous paragraph, but if basin formation is followed by renewed thickening of the back arc basin, this will also lead to retrograde near-isobaric cooling paths (Gorczyk et al., 2015; Kelsey and Hand, 2015; Walsh et al., 2015).

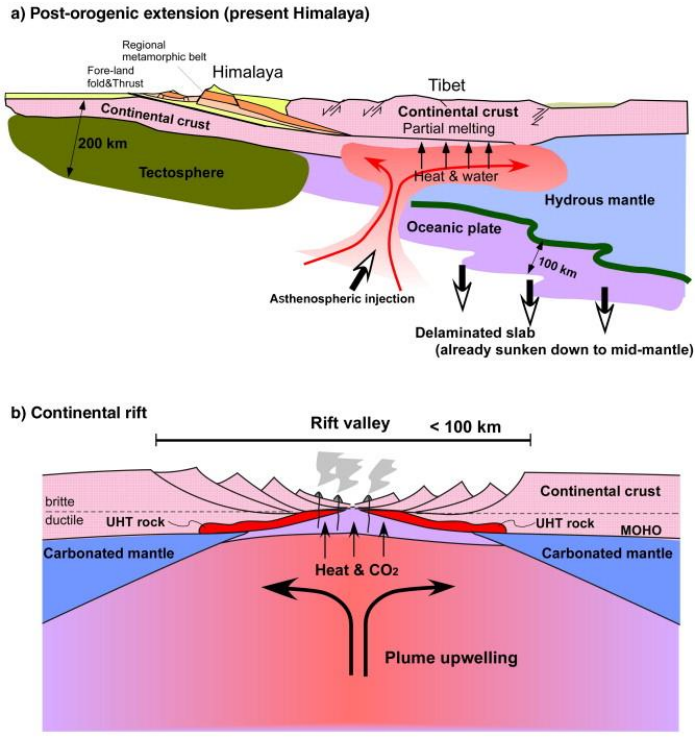

Figure 1.4. Two of multiple types of tectonic settings for UHT metamorphism, taken from Santosh and Omori (2008). A) Opening of a slab window, where hot and dry asthenosphere can reach the lower crust of the overriding plate. B) Lithospheric extension and upwelling of the asthenosphere, resulting in magmatic underplating and UHT metamorphism in the overlying lower crust.

Ridge subduction and slab windows

Most of the models above assume a 'pre-conditioned' lower crust to account for its possibility to form UHT assemblages rather than melts (Kelsey and Hand, 2015). Formation of UHT assemblages requires either water deficient conditions, or high CO_2 contents which suppress the activity of water (Clark et al., 2011; Walsh et al., 2015). However, especially back-arc basins are notoriously hydrated as the result of fluids derived from the subducting slab, while most UHT terrains are severely dehydrated (Santosh and Kusky, 2010; Santosh et al., 2011).

To solve this problem, models of ridge subduction and slab windows (fig. 1.4a) have been proposed (Brown, 1998a; Brown, 1998b; Santosh and Kusky, 2010; Santosh et al., 2011). In these models, subduction of an actively spreading ocean ridge results in a 'window' between the subducting slabs, allowing hot upwelling asthenosphere to reach the lower crust of the overriding plate. Alternatively, such a window could be formed by slab break-off during collision (Santosh and Omori, 2008). The opening of the window causes a change from hydrous mantle melting to injection of dry and hot asthenosphere, freezing the melting process and allowing UHT metamorphic conditions to occur in the lower crust.

1.3 Present knowledge of the Bakhuis belt

With its prominent location in the Guiana shield and its strongly deviating geology from the surrounding area, the Bakhuis belt can provide important information about the events that have affected the Guiana shield during the Transamazonian orogeny (Delor et al., 2003b). As described in section 1.1, the Bakhuis belt exposes a ~2.07 Ga UHT granulite complex, as well as a ~1.97-1.99 Ga suite of charnockitic and at least two generations of mafic plutonic rocks.

UHT Metamorphism and charnockites

UHT metamorphic conditions at around ~2.07 Ga with temperatures of 1050°C have recently established for the entire Bakhuis belt (de Groot, 2008; de Roever et al., 2003b; Nanne, 2013). The metamorphic

lithologies include intermediate to mafic granulites, pelitic gneisses and quartzites. For the metapelites which contain typical UHT assemblages, the P-T path was shown to be counter-clockwise, with retrograde near-isobaric cooling. The UHT metamorphism is interpreted to reflect crustal stretching and asthenospheric upwelling during the Late Transamazonian orogeny (de Roever et al., 2003b; Delor et al., 2003b)and considered to be coeval with charnockite and mafic plutons in the Bakhuis belt.
To investigate the proposed relationship with UHT metamorphism, Klaver (2011) analysed the geochemistry and age of the Kabalebo charnockites but found that they were significantly younger than UHT metamorphism and resulted from melting of UHT granulites at around ~1.99 Ga. Intrusion of the mafic plutonic rocks in the Bakhuis belt was suggested to provide the heat source for granulite melting.
While the UHT granulites and Kabalebo charnockites have been thoroughly investigated (de Groot, 2008; Klaver, 2011; Klaver et al., 2015; Klaver et al., *in press;* Nanne, 2013), much less is known about the various mafic igneous bodies and their possible relationship to UHT metamorphism.

Mafic plutonic bodies
The mafic plutonic bodies discovered in the Bakhuis belt are presently separated in three different types (de Roever et al., 2003b; Thijssen, 2015): 1) The Charlie gabbro, 2) the Moi-Moi metagabbro and 3) the Mozeskreek anorthosite.
The petrography, age and geochemistry of the Moi-Moi metagabbro and Charlie gabbro have been described by Thijssen (2015). The Moi-Moi metagabbro has been dated to 1984 ± 4 Ma using U-Pb zircon dating, and the variation and geochemistry of the bodies are interpreted to reflect hydrous Alaskan-type cumulate complexes which are associated with the root zones of an arc setting. The intrusion of the Moi-Moi metagabbro is interpreted to provide the heat source for partial melting of the UHT granulites, producing the Kabalebo charnockite magma. A characteristic feature of the Moi-Moi metagabbro is the occurrence cm-sized poikilitic hornblende crystals. Thijssen (2015) has interpreted the crystals as a late magmatic phase, based on the texture of the hornblende crystals and inclusions of plagioclase. However, mineral chemical studies to prove this hypothesis have not been performed.
The Charlie gabbro has been dated to 1970 ± 17 Ma using U-Pb baddeleyite dating, and is interpreted to have crystallised from an anhydrous tholeiitic high-alkaline basalt (HAB) magma, which is interpreted to reflect dry mantle melting possibly as part of a large igneous province.
The age of Mozeskreek anorthosite has previously been investigated for its possible relationship to UHT metamorphism (de Roever et al., 2003b). However, the obtained a Pb-Pb zircon age of 1980 ± 5 Ma indicated that the magma belongs to the ~1.97-1.99 Ga plutonic event. Consequently, the Mozeskreek anorthosite can provide valuable information about the ~1.97-1.99 plutonic event, yet at present the geochemistry and a petrogenetic interpretation for the anorthosite have not been established.
The strongly similar age, yet varying geochemistry, hydrous vs. anhydrous conditions and tectonic interpretation of the different gabbroic bodies are puzzling. Their mutual relationships are presently not well enough understood or explained by a satisfying petrogenetic model.

Metadolerite dykes and small intrusive bodies
The widespread occurrence of metadolerite dykes up to ~1 m thick has been described as a 'special characteristic of Bakhuis belt metamorphism' by de Roever et al. (2003b), who considered them to be coeval to UHT metamorphism. de Roever et al. (2003b) obtained a U-Pb zircon age for a foliated metadolerite dyke of 2060 ± 4 Ma. That conclusion was additionally supported by the (partially) syn-kinematic, folded and boudinaged character of the dykes. However, Klaver et al. (2015) has shown metadolerites also occur as deformed dykes and xenoliths in the Kabalebo charnockites indicating at least partially a co-magmatic origin. They suggest the 2060 ± 4 Ma age obtained by de Roever et al. (2003b) reflects xenocrystic zircon from the hosting granulites and the metadolerite lenses in the charnockites should be associated with the intrusion of the (meta)gabbroic bodies. However, in lack of detailed geochemical data on the metadolerite dykes and a study on the origin of zircon in the metadolerite dykes, their exact age and relationship with UHT metamorphism or younger plutonism cannot be established.

1.4 This study

1.4.1 Thesis goals and outline
Completing our present understanding of the mafic igneous bodies in the Bakhuis, this MSc thesis together with Thijssen (2015) investigates the possible relationship between mafic igneous bodies and UHT metamorphism. While Thijssen (2015) describes the age and geochemistry of the (meta)gabbroic bodies of the Bakhuis belt, this thesis describes several, more fragmented components that contribute to our understanding of the mafic magmatic history of the Bakhuis belt.

Given the strong variation in research components in this thesis, this MSc thesis would appear strongly fragmented if they are simply presented one after the other. To bring order into chaos, the results of this thesis are separated in a chapter that concerns the geochemistry of mafic plutonic bodies (chapter 4) and a chapter that concerns the geochemistry of (meta)dolerite dykes and smaller intrusive bodies (chapter 5). The goals of the different components of this thesis are explained based on the thesis outline below.

For the mafic plutonic bodies (chapter 4), the main goal was to further understand the ~1.97-1.99 Ga plutonic event and the relationship between the different mafic plutonic bodies. Chapter 4 is separated in the following sections:

4.1) **The petrogenesis of cm-sized hornblende crystals in the Moi-Moi metagabbro** is investigated using petrography and mineral chemistry. If the hornblende is of magmatic origin, this would provide indications for water in the parental magma.

4.2) **The petrography and geochemistry of the Mozeskreek anorthosite** is investigated to determine the mechanism for anorthosite formation and a possible relationship to the other plutonic bodies.

4.3) **The strontium, neodymium and hafnium isotope variation for the different bodies** are investigated to determine mutual differences or possible relationships. Also, the variation is used assess contamination or mixing with crustal magmas such as the Kabelebo charnockite.

For the metadolerite dykes and small plutons, the main goal was to establish whether these bodies are related to UHT metamorphism or to the ~1.97-1.99 Ga mafic plutonic event. Chapter 5 is separated in the following sections:

5.1) **Field observations and petrography** were investigated to determine whether the bodies show indications for a syn-metamorphic or a syn-plutonic origin to their host rocks. These interpretations were based on field observations of folding, foliation and/or boudinage in the bodies and the degree of metamorphism.

5.2) **Geochemistry** was investigated to characterise the (meta)dolerite dykes and xenoliths and to determine whether there is any geochemical overlap with the other plutonic bodies.

5.3) **The strontium, neodymium and hafnium isotope variation** were investigated to establish whether the dykes represent separate magmas or share a common mantle source with the mafic plutonic bodies. Also, possible contamination with the host rock is investigated.

5.4) **An attempt to determine U-Pb zircon or baddeleyite ages** for the metadolerite dykes and a small gabbroic granulite body is made. A common age with ~2.07 Ga UHT metamorphism or ~1.97-1.99 Ga plutonism would provide direct evidence for a synchronous origin and/or indications for a heat source for either process.

These chapters are preceded by a chapter on the geologic history of the Guiana Shield and the Bakhuis belt (chapter 2), followed by a chapter on the methodologies used in this thesis (chapter 3). Discussion of the results is in chapter six, which includes 1) the relationships between the different mafic igneous bodies, 2) the applicability of the results with the present models for both UHT metamorphism at ~2.07 Ga and mafic plutonism at ~1.97-1.99 and 3) the significance of the results for the geologic history of the Bakhuis belt and the Guiana Shield. The conclusions are summarised in chapter 7. All geochemical data are added in appendices as per the table of contents.

1.4.2 Project framework and funding

This thesis is executed as part of the master programme Earth Science, specialisation: Solid Earth at the VU University Amsterdam. The project constitutes the courses 'Master Thesis Solid Earth' (course code AM_450199) and 'Extension Master Thesis Earth Sciences' (course code AM_450149), which add up to 39 EC. Daily supervision of this thesis is executed by Dr. Emond W.F. de Roever. As Emond is retired and presently a guest-lecturer at the VU University Amsterdam, Dr. Fraukje M. Brouwer acts as a VU supervisor while Prof. Gareth R. Davies is acting as a second assessor.

This project is financially supported by the Dr. Schürmann Foundation for the costs of fieldwork and supervision and LA-ICP-MS analyses, the Molengraaff Foundation and the Faculty of Earth and Life Sciences of the VU University Amsterdam for travel and lodging costs in Suriname.

1.4.3 Nomenclature

Throughout the report, the various generation of plutonic bodies are labelled following the recent names given to the bodies by authors who have described them. The Kabalebo charnockite refer to the charnockitic bodies described in Klaver (2011). The Moi-Moi metagabbro and the Charlie gabbro refer to

the two distinct gabbroic bodies following Thijssen (2015). The Mozeskreek anorthosite is a term first introduced in this report and refers to the body of anorthosites to leucogabbros occurring at the Mozeskreek, which is described in section 4.2.
Mineral abbreviations used in this thesis are after Whitney and Evans (2010).

2. Geologic setting

2.1 Regional geology of the Bakhuis Belt

2.1.1 The Guiana shield

2.1.1.1 Location and geology

The Guiana shield (fig. 2.1) is part of the Amazonian craton, which forms the oldest continental nucleus of South America. The Amazonian shield takes up the larger part of northern and central South America and consists of the Brazil Central Shield in the south and the Guiana shield in the north, separated by the Amazon trough. The formation of the Amazon trough is associated with the breakup of Gondwana and the opening of the Atlantic Ocean since the late Paleozoic. The trough consists of an Amazonian craton basement covered by Paleozoic and Mesozoic sediments. The Guiana shield covers most of Venezuela, the Guyana's, Suriname and the part of Brazil north of the Amazon through. Its western boundary is formed by the Andean orogenic chain and it is north-eastern boundary by the passive margin to the Atlantic Ocean.

Figure 2.1. Location of the Guiana Shield and the Brazil Central Shield and the Amazon trough in between. Together, these form the Amazonian craton. Modified from da Rosa-Costa et al. (2009).

In the far west, the Imataca complex in Venezuela exposes the oldest Archean crust which has been reworked during the Paleoproterozoic, yielding protolith ages between 3.7 – 2.6 Ga (Montgomery and Hurley, 1978; Tassinari et al., 2004). Archean relics of 3.3 – 2.6 Ga are also exposed in Amapá, Brazil (Avelar et al., 2003; da Rosa-Costa et al., 2008; da Rosa-Costa et al., 2006; da Rosa-Costa et al., 2003). In between the Archean relics, the Guiana shield exposes a roughly NNW-SEE striking Paleoproterozoic belt, which consists mainly of greenstones and tonalite-trondhjemite-granodiorites (TTGs) and becomes progressively younger towards the southwest (Delor et al., 2003b). The belt is separated in a western Venezuela - Guyana belt and an eastern Suriname – French Guyana – Brazil belt, separated by the Bakhuis belt in Suriname. The belt was formed during the Transamazonian orogeny, which was the result of the collision between the West African craton and a proto-Amazonian craton during the Rhyacian. A general geologic map of the Guiana shield is shown in figure 2.2.

2.1.1.1 Tectonic history of the Guiana Shield and associated rocks

Most of the following section is adopted from Delor et al. (2003b), updated with recent literature. In his paper, he separates the Transamazonian orogeny in two phases: the Main Transamazonian event (2.26 – 2.08 Ga) and the Late Transamazonian orogeny (2.07 – 1.93 Ga). The general tectonic history is graphically summarized in figure 2.3.

Pre-Transamazonian rifting: 2.26 – 2.20 Ga

Aside the Archean relics, the oldest rocks in the Guiana shield are the Paleoproterozoic gabbro's and trondhjemites of 'Île de Cayenne' in French Guyana, dated as 2216 ± 4 Ma and 2174 Ma (Milesi et al., 1995). Locally, similar U-Pb zircon protolith ages and Sm-Nd model ages are found for greenstones and TTGs elsewhere in the TTG-greenstone belt (Delor et al., 2003a). These rocks are interpreted to reflect juvenile tholeiitic ocean floor magmatism, either in a mid-ocean ridge or a back-arc setting, indicating an early Transamazonian stage of rifting during the Eorhyacian (2.26 – 2.20 Ga) (Delor et al., 2003b).

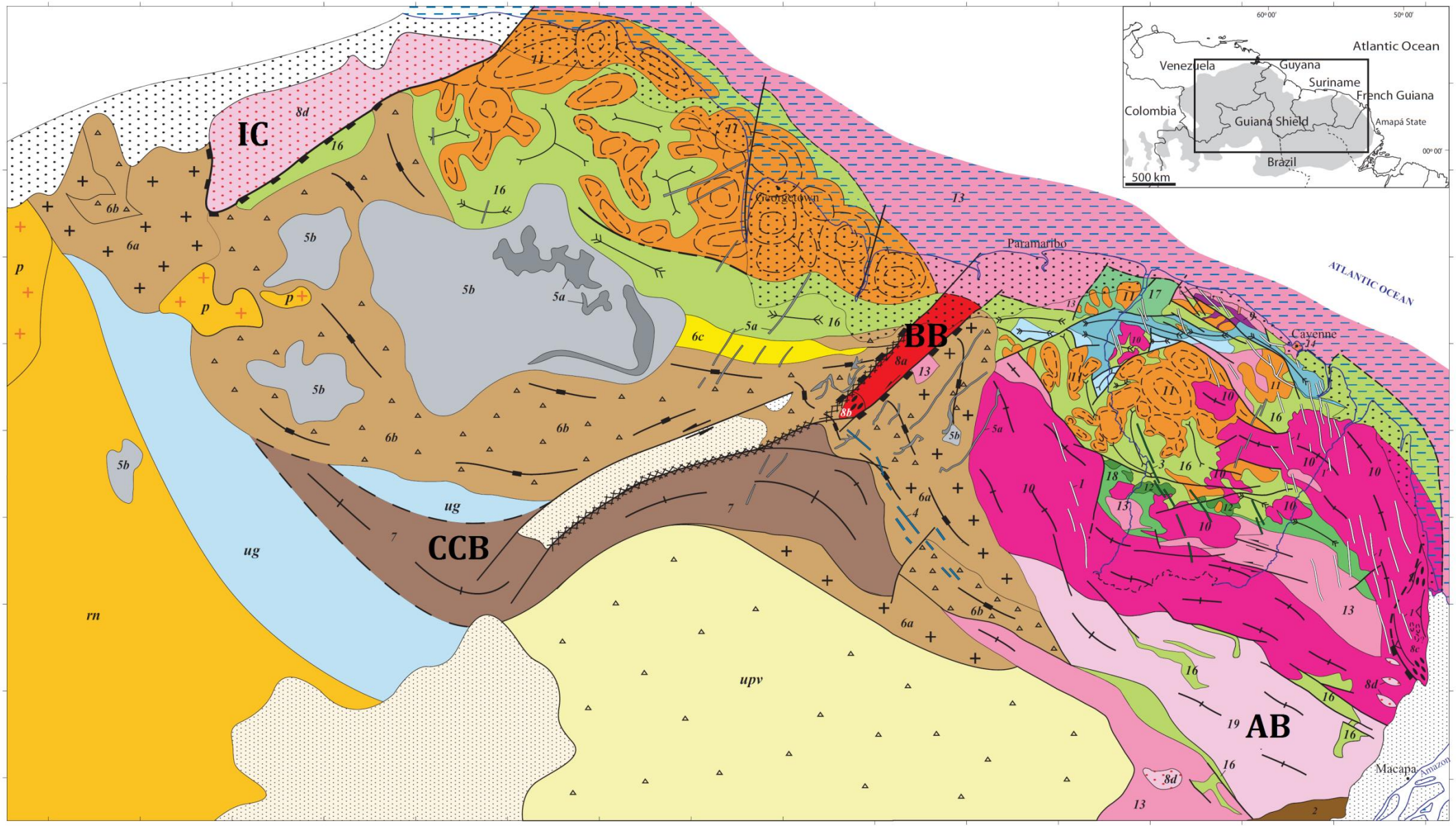
65°
63°
61°
59°
57°
55°
53°
51°
7°
5°
3°
1°
IC
BB
CCB
AB
Georgetown
Paramaribo
Cayenne
Macapa
ATLANTIC OCEAN
Atlantic Ocean
Venezuela
Guyana
Suriname
French Guiana
Colombia
Guiana Shield
Amapá State
Brazil
500 km
60° 00'
50° 00'
00° 00'
8d
16
11
6b
6a
5b
p
5a
6c
8a
8b
13
17
10
1
18
12
3
4
7
ug
rn
upv
19
2
8c

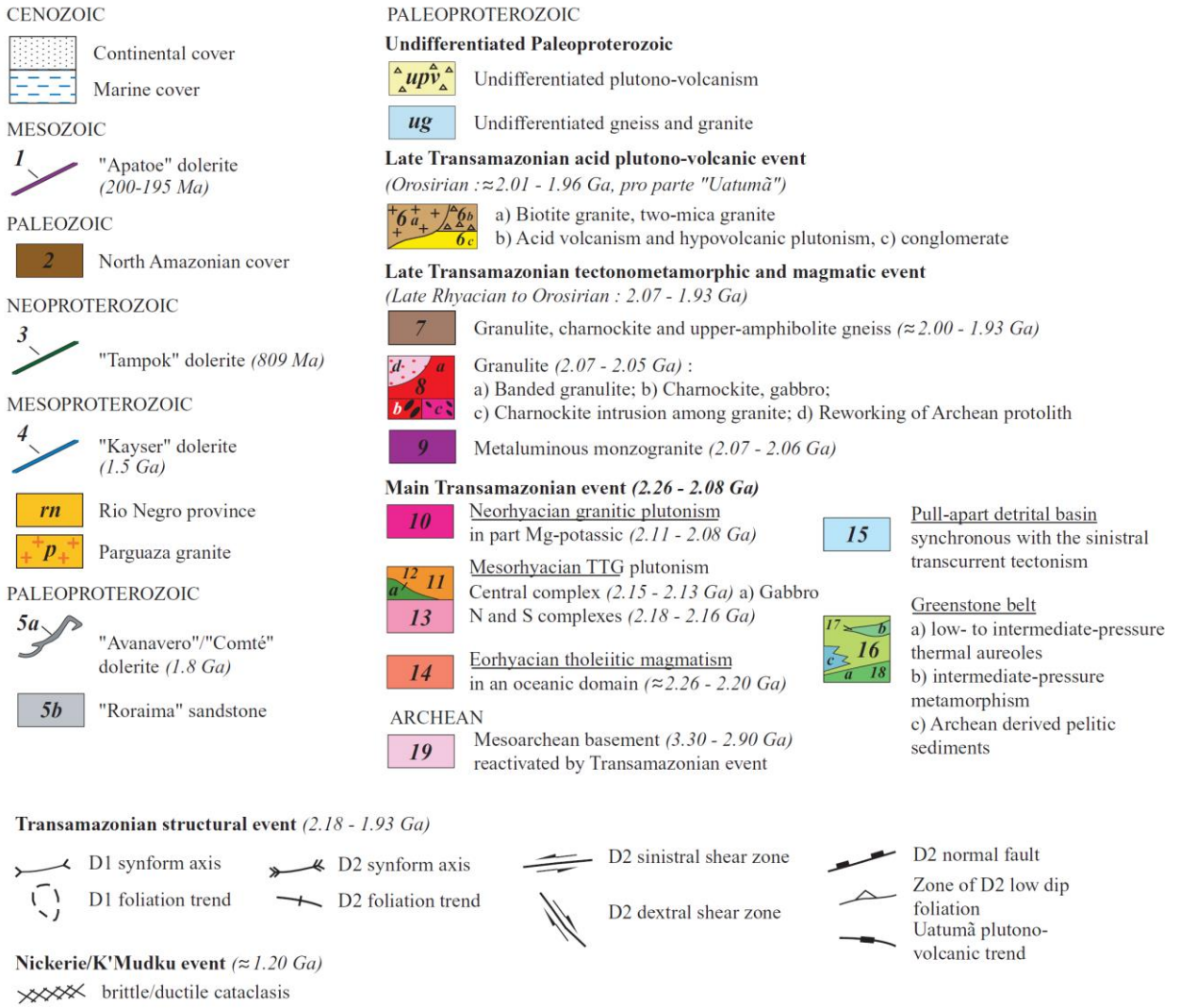

Figure 2..2 Geological map of the Guyana Shield (previous page) modified from Delor et al. (2003b). Abbreviations indicate: IC, Imataca Complex; CCB, Coeroenie – Cauarane Belt; BB, Bakhuis Belt; AB, Amapá Block.

Main Transamazonian convergence: 2.18 – 2.13 Ga

The greenstones and TTG plutonism are considered to reflect a convergent setting with southward subduction north of the Amazonian craton (Delor et al., 2003b). The formation of the eastern greenstone belt is dated as 2.18 – 2.13 Ga. It records the oldest ages for TTG plutonism of 2.18 – 2.16 Ga in its north and south extremes, whilst the center of the belt records 2.15 – 2.13 Ga TTG plutonism (Delor et al., 2003a; Delor et al., 2003b). The lower limit in ages of 2.13 – 2.12 Ga recorded in the western belt indicates a similar pattern to the eastern belt (Day et al., 1997; Norcross et al., 2000). The greenstones in the TTG-greenstone belts consist of 1) submarine volcanic sequences ranging from mafic-ultramafic lava flows to intermediate and felsic volcanic rocks and 2) sediments derived from the adjacent arc. Positive εNd ratios for felsic volcanic, sedimentary and plutonic rocks (Lafrance et al., 1999; Nogueira et al., 2000) indicate a juvenile origin for the TTG-greenstone belt, precluding involvement of Archean rocks (Delor et al., 2003b).

Main Transamazonian sinistral shear and plutonism: 2.11 – 2.08 Ga

Around 2.11 – 2.10 Ga, suturing of the West-African craton with the TTG-greenstone belts and the Amazonian craton leads to a change of direction to NE-SW compression causing sinistral wrenching and the formation of pull-apart basins between continental-scale strike-slip faults (Théveniaut et al., 2006; Vanderhaeghe et al., 1998). Collision has also lead to migmatisation of the TTG-greenstones producing granitic suites, which have been dated as 2.11 – 2.08 Ga (Delor et al., 2003b). The migmatisation of the TTG-greenstones is interpreted as the result of anomalous thermal gradients due to mantle perturbation

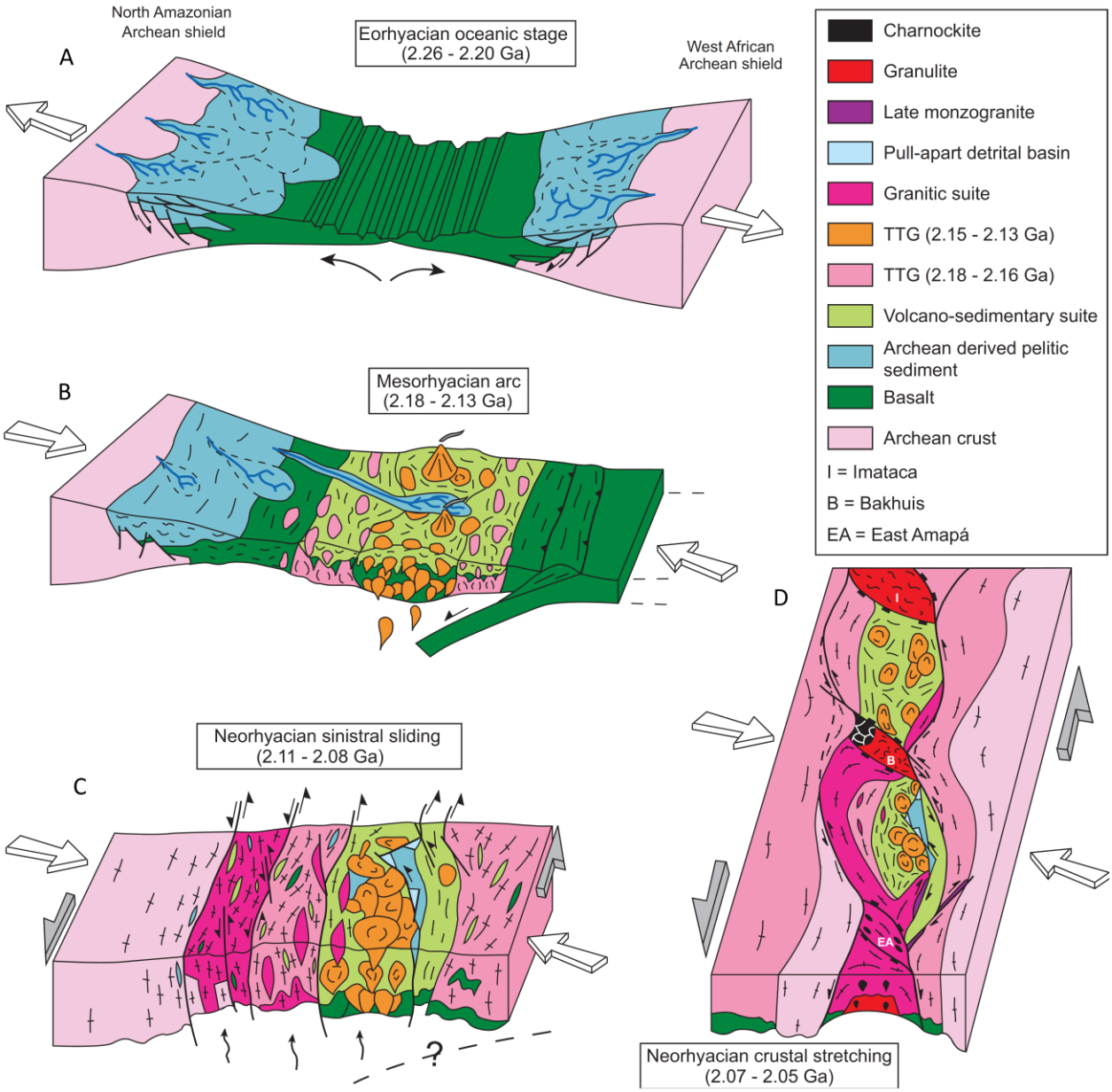

Figure 2.3 Tectonic history of the Guyana Shield after Delor et al. (2003b). A: Pre-Transamazonian rifting during the Eorhyacian. B: Convergence and southward subduction, associated with greenstone and TTG formation during the Mesorhyacian. C: Suturing and sinistral strike slip motions during the early Neorhycian. D: Formation of crustal scale boudins, separated by three granulite belts. Further explanation in text.

(Delor et al., 2003a). The granitic suites now occupy the larger part of southern French Guyana and south-eastern Suriname.

Late Transamazonian granulite metamorphism: 2.07 – 2.05 Ga

Continued sinistral shearing is transitioned into continental scale boudinage of the single TTG-greenstone belt into two separate eastern and western TTG-greenstone belts (Delor et al., 2003b). The boudinage is interpreted to be responsible for mantle upwelling, providing the heat source for (UHT) granulite metamorphism (de Roever et al., 2003b; Delor et al., 2003b). The two TTG-greenstone boudins are bounded by three granulites domains: 1) The Imataca complex in the west, 2) the Bakhuis belt in between the two boudins and 3) the Eastern Amapá belt in the east.

While the Bakhuis belt records UHT conditions at ~2.07 Ga and does not show indications for Archean protoliths (de Roever et al., 2003b; Klaver et al., 2015), the Imataca and Amapá complexes contain relict Archean crustal domains and show comparatively lower granulite facies metamorphic conditions over different timespans. The Amapá block experienced granulite metamorphism at 2.10 – 2.09 Ga, while the

Imataca shows granulite metamorphism between 2.05 – 1.98 Ga followed by amphibolite facies metamorphism at 2.01 – 1.96 Ga (Tassinari et al., 2004).

Late Transamazonian granulite metamorphism and plutonism: 2.03 – 1.96 Ga

Younger (2.0 – 1.96 Ga) high grade metamorphism is recorded in the Cauarane – Coeroeni belt which occurs south of the TTG-greenstone belt. The belt has a sinuous shape, connecting the Coeroeni group in southwest Suriname with the Kanuku Complex in central Guyana and the Cauarane group in northern Brazil (Delor et al., 2003b; Fraga et al., 2009b; Nadeau et al., 2013). The metamorphism in the Cauarane – Coeroeni belt is slightly older than the intrusion of granitic and metavolcanic rocks in a long belt south of the TTG-greenstone belt, the Cuchivero-Surumu-Iwokrama-Dalbana (CSID) igneous belt (Delor et al., 2003b), see also section 2.1.2. These phases of metamorphism and plutonism are considered the result of continued collision, causing the initiation of a N-directed subduction zone south of the TTG-greenstone belt (Fraga et al., 2009b; Klaver et al., 2015).

Post-Transamazonian: Sedimentation, the Nickerie event and dyke swarms

The stabilization of the central part of the Guiana shield is marked by the deposition of the discordant Roraima Supergroup in the western TTG-greenstone belt, starting at 1.90 Ga (Minter, 2006; Santos et al., 2003). However, recently it has been shown that the (south-)western parts of the Guiana shield experienced magmatism and metamorphism until the Mesoproterozoic (Fraga et al., 2009a and references therein).

Since stabilisation, the ~1.2 Ga tectono-thermal Nickerie event has reset the Rb-Sr and K/Ar chronometers for most of the rocks in the western part of the Guiana shield. The event is related to the formation of the Gondwana continent in the Grenvillian orogeny and is assumed to have formed mylonitic fault zones which are interpreted to have exhumed the Bakhuis belt (Cordani et al., 2010; de Roever et al., 2003b; Priem et al., 1971).

Three generations of dyke swarms cut through the Guiana shield and the covering Roraima Supergroup. The Avanavero suite is the oldest generation and consist of 1.79 - 1.78 Ga gabbroic dykes and sills and is interpreted to represent a Large Igneous Province (Norcross et al., 2000; Reis et al., 2013; Santos et al., 2003). The Kayser dolerite is an alkaline swarm of mainly NW-SE striking narrow alkali basaltic dykes, which has been dated by biotite $^{40}Ar/^{39}Ar$ dating as ~1.5 Ga.. The Apatoe dolerite is a dyke swarm of continental pigeonite tholeiites, which are related to the initial breakup of Gondwana and opening of the Atlantic Ocean around 200 – 195 Ma (Deckart et al., 1997).

2.1.2 The Bakhuis Granulite Belt and Western Suriname

The Bakhuis Belt forms a ~30 km x ~100 km horst-shaped NE-SW striking belt in western Suriname (fig. 2.4). The horst was suggested to be connected to the Kanuku horst in Guyana, but a continuation is lacking and is now considered to be a separate entity in the geology of Suriname based on e.g., its older age for metamorphism (de Roever et al., 2003b). The Bakhuis belt consists of a ~2.07 Ga metamorphic suite (de Groot, 2008; de Roever et al., 2003b; Nanne, 2013), which was intruded by ~1.97 – 1.99 Ga charnockitic and gabbroic bodies (Klaver, 2011; Klaver et al., 2015; Thijssen, 2015).

The belt is surrounded by the CSID-belt, which is a 1.99 – 1.98 Ga suite of felsic metavolcanic and plutonic rocks associated to the late Transamazonian plutonic phase. The belt is bounded by the TTG-greenstone belt to the north and the Cauarane – Coeroeni belt to its south, which extends from Venezuela to central Suriname and southwards into Brazil. Felsic igneous activity in the CSID-belt was described in detail by (de Roever et al., 2010; Delor et al., 2003b).

The belt consists of felsic metavolcanics conformably overlying a basal sequence of sandstones and conglomerates, which both show high grade metamorphism and open folding. A suite of hypabyssal leucogranites and granophyric and fine-grained granites is considered to be co-magmatic. The series are intruded by biotite granites with K-feldspar megacrysts. The granites contain xenoliths of the first generation igneous rocks, confirming the age relationships (de Roever et al., 2010; Delor et al., 2003b and references therein).

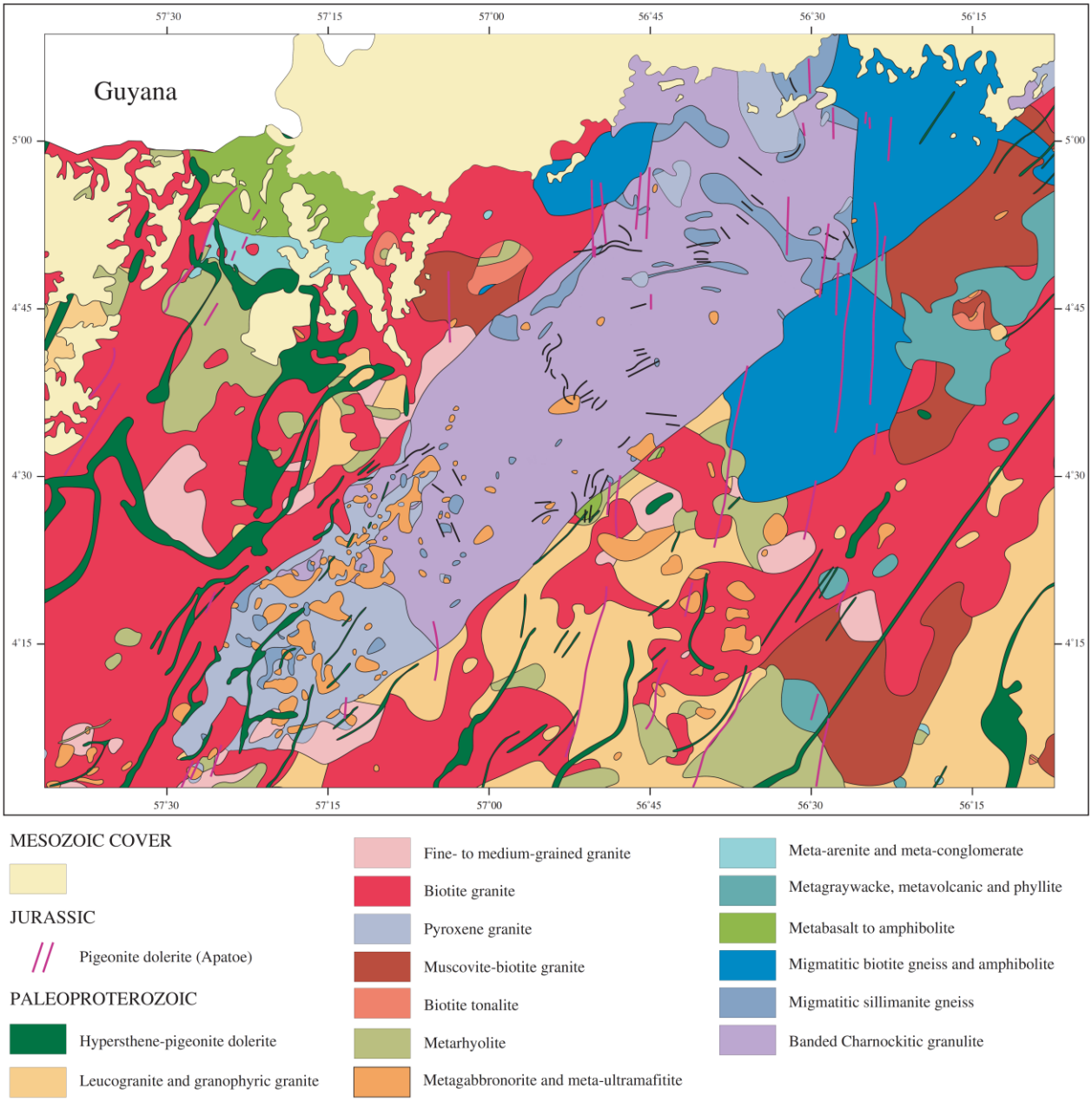

Figure 2.4. Map of the Bakhuis Belt and surrounding area, modified after de Roever et al. (2003b).

2.2 Bakhuis Granulite Belt

The belt exposes a ~2.07 Ga banded series of intermediate and mafic granulites and metapelitic gneisses and a ~1.97-1.99 Ga igneous series of charnockites and (meta)gabbroic and (meta)dolerite bodies (de Roever et al., 2003b; Klaver et al., 2015; Nanne, 2013; Thijssen, 2015). UHT metamorphic conditions were recently shown to occur over the entire belt (Nanne, 2013).

2.2.1 Structure

The Bakhuis belt is separated from the surrounding granites and metavolcanics of the CSID-belt by two NE-SW striking mylonitic boundary faults. Along the boundary faults, mylonitisation extends from the faults into Bakhuis belt over a zone of up to several 100s of meters, which is observable at the Kabalebo resort for example. In the center of the Belt, pelitic lenses and banding and foliation of the granulites are subvertical and parallel to the boundary faults. In the northeast of the belt, these structures bend towards the east forming a dome structure (fig. 2.4), which is cut by the SE boundary fault (de Roever et al., 2003b).

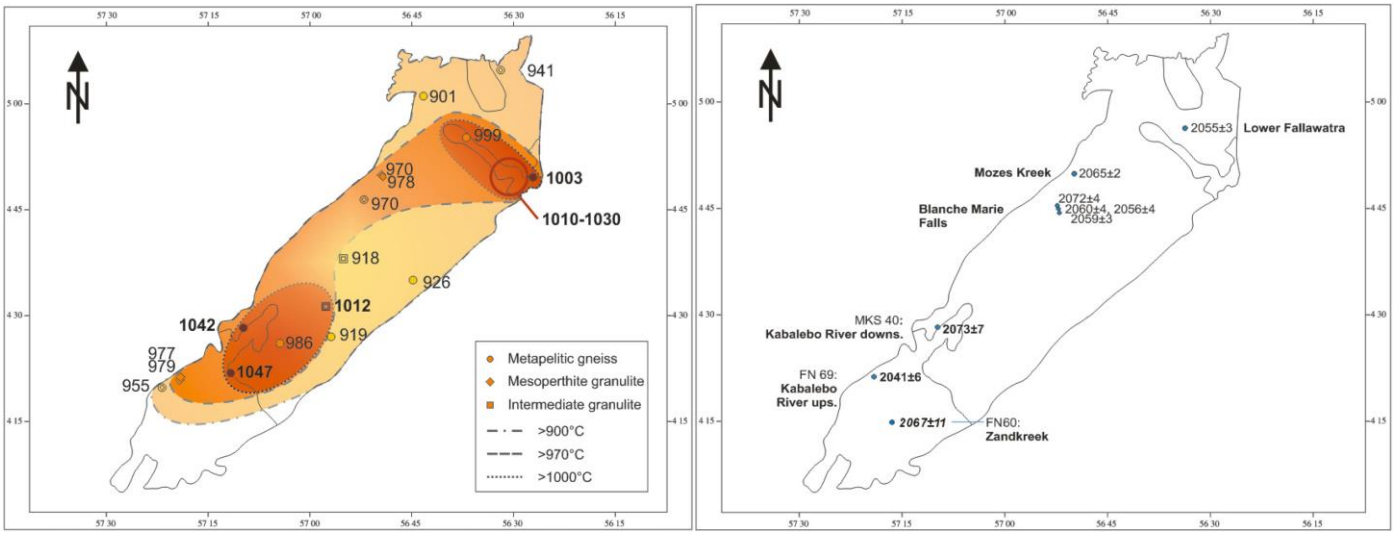

Figure 2.5. Map of peak temperatures (left) and the age of peak metamorphism (right) in the Bakhuis Belt during the ~2.07 Ga UHT metamorphic event. Both maps taken from Nanne (2013).

2.2.2 ~2.07 Ga UHT metamorphism and associated lithologies

Initially, UHT metamorphism was only thought to occur in the a rather small metapelite area in the NE of the Bakhuis belt, based on the occurrence of characteristic assemblages Opx + Sil + Qtz and Spr + Qtz, P-T conditions of 950°C and 8.5-9 kbar were inferred (de Roever et al., 2003b). More recently, feldspar thermometry has shown that conditions of >900°C extend to the entire Bakhuis belt, showing a double-dome shape (fig. 2.5a) in peak temperature conditions (Nanne, 2013). Mineralogical evidence showed the metapelites with characteristic assemblages in the NE experienced a counter clockwise P-T path; with prograde assemblages of Crd + Sil to Spr + Qtz and peak assemblages of Sil + Opx + Qtz. The retrograde path shows (near) isobaric cooling, indicated by a reduction of the aluminium contents from core to rim in orthopyroxenes (de Groot, 2008; de Roever et al., 2003b).

The age of UHT metamorphism has been established using Pb-Pb evaporation (de Roever et al., 2003b) and U-Pb LA-ICP-MS dating (Klaver et al., 2015; Nanne, 2013) on zircon from various UHT granulite lithologies. Ages range between 2040 – 2075 Ma, displaying a similar range over the entire Bakhuis belt and producing a ~30 Ma time span for UHT metamorphism (Nanne, 2013; fig. 2.5b). Older 2130 – 2150 Ma ages have been interpreted as inherited protolith ages (de Roever et al., 2003b; Klaver et al., 2015).

The exposed UHT lithologies are dominantly intermediate to mafic banded granulites, with mappable intercalations of pelitic gneisses. The granulites show compositional banding on cm to m scale and a foliation expressed in preferred orientation of both mafic and felsic minerals. Incipient migmatisation under anhydrous granulite conditions is common, forming thin granoblastic Opx-bearing quartzofeldspathic leucosomes which enhance compositional banding. The rocks show syn-metamorphic isoclinal to tight folding with steeply plunging fold axes. Intermediate granulites contain assemblages of Opx + (antiperthitic) Pl + Qz ± Cpx ± Hbl ± Bt ± K-fsp with accessory magnetite, Fe-Ti oxides, zircon and apatite. Mafic granulites contain Opx + Cpx + Pl + Hbl + Bt, ranging from pyroxene amphibolites to nearly Hbl-free granulites with abundant pyroxenes. Pelitic gneisses outside the characteristic UHT occurrence in the NE contain Sil ± Opx + Qz + (antiperthite) Pl ± Mg-rich Crd ± Bt ± Grt with accessory oxides and green spinel. The banding of the granulites indicates a supracrustal origin whilst intercalations of pelitic gneiss, quartzite and calc-silicate granulites indicate a sedimentary protolith (de Roever et al., 2003b; Nanne, 2013).

Based on a similar age for metadolerite dykes which were interpreted to be syn-kinematic, the intrusion of abundant mafic and charnockitic plutonic bodies were considered to be coeval to UHT metamorphism (de Roever et al., 2003b). Delor et al. (2003b) interpret UHT metamorphism as the result of a mantle-driven thermal perturbation and upwelling of the asthenosphere due to crustal stretching. Such a scenario would be consistent with the counter clockwise P-T path found by de Roever et al. (2003b). However, most mafic bodies have recently been shown to be younger than UHT metamorphism (Klaver et al., 2015; Thijssen, 2015).

2.2.3 Igneous bodies and their relationship to UHT metamorphism

The UHT granulites are intruded by various magmatic bodies. The results and conclusions of the MSc thesis of Thijssen (2015) are included to provide a full overview of the present knowledge of the igneous bodies. Mafic and charnockitic plutonic bodies have been dated to intrude around ~1.99 – 1.98. Much less is known about the (meta)dolerite dykes, which occur in both UHT granulitic and plutonic lithologies (de Roever et al., 2003b; Klaver et al., 2015; Klaver et al., *in press;* Thijssen, 2015).

2.2.3.1 ~1.99 – 1.97 plutonism

Orthopyroxene bearing granitoids (named Kabalebo charnockites) are the dominant lithology in the southwest of the Bakhuis belt and have intruded in between relict occurrences of banded granulites and pelitic gneisses. The Kabalebo charnockites co-occur with smaller, km-scale, mafic-ultramafic bodies which were separated by Thijssen (2015) in two groups: 1) the hydrous Moi-Moi metagabbro containing cm-sized poikilitic hornblende and 2) the anhydrous tholeiitic Charlie gabbro. A small 3 x 4 km body of anorthosites and leucogabbros is exposed in the centre of the belt (de Roever et al., 2003b), which is here named the Mozeskreek anorthosite.

Kabalebo Charnockites

The Kabalebo charnockite have a homogeneous, massive appearance and commonly show primary porphyritic textures with no evidence for metamorphism, although mylonitisation commonly overprinted the magmatic textures. The charnockites typically contain plagioclase, alkali-feldspar, ortho- and clinopyroxene, quartz and biotite with accessory apatite, zircon and Fe-Ti oxides which are also partly secondary. Antiperthitic exsolution in feldspar and inverted pigeonite indicate high crystallisation temperatures of up to 960 – 990°C. U-Pb zircon dating record crystallisation ages of 1993 – 1984 Ma (Klaver et al., 2015). The ≥60 Ma time gap with ~2.07 Ga UHT granulite metamorphism lead Klaver et al. (2015) to invoke a second UHT-like event around 1980 Ma. However, no evidence for UHT conditions during a second event is documented in the granulites, indicating the > 900°C temperatures are restricted to crystallising igneous bodies and the event falls outside the definition of UHT metamorphism (Harley, 1989; Kelsey and Hand, 2015). Based on elevated potassium, zircon, REE and barium contents, it is interpreted that melting of intermediate UHT granulites provided the source of the charnockite magma. The presence of co-magmatic metadolerite enclaves in the charnockites is interpreted to indicate that mafic magmatism was the heat source for melting of the granulites (Klaver et al., 2015).

Moi-Moi Metagabbro (formerly 'De Goeje' gabbro)

A suite of numerous, km-scale metagabbroic bodies in the Bakhuis belt has been named the Moi-Moi metagabbro by Thijssen (2015). Previous work has described these bodies as 'De Goeje gabbro' and shown that they are also common in the north- and southwest of Suriname outside the Bakhuis belt (Bosma et al., 1984).

The suite shows a strong variation in lithologies which are commonly found in close association, ranging from quartz diorites to peridotites-dunites, where hornblende-bearing gabbronorites are the dominant variety. A gradual transition from pyroxenites at the base to gabbronorites at the top has been observed in drill cores. Field exposures show lateral variation from ultramafics in the core to gabbronorites to quartz-diorites at the boundary of the body. The variation is interpreted to reflect accumulation and fractionation processes of a similar gabbroic parental magma (Bosma et al., 1984).

A typical characteristic for the bodies is the presence of up to 5 cm large poikilitic hornblende crystals, which enclose commonly only feldspar, but in some rocks also pyroxene and olivine. Red-brown biotite and phlogopite are also common, providing more indications for the presence of water (Bosma et al., 1984). Other textures and mineralogy may vary between localities. Metamorphism of the body in greenschist or amphibolite facies is common, yet strongly depends on local conditions (Bosma et al., 1984). In the Bakhuis belt, primary magmatic textures are commonly obscured by subsequent metamorphism, which has given the rocks a granoblastic texture. Inside poikilitic hornblende, lath shaped feldspar crystals still indicate primary magmatic textures (Thijssen, 2015).

The geochemistry indicates a subduction signature, with LILE enrichment a Nb-Ta and HFSE depletion. The bodies have a large similarity to Alaskan-type complexes which are associated with the root zone of volcanic arc complexes. Based on the age relationships, intrusion of the Moi-Moi metagabbro is considered to be responsible for Kabalebo charnockite magmatism (Thijssen, 2015).

Charlie Gabbro

A suite of gabbroic rocks is described for the first time and named the Charlie Gabbro by Thijssen (2015). The suite is so far exclusively described in the Bakhuis Belt and occurs as massive cumulates of plagioclase

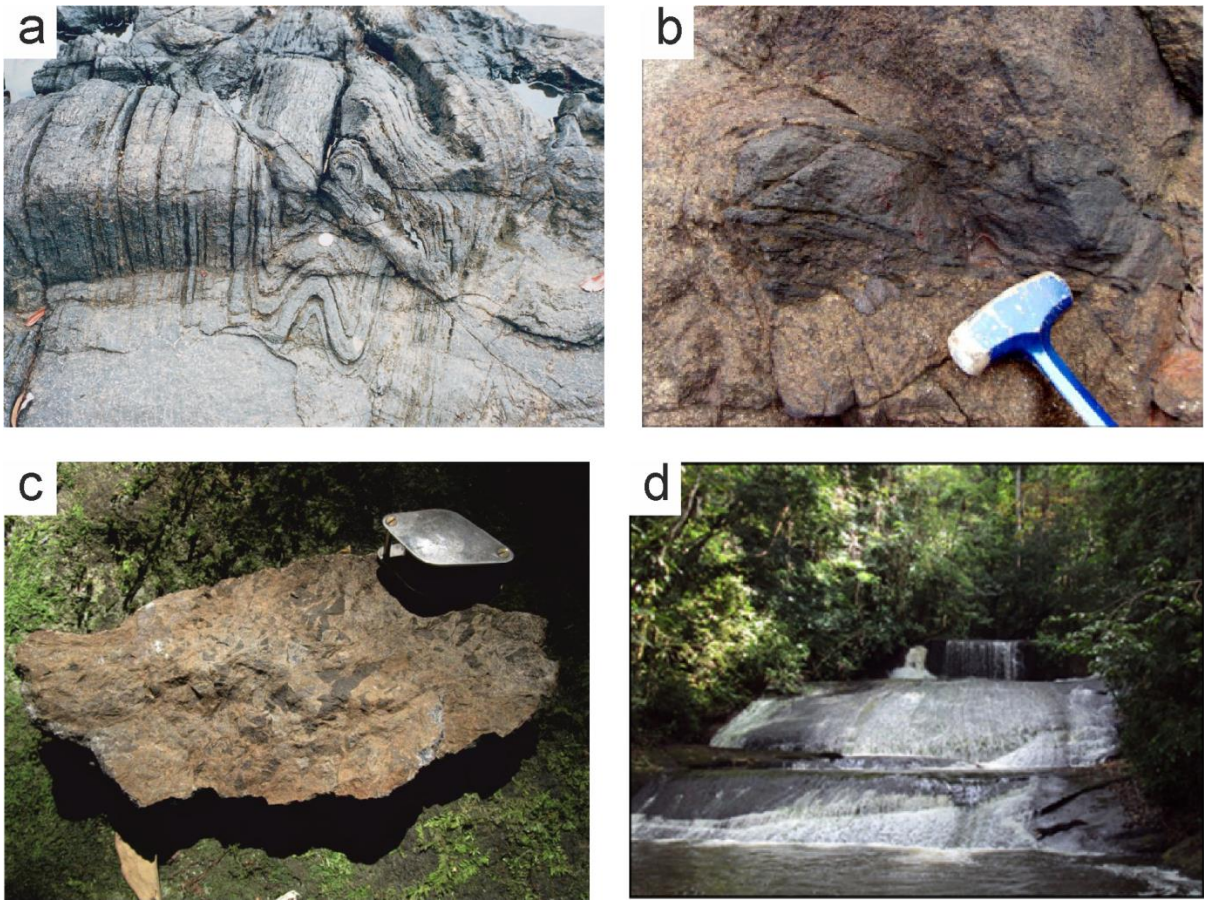

Figure 2.6. Field photographs and typical textures for the different lithologies of the Bakhuis Belt. A) Tight to isoclinal folding of banded intermediate UHT granulites. The folding is cut by a discordant amphibolitic dolerite dyke. Taken from (de Roever et al., 2003b). B) Irregular metadolerite xenolith in an exposure of Kabalebo charnockites. Taken from (Klaver et al., 2015). C) Ophitic magmatic textures of the Charlie gabbro well shown by weathering. White feldspar laths are enclosed by interstitial pyroxenes (black). Taken from Thijssen (2015). D) Massive field appearance of Kabalebo charnockites at Moi-Moi falls. Taken from (Nanne, 2013).

and minor or no olivine to olivine-rich cumulates with intercumulus ortho- and clinopyroxene. Olivine is commonly surrounded by corona's and is not always found fresh or present at all, but is assumed to be an important mineral in the suite. Pyroxenes show inverted pigeonite textures (Thijssen, 2015). Hornblende and biotite are rare and show indications for a secondary origin, indicating the magma is essentially anhydrous. The suite shows no evidence for metamorphism.
Geochemically, the suite falls in the High Alumina Basalt (HAB) series. The geochemistry also shows a subduction signature, which is interpreted to reflect a previously metasomatised mantle rather than a syn-subduction origin of the magma, given the anhydrous character of the suite.
Field relationships and the absence of metamorphic textures indicate the suite is younger than the Moi-Moi metagabbro. The Charlie gabbro has been dated using U-Pb dating on baddeleyite to 1970 ± 17 Ma. While the age is within error of the Moi-Moi metagabbro age, the lack of metamorphism indicates a younger age for the Charlie gabbro (Thijssen, 2015).

Mozeskreek anorthosite
A 3 x 4 km partly massive, partly layered anorthosite to leucogabbro occurs in the centre of the Bakhuis belt (de Roever et al., 2003b). It is presently covered by a bauxite cap, limiting the exposures to the incised Mozeskreek. Consequently, the body is named the Mozeskreek anorthosite for this thesis. The body shows cm-scale pyroxene bands and thicker leucogabbronorite bands. Layering is tilted sub-vertical, subparallel to surrounding granulites (de Roever et al., 2003b). The body has been dated using Pb-Pb evaporation on zircon, recording an age range 1975 – 1995 Ma, averaging at 1980 ± 5 Ma (de Roever et al., 2003b). Although only a single body is found at present, it is possible that other bodies are overlooked due to preferential weathering. Two other bauxite caps occur in the Bakhuis belt, which could indicate other

occurrences of anorthosite bodies. The geochemistry and petrogenesis of the anorthosite body have not previously been studied and is subject of this thesis.

2.2.3.2 (Meta)dolerite dykes

Fine-grained pyroxene-amphibolite metadolerite dykes have been described for the Bakhuis belt. The dykes are usually straight and discordant with thicknesses up to ~1 meter, but in some cases slightly folded or boudinaged (de Roever et al., 2003b) and boudinaged dykes and metadolerite enclaves in also occur in plutonic bodies (de Roever et al., 2003b; Klaver, 2011; Nanne, 2013).

Their widespread occurrence has been described as a 'special characteristic of Bakhuis belt metamorphism' by de Roever et al. (2003b), as they do not occur in other metamorphic terrains such as the Coeroeni Gneiss. de Roever et al. (2003b), considered them to be syn-metamorphic, as they obtained a 2060 ± 4 Ma U-Pb zircon age for foliated metadolerite dykes.

However, Klaver (2011) and Klaver et al. (2015) have shown metadolerites also occur as short dykes and xenoliths in the ~1.99 – 1.98 Ga Kabalebo charnockites indicating at least partially a contemporaneous origin. (Klaver et al., 2015) suggest the 2060 ± 4 Ma age obtained by (de Roever et al., 2003b) reflects xenocrystic zircon from the hosting granulites (Klaver, 2011).

3. Methods

3.1 Fieldwork and sample selection

3.1.1 Fieldwork and sampling

The Bakhuis belt has been exhumed since the Proterozoic and is presently covered by tropical rainforest. Performing systematic fieldwork is hampered by 1) extensive weathering; 2) poor exposure and 3) limited accessibility. Weathering in the moist and hot conditions of equatorial regions has developed up to 20m thick soils and as a consequence, hill slopes commonly yield no or strongly weathered outcrops. Unaltered outcrops of bedrock are restricted to riverbeds, large rapids or small waterfalls where erosion is recent. While these riverbeds yield excellent exposures in dimensions up to tens of meters with only minor alteration, similar to what is found in non-tropical terrains (fig. 3.1); sample collection and correlation of field relationships are restricted to the naturally established river network. The accessibility of the river networks in the Bakhuis belt is further limited by its remote location and the absence of infrastructure covering the entire belt.

The Bakhuis belt was accessed in two field campaigns between October 14th and November 8th 2012 in the dry season to maximize exposure in riverbeds. In a first 10-day field campaign mafic bodies along a segment of the Kabalebo river and its local tributaries Zandkreek, Kilodrie Creek and Misty Mountain Creek were studied and sampled from the Kabalebo Nature Resort in the southwest of the Bakhuis belt. In some locations, guides of the resort cut a trail through the rainforest to additionally access upstream locations of the tributaries which could not be accessed by boat due to the low water levels. In a second 3-day field campaign, the mafic bodies in riverbeds of Mozeskreek and the Blanche-Marie Falls in the north of the Bakhuis Belt were accessed by 4X4 through a limited infrastructure remaining from mineral exploration. A fraction of the infrastructure is still useable as it is currently used for touristic purposes, but most is overgrown by rainforest.

Given the limitations of the fieldwork area, geologic mapping was impossible and fieldwork instead focused only on geochemical sampling and determining age relationships in the outcrop scale. Additionally, the samples for this project were supplemented by relevant samples taken from mafic bodies during other studies in the Bakhuis Belt. Samples with an AT prefix were collected by Inja Thijssen for her own MSc thesis in the same field campaign. Samples with MKS and FN prefixes were collected by VU-students Martijn Klaver in February 2010 and Fienke Nanne in February 2012, respectively. Samples with LA and LD prefixes are parts of drill cores collected from the archives of the Geological and Mining Service (GMD) of Surinam, who have mapped and sampled the Bakhuis belt in the 1960's and 1970's. Samples with an ER and SUR prefix were collected by supervisor Dr. Emond de Roever in various previous field campaigns resp. Prof Dr. H.N.A. Priem during sampling for geochronology in the 70's.

3.1.2 Sample selection

26 samples from metadolerites, mafic xenoliths in Kabalebo charnockites, the Charlie gabbro and the Mozeskreek anorthosite were selected for major and trace elements analysis by XRF, which complete the XRF dataset of Thijssen (2015). Based on the major and trace element compositions, as determined by XRF analysis in this study and Thijssen (2015), 16 samples representing the most primitive magmatic

Figure 3.1 Typical exposure for the Bakhuis Belt; left: small outcrop near the Kilodrikreek of a stretched mafic xenolith in a charnockite mylonite, fresh surface exposed after hammering. Right: Larger outcrop of granulites in a dry riverbed near Blanche Marie Falls, hammer and field book in front for scale.

compositions of the different mafic bodies were selected for isotope dilution and Sr, Sm-Nd and Lu-Hf analysis. ICP-MS data was measured for these samples to determine the major and trace element compositions more precisely. Six metagabbroic samples that yield large hornblende crystals were selected for microprobe analysis to determine whether the crystals were magmatic or metamorphic (see section 1.4.1). Sample BU10a and BU13 of the metagabbro body at the Blanche Marie falls was selected for zircon separation, while only BU13 was selected for U-Pb dating by Laser-ablation ICP-MS, to determine whether this body is related to UHT metamorphism (see section 5.4.1).

3.2 Whole-rock processing

3.2.1 Coarse processing

All 26 samples selected for geochemical analysis were processed at the Geological Technical Laboratory and Mineral Separation Laboratory at the VU University Amsterdam. Samples were cut by a diamond blade saw to inch-sized blocks that could be further processed. One representative rectangular piece was chosen for preparation of a thin section of ~30 µm in the Geological Technical Laboratory. Remaining pieces that did not show weathering or alteration were crushed by a steel jawcrusher, which was thoroughly cleaned after each sample using a steel brush, a vacuum cleaning system, compressed air and ethanol to avoid cross-contamination. A ~100 g split was taken and processed using an agate ring mill for 1 minute, and an agate planetary ball mill for 1 hour, to reduce the sample to a homogenized powder. Using agate has the advantage that it only contaminates the samples with minor and equal amounts of SiO_2, which is generally not used in interpretation of geochemical data. All agate components were cleaned after every sample by repeating the procedure with clean quartz sand and water, which erodes possible contaminants off the agate, following by a thorough wash with demineralised water and ethanol. Additional whole rock powders that were chosen for isotope dilution were obtained from Inja Thijssen, Martijn Klaver and Emond de Roever, who produced the powders following the same procedure (as described by Thijssen, 2015; Klaver, 2011).

3.2.2 Preparation of beads and pellets for XRF analysis

For all 26 samples selected for XRF-analysis, both fused glass beads and pressed powder pellets where produced to determine the concentration of both major and minor elements respectively. From the ~100 g whole rock powder that was produced, 15 g was put in clean glass vials and dried in a stove overnight. After drying, the powder was stored in a dehumidifier.

3.2.2.1 Fused glass beads

Before producing fused glass beats, a Loss on Ignition (LOI) procedure was performed to determine the amount of lattice-bound volatiles. About 2 g of material was put in ceramic crucibles which were heated for 30 minutes in an oven at 1000^0C. The volatile content can be determined by measuring the weight of the sample before and after ignition. A factor complicating this procedure is that upon heating, oxidation of iron to Fe_2O_3 consumes oxygen from the air into the sample, counteracting weight loss from volatile release. All samples have very little loss of volatiles where LOI <0.5 weight %, and some samples have a negative loss. The negative loss indicates that the oxidation of Fe_2O_3 takes up more weight in oxygen than the weight of volatiles that are lost.

For the preparation of glass beads, 1.0 g of ignited sample was mixed and homogenised with 4.0 g of Spectroflux 110, which consists of 50% lithiummetaborate and 50% lithiumtetraborate, significantly reducing the melting temperature, achieving a homogeneous melt of the sample at lower temperatures. The samples were loaded in a clean platinum crucible and fused in a Philips PerlX3 machine at ~1150^0C, after which they were cast in a platinum cast dish and allowed to cool. All platinum components were cleaned in an ultrasonic bath in 20% citric acid for at least 10 minutes and washed with demineralised water and ethanol to avoid cross-contamination. In 3 cases the fused beads cracked upon cooling, after which the procedure in the machine was repeated.

3.2.2.2 Pressed powder pellets

For the production of pressed powder pellets, 4.500 g of unignited sample was mixed and homogenised with 0.450 g of EMU 120 FD organic binder. The mixture was loaded in clean aluminium cups which were pressed in an X-press pneumatic press at 20 tons for 30 seconds. The samples were gradually decompressed to avoid cracks and flakes coming off the samples.

3.3 Isotope dilution, sample dissolution and chemical chromatography

3.3.1 Clean lab facilities and procedures

All samples were processed in the clean lab of the Isotope Geochemistry Laboratory at the VU University Amsterdam. The lab is kept at an overpressure of filtered air to lower air particle densities. All procedures were executed in laminar flow hoods to further reduce contamination from air particles. All acids used for cleaning and sample dissolution are double distilled.
Sample solutions were stored in clean perfluoralkoxy (PFA) Savillex® beakers of 5 ml, 15 ml or 30 ml depending on the size of the solution. The PFA Savillex® beakers were coarsely cleaned by heating them in 6-7N HNO_3 and 6-7N HCl subsequently for 1 hour each. The beakers were thoroughly cleaned with 6-7 N HCl and 2-3 drops of concentrated HF on a hotplate for at least 3 days, after which they were rinsed with MiliQ water. Pipet tips were cleaned by submerging them in 6-7 N HCl for at least 7 days. Pipet tips used for transferring sample solutions were replaced after each use, pipet tips used for adding acids were replaced every ~5 uses. Aside the 16 chosen samples, USGS reference materials BHVO-2 and BCR-2 as external standards and 2 procedure blanks were included in sample processing.

Hf	**%**
^{176}Hf	0.2194
^{177}Hf	1.5164
^{178}Hf	94.7608
^{179}Hf	1.8316
^{180}Hf	1.6718
Lu	**%**
^{175}Lu	35.3254
^{176}Lu	64.6746
Lu/Hf	**0.1164**

Table 3.1. Isotopic abundances and ratio of the Lu/Hf mix-spike

Sm	**%**
^{144}Sm	0.041
^{147}Sm	0.203
^{148}Sm	0.992
^{149}Sm	96.612
^{150}Sm	1.342
^{152}Sm	0.603
^{154}Sm	0.207
Nd	**%**
^{142}Nd	0.505
^{143}Nd	0.315
^{144}Nd	0.682
^{145}Nd	0.230
^{146}Nd	0.471
^{148}Nd	0.258
^{150}Nd	97.538
Sm/Nd	**0.8674**

Table 3.2. Isotopic abundances and ratio of the Sm/Nd mixspike

3.3.2 Isotope dilution and error magnification

Lu/Hf and Sm/Nd mixspikes of known isotopic ratio were added in the dissolution procedures to more accurately determine the isotope ratios of the samples. The isotopic abundances of the elements in the spike and the ratio of mixspikes are given in table 3.1 for Lu/Hf and table 3.2 for Sm/Nd.

The added spike weights were chosen to be a factor 10 underspike of the ideal spike weight, based on the weights of the sample extract for dissolution and the concentrations of spiked elements by ICP-MS. The underspike ensures low enough error magnification while making efficient use of the available mixspike.

Error magnification factors for the concentrations for Sm and Nd was determined using the spike/sample ratio following formula 1 and 2 respectively, where ratios denoted with m indicate measured ratios, s indicates spike ratio and n indicates natural (i.e. assumed sample) ratios.

$$\boldsymbol{Error\ magn.\ Nd} = \frac{(150Nd/144Nd)m \times ((150Nd/144Nd)s - (150Nd/144Nd)n)}{((150Nd/144Nd)m - (150Nd/144Nd)n) \times ((150Nd/144Nd)s - (150Nd/144Nd)m)} \quad (1)$$

$$\boldsymbol{Error\ magn.\ Sm} = \frac{(149Sm/152Sm)m \times ((149Sm/152Sm)s - (149Sm/152Sm)n)}{((149Sm/152Sm)m - (149Sm/152Sm)n) \times ((149Sm/152Sm)s - (149Sm/152Sm)m)} \quad (2)$$

Nd and Sm magnification factors are < 3 for all samples, except for AT09b (<4) and BU10a (<7) which turned out to contain higher concentrations of Nd and Sm than was determined by ICP-MS. Errors on the determination of Nd and Sm concentrations were calculated by multiplying the error magnification factors with the two sigma error on the spiked ratio (e.g. ^{150}Nd/^{144}Nd for neodymium) and the concentration of the element (e.g. Nd for neodymium).

Two sigma errors for the ^{147}Sm/^{144}Nd ratios were propagated using simple propagation laws for multiplication and division, using the two sigma errors of the determinations of the samarium and neodymium concentrations, multiplied by the ^{147}Sm/^{144}Nd ratio, following formula 1.
Errors for the initial ^{143}Nd/^{144}Nd values were propagated using simple propagation laws for addition and substraction, using the error on the ^{143}Nd/^{144}Nd measurement and the error on the ^{147}Sm/^{144}Nd ratio multiplied by the e power to correct for the decrease in ^{147}Sm/^{144}Nd ratio over time t, following formula 2.
Finally, the error on the initial ƐNd was determined by correcting the error on the initial ^{143}Nd/^{144}Nd value 10.000 factor in epsilon values and for the change in the ^{143}Nd/^{144}Nd ratio of CHUR over time t following formula 3.

$$\boldsymbol{\sigma\ 147Sm/144Nd} = 147Sm/144Nd \times \sqrt{(\frac{\sigma\ Sm}{Sm})^2 + (\frac{\sigma\ Nd}{Nd})^2} \quad (3)$$

$$\boldsymbol{\sigma\ (143Nd/144Nd)initial} = \sqrt{(\ e^{\lambda 147Sm \times t - 1} \times \sigma\ 147Sm/144Nd)^2\ +\ \sigma\ 143Nd/144Nd^2} \quad (4)$$

$$\boldsymbol{\sigma\ \varepsilon Ndi} = \sigma\ (143Nd/144Nd)i \times \frac{10.000}{143Nd/144Nd\ CHUR,0 - (143Nd/144Nd\ CHUR,t \times e^{\lambda 147Sm \times t - 1)}} \quad (5)$$

Error magnification factors on the concentrations for Lu and Hf were determined in a similar way to the neodymium data following formula 6 and 7.

$$\boldsymbol{Error\ magn.\ Hf} = \frac{(178Hf/177Hf)m \times ((178Hf/177Hf)s - (178Hf/177Hf)n)}{((178Hf/177Hf)m - (178Hf/177Hf)n) \times ((178Hf/177Hf)s - (178Hf/177Hf)m)} \quad (6)$$

$$\boldsymbol{Error\ magn.\ Lu} = \frac{(176Lu/175Lu)m \times ((176Lu/175Lu)s - (176Lu/175Lu)n)}{((176Lu/175Lu)m - (176Lu/175Lu)n) \times ((176Lu/175Lu)s - (176Lu/175Lu)m)} \quad (7)$$

Hf and Lu magnification factors are < 3 for all samples, except for AT09b (<4), BU10a (<5), AT06b (<4) and BU04a (<4), which turned out to contain higher concentrations of Lu and Hf than was determined by ICP-MS. Errors on the hafnium isotope data were propagated in a similar way to the neodymium data following formulas 8, 9 and 10.

$$\boldsymbol{\sigma\ 176Lu/177Hf} = 176Lu/177Hf \times \sqrt{(\frac{\sigma\ Lu}{Lu})^2 + (\frac{\sigma\ Hf}{Hf})^2} \quad (8)$$

$$\boldsymbol{\sigma\ (176Hf/177Hf)initial} = \sqrt{(e^{\lambda 176Lu \times t - 1} \times\ \sigma\ 176Lu/177Hf)^2\ +\ \sigma\ 176Hf/177Hf^2} \quad (9)$$

$$\boldsymbol{\sigma\ \varepsilon Hfi} = \sigma\ (176Hf/177Hf)i \times \frac{10.000}{176Hf/177Hf CHUR,0 - (176Hf/177Hf\ CHUR,t \times e^{\lambda 176Hf \times t - 1)}} \quad (10)$$

3.3.3 Sample dissolution

Whole rock powders were homogenized and a carefully weighed 80 ± 5 mg of sample was taken for dissolution, see table 3.3 for the exact weights. To ensure all mineral phases in the samples would be dissolved (including rutile, garnet and zircon), samples were dissolved in Parr-bombs following procedures of Mahlen et al. (2008). Dissolution of zircon is crucial for Lu-Hf analysis, as zircon includes most of the Hf present in a sample.

Sample	Sample (g)	Sm/Nd (g)	Lu/Hf (g)
Session 1			
AT01	0.07698	0.1031	0.0551
AT34d	0.08407	0.0978	0.0487
Sur207	0.08535	0.0904	0.0487
AT09b	0.07707	0.0933	0.0576
ER1109	0.07954	0.0919	0.0608
AT36A	0.08258	0.0908	0.0571
AT37B	0.07706	0.0711	0.0550
LA 148-40	0.07683	0.0967	0.0535
BHVO-2	0.07190	0.0978	0.0519
Blank-1	-	-	-
Session 2			
LA-148-58	0.08094	0.0915	0.0518
BU09	0.07994	0.0721	0.0533
BU10a	0.08313	0.0716	0.0544
BU05	0.08091	0.0829	0.0492
AT06b	0.08570	0.0928	0.0618
MKS32	0.08548	0.0930	0.0567
BU04a	0.08190	0.0943	0.0519
BU20	0.08556	0.0570	0.0263
BCR-2	0.08614	0.0846	0.0554
Blank-2	-	-	-

Table 3.3 Isotopic abundances of the elements in the spike and the spike ratio.

Before dissolution, both the inner PTFE Teflon ® bombs as well as the exterior steel jacketed Parr bombs were cleaned with 6-7 M HCl overnight on a hotplate kept at 120^{0}C. The inner PTFE bombs were then cleaned inside the Parr bombs with concentrated HF/HNO_3 in an oven kept at 200^{0}C for one night.

After cleaning, the samples were weighed and loaded in the inner PTFE bombs, after which the mixspikes was added. The exact weights were determined by weighing the spike vials before and after spiking each sample and are given in table 3.3. To dissolve the samples, 3 mL of concentrated HNO_3 and 30 drops of HF were added. The inner bombs are then placed in the outer Parr bombs and placed in the oven kept at 200^{0}C. After 3 days, the bombs were opened and all samples were washed into Savillex® beakers

using 6-7 M HCl. The samples were dried down at 120^{0}C and nitrated twice with 20 drops of concentrated HNO_3 to break down any chloride and fluoride salts. Finally, the samples were dissolved in 3 M HNO_3.

After dissolution, an aliquot equivalent of ~1 mg of sample was taken and diluted 5000 ± 500 times with 5% HNO_3. Exact dilution factors were determined by carefully weighing after every step.

3.3.4 Chromatographic separation

3.3.4.1 Strontium

Strontium chromatographic separation was achieved using Eichrom® Sr-spec resin loaded in quartz columns with 1 CV = 0.085 mL. Samples were dissolved overnight in 3 M HNO_3 on a hotplate kept at 120^{0}C. The samples were subsequently exposed to sonic waves for 1 hour and centrifuged for 5 minutes at 4000 rpm. A fraction equivalent to 300 ng strontium was taken from each sample solution and loaded onto the columns, consuming between 0.6 mg and 2.4 mg from the total weight of the dissolved samples. Steps in column separation are shown in table 3.4. After the separation, one drop of 0.5% H_3PO_4 was added before they were dried down overnight. After drying, the samples were nitrated twice with 3 drops of concentrated HNO_3 to break any organic compounds. After separation, the columns were cleaned and the Sr-spec resin was removed. Procedure blanks were spiked with a weighed 3 drops of ^{84}Sr blank spike to determine the blank value for Sr with TIMS. Procedure blank 1 resulted in 65.9 pg of Sr and procedure blank 2 in 84.9 pg of Sr.

Step	Acid	Volume	Comment
Precleaning	3 M HNO_3	10 CV	
Wash	H_2O	10 CV	Repeat cleaning/wash 3 times
Conditioning	3 M HNO_3	5 CV	
Loading	3 M HNO_3		
Prefraction	3 M HNO_3	30 CV	Removes matrix elements
Sr fraction	**H_2O**	**10 CV**	**Collect Sr fraction**

Table 3.4 Steps for chromatographic column separation of Sr out of the matrix elements. 1 CV = 0.085 mL

3.3.4.2 Lutetium and hafnium

Lutetium and hafnium were separated from the sample solutions using Eichrom® Ln-spec resin in a 1 CV = 1 mL PE-column, following the one column procedure of (Münker et al., 2001). The Ln-spec resin is fixed in the columns and can be used multiple times. The procedure requires several distinctive acids such as ascorbic acid and an acid containing H_2O_2, which were all freshly prepared on the day of the separation. Samples dissolved overnight in 5 mL 2-3 M HCl on a hotplate kept at 120^{0}C. 0.5 M Ascorbic acid was added to reduce Fe^{3+} to Fe^{2+}. The samples were subsequently exposed to sonic waves for 1 hour and centrifuged for 5 minutes at 4000 rpm. The entire sample weight was loaded onto the columns. Steps in column separation are shown in table 3.5. The pre-fraction was collected and dried down for Sm-Nd separation as described in 3.3.4.3. After collecting the fractions, the Hf fractions were dried down and re-dissolved in 1.5 – 9 mL of 2% HNO_3/0.4 M HF, achieving a ~50 ppb solution of each sample for MC-ICP-MS measurement. Lu fractions were all dissolved in 1 mL of 2% HNO_3/0.4 M HF, achieving 4 – 40 ppb solutions as the Lu concentration in the samples was lower.

Step	Acid	Volume	Comment
Precleaning	2 M HF	15 CV	
Precleaning	6 M HCl	15 CV	Repeat both steps, store overnight
Conditioning	3 M HCl	2x 7.5 CV	
Loading	3 M HCl	5 CV	
Prefraction	3 M HCl	5 CV	Collect for Sm-Nd
Lu fraction	**6-7 M HCl**	**12 CV**	**Collect Lu fraction**
Wash	6-7 M HCl	25 CV	Removes excess Lu
Conditioning	H_2O	2x 2 CV	
Wash	0.09 M HCit/0.4 M HNO_3/1% H_2O_2	40 CV	Removes Ti and Zr fractions
Conditioning	H_2O	2x 2 CV	
Hf fraction	**6 M HCl/0.24 M HF**	**12 CV**	**Collect Hf fraction**
Cleaning	2 M HF	15 CV	
Cleaning	6 M HCl	15 CV	Repeat last 2 steps
Wash	0.165 M HCl	2 CV	Wash and store

Table 3.5 Steps for chromatographic column separation of lutetium and hafnium out of the matrix elements. 1 CV = 1 mL

3.3.4.3 Samarium and neodymium

Samarium and neodymium separation was achieved using a double column procedure, where LREE are separated from the matrix using TRU-spec columns, and samarium and neodymium are subsequently separated from the LREE using LN-spec columns. HREE were already removed from the samples through Lu-Hf column separation as described in 3.3.4.2.

TRU-spec

LREE elements were separated from the matrix using Eichrom® TRU-spec resin, loaded in 1 CV = 0.3 mL quartz columns. Samples were dissolved overnight in 5 mL 2M HNO_3 on a hotplate kept at 120^{0}C. The samples were subsequently exposed to sonic waves for 1 hour and centrifuged for 5 minutes at 4000 rpm. The entire sample was loaded onto the columns. Steps in column separation are shown in table 3.6. The collected LREE-MREE fraction was dried down overnight. After drying, the samples were nitrated twice with 3 drops of concentrated HNO_3 to break any organic compounds. After separation, the columns were cleaned and the TRU-spec resin was removed.

Step	Acid	Volume	Comment
Precleaning	2 M HNO_3	10 CV	
Precleaning	H_2O	10 CV	Repeat both steps 2 times
Conditioning	2 M HNO_3	3 CV	
Loading	2 M HNO_3	-	
Prefraction	2 M HNO_3	25 CV	Removes major elements
REE fraction	**0.05 M HNO_3 or H_2O**	**10 CV**	**Collect LREE-MREE fraction**

Table 3.6 Steps for chromatographic column separation of lutetium and hafnium out of *the matrix elements. 1CV = 0.3 mL.*

LN-spec

Sm and Nd were separated from the LREE-MREE fraction through using Eichrom® LN-spec resin in a 1CV = 0.75 mL PE-column. Samples were dissolved overnight in 1 mL 0.165M HCl on a hotplate kept at 120^{0}C. The samples were subsequently exposed to sonic waves for 1 hour and centrifuged for 4 minutes at 12000 rpm. The entire sample was loaded onto the columns. Steps in column separation are shown in table 3.7. After the collection of the Nd and Sm fractions, one drop of 0.5% H_3PO_4 was added before they were dried down overnight. Procedure blanks were spiked with a weighed 2 drops of ^{150}Nd blank spike to determine the blank value for Nd with TIMS. Procedure blank 1 resulted in 3.03 pg of Nd and procedure blank 2 in 58.34 pg of Nd.

Step	Acid	Volume	Comment
Precleaning	6-7 M HCl	5 CV	
Precleaning	2 M HF	5 CV	
Precleaning	H_2O	5 CV	
Precleaning	6-7 M HCl	5 CV	
Conditioning	0.165 M HCl	1 mL	Store overnight
Conditioning	0.165 M HCl	5 CV	
Loading	0.165 M HCl	1 mL	
Prefraction	0.165 M HCl	9.5 mL	
Nd fraction	**0.3 M HCl**	**4 mL**	**Collect Nd fraction**
Wash	0.3 M HCl	2 mL	Removes Pr and leftover Nd
Sm fraction	**0.5 M HCl**	**5 mL**	**Collect Sm fraction**
Cleaning	6-7 M HCl	5 CV	Removes Sm, Gd, Yd and Eu
Cleaning	0.165 M HCl	1 mL	Store

Table 3.7 Steps for chromatographic column separation of lutetium and hafnium out of the matrix elements. 1CV = 0.3 mL

3.4 Whole rock analyses

3.4.1 XRF analysis

Major and minor element concentrations were measured on the (modified) Philips Panalytical MagiXPro XRF spectrometer at the Isotope Geochemistry Laboratory of the VU University Amsterdam. In the XRF, spectra intensities were converted to concentration using a calibration curve, consisting of 30 natural calibration standards with varying compositions.

The fused glass beads were measured for major elements at an acceleration voltage of 40 kV and a beam current of 90 mA. The elements were measured as weight percent oxides for Fe_2O_3, MnO, TiO_2, CaO, K_2O, P_2O_5, SiO_2, Al_2O_3, MgO, Na_2O and BaO. All iron is measured as ferric Fe_2O_3, as it is assumed that iron is fully oxidised during ignition. Pressed powder pellets were measured for minor and trace elements at an acceleration voltage of 60 kV and a beam current of 60 mA. Analysis included Ni, V, Cr, Co, Sr, Rb, Ba, Pb, Th, Zr, U, Nb, Hf, Ta, Y, La, Ce, Pr, Nd, Sm, Er, Yb and Dy.
In all runs, USGS reference materials AGV-1, GSP1, BHVO-2 and BCR-2 were measured as external standards to measure the precision of the measurements. Selected measurements of major and trace elements and deviations of recommended values are shown in table 3.8. Most measurements, especially of major elements commonly deviate little from recommended values (<5%). However, minor elements commonly show a larger deviation, which increases rapidly when elements have a very low concentration (Yb in table 3.8 for example).

	SiO2 (%)	Fe2O3 (%)	MgO (%)	CaO (%)	La (ppm)	Sm (ppm)	Sr (ppm)	Yb (ppm)
AGV-1								
Measured	59,884	6,811	1,488	5,007	39,88	5,48	661,17	4,59
Recommended	59,3	6,69	1,79	5,2	38	5,7	658	1,6
Deviation (%)	**-1,0**	**-1,8**	**16,9**	**3,7**	**-4,9**	**3,9**	**-0,5**	**-186,9**
GSP-1								
Measured	67,025	4,215	0,936	1,993	162,35	24,11	232,89	4,63
Recommended	66,6	4,9	0,96	2,1	180	27	240	1,6
Deviation (%)	**-0,6**	**14,0**	**2,5**	**5,1**	**9,8**	**10,7**	**3,0**	**-189,4**
BHVO-2								
Measured	48,869	12,141	7,058	11,216	9,63	6,49	398,9	3,85
Recommended	49,9	12,3	7,23	11,4	15	6,2	389	2
Deviation (%)	**2,1**	**1,3**	**2,4**	**1,6**	**35,8**	**-4,7**	**-2,5**	**-92,5**
BCR-2								
Measured	53,673	13,684	3,526	7,063	23,35	6,58	349,76	6,25
Recommended	54,1	13,8	3,59	7,12	25	6,7	340	3,5
Deviation (%)	**0,8**	**0,8**	**1,8**	**0,8**	**6,6**	**1,8**	**-2,9**	**-78,6**

Table 3.8 Selected XRF major and trace element measurements of external standards AGV-1, GSP-1, BHVO-2 and BCR-2 and their deviation from recommended values.

3.4.2 ICP-MS analysis

Trace element concentrations for all 16 samples dissolved for isotope dilution were measured on the Thermo X-Series II ICP-MS at the VU University Amsterdam. The instrument is tuned using different tuning solutions before each measurement sequence. The measurements are corrected to a BHVO-2 solution as an internal standard. The solution is measured at the start and every 4-7 samples allowing a calibration for all measurements and correction for any possible drift of the instrument.
External standards BHVO-2 and BCR-2 are measured to determine the precision of the measurements. Selected measurements of major and trace elements and deviations of recommended values are shown in

	Li (ppm)	V (ppm)	Rb (ppm)	Sr (ppm)	Ba (ppm)	Nd (ppm)	Sm (ppm)	Hf (ppm)	Th (ppm)
BHVO-2									
Measured	4,74	298,27	9,11	370,43	121,39	23,19	5,66	5,28	1,21
Recommended	5	317	9,8	389	130	25	6,2	4,1	1,2
Deviation (%)	**5,2**	**5,9**	**7,1**	**4,8**	**6,6**	**7,3**	**8,6**	**-28,8**	**-0,7**
BCR-2									
Measured	9,42	398,07	47,82	324,41	658,27	27,30	6,30	5,66	5,93
Recommended	9	416	48	340	683	28	6,7	4,8	6,2
Deviation (%)	**-4,7**	**4,3**	**0,4**	**4,6**	**3,6**	**2,5**	**5,9**	**-17,9**	**4,4**

Table 3.9 Selected ICP-MS minor and trace element measurements of external standards BHVO-2 and BCR-2 and their deviation from recommended values.

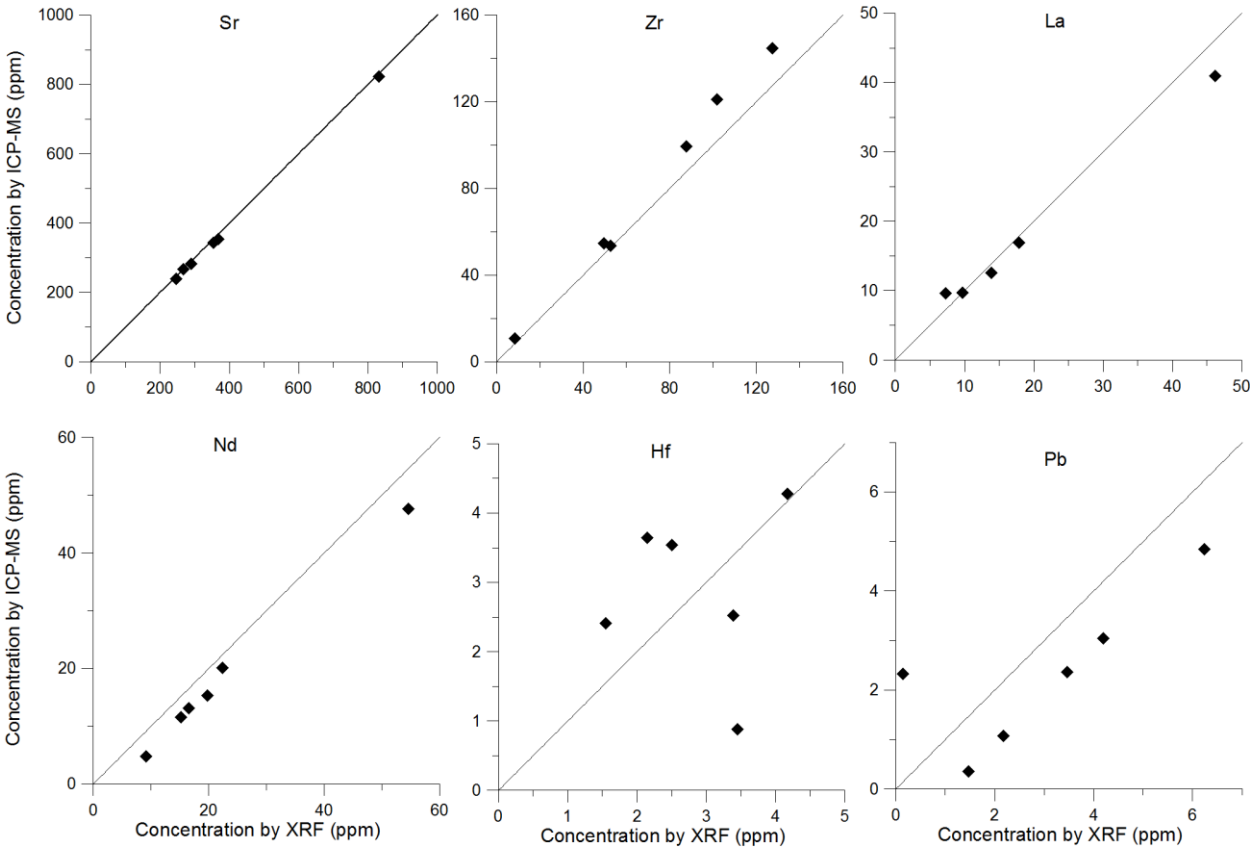

Figure 3.2. Comparison between XRF and ICP-MS data of selected trace elements.

table 3.9. Concentrations are in good agreements with recommended values, and deviation is commonly ~5%. Elements with low concentrations such as Hf, deviations increase. However, deviations for ICP-MS measurements on low concentrations are much smaller than deviation for XRF measurements on low concentrations.

For 6 samples, trace element concentrations were determined by both XRF and ICP-MS, allowing a comparison between the data from both instruments (fig. 3.2). For elements with high concentrations such as Sr, there is an excellent correlation between different instruments. For lower concentrations such as Zr, La and Nd the correlation becomes weaker. For <10 ppm elements such as Hf there is no more correlation, and the data just scatter. For other elements such as Pb, there is a consistent offset of the data, most likely caused by contrasting corrections for isobaric interferences.

3.4.3 Thermal Ionisation Mass Spectrometry

Strontium, samarium and neodymium isotope compositions have been measured using Thermal Ionisation Mass Spectrometry (TIMS).

3.4.3.1 Strontium

Strontium isotope measurements were performed using a MAT 262 RPQ+ TIMS at the Isotope Geochemistry Laboratory of the VU University Amsterdam.

Annealed rhenium single filaments were cleaned and outgassed for loading the strontium samples. Strontium fractions were dissolved in 4-6 µL 10% HNO_3. Half of the fraction was loaded onto the filaments, together with 2 µL of $TaCl_5$ activator, which lowers and stabilizes the evaporation of strontium from the heated filament. An NBS987 external standard was also loaded on a filament and measured to determine the precision of the measurements. The filaments were loaded and measured on two 13 slot turrets.

Filaments were slowly heated to about 1350°C before the signal was manually focused. A gain calibration was performed while slowly heating the filament of each sample. The filament current was increased until

Cup	**L2**	**L1**	**C**	**H1**	**H2**	**H3**
Isotopes	^{84}Sr	(^{85}Rb)	^{86}Sr	-	^{87}Sr	^{88}Sr

Table 3.10 Cup configurations on the MAT 262 for strontium isotope measurement.

the signal intensity was above 3 V, which was usually achieved at a filament temperature of about 1400°C. When the signal was stable, a measurement sequence in static data collection mode was started (see table 3.10 For cup configuration). The sequence consists of up to 12 blocks of 10 cycles and was manually quit as soon as the 2σ error on the $^{87}Sr/^{86}Sr$ ratio was < 10^{-6}. Each block started with a peakcenter and a baseline measurement. Afterwards, the filament was cooled down and the turret was rotated to a new filament position.

The measurements have been corrected for mass-dependent fractionation of Sr isotopes and for isobaric intereference of ^{87}Rb on ^{87}Sr. Mass-dependent fractionation, as the result of favoured isonisation of light isotopes during filament heating, was corrected by normalising to the natural non-radiogenic $^{86}Sr/^{84}Sr$ ratio using an exponential fractionation law (Thirlwall, 1991). Isobaric interference of ^{87}Rb on ^{87}Sr was corrected by measuring ^{85}Rb and correcting for the natural ratio of $^{87}Rb/^{85}Rb$ = 0.3857. However, measured ^{85}Rb contents were usually very low where $^{85}Rb/^{86}Sr < 10^{-4}$ V.
Measurements of the internal NBS987 standard shows considerable variation in $^{87}Sr/^{86}Sr$ ratio. Two measurements of one sample of NBS987 on the first turret resulted in $^{87}Sr/^{86}Sr$ ratios of 0.710259 ± 8, 0. 710284 ± 8. On the second turret, two measurements of one sample resulted in $^{87}Sr/^{86}Sr$ ratios of 0.710274 ± 8 and 0.710235 ± 9. All measurements deviate from the commonly accepted value of 0.710245, but they do not deviate consistently positive or negative (which would indicate long term detoriation of the detectors) nor do they deviate consistently for each filament (which would indicate contamination of the loaded NBS987 standard). This indicates that the variation should be interpreted as a seemingly random drift in the detectors of the 262. All measurements, including the external BCR-2 and BHVO-2 standards, should then exhibit the same drift. However, our values of 0.705007 ± 7 for BCR-2 and 0.0703493 ± 9 are in perfect agreement with values both in literature and as previously obtained at the VU University Amsterdam (Elburg et al., 2005; Raczek et al., 2003; Weis et al., 2006). Additionally, long term averages of the measurement of NBS987 standard show similar scatter, so it most likely reflects a decline in the machine's precision and a correction can not be made.

3.4.3.2 Samarium & Neodymium

Samarium and neodymium measurements were performed using a Thermo Scientific TRITON MC-TIMS at the Isotope Geochemistry Laboratory of the VU University Amsterdam. For the cup configuration, see table 3.11
Annealed rhenium double filaments were cleaned and outgassed for loading the neodymium and samarium samples. Both fractions were dissolved in 4 µL and half of the fractions were loaded onto one of the filaments. An in-house CIGO-1 standard for Nd and a Sm standard were also loaded on filaments and measured to determine the precision of the measurements. The filaments were loaded onto one 21 slot turret.

Neodymium measurement and corrections

Filament heating, focussing and the measurement were performed automatically using the Triton software. Filament currents for evaporation and ionisation were initially raised 0.01 V before automatic focussing was performed on the intensity of the center cup (^{146}Nd). After focussing, the filament currents were heated until the signal was above 0.9 V, which was usually achieved at a temperature of ~1600°C. The measurement sequence in static data collection mode (see table 3.11 for cup configuration). The sequence consists of 10 blocks of 30 cycles, where each block started with a peakcenter and a baseline measurement. Afterwards, the filament was automatically cooled down and the turret was rotated to a new filament position. The measurement procedure was performed manually for the procedure blanks and for measurement of 1 sample, as the Triton software could not get a signal by automatic heating and focusing.
The measurements have been corrected for mass-dependent fractionation of Nd isotopes and for isobaric interference of ^{144}Sm and ^{144}Nd. Mass-dependent fractionation was corrected by normalising to the natural non-radiogenic $^{146}Nd/^{144}Nd$ ratio. Isobaric interference of ^{144}Sm on ^{144}Nd was corrected by measuring ^{147}Sm and correcting for the natural ratio of $^{144}Sm/^{147}Sm$ = 0.2049. However, measured ^{147}Sm were usually very low where $^{147}Sm/^{144}Nd < 10^{-5}$ V.
Measurements of the internal CIGO-1 Nd standard are in perfect agreement with long term averages at the VU University Amsterdam. Also, external standards BHVO-2 and BCR-2 are in close agreement with

Cup	**L3**	**L2**	**L1**	**C**	**H1**	**H2**	**H3**	**H4**
Nd	^{143}Nd	^{144}Nd	^{145}Nd	^{146}Nd	^{147}Sm	-	-	^{150}Nd
Sm	**-**	^{146}Nd	^{147}Sm	^{148}Sm	^{149}Sm	^{150}Sm	^{152}Sm	-

Table 3.11 Cup configurations on the TRITON for neodymium and samarium isotope measurement.

$^{143}Nd/^{144}Nd$ ratios previously obtained in literature (Raczek et al., 2003; Weis et al., 2006; Weis et al., 2005).

Samarium measurement and corrections

Filaments for evaporation and ionisation were slowly heated to about 1450°C before the signal was manually focused. The filament currents were increased until the signal intensity was above 30 mV for ^{150}Sm, which was usually achieved at a filament temperature of about 1600°C. When the signal was stable, a measurement sequence in static data colletion mode was started (see table 3.? For cup configuration). The sequence consists of 3 blocks of 30 cycles, which were enough to accurately determine the Sm concentration. Each block started with a peakcenter and a baseline measurement. Afterwards the filament was cooled and the turret was rotated to a new filament position.

The measurements have been corrected for mass-dependent fractionation of Sm isotopes and for isobaric interferences of ^{148}Nd on ^{148}Sm and ^{150}Nd on ^{150}Sm. Mass dependent fractionation was corrected for by normalising to the natural non-radiogenic $^{144}Sm/^{146}Sm$ ratio. Isobaric interference of ^{148}Na on ^{148}Sm and ^{150}Nd on ^{150}Sm were corrected by measuring ^{146}Nd and correcting for the natural ratios of $^{148}Nd/^{146}Nd = 0.3346$ and $^{150}Nd/^{146}Nd = 0.3275$. However, measured ^{146}Nd were usually very low where $^{146}Nd/^{152}Sm < 10^{-3}$. There are no long-term averages for the in-house Sm standard as Sm is rarely measured at the VU. However, the determined Sm concentrations for BHVO-2 (5.9814 ± 0.0005) and BCR-2 (6.4806 ± 0.0012) closely resemble the values known in literature (Raczek et al., 2001).

A problem arose when the data was used to calculate the initial values. All the data from the samples plotted strongly off the mantle array (Vervoort et al., 1999). Also, εNd values for the BHVO-2 and BCR-2 were found to be about ~6-7% off from what they should be. After checking the data carefully, it was discovered that a drift was occurring during the measurement of samarium by the Triton, resulting in anomalous Sm/Nd ratios. The drift was corrected using the values for the external standards as a calibration, which resulted in values that plot around the mantle array.

3.4.4 Multi-Collector Inductively Coupled Plasma Mass Spectrometry by NEPTUNE

Lutetium and hafnium measurements were performed on a Thermo Scientific Neptune Multicollector ICP-MS at the Isotope Geochemistry Laboratory of the VU University Amsterdam. The sample solutions for Lu and Hf obtained from the column separation described in 3.3.4.2 were ready to be measured with the Neptune.

3.4.4.1 Hafnium

Solutions were measured in a sequence which started with 5 measurements of the JMC475 standard and 5 measurements of an in-house 50 ppb standard. Unknowns were measured in blocks of 4, after which both standards were measured again once or twice. One unknown (AT09b) was measured at the end of each block, to check the consistency of the analysis. The cup configuration for hafnium is shown in table 3.12. Every measurement consisted of 90 cycles.

The measurements have been corrected for mass-dependent fractionation of Hf isotopes and for isobaric interferences of ^{176}Yb and ^{176}Lu on ^{176}Hf and ^{180}W on ^{180}Hf. Mass dependent fractionation was corrected for by normalising to the natural non-radiogenic $^{197}Hf/^{177}Hf$ ratio. Isobaric interferences of ^{176}Yb and ^{176}Lu on ^{176}Hf and ^{180}W on ^{180}Hf were corrected by measuring ^{171}Yb, ^{173}Yb, ^{175}Lu and ^{182}W and correcting for the natural ratios of $^{171}Yb/^{173}Yb = 0.882858$, $^{176}Yb/^{173}Yb = 0.796218$, $^{176}Lu/^{175}Lu = 0.02655$ and $^{180}W/^{182}W = 0.004521$.

Measurements of the JMC475 standard are in perfect agreement with long term averages at the VU University Amsterdam and available data from literature (Blichert-Toft et al., 1997; Nowell et al., 1998; Vervoort and Blichert-Toft, 1999).

3.4.4.2 Lutetium

Solutions were measured in a sequence which started with the measurement of a 50 ppb Lu in-house standard. The cup configuration for lutetium is shown in table 3.12. The standard was measured in 1 block of 10 cycles for every 3 unknowns, which were measured in 2 blocks of 10 cycles.

The measurements have been corrected for mass-dependent fractionation of Lu isotopes and for isobaric interferences of ^{176}Yb and ^{176}Hf on ^{176}Lu**.** Mass dependent fractionation was corrected for by determining

Cup	**L4**	**L3**	**L2**	**L1**	**C**	**H1**	**H2**	**H3**	**H4**
Hf	^{171}Yb	^{173}Yb	^{175}Lu	^{176}Hf	^{177}Hf	^{178}Hf	^{179}Hf	^{180}Hf	^{182}W
Lu	^{171}Yb	^{173}Yb	^{175}Lu	^{176}Lu	^{177}Hf	-	-	^{185}Re	^{187}Re

Table 3.12 Cup configurations on the NEPTUNE for hafnium and lutetium isotope measurement.

the mass dependent fractionation for $^{185}Re/^{187}Re$ and normalising lutetium data to it. Isobaric interferences of ^{176}Yb and ^{176}Hf on ^{176}Lu were corrected by measuring ^{171}Yb, ^{173}Yb and ^{177}Hf and correcting for the natural ratios of $^{171}Yb/^{173}Yb = 0.882858$, $^{176}Yb/^{173}Yb = 0.796218$ and $^{176}Hf/^{177}Hf = 0.28216$.
Measurements of the in-house standard are in perfect agreement with the long term averages at the VU University Amsterdam. Also, the determined Lu concentrations for BHVO-2 (0.>) and BCR-2 (0.4868 ± 0.0002) are in perfect agreement with values known in literature (Raczek et al., 2001).

3.5 Hornblende microprobe analysis

Six selected polished thin sections for microprobe analysis were coated with a conductive carbon coating to prevent the samples from becoming charged during the measurements. Hornblende compositions were determined using the Jeol JXA-8800M SuperProbe electron microprobe at the VU University Amsterdam. For each thin section, between 15 and 40 points were selected to represent the most unaltered original compositions of the hornblende. An electron beam diameter of 10 micron was used, with an acceleration voltage of 15 kV and a beam current of 15 nA. The measured elements, the channel configuration and the mineral standards used to calibrate the measurements using a ZAF-method are shown in table 3.13. In the measurement sequence, a natural diopside and amphibole crystal were measured as unknowns to determine the precision of the measurements. Amphibole compositions were calculated following Holland and Blundy (1994), allowing the calculation of Fe^{3+} and Fe^{2+} and partitioning of aluminium in the framework cations as Al^{IV} and Al^{VI}.

Element	Channel	Mineral Standard
Si	1 TAP	Orthoclase
Ca	2 PET	Diopside
Fe	3 LiF	Fayalite
Al	1 TAP	Orthoclase
K	2 PET	Orthoclase
Mn	3 LiF	Tephroite
Mg	1 TAP	Olivine
Ti	2 PET	Ilmenite
Na	1 TAP	Jadeite
Cr	2 PET	Chromium(III)oxide
F	1 TAP	Fluorite

Table 3.13 Measured elements, the channel and crystal the element is measured on and the mineral standard used to calibrate the measurements.

3.6 Zircon U-Pb dating

3.6.1 Zircon separation

Samples BU13 and BU10a were selected for zircon separation. Polished thin sections for both samples were made and analysed by microprobe to check the presence and habit of zircon in the samples. Zircon was separated out of the rock using mineral separation techniques available at the Mineral Separation Laboratory at the VU Amsterdam (see fig. 3.3).
About 2-3 kg for each sample was crushed using a steel jawcrusher and a disc mill, each in several steps to achieve a <250 µm grain-size. In between each step, the fractions <250 µm were sieved out to reduce crushing damage to the zircon. After each sample, both machines were thoroughly cleaned using a steel brush, a vacuum cleaning system, compressed air and ethanol to avoid cross-contamination. The <250 µm was automatically deslimed in several steps based on Stoke's law, where the samples was submerged in a water column. After a given time allowing larger particles to settle at the bottom, the smaller particles (approximately <30 µm) still in suspension were sucked out with the water.

First step in mineral separation was density separation by heavy liquids in a Liquid Overflow Centrifuge (LOC), using almost pure methylene iodide (ρ = 3.325 g/cm3). The centrifuge accelerates the density separation, where fragments with $\rho_{fragment} < \rho_{liquid}$ are overflown as 'float' out of the centrifuge, and fragments with $\rho_{fragment} > \rho_{liquid}$ remain as 'sink' in the centrifuge. As zircon has a density of ρ = 4.6-4.7, using a liquid of ρ = 3.325 g/cm3, separates most minerals out as float, while zircon remains in the sink.
The remaining minerals were separated using a Frantz magnetic separation. The sample was sieved in >180 µm, 120-180 µm, 90-120 µm, 60-90 µm and <60 µm fractions. While most minerals with ρ > 3.325 have a high magnetic susceptibility, zircon has a very low susceptibility. By using the high currents for the Frantz magnet, an almost pure zircon fraction resulted for each grain size fractions. The fraction with the biggest euhedric zircons (90-120 µm for BU13 and >180 µm for BU10a) was handpicked for further analysis.

The picked zircons were mounted in a clear epoxy resin, polished and carbon coated. Back-scatter electron images of the zircons were produced in the Jeol JXA-8800M SuperProbe electron microprobe at the VU University Amsterdam. Based on those photographs, only sample BU13 was selected for U-Pb dating, as BU10a yielded large complex zircons, which are interpreted as potential xenocrysts (see section 5.4.1).

3.6.2 U-Pb by LA-ICP-MS analysis

U-Pb dating has been performed by LA-ICP-MS at the Institut für Mineralogie of the Westfälische Wilhems-Universität Münster. The setup consists of a 193-nm ArF Excimer laser system (UP193HE, New Wave Research) connected to a Thermo Scientific ELEMENT 2 ICP-MS.

The laser was operated at a fluence of 3 J/cm^2 and a repetition rate of 10 Hz. The laser spot size was chosen to be 35 µm and the samples were ablated for 37 seconds, followed by a 37 second washout with He. The Element 2 ICP-MS is tuned at the start of a session using a NIST-612 trace element glass. The scanned masses include ^{204}Pb, ^{206}Pb, ^{207}Pb, ^{235}U and ^{238}U. Additionally, ^{202}Hg was measured to determine the isobaric interference of ^{204}Hg on ^{204}Pb, which is necessary to correct the data for common lead. Samples were analysed in 81 experiment sequences with 3 analyses of GJ 1 as a calibration standard after each 10 unknowns. Over the sequence, Z91500 was measured 3 times as an external standard to determine the precision of the machine. The measurements resulted in ^{206}Pb/^{238}U ages of 1069.4 ± 15.5, 1069.2 ± 16.5 and 999 ± 19.3 Ma. The first two ages are in good agreement with the recommended 1065 Ma age for the Z91500 zircon. The last analysis is considered an outlier, especially since the ^{207}Pb/^{235}U and ^{207}Pb/^{206}Pb ages result in even younger ages.

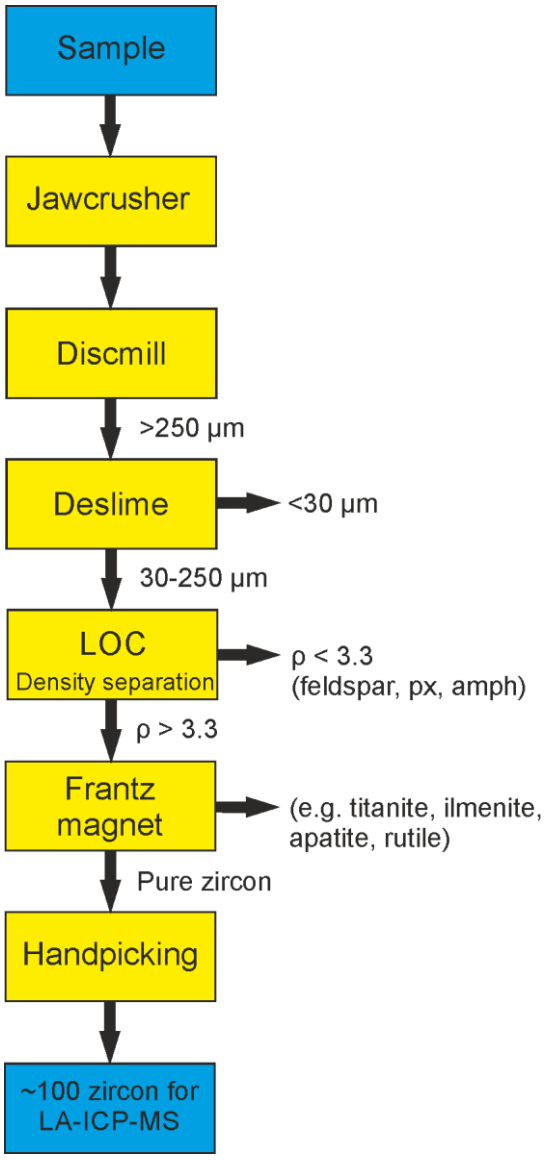

Figure 3.3 Mineral separation scheme for the separation of zircon. Arrows on the right side show which fragments were separated out in each step to achieve a zircon concentrate.

Data reduction was carried out in Münster using in-house software. The software corrects for static and time dependent fractionation during laser ablation. The software calculates a final ^{206}Pb/^{204}Pb ratio, which allows a determination of the presence of common lead. When present, the common lead was corrected for. In total, 6 of 60 analyses were considered outliers (including the last measurement of Z91500) and are left out of the results. A ^{207}Pb/^{206}Pb probability density plot and histogram, and a concordia diagram (Wetherill, 1956) were plotted using IsoPlot 4.15.

4. Mafic plutonic bodies in the Bakhuis Belt

The occurrence, petrography and geochemistry of gabbroic bodies are described in detail in Thijssen (2015). This section describes the petrogenesis of cm-sized poikilitic hornblende (section 4.1) in the Moi-Moi metagabbro of Thijssen (2015), the petrography and geochemistry of an anorthosite body at Mozeskreek (section 4.3) and whole rock radiogenic isotopes for the different gabbroic bodies to investigate their relationship and petrogenesis (section 4.3). All results are briefly discussed at the end of each section.

4.1 Petrogenesis of hornblende in the Moi-Moi metagabbro

4.1.1 Field description and sample selection

Hornblende occurs in the Moi-Moi metagabbro as large (cm-scale) poikilitic crystals. In the field, it can easily be recognised as black coloured amphiboles with $60/120^0$ and a shiny lustre reflecting light homogenously over the cm-scale crystals. Inclusions in the samples are not easily distinguished as the crystals are very dark.

To investigate the petrogenesis and mineral chemistry of hornblende in metagabbros, 6 samples were chosen for petrographic and microprobe analysis (see fig. 4.1 for locations). Of the six samples, four were taken in the Bakhuis belt. AT07d and AT13b were taken at the respective center and southern boundary of the occurrence at Moi-Moi Falls. AT38 was taken from an outcrop upstream a small tributary to the Zandkreek and ER1202 about 3 km north of the Blanche Marie Falls. Two of the six samples were taken of gabbroic bodies with poikilitic hornblende outside the Bakhuis Belt, to investigate the hornblende without the influence of Bakhuis metamorphism: LD14-100 is a drill core sample from Stontabriki along the Coppename river and EG1665 is a sample taken near the Coeroeni river from the Coeroeni Gneiss in south-western Suriname.

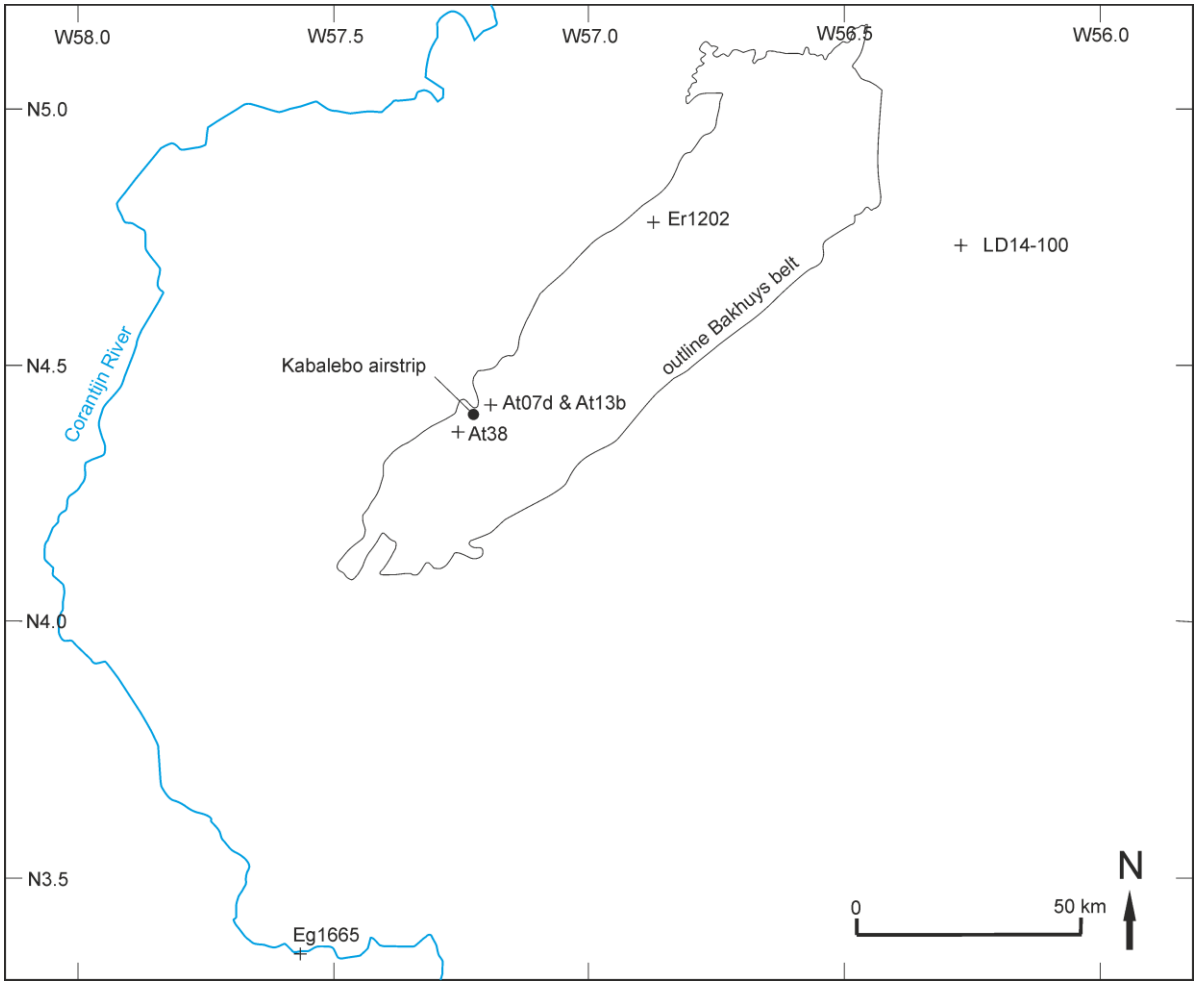

Figure 4.1. Sample locations for hornblende-bearing samples of the Moi-Moi metagabbro. AT07d and AT13b were taken from the same occurrence at Moi-Moi falls. AT38 was taken close to Zandkreek and ER1202 near Blanche Marie falls. EG1665 is taken from an metagabbroic intrusion in the Coeroenie Gneiss along the Corantijn river. LD14-100 is taken from a drill core (at 100 m depth) which was drilled near the Coppename river.

4.1.2 Sample petrography and spot selection

Texturally, the samples can be separated in two groups; 1) where plagioclase, olivine and pyroxenes are stable, euhedral crystals inside hornblende crystals (AT38 and LD14-100) and 2) where only plagioclase are stable, euhedric crystals and both olivine and pyroxene are absent or only as relict, embayed crystals in hornblende crystals (AT07D, AT13b, ER1202 and EG1665). See figure 4.2 for the typical textures for the hornblende.

Group 1: Poikilitic hornblende enclosing olivine, pyroxene and plagioclase

AT38 is an olivine hornblende pyroxenite which, based on field relations, is interpreted to be part of olivine-rich cumulates (Thijssen, 2015). Hornblende is a poikilitic intercumulus phase up to 1 cm, enclosing dominantly olivine, clinopyroxene, orthopyroxene and minor plagioclase. Locally, plagioclase is also the intercumulus phase. Hornblende pleochroism is light yellow to olive-green or brown-green. Hornblende shows dark exsolution along one cleavage plane leading up to black patches in browner parts of the crystals. Browner parts without too much exsolution were selected for EMP analysis.

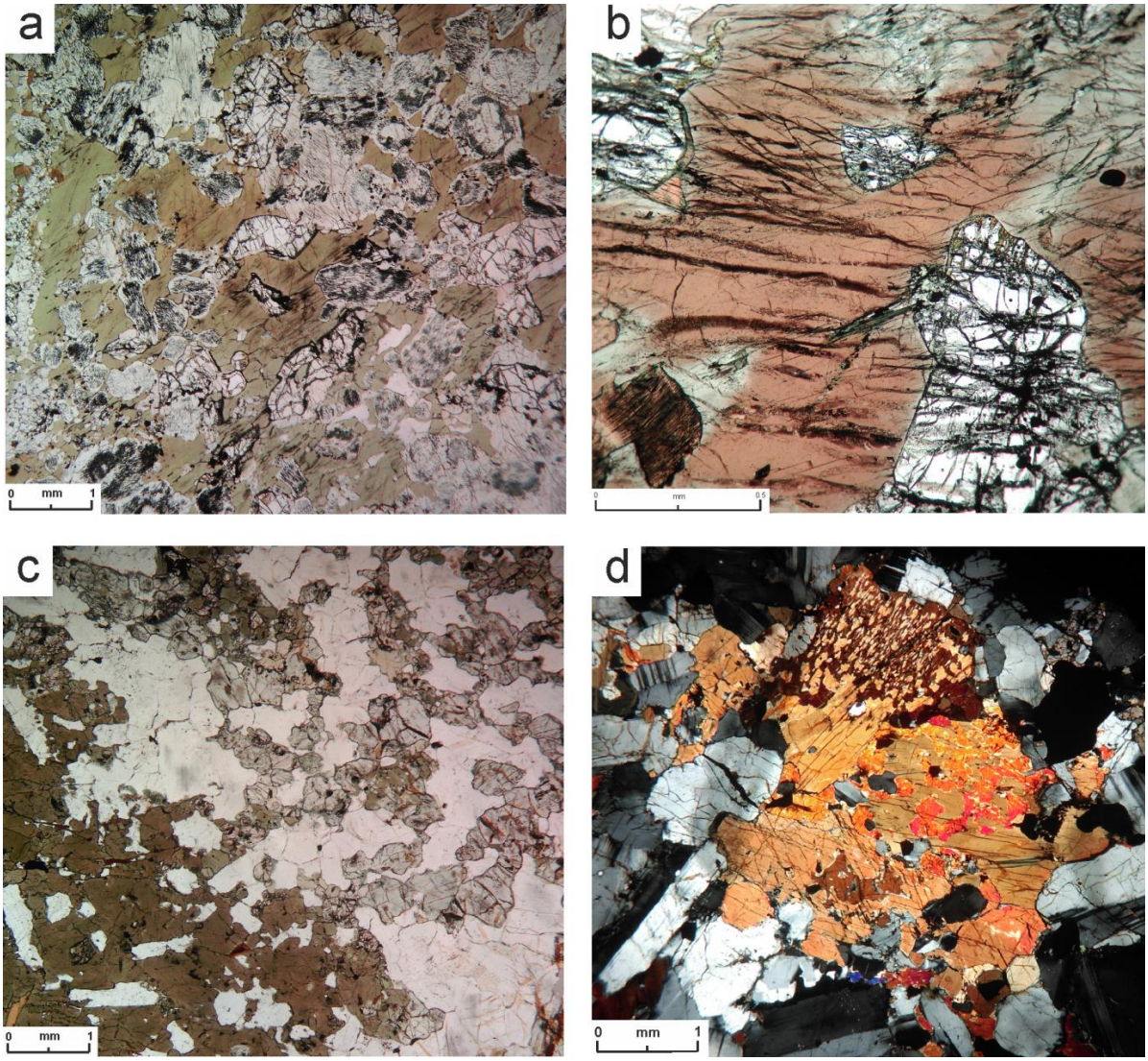

Figure 4.2 Thin section photographs of typical textures for the hornblende. a) Sample AT38 of group 1: Olivine (white, high relief), clinopyroxene (white, low relief) and orthopyroxene (light pink, low relief) as stable inclusions in a large brown hornblende. b) Sample LD14-100 of group 1: subhedral stable olivine crystals in a fractured hornblende crystal. Brown hornblende has green patches in the top right and top middle and in a thin zone around olivine inclusions. c) Sample AT07d of group 2: Large brown hornblende crystals with monomineralic inclusions of subhedral plagioclase laths in the bottom left half. Across the hornblende boundary, the rock has a granular texture of pyroxenes and plagioclase in the top right half. At the hornblende boundary, pyroxenes show reaction textures to hornblende. This texture is typical for group 2 samples. d) Sample ER1202 of group 2: Reaction texture of 2 clinopyroxene crystals (bright orange and dark orange colours) into hornblende (light brown to yellow colours) surrounded by subhedral to granular plagioclase.

LD14-100 is a cumulate olivine gabbro with poikilitic plagioclase as the dominant intercumulus phase, enclosing subpoikilitic clinopyroxene and smaller olivine crystals. A single large (~1 cm) orthopyroxene poikiloblast has formed a rim of biotite, showing embayment textures. One ~1 mm poikilitic hornblende crystal is present in the thin section, enclosing multiple euhedric to subhedral olivine crystals. The hornblende shows variation in colour with patches of light yellow to light green pleochroism in a light yellow to brown pleochroic matrix. Green hornblende also occurs as smaller alteration products. The brown parts of the hornblende crystal were selected for EMP analysis.

Group 2: Poikilitic hornblende enclosing only plagioclase

AT07d is a medium grained pyroxene hornblende gabbronorite with subhedral plagioclase laths preserved within hornblende crystals, which lie in an otherwise granular plagioclase + clinopyroxene metagabbro (group 1 of Thijssen, 2015). Parts of three >1 cm hornblende crystals are visible in the thin section. Two are still intact crystals while one shows minor cracks and sub-grain formation. This is interpreted to be the effect of the same metamorphism responsible for the granular texture outside the crystals. The cracked hornblende shows a light yellow to dark brown-green pleochroism, while the other two show an olive-green to brown-green pleochroism. Biotite is forming in larger cracks and along the cleavage planes and all three hornblendes contain very small black spots indicating exsolution of oxides. Brown parts of all three hornblende crystals were selected for EMP analysis.

AT13b is a fine grained pyroxene hornblende gabbronorite with subhedral plagioclase laths preserved within hornblende crystals, which lie in an otherwise granular plagioclase + clinopyroxene + orthopyroxene metagabbro (group 1 of Thijssen, 2015). The rock is generally richer in plagioclase than AT07D, leading to more inclusions of plagioclase in hornblende crystals. Hornblendes are up to 1 cm in size and commonly show cracks and sub-grain formation, showing a light yellow to brown-green or brown pleochroism. Most hornblendes show biotite forming in larger cracks and contain very small black spots indicating exsolution of opaque oxides. Brown parts of 4 hornblende crystals were selected for EMP analysis.

ER1202 is a medium grained hornblende gabbronorite with subhedral plagioclase laths preserved in hornblende crystals. Outside hornblendes, a relict texture of plagioclase laths separated by intercumulus orthopyroxene is visible; however the texture is commonly obscured by metamorphism into a granular texture. Hornblendes are up to 0.5 cm in size, and relict pyroxenes are present as embayed fragments. Hornblende shows dark exsolution along one cleavage plane forming black patches. Larger pyroxenes show reaction textures to poikilitic hornblende. Brown parts of larger hornblendes enclosing plagioclase laths as well as closer to pyroxene reaction textures were selected for EMP analysis.

EG1665 is a hornblende gabbronorite with aggregates of poikilitic hornblendes enclosing subhedral plagioclase laths. The texture outside hornblendes consists of plagioclase laths separated by intercumulus orthopyroxene and clinopyroxene. Hornblende forms aggregates of multiple smaller hornblende crystals instead of a single large crystal. Intercumulus pyroxenes show reaction textures to hornblende.

4.1.3 Mineral chemistry

All results of microprobe analysis of Hbl are added in appendix I. Relevant data is plotted in fig. 4.3.

In the amphibole classification of (Leake et al., 1997), the hornblende analyses show 2 different compositional groups (fig 4.3a and b). Hornblendes from group 1 samples display pargasite compositions (fig. 4.3a) with $(Na+K)_A$ ranging between 0.6 – 0.84, $Mg/(Mg+Fe^{2+})$ ranging between 0.76 – 0.85 and Si ranging between 6.05 – 6.3. Hornblendes from group 2 samples display Tschermakite to Magnesiohornblende compositions (fig. 4.3b) with $(Na+K)_A$ ranging between 0.37 – 0.52, $Mg/(Mg+Fe^{2+})$ ranging between 0.65 – 0.75 and Si ranging between 6.25 – 6.6. The Al^{IV} and Al^{VI} contents (fig. 4.3c) for the Group 2 samples and LD14-100 show a general trend varying between 0.25 – 0.60 Al^{VI} p.f.u. and 1.4- 1.85 Al^{IV} p.f.u. The Al^{IV}/ Al^{VI} ratio is considerably high and ranges between 7.5 and 2.5 Sample AT38 has slightly higher Al contents of up to 0.635 for Al^{VI} and 1.91 for Al^{IV}, yet overlapping ratios between 3.9 and 2.7. The Ca + Na + K occupancy of the A and B sites (fig. 4.3d) of group 1 samples ranges between 2.7 and 2.9. For group 2 samples, the Ca + Na + K contents are considerably lower, ranging between 2.3 – 2.6.

The Ti contents (fig 4.3e) for the samples taken in the Bakhuis belt are considerably lower than the samples taken outside the Bakhuis belt. The Bakhuis belt samples show Ti contents between 0.26 – 0.14. Outside the Bakhuis belt, Ti contents are as high as 0.37. In the same plot, there is also a consistent variation in the Mg#. Group 1 samples have considerably higher Mg# (75 — 85) than samples from group 2 (65 — 75). Although overlapping, Fe^{3+} contents are significantly lower for group 1 samples (0.1 — 0.4) than group 2 samples (0.2 — 0.55), where samples in group 2 also show considerable variation.

4.1.4 Discussion of hornblende petrogenesis

Petrography

The textures observed in group 1 samples indicate equilibrium between hornblende, olivine and both orthopyroxene and clinopyroxene. However, if the hornblende has formed by metamorphism, it is expected that it is formed as a breakdown product of olivines and pyroxenes, as is visible in group 2 samples. The presence of hornblende in textural equilibrium with olivine thus indicates that the hornblende is primary.

The textures observed in group 2 indicate formation of hornblende out of olivine and pyroxene. This reaction is intuitively secondary, by introduction of water during amphibolite facies metamorphism, but can also be late primary, by interaction of olivine and pyroxenes with an evolved hydrous magma (Costa et al., 2002; Prouteau et al., 2001; Yan et al., 2015).

None of the hornblende show oscillatory zoning, which would provide direct evidence for a magmatic origin. However, such zoning can easily be obscured during subsequent metamorphism and is rarely observed in thin sections of amphiboles. Conversely, the absence of any schistose fabric in hornblendes argues against a metamorphic origin for the hornblende. Also, the hornblendes contain lath-shaped

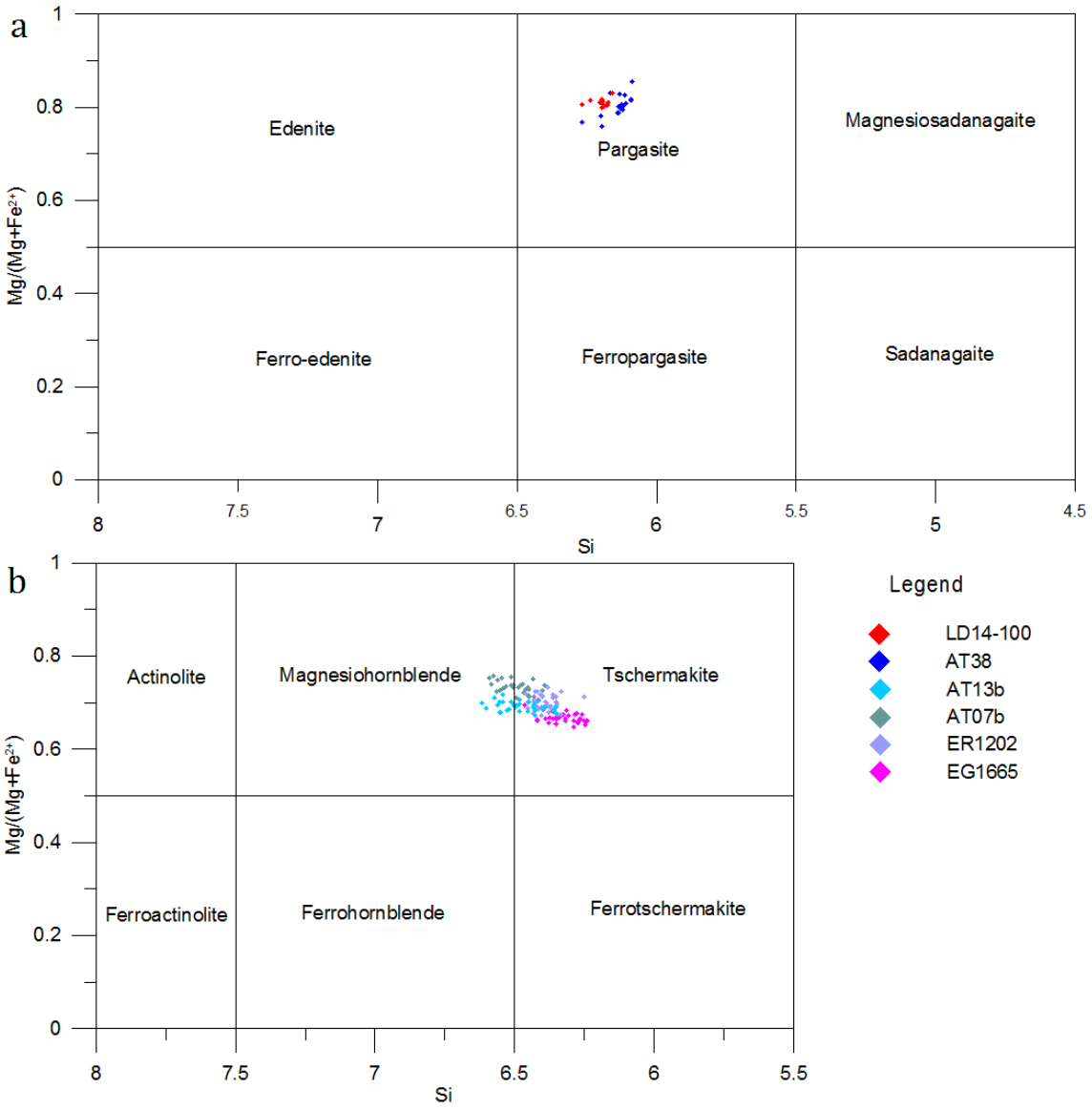

Figure 4.3 (continues on next page). a & b) Chemical classification for calcic amphiboles ($Ca_B \geq 1.50$) after (Leake et al., 1997), where in a $(Na + K)_A \geq 0.50$ and in b $(Na + K)_A < 0.50$. c) Plot of Al^{IV} vs Al^{VI} partitioning following (Fleet and Barnett, 1978), who defined the field of $Al^{IV}/Al^{VI} > 3.3$ as the igneous field. d) Ca + Na + K occupancy of the A and B sites of the amphibole crystal structure e) Ti content p.f.u. vs Mg#, the latter is used as a proxy for how evolved the magma was. f) Fe^{3+} vs Si content p.f.u.

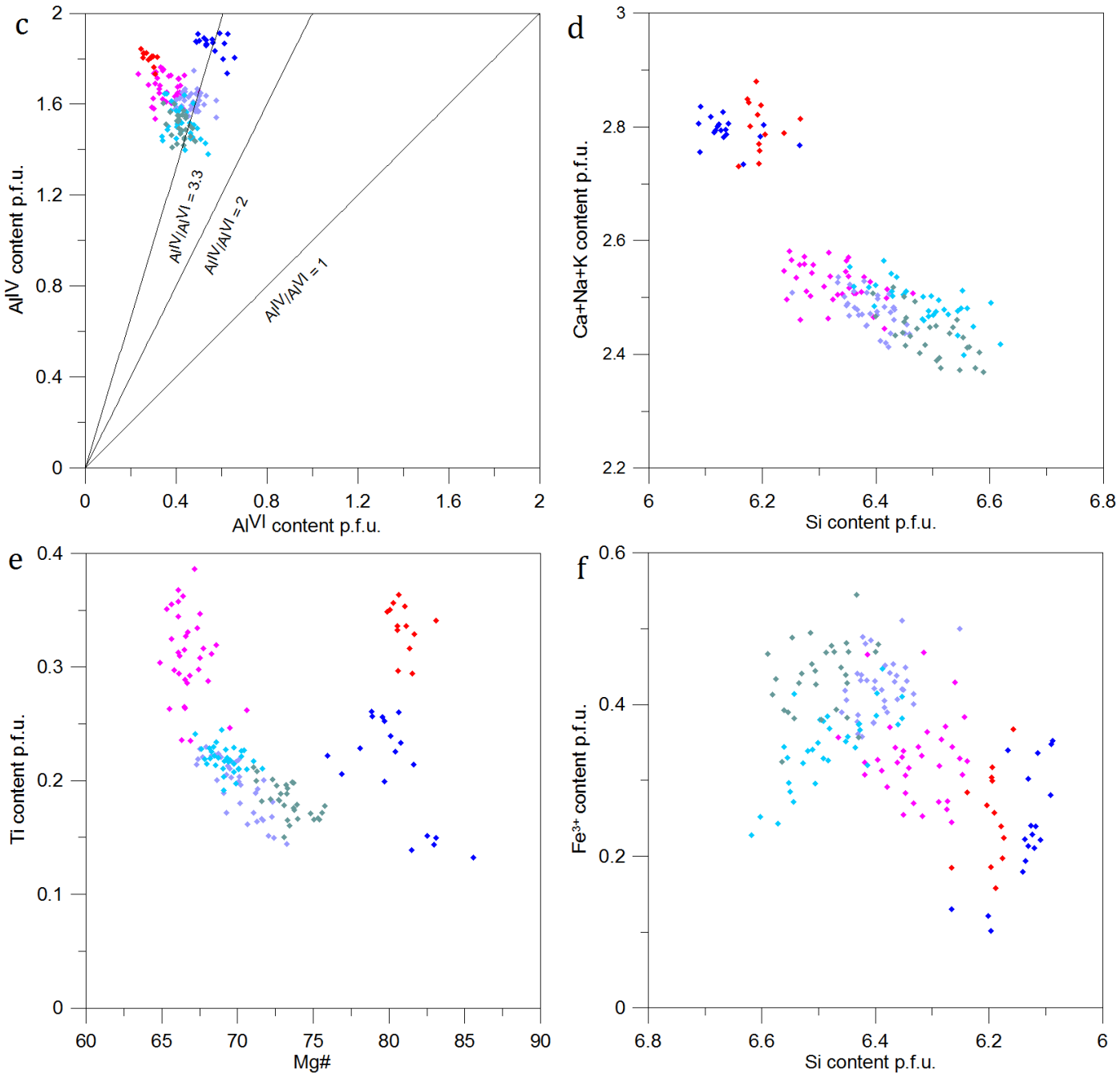

feldspars, indicating hornblende growth occurred over the primary magmatic texture. Some hornblendes show evidence for sub-grain formation but this occurs following original crystallisation. In any case, metamorphic poikiloblastic hornblende crystallisation requires fully static conditions, which would only be possible in contact metamorphism. However, contact metamorphism does not explain the widespread occurrence of these hornblendes.

Conditions for hornblende crystallisation

Al contents of hornblende are commonly used as a geobarometer (Hammarstrom and Zen, 1986; Johnson and Rutherford, 1989; Rutter et al., 1989), but this is only applicable to Qz bearing felsic to intermediate rocks such as tonalities and granodiorites and not to the gabbro's from this study. For gabbros, Al^{IV}/Al^{VI} partitioning, Ti and Fe^{3+} contents are commonly used as an indicator for the P-T conditions of hornblende crystallisation (Fleet and Barnett, 1978; Hammarstrom and Zen, 1986; Holland and Blundy, 1994; Spear, 1981). As gabbroic plutonism can also occur under the conditions for UHT metamorphism in the Bakhuis belt, these constraints do not provide evidence for either a magmatic or a metamorphic origin. However, by comparing the chemistry of samples taken in- and outside the Bakhuis belt, the relative preservation or

loss of compositions indicating P-T conditions can provide indications on whether hornblende has experienced multiple chemical equilibration events. If so, the composition of primary crystallisation can be established outside the Bakhuis and a possible metamorphic control on hornblende inside the Bakhuis belt compositions can be established.
All hornblende show a similar trend in Al partitioning, where most of the hornblende show an Al^{IV}/Al^{VI} ratio of > 3.3 which is defined as the igneous hornblende field by Fleet and Barnett (1978). Sample AT38 has slightly higher contents for Al, which is interpreted to be the result of the absence of (cumulus) plagioclase in the rock, causing excess Al to go into hornblende.
The fact that all samples of group 1 and LA14-100 of group 2 form a common trend in Al contents and partitioning indicates that they have experienced similar crystallisation conditions. As the metamorphic conditions have been different for samples in- and outside the Bakhuis belt, this is interpreted to reflect crystallisation conditions during initial primary crystallisation. Apparently, this signature has subsequently been preserved regardless of any metamorphic history.
Ti contents for samples within the Bakhuis Belt are consistently lower than the 2 samples outside the Bakhuis belt. This indicates that during metamorphism, the Ti content in hornblende is lowered and they no longer reflect primary crystallisation. An indication for this is that samples for the Bakhuis contain tiny black spots or black patches along cleavage planes, which could be Fe-Ti-oxides. When compared to literature values; the Bakhuis Ti values of 0.15-0.25 are consistent with what is known for hornblende of amphibolite facies, while the Ti values of 0.25-0.4 for samples outside the Bakhuis are consistent with either granulite facies metamorphism or a magmatic origin (Raase, 1974).
Igneous amphiboles are commonly considered to closely reflect the composition of their magmas (Martin, 2007). If it is interpreted that the Mg-number of amphiboles is a proxy for how evolved a magma is that the amphibole crystallised from, figure 4.3e shows that group 1 hornblendes show a group of considerably higher Mg-number than the group 2 hornblendes.
Fe3+ contents have also previously been used to infer crystallisation conditions (Raase, 1974 and references therein), where lower Fe3+ contents indicate higher crystallisation conditions. The very low Fe3+ contents additionally indicate high grade conditions for hornblende formation, and that the group 1 hornblende have seen slightly higher conditions than the group 2 hornblendes. However, there is a lot of scatter in the data.

Summary and interpretation
Based on the texture and mineral chemistry, hornblendes in group 1 are interpreted to have formed as primary, intercumulus hornblende. Such primary growth has also been described for other hornblende bearing gabbros (Beard and Borgia, 1989; Conrad and Kay, 1984; Wan et al., 2013a). Hornblende in group 2 is interpreted to reflect late primary magmatic hornblende, formed by a reaction between olivine and pyroxenes and an evolved hydrous melt. Such growth has also been described for hornblende bearing gabbros (Costa et al., 2002; Prouteau et al., 2001; Yan et al., 2015). It cannot be excluded that group 2 hornblendes started as group 1 hornblendes, so as a magmatic intercumulus phase, and subsequently experienced further growth due to the reaction between olivine and pyroxenes and an evolved hydrous melt. However, this process cannot have operated at a regional scale, since it has not influenced the stability of olivine and pyroxenes with hornblende in samples AT38 and LD14-100.
Hornblendes in the Bakhuis Belt have subsequently been influenced by amphibolite facies metamorphism, lowering the Ti content by exsolution into very small Fe-Ti-oxides and giving the hornblendes a greener colour. Brown hornblendes outside the Bakhuis have retained their high Ti content which represents conditions during magmatic crystallisation. Despite amphibolite facies retrograde metamorphism in the Bakhuis belt, all samples have preserved the Al^{IV}/Al^{VI} partitioning representative of primary crystallisation. This indicates that the partitioning is a good constraint on the conditions during igneous crystallisation for hornblende that has not completely recrystallized.
The conclusion that the Moi-Moi metagabbro contains primary hornblende has important implications for the petrogenesis of the magma. To crystallize hornblende out of a magma, it must contain significant amounts of water. Gabbro's with primary hornblende are common for arc related magmatism and relatively rare for MORB melts (Deer et al., 1992). This is consistent with whole rock chemistry of Thijssen (2015), which shows the signature of an arc magma origin. The geodynamic implications of this conclusion are discussed in the general discussion (section 6.1).

4.2 Petrography and geochemistry of the Mozeskreek anorthosite

4.2.1 Field relationships and sample petrography

4.2.1.1 Field description and sample selection

The Mozeskreek anorthosite body is a suite of partially metamorphosed plagioclase-rich igneous rocks exposed in the Mozeskreek, a small river in the centre of the Bakhuis belt. The entire body is approximately 3 x 4 km in size (de Roever et al., 2003b), but is in most places covered by a bauxite cap. The body shows a layering (fig. 4.5b) in cm-scale pyroxene bands (fig. 4.5d) and thicker leucogabbro-noritic bands, where layers dip angle about 40-50° to sub-vertical, roughly sub-parallel to the foliation in surrounding UHT granulites. In the Mozeskreek, the anorthosite body is almost continuously exposed, and the lithological variation is well expressed in both outcrop and float. Near the location for sample ER1225, a magmatic breccia of up to ~20 cm sized anorthosite clasts in a pyroxene-rich gabbroic matrix with zones that are rich in centimetre-sized hornblende.

In total 11 samples were taken from both outcrop and float in a ~1.5 km long part of the riverbed just northwest of the termination of the railway that was constructed to facilitate mining, but was never taken in use (see fig. 4.4 for sample locations). Samples were supplemented with 3 drill core samples (ER108, ER117 and ER120), which were drilled close to the Mozeskreek as part of bauxite exploration in the 70's.

4.2.1.2 Sample petrography

The suite is predominantly a medium to coarse grained (leuco)gabbronorite to rarely a real anorthosite. Assemblages include plagioclase feldspar, clinopyroxene, orthopyroxene, minor hornblende and opaque minerals.

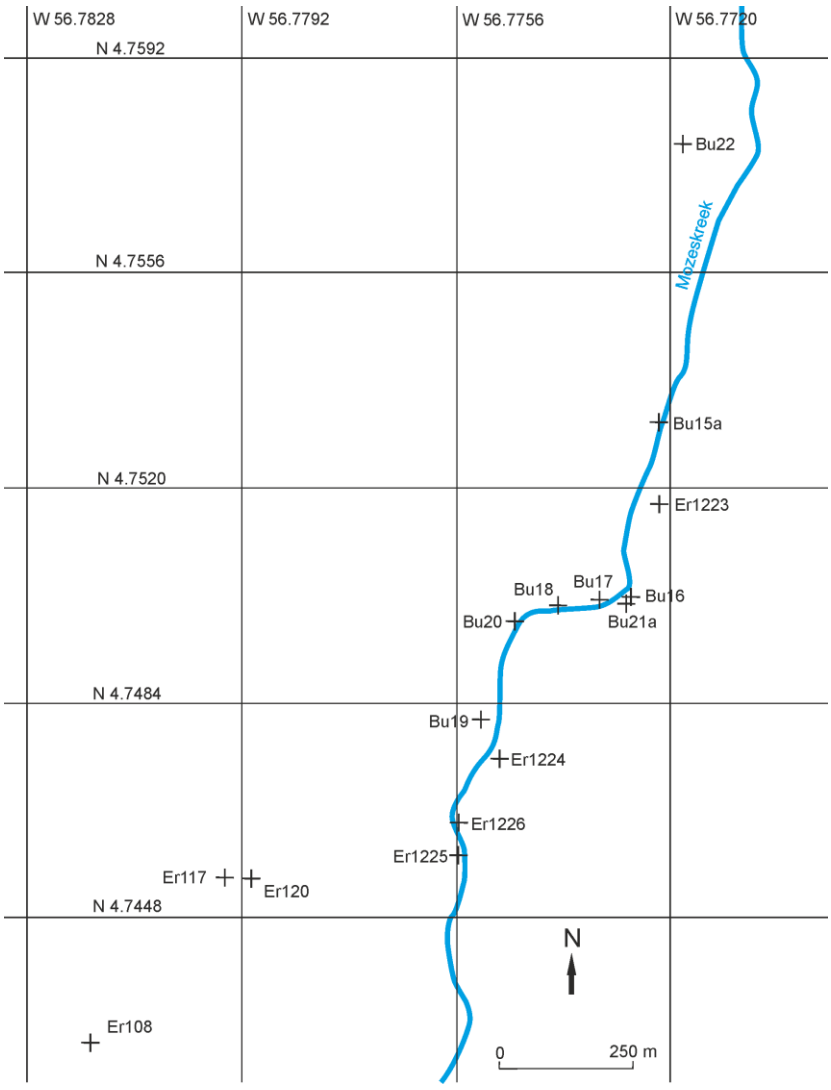

Figure 4.4 Sample locations for the anorthosite body along the Mozeskreek. Grid coordinates are in decimal degrees. Sample BU22 is a piece of float outside the body, which starts just north of BU15a.

The bulk of the samples

Mineral ratios vary from ~40% plagioclase feldspar and up to 50 % pyroxenes in the relatively rare gabbronorites to >90% feldspar with little intercumulus pyroxenes in the true anorthosites. The bulk of the sample contains 65% feldspar and upwards, classifying as leucograbbros to anorthosites. Samples ER1223 and BU15b show a preferred orientation of mafic minerals, exhibiting a weak foliation (fig. 4.5f) but most samples show a granoblastic texture (fig. 4.5e and g).

Plagioclase – Plagioclase feldspars commonly display a typical lamellar albite twinning and more rarely Carlsbad twinning. Plagioclase crystals are highly inequigranular, forming larger subhedral laths to granular textures. Larger crystals commonly show kinking, grain

Figure 4.5 Outcrop photographs and thin section scans of the Mozeskreek anorthosite. A) Homogeneous outcrop of leucogabbro with an elongate mafic xenolith. The black spot just above hammer tail is a patch of moss. B) Preferential weathering as the result of igneous layering. The resistant band just right of the pen is a pyroxene rich layer in between layers more abundant in plagioclase. C) Breccia of up to ~30 cm sized clasts in a mafic gabbroic matrix. D) Thin mafic band in a loose block of leucogabbro. E) Thin section of a coarse granular gabbro BU20. Pink-brown crystals are OPX, grayish-blue crystals are CPX, white is plagioclase and green is hornblende. F) Thin section of a weakly foliated leucogabbro BU19. G) Thin section photograph of a hornblende rich leucogabbro.

boundary bulging and deformation twinning, indicating significant deformation. Feldspars do not show any antiperthite exsolution.

Orthopyroxene – Orthopyroxenes vary from up to 5 mm euhedral/subhedral crystals in mafic samples to medium and fine grained aggregates in plagioclase rich samples. Orthopyroxenes have pink to light grey pleochroism and are identified by typical straight extinction and lower order interference colours. Orthopyroxenes contain many red brown patchy oxides, interpreted to have formed after crystallisation. A cleavage plane is commonly not developed, but expressed in the preferred orientation of the brown oxides.

Clinopyroxene – Clinopyroxene display the same size variation as orthopyroxenes. They appear as non-pleochroic light grey crystals with higher order interference colours. One cleavage plane is commonly well developed and thin lamella of OPX indicate low temperature exsolution.

Hornblende – Hornblende is identified by its dark green to brown colour and amphibole cleavages. Hornblende is dominantly a secondary mineral, statically replacing pyroxenes along their

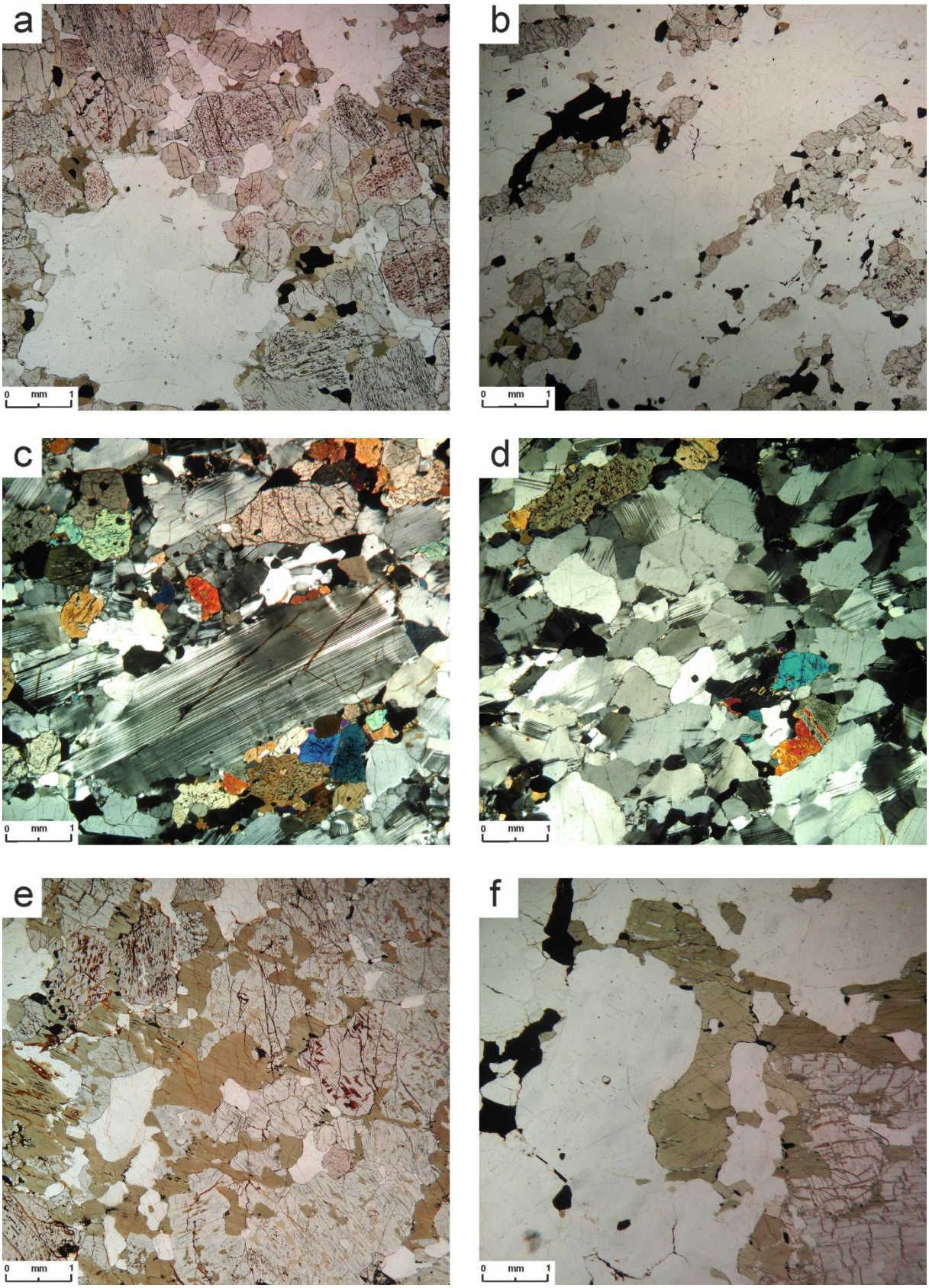

Figure 4.6 Thin section photographs of the Mozeskreek anorthosite. A) Aggregates of plagioclase in surrounded by orthopyroxene (pink, spotted), clinopyroxene (gray to lime-green) and minor plagioclase. Sample BU20. B) Intercumulus pyroxenes showing a preferred orientation which could be described as weak layering or foliation. Sample ER1223. C) Preserved larger plagioclase lath in a, due to metamorphism, more granular groundmass of plagioclase and pyroxenes. Sample BU19. D) Metamorphic granoblastic texture of a true anorthosite (>90% plagioclase). Sample BU15b. E) Poikiloblastic hornblende enclosing plagioclase and (embayed and reacting) ortho- and clinopyroxenes. Sample BU21a. F) Granular hornblende crystals in an intercumulus texture between plagioclase, and replacing a larger orthopyroxene crystal in the bottom right. Sample BU22.

boundaries and in patches within the crystals. The degree of hornblende replacement varies over the samples. However, in BU21a cm-sized primary poikilitic hornblende encloses plagioclase and pyroxenes, suggesting the presence of water in the magmatic evolution similar to the Moi-Moi metagabbro (see section 4.1).

Opaque minerals – The amount of opaque minerals varies strongly between the samples, showing a negative correlation with the amount of pyroxene. It is interpreted that, at e.g. low Mg content, Fe goes preferentially into oxides as pyroxenes cannot be formed. The amount of oxides is not correlated to the titanium contents (see section 4.2.2).

4.2.2 Geochemistry

4.2.2.1 Major element variation

Harker diagrams of the major element variation are plotted in figure 4.7. The major elements have been plotted against MgO, as this gives a better constraint on fractionation processes for mafic rocks. The compositions of the Moi-Moi metagabbro and the Charlie gabbro from Thijssen (2015) have been plotted as polygons to compare them to the Mozeskreek anorthosite.

MgO ranges between 1 and 14%, forming three clusters of 1 – 2%, 4 – 7% and ~13%. SiO_2 contents range between 44-50%. Most major elements show a single linear trend when plotted against magnesium. Aluminium (10.6 – 29.8%), calcium (8.7 – 14.9%) and sodium (0.8 – 2.9%) show a decreasing trend with increasing magnesium. Manganese (0.04 – 0.3%) and iron (4 – 17.5%) show an increasing trend with increasing magnesium, Titanium shows a seemingly random scatter unrelated to the magnesium content. Potassium contents are very low and show a very weakly negative trend with increasing MgO. The magnesium number increases with increasing magnesium. The CaO/Al_2O_3 ratios, as a measure for clinopyroxene and/or plagioclase crystallisation and accumulation, are commonly low for the magnesium-poor samples but show slightly elevated values for the magnesium rich samples.

The Mozeskreek anorthosite shows a better compositional overlap with the Moi-Moi metagabbro than with the Charlie gabbro. A consistent >5 samples plot outside of the Charlie gabbro field and for silica and in particular sodium, the Mozeskreek anorthosite and the Charlie gabbro show different parallel trends; where the Charlie gabbro shows a trend with higher silicon and sodium. The trends in the Mozeskreek anorthosite fit well with the trends in the Moi-Moi metagabbro. The three samples in the 1 – 2% MgO group always plot outside the Moi-Moi metagabbro field; however for most elements (aluminium, calcium, iron, manganese) they plot in a continuation of trends in the Moi-Moi metagabbro data. The potassium contents are consistently lower, which can be the result of plagioclase accumulation processes and might indicate less contamination with alkali-feldspar than the Moi-Moi metagabbro samples. Also, the anorthosite shows much less evidence in CaO/Al_2O_3 ratios for pyroxene accumulation.

A CIPW-norm has been calculated for the major elements of the samples following the method described in the appendix of (Winter, 2010), using a Fe_2O_3/FeO ratio of 0.15 Normally, a CIPW cannot be calculated for samples that contain hydrous minerals such as hornblende. Given the low abundance of hornblendes, the calculation is made on the assumption that the hornblende has formed as the breakdown of pyroxenes and represents primary pyroxene. An AFM diagram has been plotted in figure 4.8. The Mozeskreek Anorthosite follows a well-developed tholeiitic trend, largely overlapping with the tholeiitic trend in the Moi-Moi metagabbro.

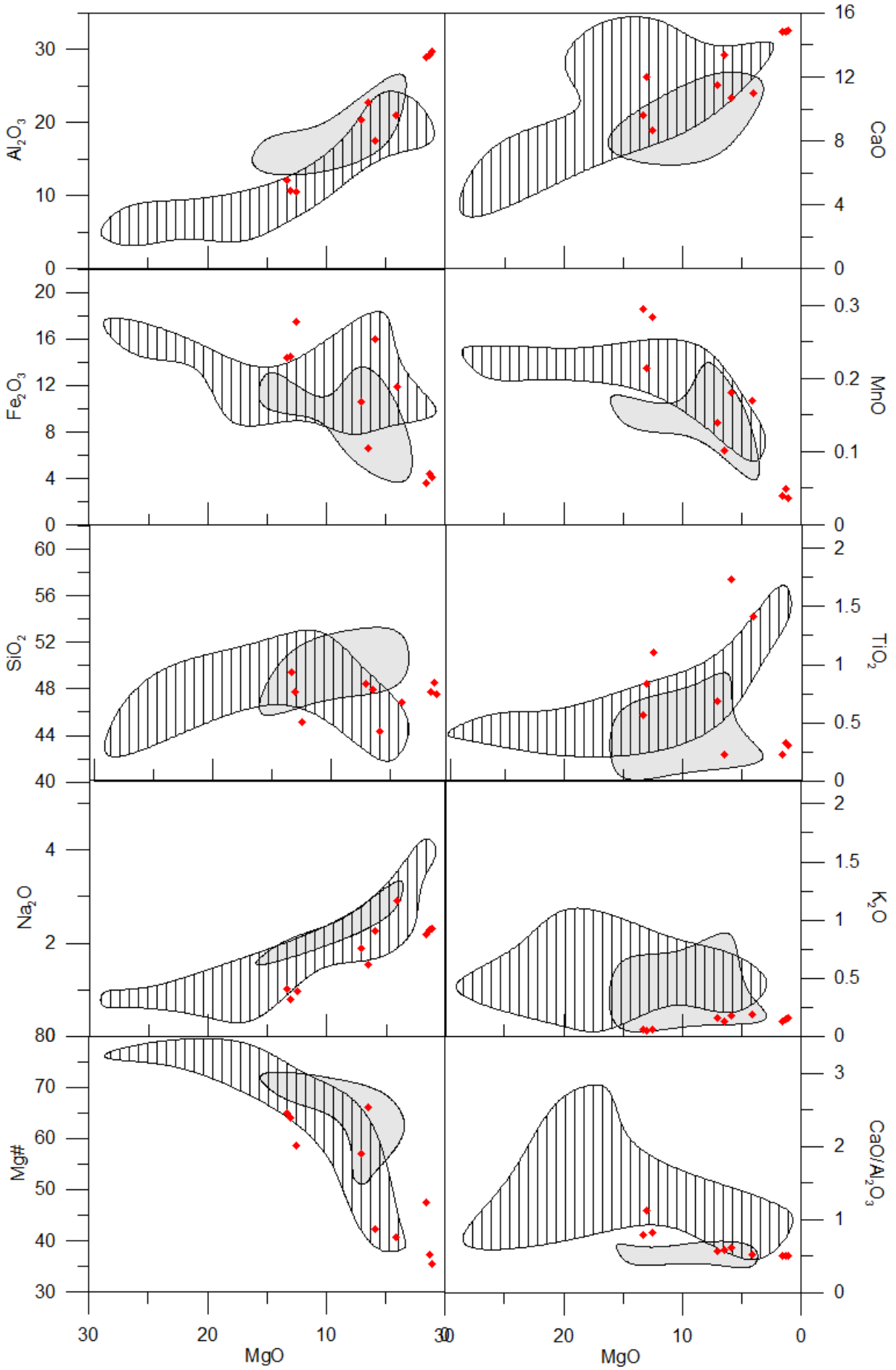

Figure 4.7 Major elements vs MgO in Harker-type diagrams for the Mozeskreek anorthosite. All values are in weight %. The grey striped polygons indicate the range of compositions found for the Moi-Moi metagabbro and the gray shaded polygons indicate the range of compositions found for the Charlie gabbro by Thijssen (2015).

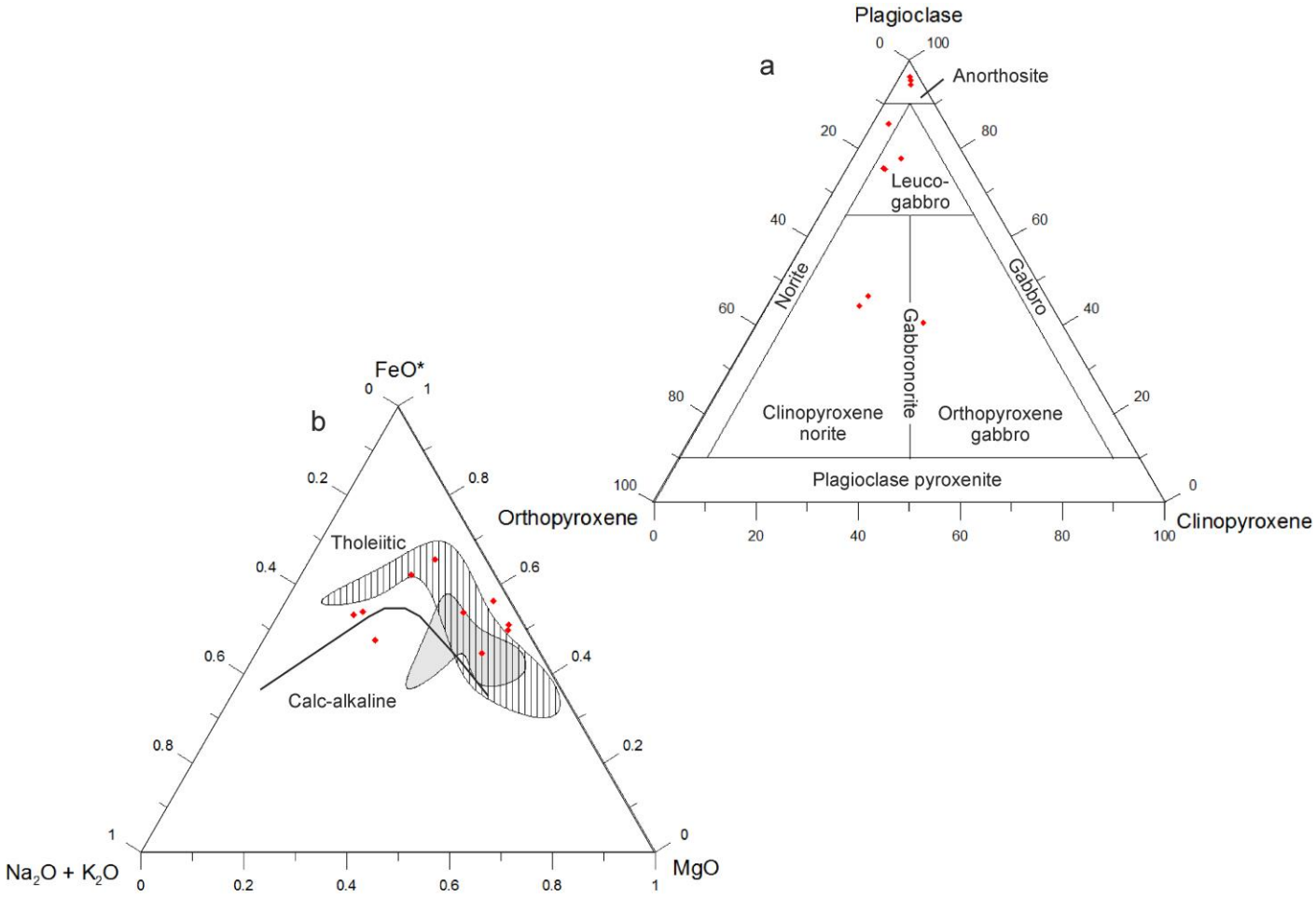

Figure 4.8. a) Gabbro classification diagram after Le Maitre (2002). Modal abundances were calculated using the CIPW-norm after Winter (2010) and normalised to 100% plagioclase, OPX and CPX. b) AFM-diagram for the Mozeskreek anorthosite with tholeiitic – calc-alkaline divide after (Irvine and Baragar, 1971). The striped polygon indicatse the range of compositions found for the Moi-Moi metagabbro and the gray shaded polygon indicates the range of compositions found for the Charlie gabbro by Thijssen (2015).

4.2.2.2 Trace element variation

Rare earth elements and some trace elements like lead, thorium, uranium have very low abundances (<10 ppm) in the anorthosite. As a consequence, the analytical errors are very large on the XRF measurements and the data scatters when plotted (see also section 3.4.2 and figure 3.2e). This section only describes the elements that have high enough abundances to display a geochemically significant spread. Low abundance elements are included in 4.2.2.3 based on ICP-MS analysis on four anorthosite samples.

Compatible elements

Compatible element variation for nickel, vanadium, chromium and cobalt has been plotted in figure 4.9. As compatible elements preferentially go into mafic solid phases, they indicate fractionation of mafic minerals. Nickel and cobalt preferentially go into olivine, while chromium preferentially goes into pyroxene. Vanadium commonly replaces titanium and indicates formation of titanium rich phases.

All of the compatible elements show a weak positive relationship with increasing magnesium. Ni shows a compositional trend from 20 to 200 ppm in the bulk of the samples while 2 of the samples plot above the trend. Vanadium concentrations range between 85 and 350 ppm. Chromium contents are very low reaching up to 500 ppm, while the gabbroic bodies yield samples with higher concentrations. Cobalt shows an increasing trend going up to 100 ppm. The trends overlap well with the Moi-Moi metagabbro and for nickel, vanadium and chromium show a larger spread than the Charlie gabbro.

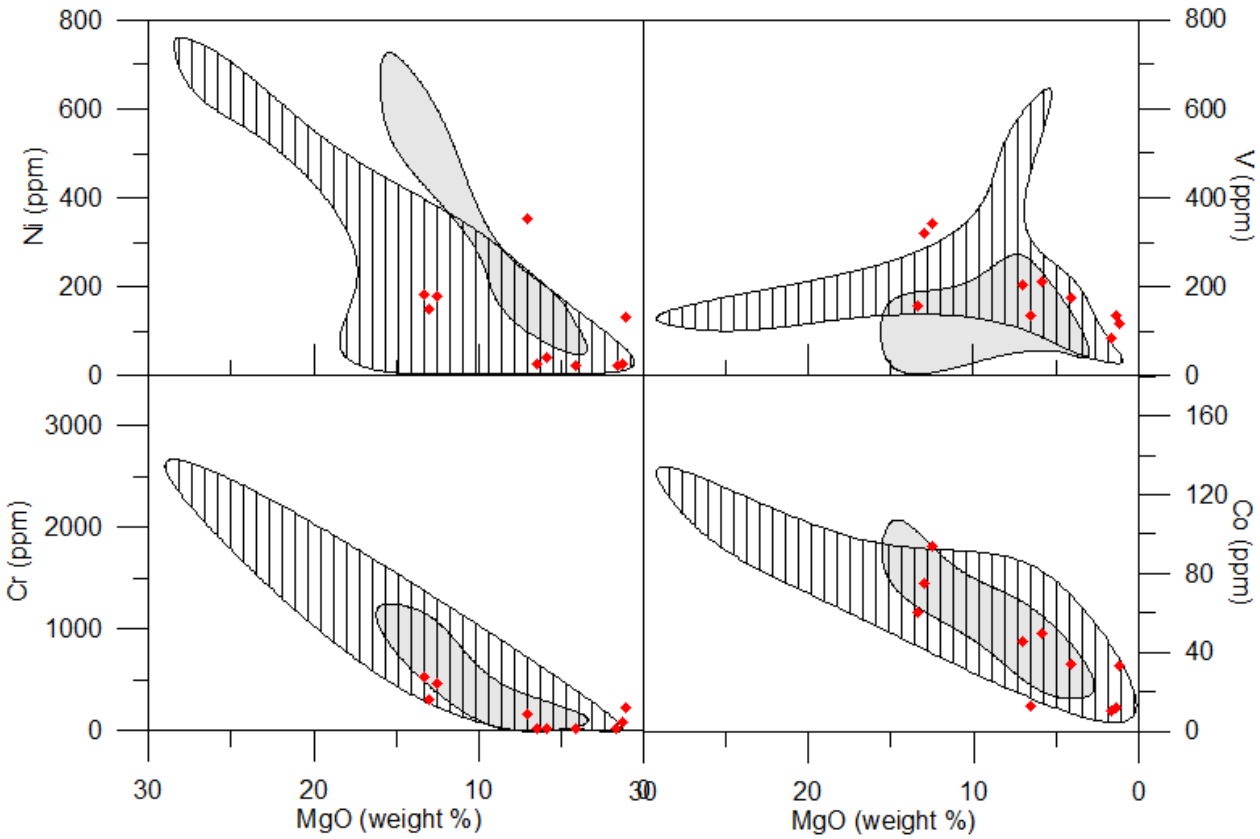

Figure 4.9. Compatible elements vs MgO in Harker-type diagrams for the Mozeskreek anorthosite. All values are in weight %. The grey shaded polygons indicate the range of compositions found for the Moi-Moi metagabbro and the striped polygon indicates the range of compositions found for the Charlie gabbro by Thijssen (2015).

Incompatibles: large ion lithophile elements

Variation for the LILE rubidium, strontium and barium has been plotted in figure 4.10. The LILE preferentially incorporate into alkali-feldspar (rubidium, barium) or plagioclase (strontium). The LILE are highly mobile and are quickly lost during metamorphism. For primary gabbroic magmas, they are a good indicator for contamination or mixing with felsic magmas.

Rubidium and barium contents are very low, reaching only 5 ppm and 150 ppm respectively. Barium shows a weakly increasing trend with decreasing magnesium. Strontium contents are higher and show an increasing trend with decreasing magnesium, ranging between roughly 300 and 800 ppm. Ba/Sr ratios are very low due to the low barium contents. They show no consistent relationship with magnesium. The low rubidium and barium contents are different from both the Moi-Moi metagabbro and the Charlie gabbro.

Incompatibles: High field strength elements

Variation for a selection of HFSE has been plotted in figure 4.11. Uranium and thorium are often included in HFSE plots, but for the anorthosite, uranium contents were below XRF detection limits and thorium concentrations were very low, producing a geochemically insignificant scatter. HFSE are commonly not incorporated in silicate minerals but concentrated in accessory phases. Low HFSE contents can indicate residual accessory phases during melting or that the magma is not very evolved.

The data show different behaviour for niobium and zirconium than for hafnium and tantalum. Niobium and zirconium show very low concentrations reaching only up to 1 ppm and 13 ppm respectively. Very few samples yielded tantalum concentrations above the XRF detection limits, and the resulting data yield a scatter with no relationship to magnesium. The scatter may also be an artefact of low concentrations. Hafnium concentrations show a poorly developed decreasing trend with decreasing magnesium. The anorthosite has lower niobium and zirconium contents than the gabbroic bodies, while the tantalum and hafnium concentrations show overlap.

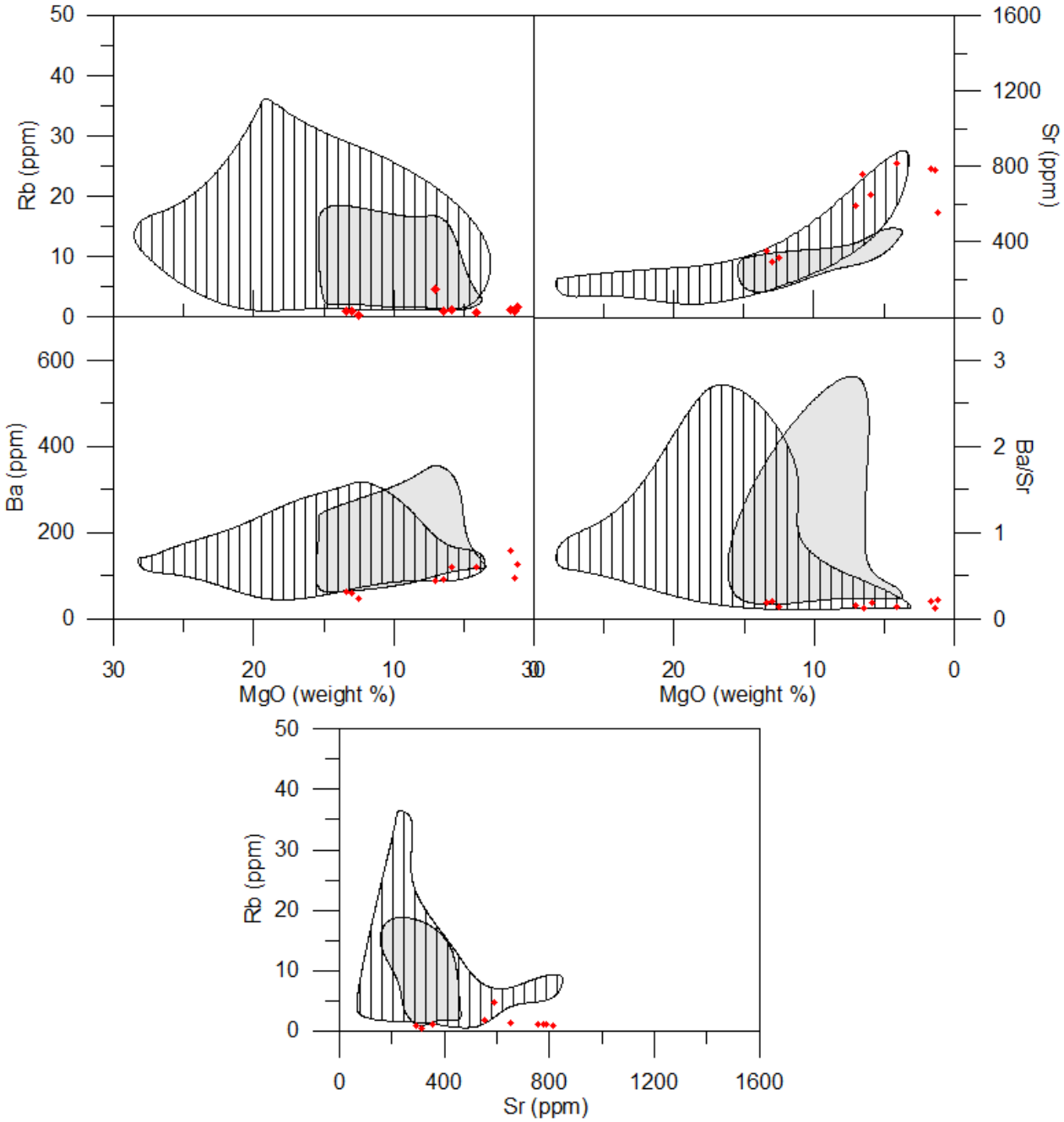

Figure 4.10 Large ion lithophile elements vs MgO in Harker-type diagrams for the Mozeskreek anorthosite. All values are in weight %. The grey shaded polygons indicate the range of compositions found for the Moi-Moi metagabbro and the striped polygon indicates the range of compositions found for the Charlie gabbro by Thijssen (2015).

4.2.2.3 Multi element variation and rare earth elements

Based on the spread in XRF data, four samples (BU15b, BU20, ER1224 and ER120) were selected to perform ICP-MS analysis for low abundance trace elements and rare earth element compositions. Rare earth and multi-element variation patterns have been plotted in figure 4.12a and b. A trace element tectonic discrimination diagram is commonly plotted for mafic magmas (Pearce, 2008; Pearce and Cann, 1973). Given the plagioclase accumulation processes that have affected the Mozeskreek anorthosites, the samples plot in odd locations for all possible trace element discrimination diagrams. Consequently, the diagrams have been omitted.

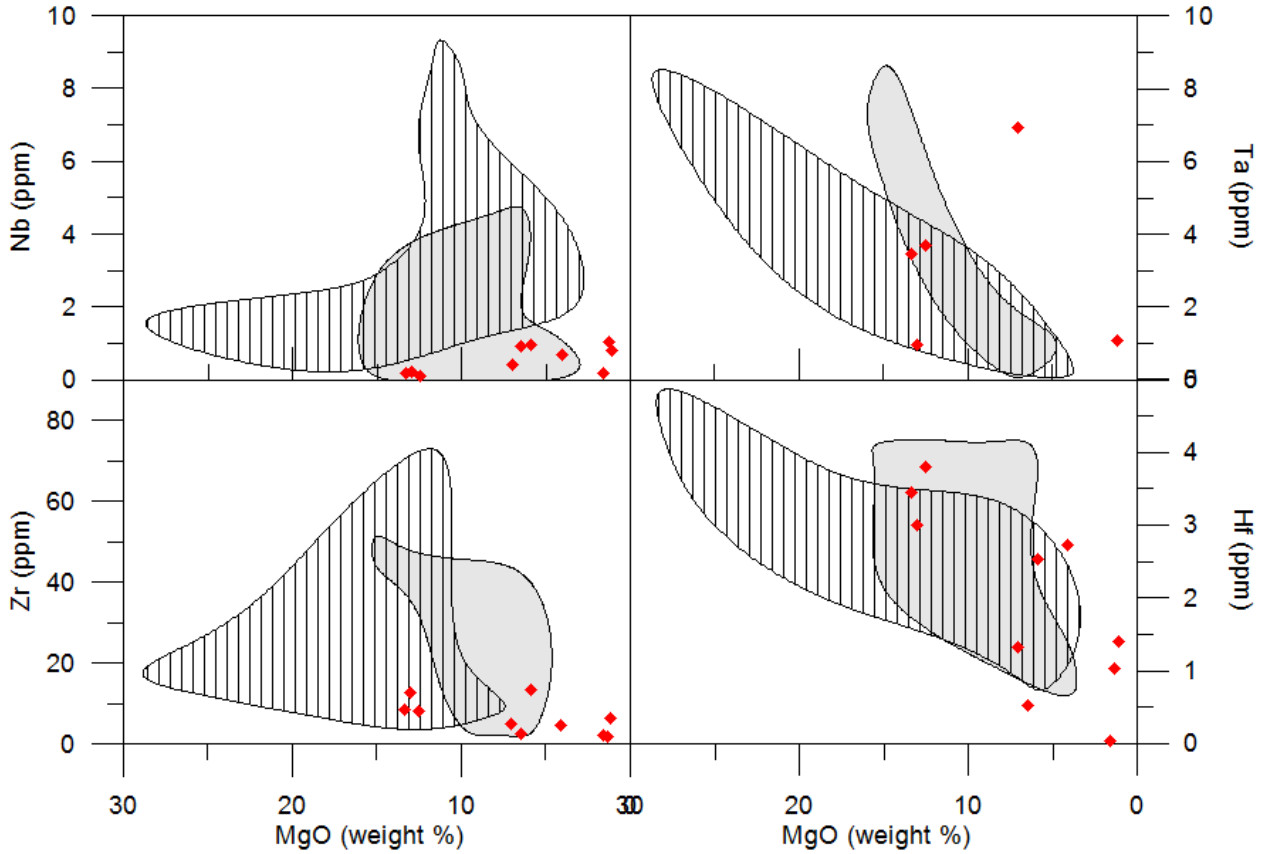

Figure 4.11 High field strength elements vs MgO in Harker-type diagrams for the Mozeskreek anorthosite. All values are in weight %. The grey shaded polygons indicate the range of compositions found for the Moi-Moi metagabbro and the striped polygon indicates the range of compositions found for the Charlie gabbro by Thijssen (2015).

Rare earth elements

The REE patterns display an order of magnitude variation in enrichment with respect to chondrite. The REE patterns for BU15b, ER1224 and ER120 show a varying moderately negative slope from LREE to HREE, where normalised La/Yb values range between 3.7 – 10. The slope is generally steeper for the LREE than the HREE, where La/Sm ~ 1.6 – 3.3 and Dy/Lu ~1.4 – 1.5. BU20 shows a weak positive slope for LREE (La/Sm ~ 0.89) and continues as a flat to weakly negative slope for the MREE and LREE where Sm/Lu ~1.5. All samples show a positive europium anomaly, consistent with the high plagioclase content of the samples. The size of the anomaly varies, where Eu/Eu* = 2.7 for ER120 as a true anorthosite and Eu/Eu* = 1.2 for BU20 as a gabbronorite.

The patterns for the anorthosite show good overlap with the Charlie gabbro, while the patterns plot at or below the lower boundary of the range in Moi-Moi metagabbro patterns. Compared to both types of gabbroic bodies, the anorthosite shows a more pronounced europium anomaly.

Multi element variation diagram

The anorthosite patterns show a slight enrichment in LILE elements (on the left of the patterns) and a pronounced depletion in HFSE (right end of the patterns) with respect to N-MORB. The depletion indicates that the plagioclase cumulates formed out of a relatively primary melt, leaving the incompatible rare earth elements behind in the melt. The patterns show a weakly negative rubidium anomaly, just above the value for N-MORB. This was also apparent from the relatively low compositions in the XRF trace element measurements of section 4.2.2.2. The patterns show a pronounced negative tantalum and niobium anomaly and a positive lead anomaly, which are consistent with a subduction origin of the melt (e.g. (Baier et al., 2008)). The patterns show a negative thorium, uranium and zirconium anomaly. As they all go into accessory phases such as zircon (for U, Th and Zr) and/or apatite (for U and Th), their depletion perhaps indicates zircon had already crystallised out of the magma. A more likely scenario is that the magma was relatively primary the formation of accessory phases did not occur yet during plagioclase accumulation, leaving the residual magma enriched in these elements. The relative positive europium

anomaly as discussed for the rare earth patterns is also present in the multi element variation diagram, yet most of the positive anomalies still plot below the value for N-MORB.
Compared to the Moi-Moi metagabbro, all incompatible elements are relatively less enriched. The patterns show better overlap with the Charlie gabbro. The anomalies are mostly parallel, but less well developed. Only the positive strontium anomaly and the negative zirconium anomalies are more pronounced in the Mozeskreek anorthosite patterns, which are considered the result of the plagioclase accumulation.

4.2.3 Discussion

Magmatic petrography
In mineral abundances, the Mozeskreek Anorthosite is comparable to other Proterozoic anorthosite occurrences, which usually range in 75 – 95% plagioclase (Ashwal, 1993). The three samples that are relatively mafic represent a sample bias to determine the geochemical variation of the body. The weak metamorphism causing a granular texture (for most samples) to a minor foliation (BU15b and ER1223) has obscured most primary magmatic textures of the Mozeskreek anorthosite. Relict large crystals of euhedral lath-shaped plagioclase (ER1223, fig. 4.6c) and circle shaped plagioclase clusters (BU20, fig.

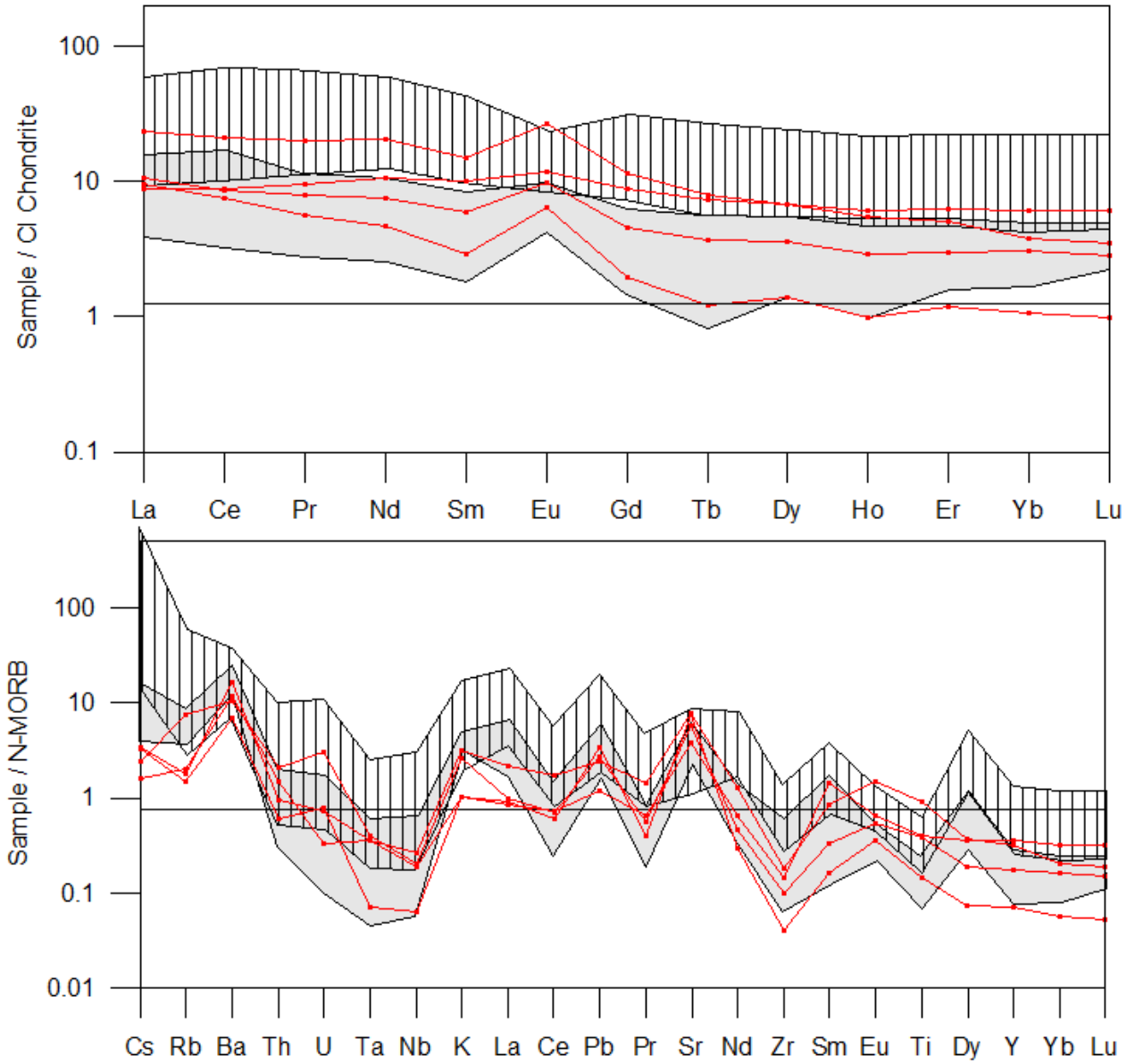

Figure 4.12. Above: REE diagram with samples normalised over CI chondrite (McDonough and Sun, 1995). Lutetium is included for interpretation of radiogenic isotopes in section 4.3. Below: A multi element variation diagram with values normalised over N-MORB (Sun and McDonough, 1989).

4.6a) are interpreted to reflect primary magmatic accumulation. These textures are consistent with a plagioclase cumulate origin commonly assumed for anorthosites (see Ashwal, 1993 for a review).
The presence of hornblende as a late intercumulus phase coexisting with pyroxenes (e.g. BU20, fig. 4.6a and BU22, fig. 4.6f), but also as cm-sized poikilitic crystals (e.g. BU21a, fig. 4.6e), indicate the presence of water in the magma. The poikilitic crystals of sample BU21a show group 2 textures of section 4.1 (breakdown of pyroxene to hornblende), and are similarly interpreted to be reflect primary textures (see 4.1.4 for discussion). The field relationships shown in fig. 4.5c, where anorthosite clasts occur in a metagabbroic matrix, which locally contains cm-sized hornblende crystals, could indicate that water was introduced in a late stage when the partly crystallized Mozeskreek anorthosite was intruded by more a pulse of a more hydrous magma.

Interpretation of geochemistry

Caution must be taken when analysing classical major element variation diagrams for anorthosites, as they are usually considered to reflect the plagioclase accumulation and the open-system exchange of the interstitial liquid, rather than provide constraints on the composition of the parental liquid (Ashwal, 1993). Typical features of this problem are the simple, single fractionation trend found in the major elements (fig. 4.11), the positive europium and strontium anomalies in the rare earth and multi element variation patterns (fig. 4.12). However, some of the data show variation which cannot be explained by pure plagioclase accumulation, indication a role for the parental magma.
Major and trace elements show a trend that is consistent with plagioclase accumulation; samples with more plagioclase show lower contents of magnesium, iron and compatible elements yet higher sodium, calcium, aluminium and strontium. The extremely low barium and rubidium contents, even for pyroxene rich samples, indicate the source or a possible contaminant did not contain alkali-feldspar. This rules out, for example, interaction with the Kabalebo charnockites or intermediate granulites and pelitic gneisses, which both have strongly enriched barium contents (Klaver, 2011).
The strong variation in REE enrichment is interpreted to be the effect of accumulation of plagioclase. The variation is consistent with the strong variation in major elements and indicates that various degrees of plagioclase accumulation are achieved in the sequence. The negative niobium and tantalum anomaly and HFSE depletion and the positive lead anomaly and LILE enrichment are consistent with a subduction type origin. The negative uranium, thorium and zirconium are most likely the result of plagioclase accumulation processes while no zircon is formed, leaving the residual magma enriched in all elements that normally partition into zircon.

Anorthosite models and petrogenesis of the Mozeskreek anorthosite

Several models for anorthosite formation have been

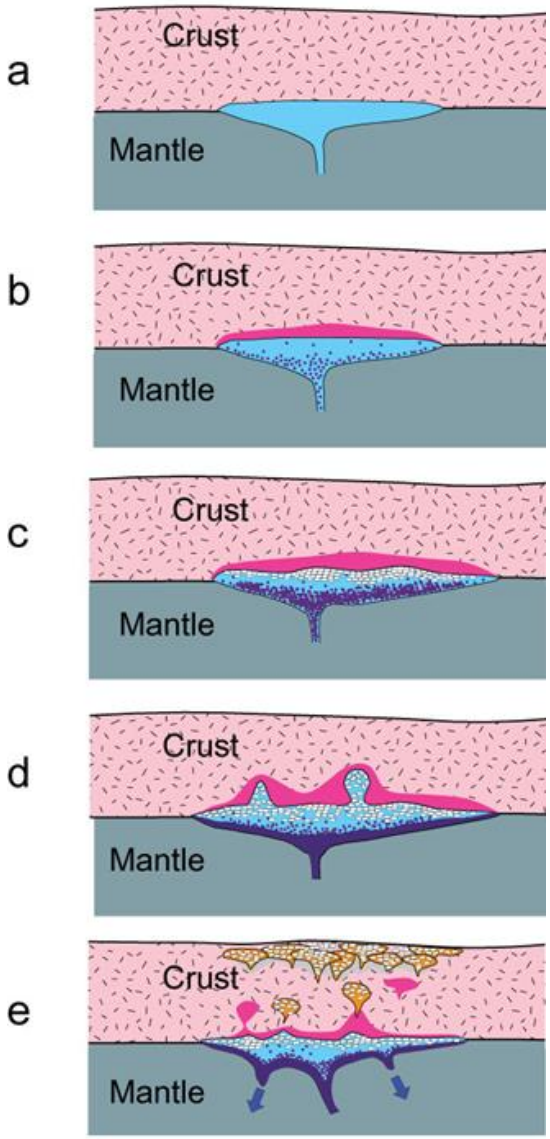

Figure 4.13 Model for the formation of anorthosites in general, and Proterozoic massif-type anorthosites in particular. After (Ashwal, 1993). A) Mantle-derived magma underplates the crust. B) Crystallisation of mafic phases which sink and partial melting of the crust above the magma. C) Plagioclase forms when the melt is sufficiently enriched and rises to the top of the magma chamber while mafic minerals sink. D) Plagioclase, accumulated in 'crystal mushes' become less dense than the crust and start ascending. E). Plagioclase plutons form massif anorthosites, whereas charnockite crustal melts rise to shallow levels as well.

proposed in the literature. In general, it is accepted that anorthosites form by plagioclase accumulation processes, in some cases assisted by ascent of crystal mushes into the crust where the crystal mush becomes separated from the parental magma (see figure 4.13 for details). (Ashwal, 1993) describes six types of anorthosites that each have their own characteristics and specific model for formation: 1) Archean megacrystic anorthosites, 2) Proterozoic (massif-type) anorthosites, 3) Anorthosites in layered mafic complexes, 4) Thin anorthosite layers in oceanic settings, 5) Anorthosite inclusions in other rock types and 6) Extraterrestrial anorthosites. The petrogenesis of the Mozeskreek anorthosite is discussed in the light of the existing models. The first, fourth, fifth and sixth groups can immediately be ruled out based on the age and location of the Mozeskreek anorthosite.

While the layering in the Mozeskreek anorthosite shows some characteristics of the model for anorthosites in layered mafic complexes, the relative proportions of anorthosite (6 – 21%) layers compared to mafic cumulate layers (79 – 94%) are much lower (Ashwal, 2010). On the contrary, almost the entire body of the Mozeskreek anorthosite is comparatively plagioclase rich, and mafic cumulate layers such as pyroxenites are absent. Also, a lot of the leucogabbros and anorthosites appear massive and show very little layering. This indicates the bulk of the magma was enriched in plagioclase, rather than that plagioclase enrichment was only achieved by alternating preferred mineral crystallization periods producing the layering.

The Proterozoic massif-type anorthosites are restricted to the Proterozoic and commonly appear as large batholith-sized (up to 20.000 km^2) bodies, associated with leucogabbros (Ashwal, 1993). While the Mozeskreek anorthosite is much smaller (only ~12 km^2), it does show the association with leucogabbros that is common for this type. It also cannot be excluded that more anorthosite bodies are hidden in inaccessible parts of the Bakhuis belt, especially given the presence of many other bauxite caps which could indicate more anorthosite occurrences. Additionally, Proterozoic massif-type anorthosites are often associated with charnockites, which are the dominant lithology in the southwest of the Bakhuis belt.

The composition of plagioclase has not been identified for this thesis. However, a rough estimation can be made based on the whole rock chemistry of sample ER120 (containing 92% plagioclase). The sample contains roughly 15% CaO, 2.3% Na_2O, 29.8% Al_2O_3 and 2.3% Na_2O. This corresponds to a Bytownite, which contains an An% of ~75%. Although at the high end, this falls within the range of An% reported for Proterozoic-massif type anorthosites (Ashwal, 2010).

Given its mixed similarities to both types, the Mozeskreek anorthosite is interpreted as a transitional type between massif-type anorthosite plutons and layered intrusions. It is interpreted that the body reflects a plagioclase-rich crystal mush which has ascended into the crust and was separated from its parental magma. The body was subsequently further crystallized as a layered mafic cumulate where more mafic cumulates and hornblende could crystallize out of the remaining mafic melt, assisted by a later pulse of more hydrous magma. A similar evolution has been described for other anorthosite complexes, such as the Proterozoic Laramie anorthosite complex in Wyoming (Lindsley et al., 2010).

Relationship to other gabbroic bodies

While the geochemistry and petrography of the Mozeskreek anorthosite is markedly different from the Charlie gabbro, several characteristics indicate similarity with the Moi-Moi metagabbro: 1) Overlapping or closely approximating geochemistry in most major and compatible elements. 2) The granular to foliated metamorphic texture. 3) The presence of water in the magma as indicated by intercumulus and poikilitic hornblende. 4) The common U-Pb zircon age around 1980 Ma for both bodies (de Roever et al., 2003b; Thijssen, 2015).

However, there are also marked differences with the Moi-Moi metagabbro. The concentrations in potassium, titanium, LILE and REE are significantly lower. The elevated levels for these elements in some samples of the Moi-Moi metagabbro are interpreted to reflect magma mixing with the Kabalebo charnockites (Thijssen, 2015). Apparently, this process did not influence the Mozeskreek anorthosite. While outcrops of the Kabalebo charnockites are dominantly ~50 km away, this also indicates the Mozeskreek anorthosite was not contaminated with possible charnockite occurrences in the subsurface. The lower levels can also be explained by relatively early plagioclase accumulation processes, leaving the parental magma more enriched in these elements. Another difference is clear layering expressed by the Mozeskreek anorthosite, where the Moi-Moi metagabbro occurrences only show a gradual variation in lithologies from core to rim without a clear and discernible layering. This difference must reflect differences in accumulation processes. Perhaps potential mafic layering is disturbed in the Moi-Moi metagabbro by mixing with the Kabalebo charnockite magmas, creating a bigger variation in magma compositions during crystallisation.

The strongly similar characteristics to the Moi-Moi metagabbro are interpreted to reflect a common parental magma. Considering the model for anorthosite formation in the previous section, it is interpreted

that the Mozeskreek anorthosite reflects a plagioclase-rich mush separated from the same hydrous parental magma, leaving it more enriched in mafic minerals. The interpretation of a similar hydrous parental magma would also explain the relatively small size and scarcity of anorthosite bodies compared to a normal Proterozoic massif-type anorthosite, as crystallisation of plagioclase can be suppressed by high water contents in a magma (Sisson and Grove, 1993). Inversely, an anorthosite can only be formed out of the Moi-Moi parental magma if it has reduced water contents. This indicates that the Mozeskreek anorthosite represents a magma derived from a relatively anhydrous part of the same magma source.
The possibility of a common magma source for the Mozeskreek anorthosite and Moi-Moi metagabbro is further explored using radiogenic isotopes in the next section.

4.3 Isotope dilution of mafic plutonic bodies

4.3.1 Sample selection

Based on the geochemistry of Thijssen (2015), three samples were selected from occurrences of the Charlie gabbro at the Misty Mountain creek, the Moi-Moi creek and the Kabalebo river. Six samples were taken from three different occurrences of the Moi-Moi metagabbro and one sample was selected from the occurrence of the Mozeskreek Anorthosite in the centre of the Bakhuis belt. Sample locations for the

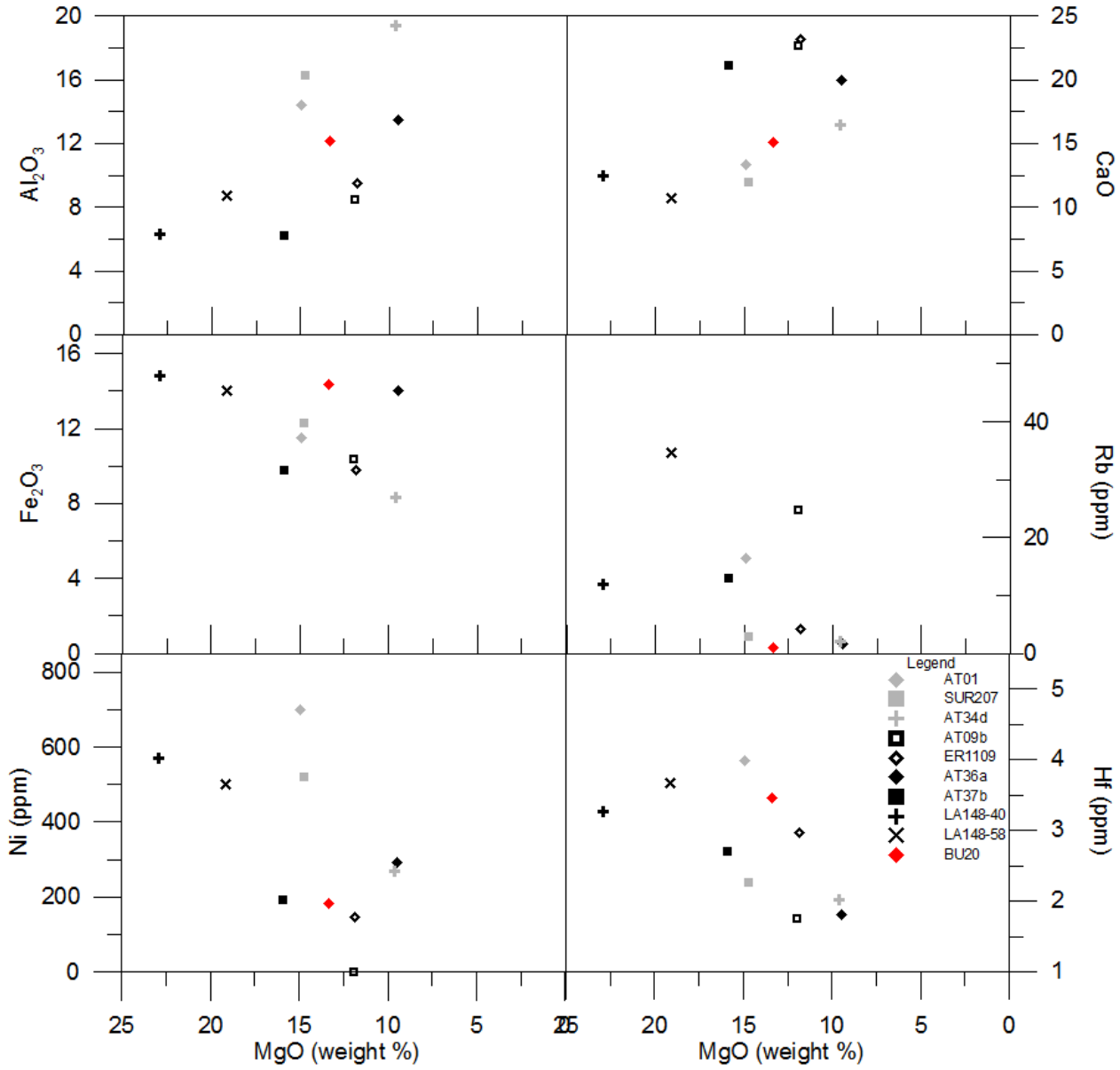

Figure 4.14. Relevant major and trace elements for the samples selected for isotope dilution. Data for Moi-Moi metagabbro (black symbols) and Charlie gabbro (gray symbols) taken from Thijssen (2015).

(meta)gabbroic samples are shown in Thijssen (2015), sample location for the anorthosite sample is already shown in figure 4.4. This section briefly characterises the different samples, for a detailed description of the samples see Thijssen (2015). Some relevant major and trace elements are plotted in figure 4.14, a REE and multi element variation diagram is plotted in figure 4.15.

Charlie gabbro

Sur207 is an olivine gabbronorite taken at the occurrence at the Misty Mountain creek. AT01 is an olivine gabbronorite taken at the Kabalebo river. AT34d is a gabbronorite taken from the Moi-Moi creek.
Geochemically, sample Sur207, AT01 and AT34d reflect the more mafic samples of the suite, with high MgO contents (14.7%, 14.9% and 9.6% respectively) and low SiO_2 contents (46.6%, 47.7% and 49.5% respectively). The samples are relatively rich in iron and manganese and relatively poor in potassium and aluminium. Sample AT01 is slightly different, as it has relatively high titanium and potassium contents.
The samples Sur207 and AT34d are relatively enriched in compatible elements (e.g. nickel and chromium) and relatively depleted in LILE (e.g. rubidium and barium) while AT01 shows the opposite. HFSE are relatively low for all samples. In trace and rare earth element patterns, two samples plot as the most

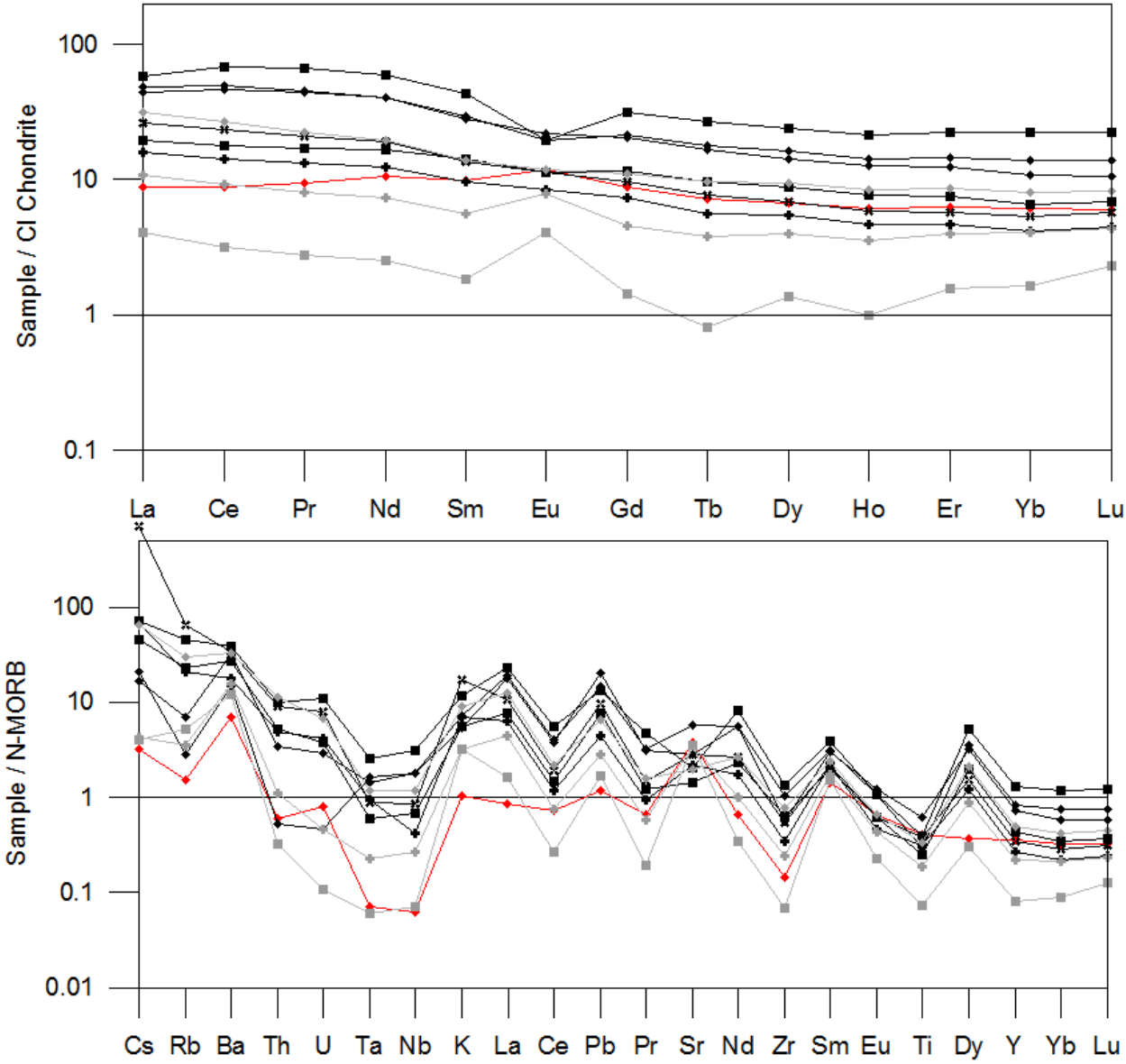

Figure 4.15. Above: REE diagram with samples normalised over CI chondrite (McDonough and Sun, 1995). Lutetium is included for interpretation of radiogenic isotopes in section 4.3. Below: A multi element variation diagram with values normalised over N-MORB (Sun and McDonough, 1989). Symbols as in figure 4.14. Data for Moi-Moi metagabbro and Charlie gabbro taken from Thijssen (2015).

enriched (AT01) and the most depleted (SUR207), while AT34d plots somewhere near the median of the patterns. AT01 does not display a positive europium anomaly, which is increasingly well developed in AT34d and Sur207. All samples show a subduction signature in anomalies of Nb, Ta and Pb and positive barium, strontium and samarium anomalies. The high titanium, potassium and the trace and rare earth elements enrichment of AT01 is interpreted by Thijssen (2015) as the result of contamination with felsic rocks (perhaps the Kabalebo charnockites), due to the close proximity of the sample to the north-western Bakhuis boundary fault.

Moi-Moi metagabbro
AT09b and ER1109 are taken at the occurrence at the Moi-Moi falls. AT36a and AT37b are taken at the occurrence west of the Zandkreek. LA148-40 and LA148-58 are taken at a depth of 40 m and 58 m of a drill core taken north-west of the Kabalebo river (see Thijssen, 2015 for sample locations).
The samples were selected to represent both primary crystallisation and cumulates. The two Moi-Moi samples and AT36a of Zandkreek have MgO contents ranging between 9-12%. AT37b of Zandkreek has an MgO content of 15.9% and the drill core samples the MgO contents were as high as 19.1 and 22.9%. For the drill core samples and AT36a of Zandkreek, silica contents are relatively low (~45.5%). The Moi-Moi samples and AT37b of Zandkreek contain relatively high silica contents (51.7 – 52.5%). The chosen samples are relatively poor in aluminium, titanium, potassium and manganese and rich in calcium. Iron contents vary strongly between the samples.
The drill core samples are relatively enriched in compatible elements such as nickel and chromium, while the samples of Zandkreek and Moi-Moi falls show a large variation. The selected samples are relatively poor in strontium but show strong variation other in LILE like rubidium and barium. HFSE contents are commonly low. In rare earth element patterns, the selected samples show a general slope from HREE to LREE and no significant europium anomaly. Multi element variation diagrams show negative niobium and tantalum anomalies and HFSE depletion and positive lead anomaly and LILE enrichment, consistent with a subduction origin. All of the selected samples show a positive samarium and dysprosium anomaly and a negative titanium anomaly.

Anorthosite
Sample BU20 was selected from the Mozeskreek anorthosite as it represents one of the more mafic samples and shows the least evidence for plagioclase accumulation. Both MgO (13.3%) and SiO_2 (49.4%) contents are the highest of the suite, while sodium (1.0%), aluminium (12.1%) and calcium (9.6%) contents are on the low side of the suite. Potassium contents (0.062%) are low, as are they for the whole suite.
The compatible elements for BU20 (fig. 4.9) are on the more enriched side of the suite, overlapping with the centre of the distribution for the other gabbroic bodies. Nickel for BU20 forms the only exception, significantly lower than the Charlie gabbro. LILE like rubidium and barium are consistently very low (fig. 4.10), strontium is on the low end of the suite as the sample contains the least plagioclase. HFSE contents are also very low (fig. 4.11).
In rare earth elements (fig. 4.12a), BU20 is the only sample that shows a weak positive slope in HREE (La/Sm = 0.89) and the sample that shows the smallest europium anomaly (Eu/Eu* = 1.2). In multi element variation diagram (fig. 4.12b), BU20 shows the deepest negative niobium and tantalum anomaly and the least positive strontium anomaly.

4.3.2 Results

4.3.2.1 Strontium, neodymium and hafnium isotopic variation
The variation in initial values for all isotopes of the Charlie gabbro, Moi-Moi metagabbro and Mozeskreek Anorthosite are plotted in figure 4.16a and b. All initial values are calculated to an average intrusion age of 1980 Ma. This is consistent with the 1980 ± 5 Ma zircon Pb-Pb evaporation age found for the Mozeskreek anorthosite (de Roever et al., 2003b) and is within error of the 1984 ± 4 and 1984 ± 5 Ma U-Pb zircon ages for the Moi-Moi metagabbro and the 1970 ± 17 U-Pb baddeleyite age for the Charlie gabbro (Thijssen, 2015).

Strontium variation
Initial $^{87}Sr/^{86}Sr_{1980}$ ratios for all types of mafic plutonic bodies plot around the 0.702272 value for the bulk silicate earth at 1980 Ma (DePaolo and Wasserburg, 1976), but also range down close to the value of 0.70085 for the depleted mantle at 1980 Ma. The Moi-Moi metagabbro shows the largest range in ratios (0.701158 – 0.702620). The Charlie gabbro (0.702203 – 0.702536) shows a smaller range fully

overlapping with the Moi-Moi metagabbro range. The Mozeskreek anorthosite sample (0.702941) plots just above the range in the gabbroic bodies.

Neodymium variation

Initial εNd_{1980} values for all mafic plutonic bodies plot above the value for CHUR yet significantly below the 3.5 value for the depleted mantle at 1980 Ma (DePaolo, 1981), ranging between εNd_{1980} = 0.3 – 1.3. The initial values for the Charlie gabbro are slightly higher, ranging between εNd_{1980} = 0.9 – 1.3, while the Moi-Moi metagabbro ranges between εNd_{1980} = 0.3 – 0.8. The Mozeskreek Anorthosite forms the lower end of the range at 0.3.

Hafnium variation

Initial εHf_{1980} values for all mafic plutonic bodies show a significant range, plotting above CHUR, towards the value of 9.6 for the depleted mantle at 1980 Ma (Vervoort et al., 2000). The full range of εHf_{1980} = 2.2 – 7.9 is expressed in the Moi-Moi metagabbro, while the Charlie gabbro shows a small overlapping range of εHf_{1980} = 4.7 – 5.7. BU20 of the Mozeskreek anorthosite shows an initial value of εHf_{1980} = 5.1.

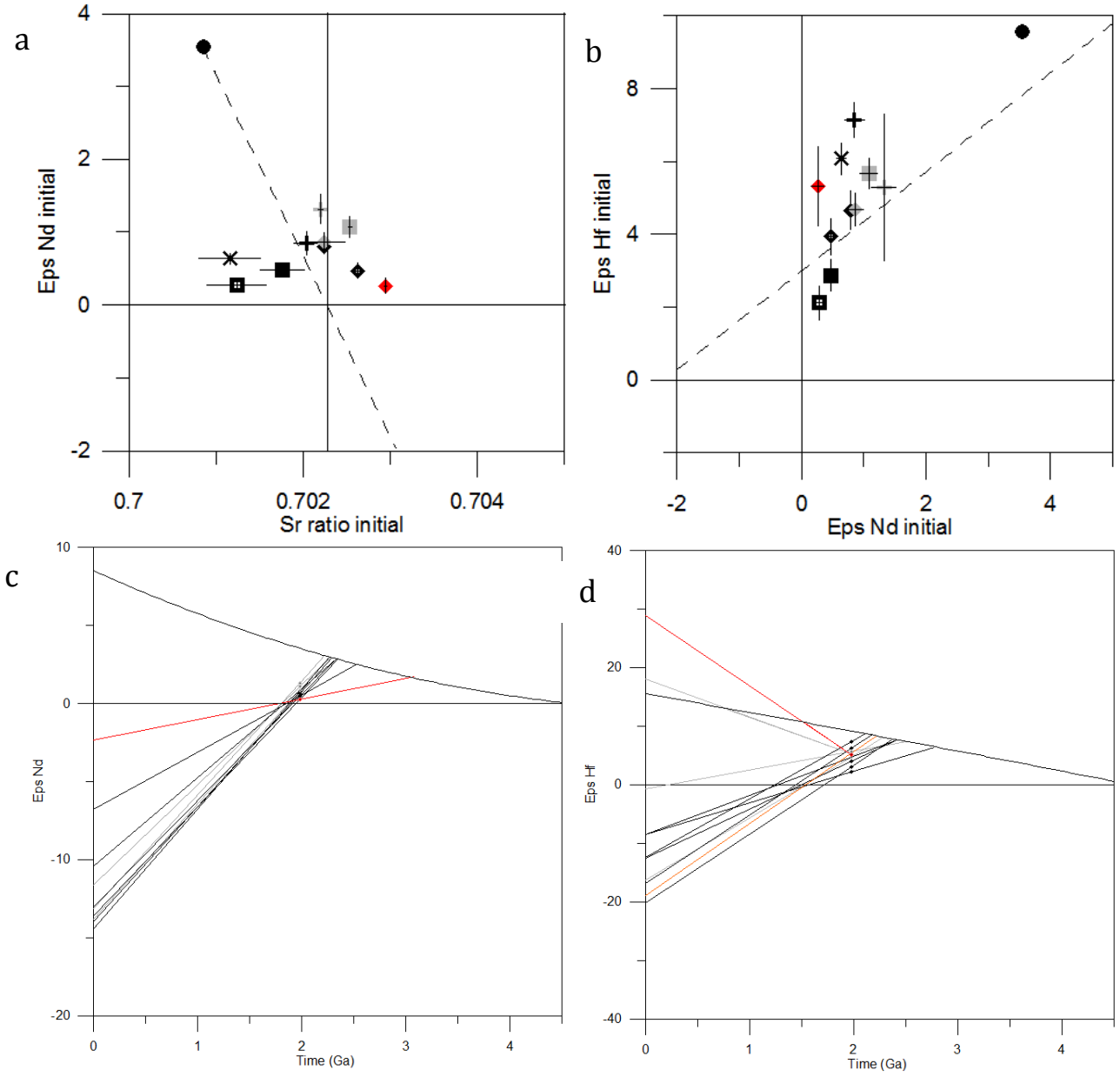

Figure 4.16. Radiogenic isotope variation for the Charlie gabbro, the Moi-Moi metagabbro and the Mozeskreek anorthosite. Symbols as in fig. 4.14. A) Initial εNd_{1980} vs initial $^{87}Sr/^{86}Sr_{1980}$ ratios. Black dot indicates composition for depleted mantle at 1980 Ma. B) Initial εHf_{1980} vs initial εNd_{1980}. Black dot indicates composition for depleted mantle at 1980 Ma. C) Neodymium evolution diagram. D) hafnium evolution diagram.

Comparing plots of initial values

Plotting the neodymium vs. strontium ratios and the hafnium vs. neodymium ratios (fig. 4.16a and b) allows a comparison of the data with the depleted mantle and the mantle array (Vervoort and Blichert-Toft, 1999). The plots show that the ranges in isotopic compositions are generally wider in the initial hafnium and strontium data than in the initial neodymium data.

In the εNd_{1980} vs. $^{87}Sr/^{86}Sr_{1980}$ plot (fig. 4.16a), all data plot around the line between depleted mantle and the value for bulk silicate earth at 1980 Ma. Most of the samples form a cluster just above the line. While three of the Moi-Moi metagabbro samples plot below the line at lower initial strontium ratios. In the εHf_{1980} vs. εNd_{1980} plot (fig. 4.16b), the data plot along both sides of the mantle array of Vervoort et al. (1999). While the Charlie gabbro samples form more or less a cluster just above the line, the Moi-Moi metagabbro samples show an apparent steep trend that crosses the line. The Mozeskreek anorthosite plots above the mantle array.

4.3.2.2 Neodymium and hafnium evolution and model ages

Neodymium and hafnium depleted mantle model ages have been calculated. The model ages are solved for the depleted mantle evolution for neodymium of DePaolo (1981) and for hafnium of Vervoort et al. (2000). The evolution lines and model ages are plotted in figure 4.16c and d.

Neodymium evolution and model ages

The Charlie gabbro and Moi-Moi metagabbro show a similar negative evolution towards present day εNd_0 values between -10 and -15, AT37b shows a slightly less negative evolution towards a εNd_0 of 6.8, consistent with its more flat rare earth pattern as described by Thijssen (2015), which is most likely the result of fractionation processes. Mozeskreek anorthosite sample BU20 shows a very weak negative evolution towards a present day εNd_0 of -2.36, consistent with its flat REE pattern with a weakly positive slope in LREE (see section, 4.2.2.3)

Most neodymium T_{DM} ages for the Charlie gabbro and Moi-Moi metagabbro range between 2.22 and 2.34 Ga. The anomalous Sm/Nd ratios for AT37b and BU20 lead to erroneous model ages of 2.53 Ga and 3.07 Ga respectively. An actually older mantle extraction age for these samples is unlikely, given the similarity in geochemistry to the other samples. It is more likely that partial melting or fractionation processes elevated the Sm/Nd ratio before the ~1980 Ma crystallization age.

Hafnium evolution model ages

Hafnium evolution shows a stronger variation than neodymium. For the Moi-Moi metagabbro, evolution is variably negative towards present day values ranging between εHf0 = -8.4 to -20.2. The Charlie gabbro shows negative to positive evolutions towards present day values ranging from -16.3 to 18.0. The Mozeskreek anorthosite BU20 shows the strongest positive evolution towards a present day value of 29.0. The variation in evolutions is consistent with the ranges in compositions and variation in Lu/Hf ratios as documented in section 4.2.

The strong range in Lu/Hf ratios is also reflected in a considerable scatter in hafnium T_{DM} ages between 2.16 Ga and 2.85 Ga, where the bulk of the samples show 2.3 – 2.5 Ga ages. The ages are partially in agreement with the Neodymium T_{DM} model ages, but also range to an impossible age of 0.7 Ga for SUR207. The samples that show a positive evolution have an erroneous T_{DM} which is younger than their intrusion age. Similar to the neodymium model ages, the range in Hafnium model ages is interpreted to reflect disturbances in the parent-daughter Lu/Hf ratio rather than source heterogeneities.

4.3.2.3 Neodymium and hafnium isochrones

A Sm-Nd and Lu-Hf isochron was calculated using IsoPlot 4.15 for the samples of the Moi-Moi metagabbro (fig. 4.17a and b). As only three and one sample were analysed for the Charlie gabbro and the Mozeskreek anorthosite respectively, a reliable isochron age could not be calculated for these bodies. Alternatively, an isochron is calculated for all the mafic plutonic bodies (fig. 4.17c and d).

All isochrones are within error of the ~1980 Ma U-Pb zircon and baddeleyite ages for the bodies. The data for the Moi-Moi metagabbro show considerable variation in both the Sm-Nd and Lu-Hf isochrones. The Sm-Nd data results in an errorchron age of 1960 ± 190 Ma as the MSWD = 19. The Lu-Hf data results in an errorchron age of 1668 ± 900 Ma as the MSWD = 72. The data for all the mafic plutonic samples define a Sm-Nd errorchron of 1898 ± 120 Ma as the MSWD = 22. The Lu-Hf data results in an errorchron age of 1999 ± 160 Ma as the MSWD = 49.

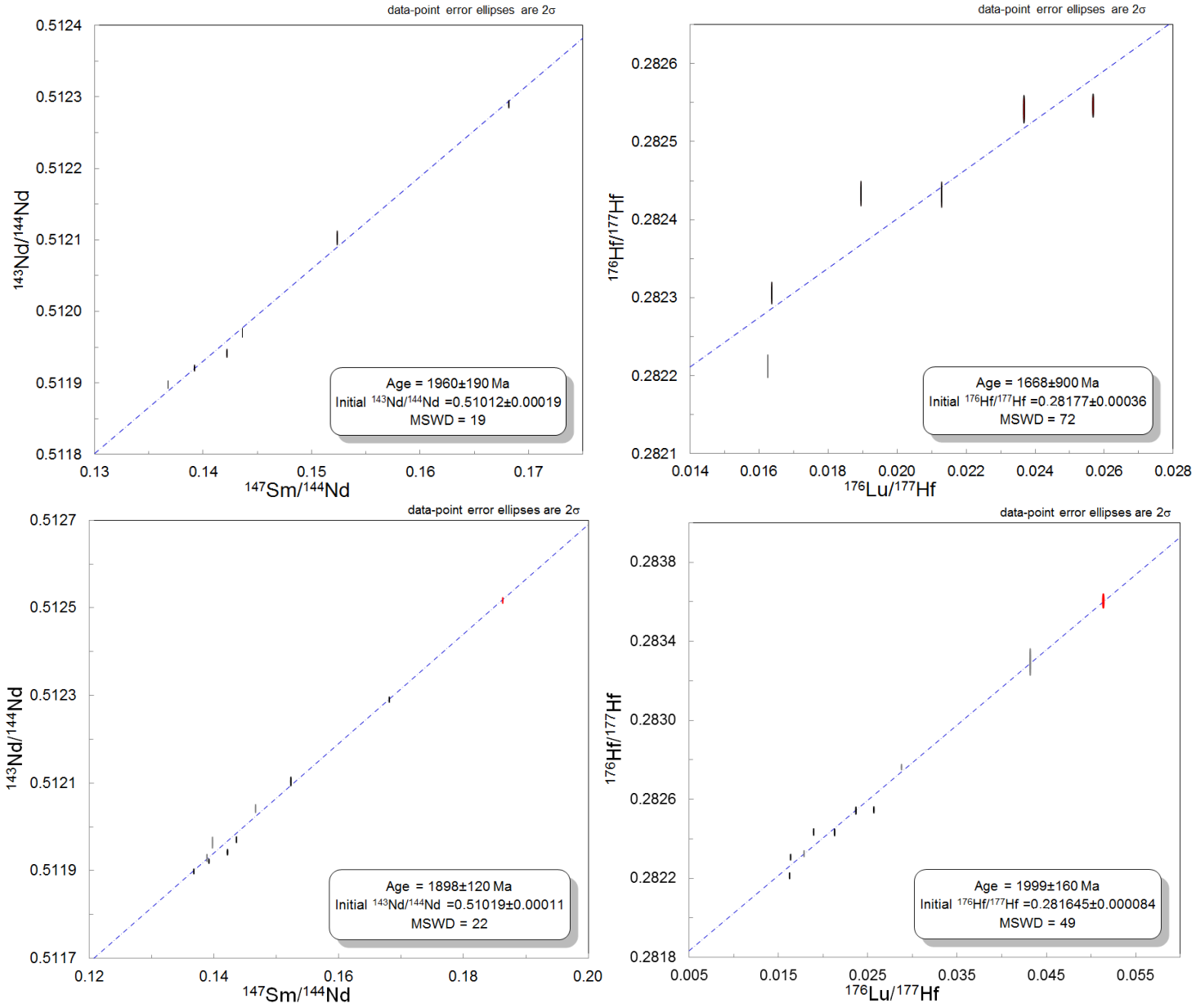

Figure 4.17. Sm/Nd and Lu/Hf isochron results for only the Moi-Moi metagabbro (above) and all mafic plutonic bodies (below), calculated with IsoPlot 4.15. Samples are plotted as error ellipses. Black ellipses are samples of the Moi-Moi metagabbro, gray ellipses are the samples of the Charlie gabbro and the red ellipse indicates the sample from the Mozeskreek anorthosite.

4.3.3 Interpretation and discussion

Initial ratios

While the initial strontium values plot around the value for bulk silicate earth for 1980 Ma, the positive initial neodymium and hafnium ratios indicate relatively depleted sources for all of the mafic plutonic bodies. The varyingly less pronounced depleted origin than a typical depleted mantle MORB melt is consistent with a subduction setting. While the hafnium and strontium initial ratios range to values close to the value for depleted mantle, the neodymium is significantly lower, which is common for arc related magmas (Hawkesworth et al., 1979).

When the data of the different bodies is compared, the differences seem subtle at first sight. The strontium and hafnium values of the Mozeskreek anorthosite and Charlie gabbro show full overlap with the values of the Moi-Moi metagabbro, while only the neodymium values are slightly lower and higher, respectively. However, the distributions are significantly different. While the Charlie gabbro shows a relatively small

cluster in figure 4.16b, the samples of the Moi-Moi metagabbro plot along a steeply positive trend between hafnium and neodymium.
The close association of the data indicates they are derived from similar depleted mantle sources, where the Charlie gabbro is derived from a source slightly more depleted in neodymium and the Moi-Moi metagabbro from a source slightly more depleted in hafnium. More importantly, the difference in distribution between the suites indicates they have experienced different partial melting, fractional crystallisation and/or magma mixing processes. While they show relatively comparable initial values, the difference in distribution is consequently interpreted to reflect the fact that the two suites represent two different magmatic generations.
For the Mozeskreek anorthosite, such a relationship is more difficult to establish given that only one sample was analysed and a possible trend cannot be discerned. The single analysed sample plots relatively close to the range in the Moi-Moi metagabbro samples, which could indicate it belongs to the same parental magma. However, given its slightly lower initial neodymium value, especially compared to the trend, it could also represent a different source.

Isochrons
Both the data for the Moi-Moi metagabbro and the data for all mafic plutonic bodies result in an errorchron age. The errorchron for the Moi-Moi metagabbro would indicate that the different samples do not belong to the same body. However, as discussed in the previous section, the range in initial values for both hafnium and neodymium is quite large which is interpreted to reflect partial melting, fractionation or magma mixing processes. The fact that the data results in an errorchron is interpreted as due to the same processes. The errorchron obtained for the data of all mafic plutonic bodies indicates they do not belong to the same magmatic event.

Neodymium and hafnium evolution and model ages
The bulk of the neodymium model ages show a cluster of values which are consistent with what is known for the Bakhuis belt (de Roever et al., 2003b; Klaver et al., 2015). Two samples (AT37b, BU20) show a more positive radiogenic evolution compared to the other mafic plutonic samples, which indicates they have elevated Sm/Nd ratios. For BU20, this is consistent with the REE diagram (section 4.2.2.3, figure 4.12), which shows a positive slope for the LREE and thus an elevated Sm/Nd ratio. The variation in REE slopes is interpreted to reflect various pyroxene (clinopyroxene lowers the LREE slope) and plagioclase (which raises the whole REE slope) processes. The deviating neodymium evolution and model age is interpreted as the effect of pyroxene accumulation. For AT37b; the REE slope is also slightly flatter than the rest of the Moi-Moi metagabbro samples (Thijssen, 2015). The sample is a pyroxene-hornblende melagabbronorite with 70% mafic minerals. So similarly to BU20, the deviating Sm/Nd evolution and model age are interpreted to reflect pyroxene accumulation processes

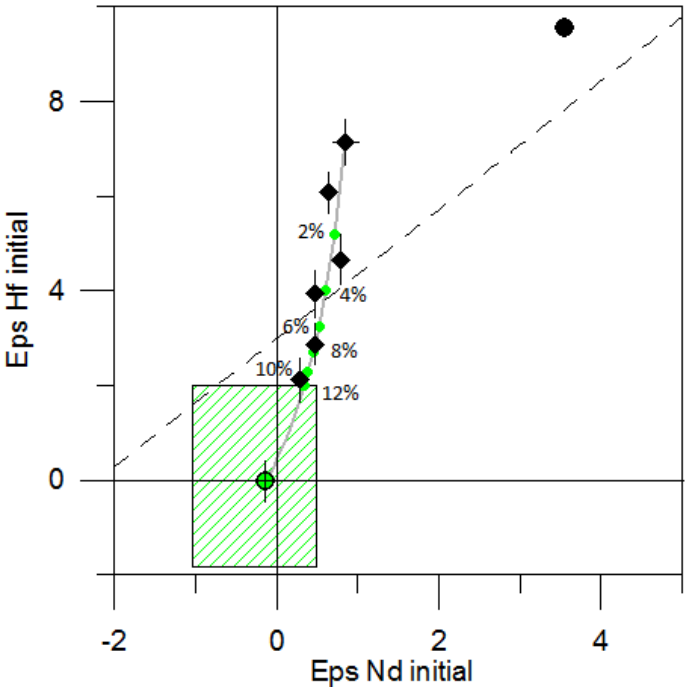

Figure 4.18. Initial hafnium vs neodymium values for different bodies, similar to 4.14b. The green striped box indicates the ranges in whole rock initial neodymium values and zircon initial hafnium values for the Kabalebo charnockites, taken from Klaver et al. (2015). The gray line drawn through the metagabbroic samples is this modelled mixing line. Mixing percentages of 2%, 4%, 6%, 8%, 10% and 12% are shown as green points on the line.

For the hafnium model ages, both the scatter in T_{DM} model ages and the positive evolution for some samples are interpreted to reflect accumulation processes. In order to raise the Lutetium hafnium ratio, hafnium must be relatively depleted or lutetium relatively enriched. Lutetium is the heaviest HREE and its enrichment is mostly related to general REE enrichment. Variation of HREE enrichment can be achieved through partial extraction or fractional

crystallization. The hafnium content is strongly dependent on accessory phases, especially zircon. Consequently, the presence or absence of zircon is an important contributor to the hafnium budget and can greatly enrich or deplete a rock in hafnium. As zircon is commonly a late magmatic phase, varying accumulation processes can enrich a residual magma in hafnium while cumulates will be depleted in hafnium. Since zircons are less abundant in gabbroic rocks compared to granitic rocks, this effect can be substantial. The hafnium isotope behavior in the data is thus interpreted to be an indicator of the presence or absence of zircon. This further illustrates the strong accumulation processes that have affected the mafic plutonic rocks of the Bakhuis Belt.

Magma mixing with Kabalebo charnockites

One of the goals of radiogenic isotope dilution for the gabbroic rocks was to investigate whether the mafic plutonic bodies show magma mixing with the Kabalebo charnockites. Their co-occurrence and mixing was suggested to explain the presence of zircon with a geochemistry consistent with the Kabalebo charnockites in sample ER1109 of the Moi-Moi metagabbro (Klaver et al., *in press*).

Normally, crustal contamination can be established by deviations of initial ratios from a typical depleted mantle signature. However, for subduction settings, initial ratios already vary from depleted mantle values due to the varying influence of a slab component. Similar, an attempt to use Th/Nd and La/Nb ratios resulted in scatted and failed to produce consistent variation. These ratios are normally used to infer a crustal component, but as this component can also be derived from the subducting slab, the scatter cannot be interpreted as reflecting mixing with the Kabalebo charnockite

However, information about mixing can be derived when the data is compared to the initial neodymium and hafnium values reported for the Kabalebo charnockites (fig. 4.16). Especially isotope dilution data is capable of recording subtle differences between initial values. Whole rock neodymium values were taken from (Klaver et al., 2015) which did not report whole rock hafnium values. Instead, the range in initial hafnium values for zircon from the Kabalebo charnockites was used, for which the trace element variation was shown to be explained by simple zircon and apatite fractionation (Klaver et al., 2015), indicating equilibrium between zircon hafnium isotopes and the charnockite magma. The range in values is plotted as a green striped box and the average value for neodymium and hafnium is plotted as a green circle in fig. 4.18.

The apparent trend shown in the Moi-Moi metagabbro intersects with the field of the Kabalebo charnockite, indicating the apparent trend can be explained by magma mixing. This is consistent with the interpretation of (Klaver et al., 2015) that the intrusion of the Moi-Moi metagabbro provided the heat source for melting of the granulites to form the Kabalebo charnockites. To obtain an estimate of the mixing factors, a two component mixing curve was calculated following (DePaolo and Wasserburg, 1979). The curve is calculated using the average values for the Kabalebo charnockites and sample LA148-40 (having the highest initial hafnium and neodymium values) for the Moi-Moi metagabbro as end member components. The mixing curve is plotted as a black line in fig. 4.16. The model results in estimated mixing factors between 3% for sample AT36a of the Zandkreek occurrence and 11-12% for sample AT09b of the occurrences at Moi-Moi falls.

Note that the mixing factors only provide an approximation as they are calculated under two assumptions. The average value for the Kabalebo charnockites was assumed to be the end-member component for the Kabalebo charnockites, while in reality it most likely is an average from samples that have already been affected by various degrees of mixing with the Moi-Moi metagabbro. This leads to an underestimation of the mixing factors. While the end member component of the Moi-Moi metagabbro (LA148-40) is sampled relatively far from larger charnockite occurrences and reflects the least mixed sample, it is also possible that magma mixing occurred in the parental magma during melting of the lower crust before magma ascent. This would also lead to an underestimation of the mixing factors. As both factors would lead to an underestimation, the 11-12% factor is considered as a minimum constraint on the magma mixing factors.

When the initial neodymium and hafnium values for the samples of the Moi-Moi metagabbro would be corrected for mixing with the Kabalebo charnockite, they would plot in a cluster around sample LA148-40 of approximately $\varepsilon Nd_{1980} \sim 1$ and $\varepsilon Hf_{1980} \sim 8$. Consequently, they would become significantly different from the Charlie gabbro hafnium and neodymium data clustering around εNd_{1980} of ~ 1.2 and lower εHf_{1980} of ~ 5. Also, the magma mixing visible in the Moi-Moi metagabbro is not expressed in the Charlie gabbro. These inferences further indicate that the two suites are derived from a different magma source and have experienced a different magmatic evolution. Similarly, the Mozeskreek anorthosite sample plots below a hypothetical corrected range for the Moi-Moi metagabbro samples. However, the errors on the hafnium values are relatively big and the sample could fall within error of the range in Moi-Moi metagabbro samples. Given that only one sample is analysed, the data provides no conclusive evidence for either a similar or deviating origin for the Mozeskreek anorthosite.

5 Mafic dykes and small intrusive bodies

5.1 Field observations and sample petrography

5.1.1 Metadolerite dykes and intrusives in the Blanche Marie granulite

The different rock types occurring in the Blanche Marie section have been described in detail by Klaver (2011) and Nanne (2013). The Blanche Marie section exposes 1) UHT-metamorphic and migmatitic granulites, locally intercalated with pelitic gneisses, which are cut by lightly folded and boudinaged mafic amphibolitic dykes of up to ~1m thick, 2) an at least ~100m thick syn-metamorphic foliated gabbroic body starting at the base of the Blanche Marie falls. This section shortly describes the UHT granulites (5.1.1) and focuses on the dykes in the granulites (5.1.2) and the syn-metamorphic gabbroic body (5.1.3). All sample locations are given in figure 5.1

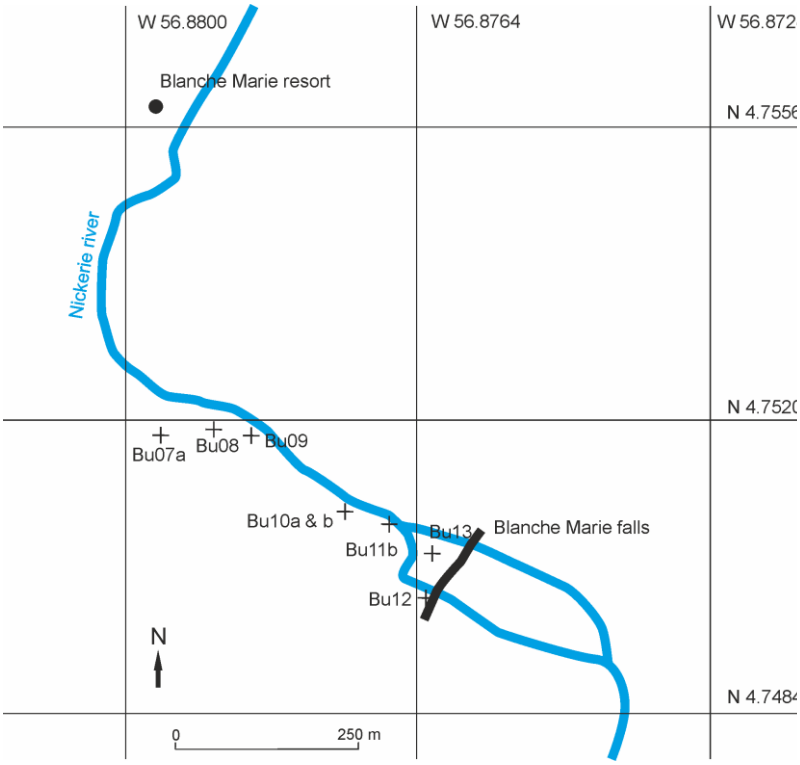

Figure 5.1. Sample locations along the Nickerie river near the Blanche Marie falls. Grid coordinates are in decimal degrees. Blanche Marie resort and the falls are indicated in the map.

5.1.1.1 UHT granulites

The UHT granulites at the Blanche Marie falls are foliated intermediate and mafic granulites. At one location calc-

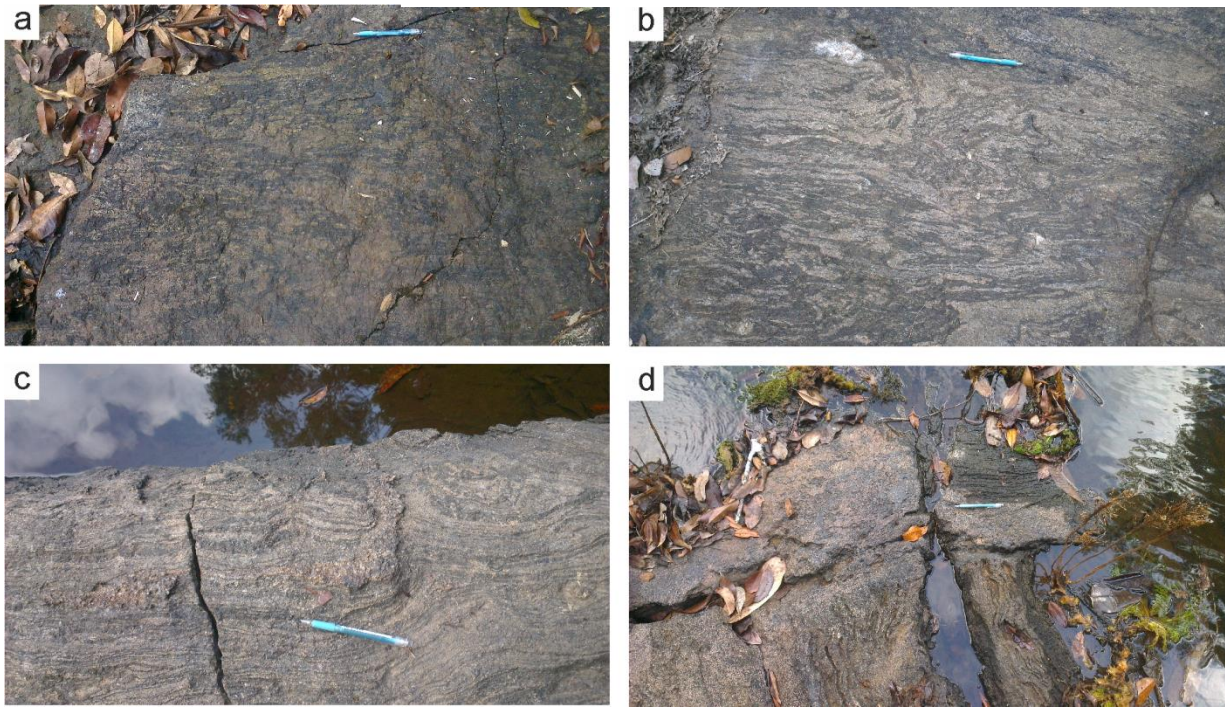

Figure 5.2 Field photographs of the UHT granulites at Blanche Marie falls. A) Mafic calc-silicate granulite with a melanosome rich in green pyroxene and a light leucosome. B) Strongly migmatised and folded metapelitic gneiss with a leucosome of quartz and feldspar and a melanosome of sillimanite, garnet, biotite and locally corundum. C) Typical foliation in the pelitic granulites with a small pegmatite vein starting at the tip of the pencil. D) blocks with perpendicular foliation separated by a 10 cm pegmatite vein parallel to the pencil for scale.

silicate granulites (fig. 5.2a) and metapelitic gneisses occur (fig. 5.2b), the latter with a typical assemblage of Sil + Grt + Qz + Fsp + Bt. The abundance of Al bearing phases indicates that the gneisses are indeed pelitic. The series has developed a thinly spaced foliation (fig. 5.2c) which is often isoclinally folded. The metapelitic gneisses are migmatised, where sillimanite, garnet and biotite form the melanosome and quartz and feldspar the leucosome (fig. 5.2c). Leucosomes form connected pegmatite veins, which are locally developed to the degree that they have disrupted the foliation (fig. 5.2d).

5.1.1.2 Metadolerite dykes in granulites

The UHT granulites are cut by a series of narrow amphibolite facies metadolerite dykes. The dykes are easily distinguished in the field as fine grained, black and smoothly weathered structures in outcrop. They are discordant with varying thicknesses between a couple of centimetres to 1 meter and have not developed the metamorphic foliation. Some of the dykes have developed an internal foliation and are weakly folded or show boudinage, indicating they have experienced some deformation. However, they are never concordant to the metamorphic foliation, indicating they are at best late syn-kinematic and have not experienced the peak of UHT metamorphism and associated deformation. Samples BU07a, BU08, BU09, BU10a & b, and BU11b were taken from the dykes at Blanche Marie. The series was completed with samples ER1228 and ER1232, which were taken from metadolerite dykes cutting through the granulites at the Mozeskreek.

BU07a is taken from an odd, ball shaped ~10 cm mafic inclusion in the metapelites (fig. 6.2d), which most likely represents a fragment of a boudinaged dyke. The sample is a medium-grained granular metadolerite consisting of dominantly anhedral olive-green hornblende with minor anhedral plagioclase. Orthopyroxene and clinopyroxene are rare and form fine grained round granular aggregates in the hornblende and plagioclase matrix. The sample has no discernible foliation.

BU08 is taken from a thin (2-3 cm) weakly foliated dyke. The dyke is visible in figure 3c of (de Roever et al., 2003b) where it cuts through folds in the granulites. In its continuation in the outcrop, the dyke is also fractured and duplicates (fig. 5.2a). The dyke is a fine-grained equigranular metadolerite consisting of mostly hornblende and plagioclase, with minor clino- and orthopyroxene. The foliation is expressed by a preferred orientation of granular hornblende crystals, showing a common olive-green to

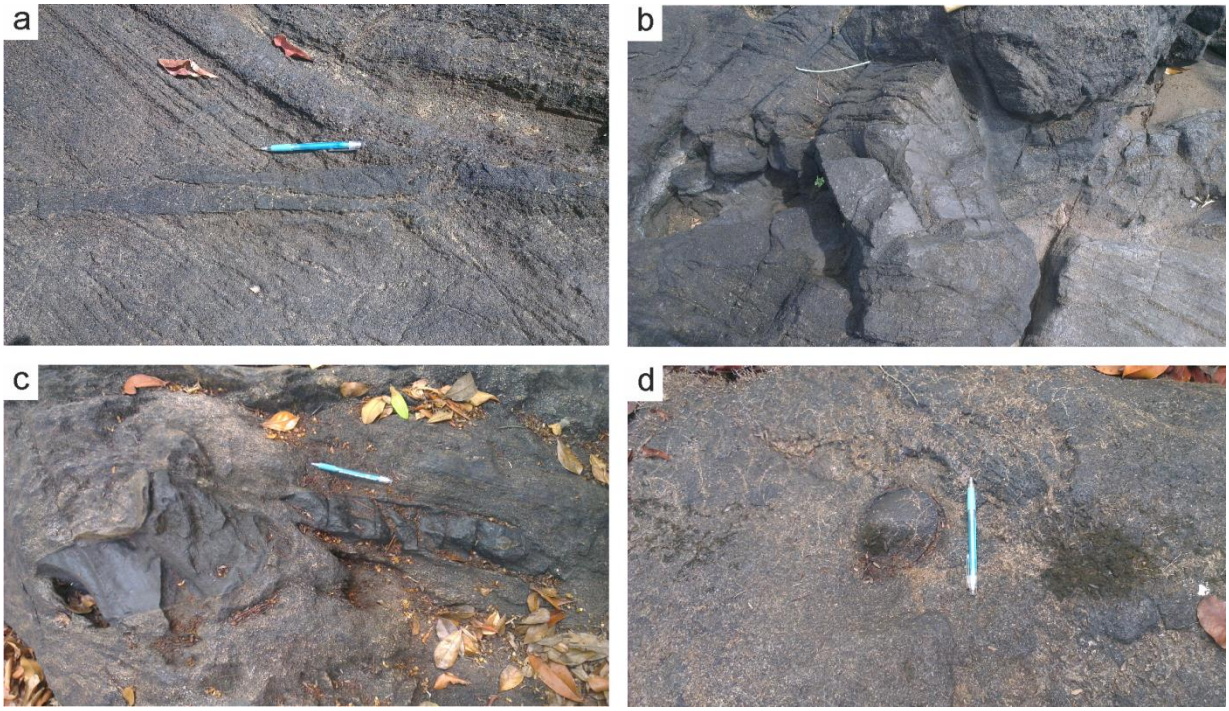

Figure 5.3 Field photographs of the mafic dykes UHT granulites at Blanche Marie falls. A) Thin (2-3 cm wide) foliated dyke discordant to the granulite foliation. The dyke shows overthrusting in a small fault below the pencil for scale. Sample location for BU08. B) ~20 cm wide straight dyke of BU09. Photograph shows typical smooth black weathering which separates the dykes from the foliated granulites in outcrop. C) Boudinaged and folded dyke of sample BU11b, showing thickness variation between different boudins. D) Mafic metadolerite lump (sample BU07a) within UHT metapelites. most likely representing a fragment of a boudinaged dyke.

pale yellow pleochroism. The thin section contains a zone with a single large orthopyroxene and an aggregate of plagioclase, possibly xenocrysts.

BU09 is taken from a 20 cm thick straight amphibolitic metadolerite dyke (fig. 5.3b). The sample is a fine-grained metadolerite consisting of mostly anhedral hornblende and minor anhedral plagioclase. Orthopyroxene crystals occur as fine-grained round granular aggregates in a coarser granular matrix of hornblende and plagioclase. The sample has no discernible foliation.

BU10a is taken from a ~70 cm thick medium-grained dyke, striking roughly N080E. The thin section contains dominantly medium-grained granular olive-green hornblende with minor plagioclase. The section shows zones of coarser and finer hornblende crystals. Fine grained aggregates contain relic pyroxenes. Biotite forms at the expense of hornblende along the grain boundaries. The sample has no discernible foliation.

BU10b is a thin foliated metadolerite dyke of up to 20 cm thick striking N020E, close to the BU10a dyke. The age relationship between BU10a and BU10b is not visible in outcrop. The dyke is a fine to medium grained amphibolite, containing hornblende and plagioclase and no pyroxenes. Hornblende defines a foliation with common olive-green to yellow pleochroism. However, granular aggregates of larger hornblende crystals do not show the foliation. Biotite forms at the expense of hornblende along the grain boundaries. A ~1 mm wide vein of quartz, feldspar and minor calcite cuts through the amphibolite parallel to the foliation.

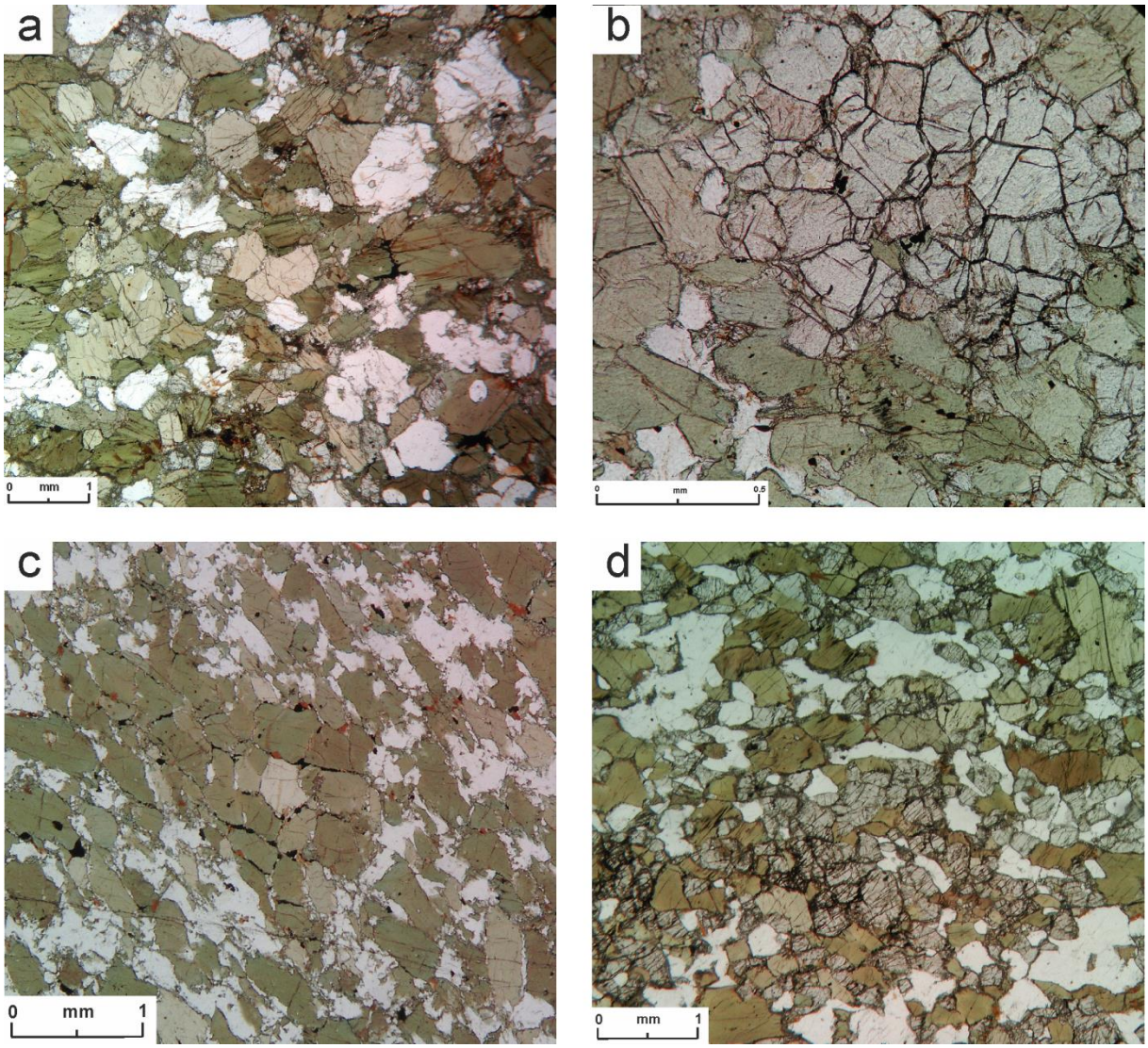

Figure 5.4 Thin section photographs of the mafic dykes at the Blanche Marie falls. A) Typical amphibolitic texture of a metadolerite, sample BU07a. B) Orthoyroxene aggregates in an amphibolitic metadolerite, sample BU09. C) Hornblende aggregates in an otherwise foliated amphibolitic metadolerite, sample BU10b. D) Texture for ER1228 with granular pyroxene, hornblende and plagioclase.

BU11b is an up to 20 cm thick boudinaged dyke (fig. 5.3c). The thin section shows a similar texture to BU10b, with hornblende and plagioclase forming a pronounced foliation which is not expressed in aggregates of larger hornblende crystals. Biotite formation out of hornblende is better developed than in BU10b, forming small poikilitic crystals enclosing plagioclase and relic hornblende.

ER1228 is taken from a series of three parallel, 30 cm thick dykes which have intruded into the axial plane foliation of folds in the UHT granulites at the Mozeskreek. The sample is different from the Blanche Marie samples, displaying a granular texture

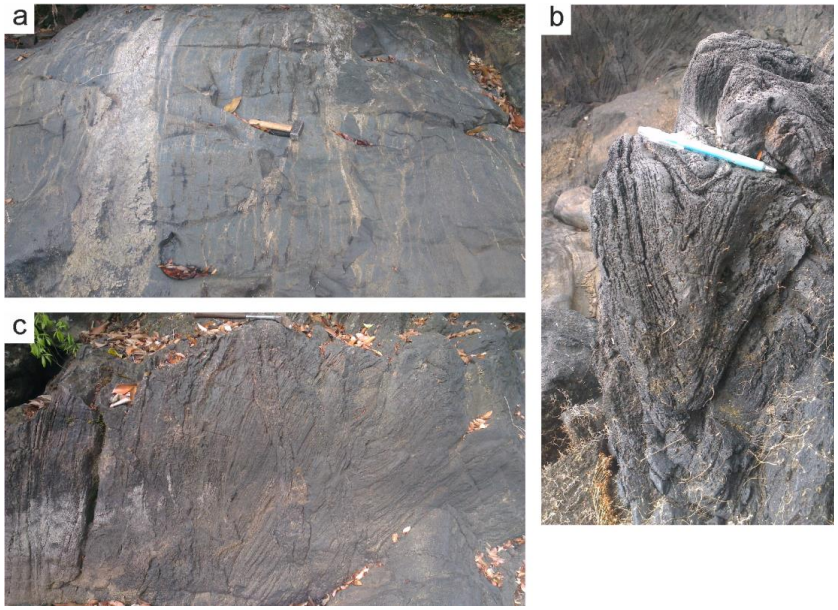

Figure 5.5 Field photographs of the metagabbroic body at Blanche Marie falls. a) Up to 50 cm thick pegmatitic veins cutting through the metagabbro. b) isoclinal folding in the foliated gabbro, indicating the gabbro is at least synkinematic. c) pegmatite veins cutting through the gabbroic granulite

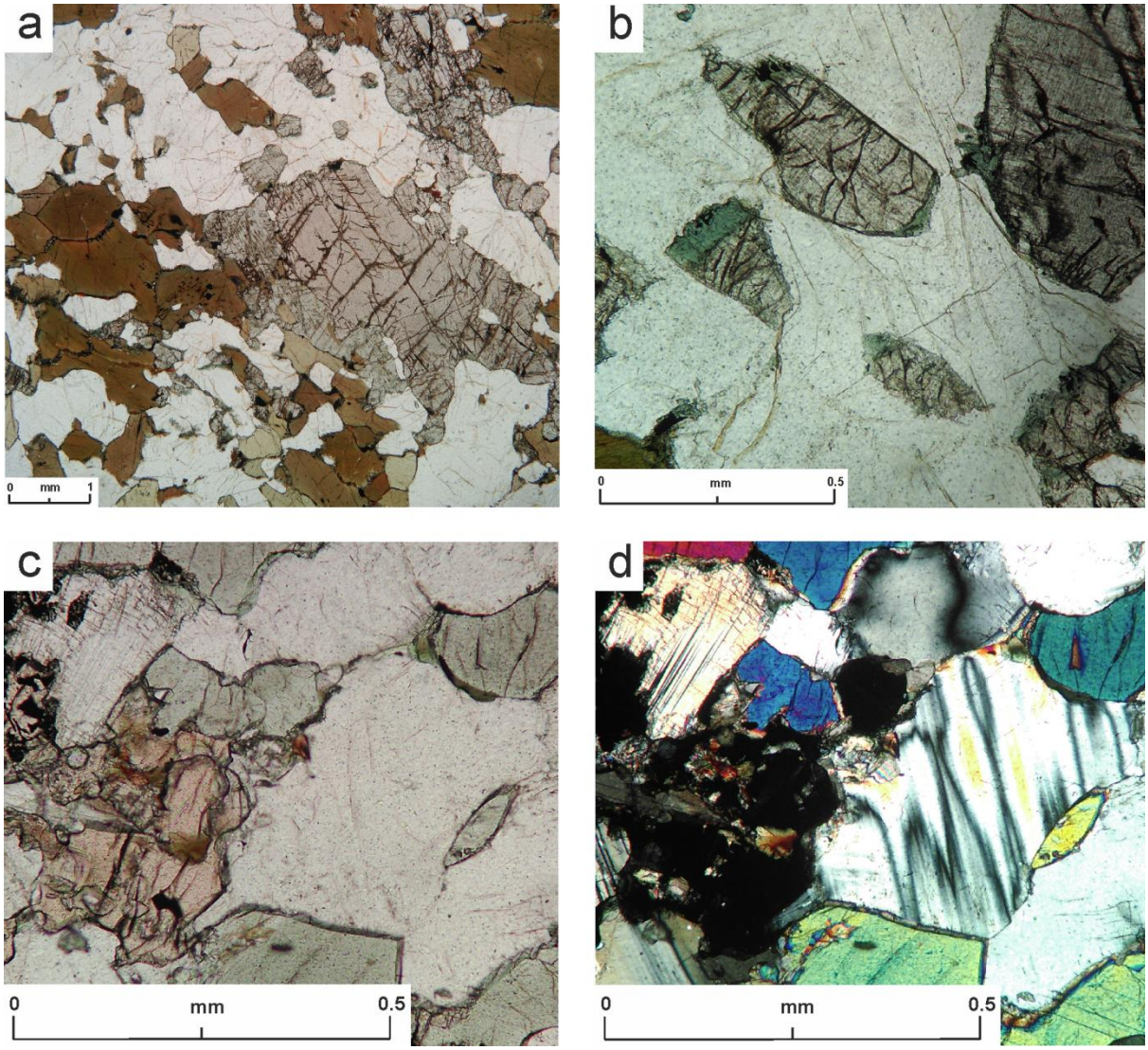

Figure 5.6 Thin section photographs of the gabbroic granulity body at the Blanche Marie falls. A) Texture of the coarse metagabbroic sample BU13. Faint pink crystal is OPX, lime-green is CPX and brown is hornblende. B) Corona of blue-green hornblende forming around pyroxenes, sample BU13. C) Garnet forming out of hornblende, in BU12, PPL. D) Same image in XPL.

of hornblende, plagioclase and abundant clino- and orthopyroxene. Hornblende is relatively yellow to brown and pyroxenes do not form aggregates but are comparatively large and stable. Biotite formation out of hornblende is rare. The sample shows no discernible foliation.

ER1232 is taken from a straight ~50 cm thick dyke in the granulites at the Mozeskreek, showing no discernible foliation. The sample is a fine-grained amphibolitic metadolerite consisting of mostly equigranular hornblende and plagioclase, with locally relict pyroxene in groundmass. Slightly larger pyroxenes show reaction textures to hornblende. Lath shaped aggregates of plagioclase (sub)grains indicate the former magmatic texture.

5.1.1.3 Gabbroic granulite

At the base of the Blanche Marie falls, a mafic granulite body is exposed that does not show any compositional banding which is so typical for the UHT mafic granulites. However, the body shows a clear assemblage of Opx + Cpx + Hbl indicating granulite facies metamorphism and is strongly foliated and folded, indicating it has experienced UHT metamorphism as the other granulites. The body is strongly migmatised and cut by small (mm-scale) and thicker (up to 50 cm) pegmatitic qz + fsp + bt + px veins (fig. 5.5a), with a dominant strike of N040E. Samples BU12 and BU13 were taken from the ~100 m thick metamorphic gabbroic body.

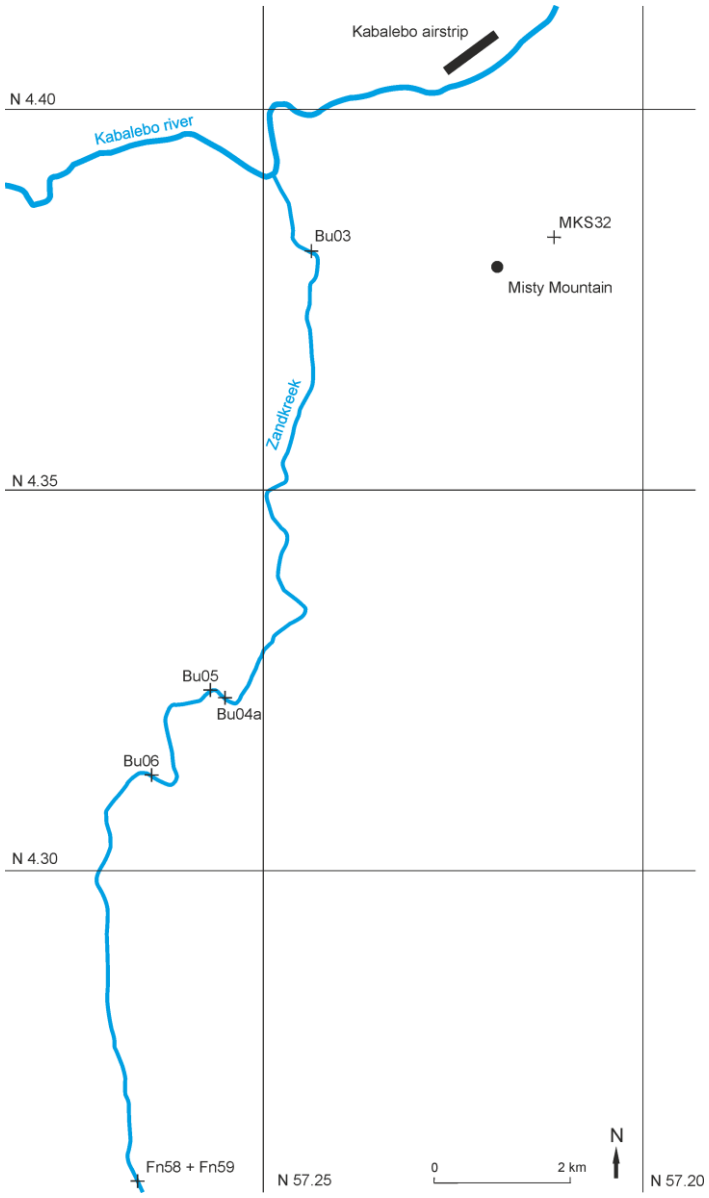

Figure 5.7. Sample locations along the Zandkreek river and near the Misty Mountain. Grid coordinates are in decimal degrees. The Kabalebo airstrip and Misty Mountain are indicated on the map.

BU12 is a relatively fine-grained equigranular, thinly foliated mafic granulite consisting of mostly granular pyroxenes and plagioclase. Locally, garnet replaces pyroxenes indicating retrograde reactions following granulite facies metamorphism. Retrograde amphibolite facies metamorphism is also shown replacement of pyroxenes by hornblende.

BU13 is a coarsely foliated mafic granulite. The thin section contains discontinuous bands of hornblende and plagioclase alternated with bands of orthopyroxene, clinopyroxene and plagioclase. Orthopyroxene is surrounded by a rim of hornblende along boundary contacts with feldspars, indicating retrograde metamorphism.

5.1.2 (Meta)dolerite dykes and xenoliths in plutonic bodies

5.1.2.1 (Meta)dolerite dykes and xenoliths in the Kabalebo charnockites

The occurrence and petrography of the charnockites has extensively been described by Klaver (2011). The charnockite exposures at the Zandkreek contain numerous small, short mafic dykes and enclaves of both metadolerites and foliated granulites, the latter are not incorporated in this study but were described by Klaver (2011). The small dykes are interpreted to be contemporaneous with charnockite

intrusion as they are slightly deformed and fractured by charnockite veins. The mafic enclaves range in size from a couple of cm to ~1 m but are most commonly ~10-20 cm rounded mafic xenoliths. Samples BU03 and BU05 were taken from the dykes in the Kabalebo charnockites. Samples BU04a and BU06 are mafic enclaves. The petrographic and geochemical studies were extended with samples FN58 and FN59, which are parts of metadolerite enclaves in a charnockitic to granitic body along the Zandkreek taken by Fienke Nanne (Nanne, 2013).

BU03 is taken from a ~20 cm thick porphyritic dolerite dyke, which shows slight folding and fracturing filled with charnockite veins. The sample has a homogeneous porphyritic texture with euhedral plagioclase laths in a fine grained matrix of pyroxene.

BU05 is taken from a ~30 cm thick dyke which shows apparent folding in the Kabalebo charnockites. The sample has a very fine-grained texture consisting of granular plagioclase and pyroxene with minor hornblende and biotite. No phenocrysts are visible, slight variation occurs in the relative abundances of minerals, where some areas are richer in plagioclase than others.

BU04a is taken from a ~20 cm foliated metadolerite enclave, which is one of a series that most likely represent a former dyke. The sample is a foliated amphibolitic metadolerite consisting of fine grained hornblende and plagioclase with minor biotite and clinopyroxene. Foliation is expressed in a preferred orientation of hornblende.

BU06 is taken from a series of ~15 cm amphibolitic xenoliths (fig. 5.8a) which most likely represent fragments of a boudinaged dyke. The sample is a metadolerite with rare plagioclase phenocrysts in a groundmass of slightly coarser anhedral granular plagioclase and hornblende and finer grained pyroxenes and biotite.

FN58 is taken from a ~60 cm mafic xenolith in a charnockitic to granitic body along the Zandkreek (Nanne, 2013). The sample is a plagioclase-rich metadolerite consisting of mostly granular plagioclase and orthopyroxene, with rare biotite.

FN59 is taken from a ~10 cm mafic xenolith in the same charnockitic to granitic body along the Zandkreek (Nanne, 2013). The sample is an amphibolitic metadolerite of connected small (up to 1 mm) hornblende poikiloblasts enclosing locally smaller plagioclase laths. The poikiloblasts are locally separated by fine grained granular aggregates of mostly orthopyroxene with minor plagioclase.

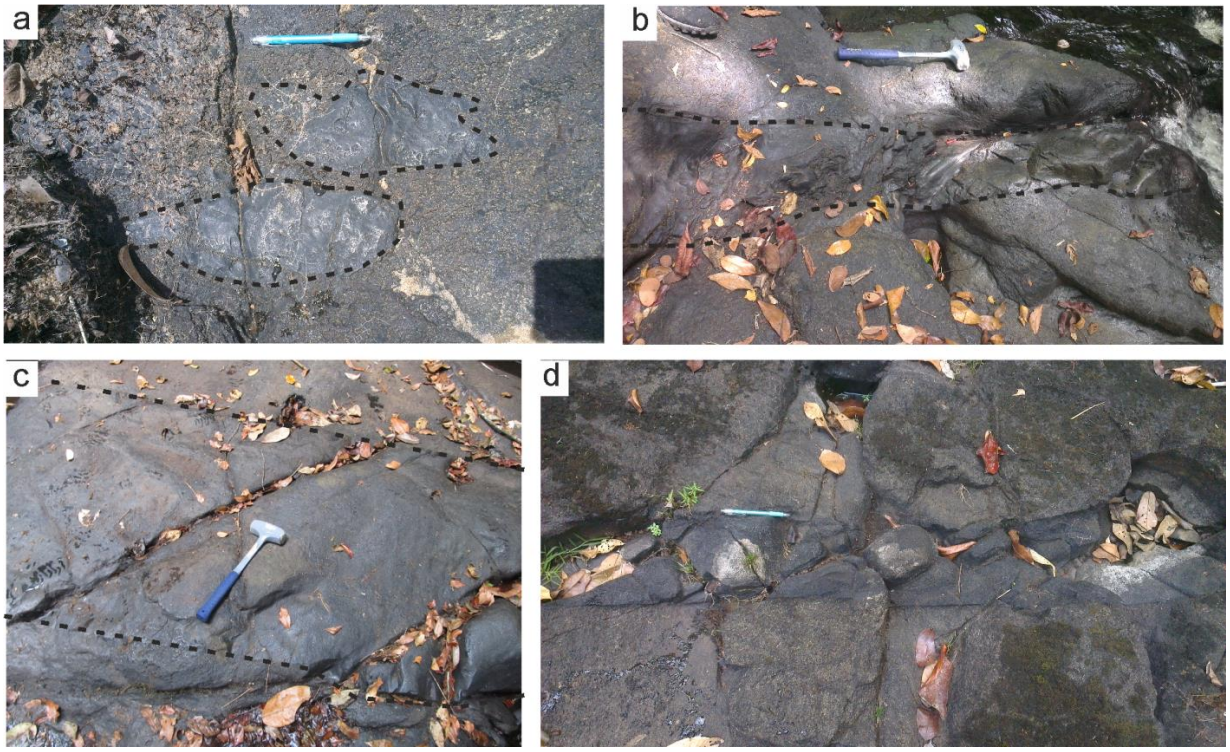

Figure 5.8 Field photographs of the mafic dykes in plutonic bodies of the Bakhuis belt. A) 2 semi rounded metadolerite xenoliths in the Kabalebo charnockites at Zandkreek. Sample location for BU04a. B) A ~20 cm thick dyke in the Misty Mountain kreek. Sample location for AT04a. C) ~1 m thick metadolerite dyke at the Misty Mountain kreek, sample location for AT06b. D) ~20 cm thick thick metadolerite dyke in the Mozeskreek Anorthosite. Sample location for BU18.

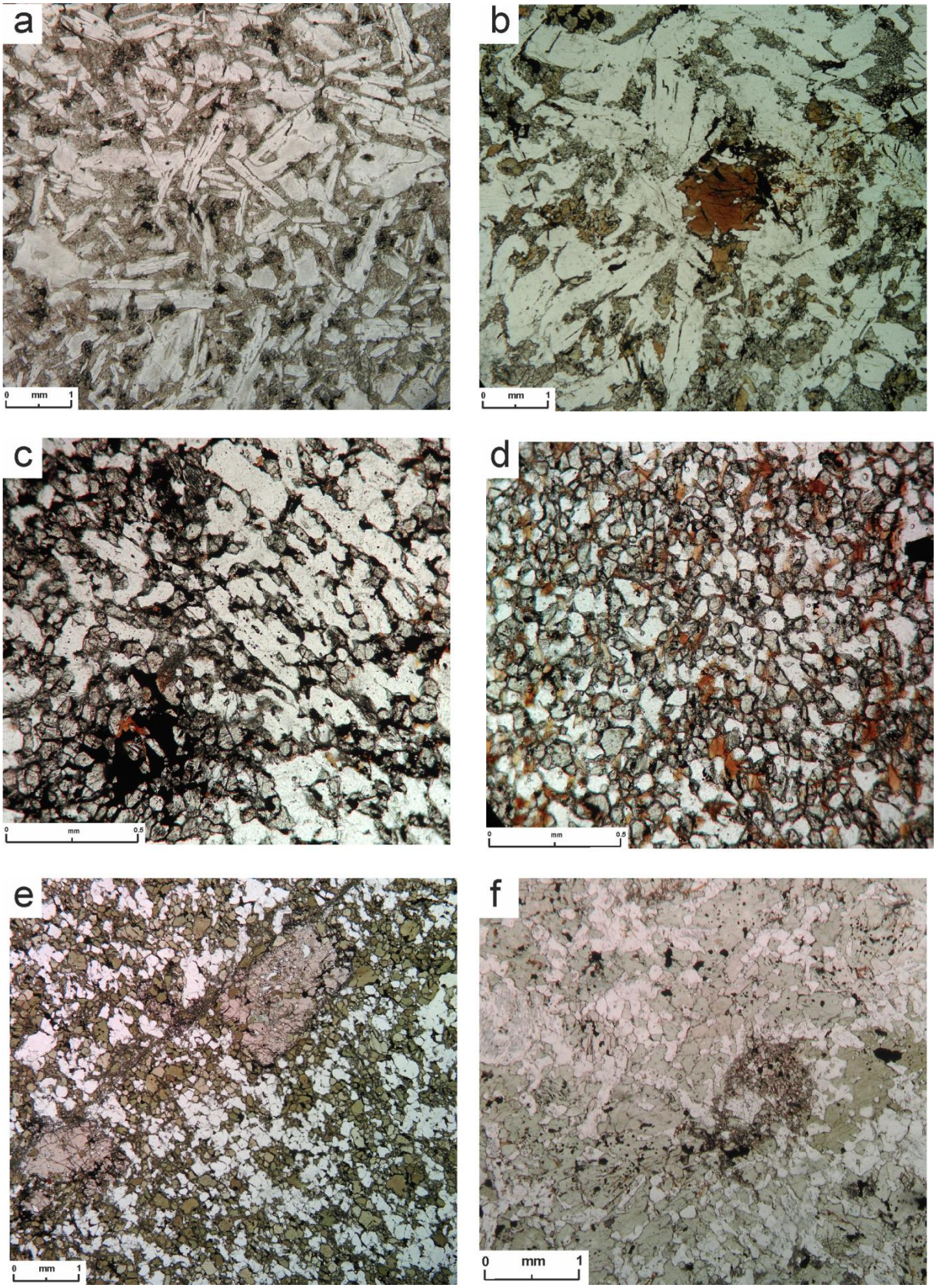

Figure 5.9 Thin section photographs of the (meta)dolerite dykes and enclaves in the plutonic bodies. A) porphyric texture with feldspar laths in a fine-grained pyroxene matrix, sample BU03. B) A similar porphyric texture with brown hornblende and a fine-grained recrystallized matrix, sample AT06b. C) Fine-grained dolerite dyke with slightly larger feldspar laths separated by smaller granular pyroxene. Granular pyroxene and opaque oxide aggregate in the lower left corner, sample AT04b. D) Fine grained dolerite of granular plagioclase, pyroxenes and biotite, sample BU05 E) Hornblende-rich amphibolitic metadolerite, with poikiloblastic garnet along a small brittle fault, sample AT16A. F) Amphibolitic metadolerite with poikiloblastic hornblende up to 1 mm and a fine-grained pyroxene aggregate in the center of the picture, sample FN59.

5.1.2.2 Dolerite dykes in the Charlie gabbro

The exposure of the Charlie gabbroic body at the Misty Mountain creek is cut by straight, continuous, up to 1 meter thick unmetamorphosed dolerite dykes. The dykes are easily distinguished in the field as fractured, fine grained, black and smoothly weathered structures in outcrop, compared to the coarse grained rounded appearance of the Charlie gabbro. All dykes have a (sub)vertical orientation.
Towards the east along the Misty Mountain creek, there is a boundary zone between the Charlie gabbro and the occurrence of Kabalebo charnockites of the Charlie falls. In the chaotic boundary zone, dolerite lenses are extensively cut by charnockitic dykes and veins, indicating the intrusion of the Kabalebo charnockites is younger than these dolerite dykes. Samples AT04b, AT05c, AT06b were taken from various dykes in the Charlie Gabbro. Samples AT15a, AT15b and AT16a were taken from the fragmented dolerite bodies and lenses that were cut by charnockite veins and dykes (Sample locations are shown in fig. 4.2 of Thijssen (2015).

AT04b is taken from a ~20 cm thick straight dolerite dyke in a loose block (fig. 4.4c of (Thijssen, 2015). Rare large phenocrystic plagioclase float in a matrix of subhedral plagioclase laths surrounded by fine grained clino- and orthopyroxenes. Fine-grained aggregates of granular orthopyroxene, plagioclase and biotite are present in the section.

AT05c is taken from a ~20 cm thick, N-S directed dolerite dyke. No thin section was taken for this sample.

AT06b is taken from a ~1 m thick straight dolerite dyke showing fine-grained chilled margins and a coarse-grained center. The sample is taken from the coarse center of the dyke. Abundant large mm-scale plagioclase phenocrysts and rare sub-mm anhedral brown hornblende phenocrysts float in a groundmass of fine-grained pyroxene and hornblende. Locally, biotite is present in the groundmass.

AT15a is a plagioclase-rich porphyritic dolerite taken from a small rapid in the Misty Mountain creek in the boundary zone near the Charlie Gabbro. The sample consists of phenocrystic mm-scale plagioclase in an equigranular groundmass of plagioclase, pyroxene and rare biotite. Locally, orthopyroxenes form slightly more coarse grained aggregates with plagioclase.

AT15b is a porphyritic dolerite from the same outcrop as AT15a. The sample contains rare phenocrystic mm-scale plagioclase laths in an equigranular groundmass of coarser feldspar laths and finer pyroxenes.

AT16a is a taken from a lense near the boundary of the charnockite and the Charlie gabbro. The sample is a fine grained amphibolite consisting of equigranular anhedral hornblende and plagioclase. Two larger plagioclase phenocrysts occur in the groundmass and rare poikiloblastic pink garnet crystals along a fracture zones enclose hornblende and plagioclase.

Metadolerite dyke in the Mozeskreek anorthosite

Sample BU18 was taken from the single straight continuous ~15 cm metadolerite dyke (fig. 5.8d) that was found in the anorthosite exposure in the Mozeskreek (sample location of BU18 shown in fig. 4.4). The dyke has a strike of N320E and does not display a foliation. No thin section was made for this sample, but in hand specimen it is a granular mafic metadolerite.

5.1.3 Estimated intrusion ages

Based on field and thin section observation and the metamorphic and magmatic events presently known for the Bakhuis belt, an estimation of the age of the various bodies can be made. The age of the different bodies with respect to the known metamorphic and magmatic events in the Bakhuis belt is discussed per locality and shown in figure 5.10.

High grade gabbroic granulite

Based on the metamorphic textures, the developed foliation and the migmatisation shown by the gabbroic granulite, it is evident that the body has experienced UHT metamorphism. Given the absence of any compositional banding, which is common in most UHT lithologies (de Roever et al., 2003b; Klaver, 2011; Nanne, 2013), the gabbroic granulite could have intruded syn-metamorphic and be related to UHT metamorphism. However, the absence of compositional banding could also be the result of a relatively homogeneous protolith, such as a thick basalt flow or a gabbro. Consequently, the high grade gabbroic granulite could have intruded during or before UHT metamorphism.

Metadolerite dykes in granulites

The foliated amphibolitic metadolerite dykes in the granulites are discordant to the foliation, but show partial syn-metamorphic folding. The syn-kinematic character was interpreted by (de Roever et al., 2003b) as indicating a late UHT metamorphic age for the dykes. However, the amphibolitic textures and

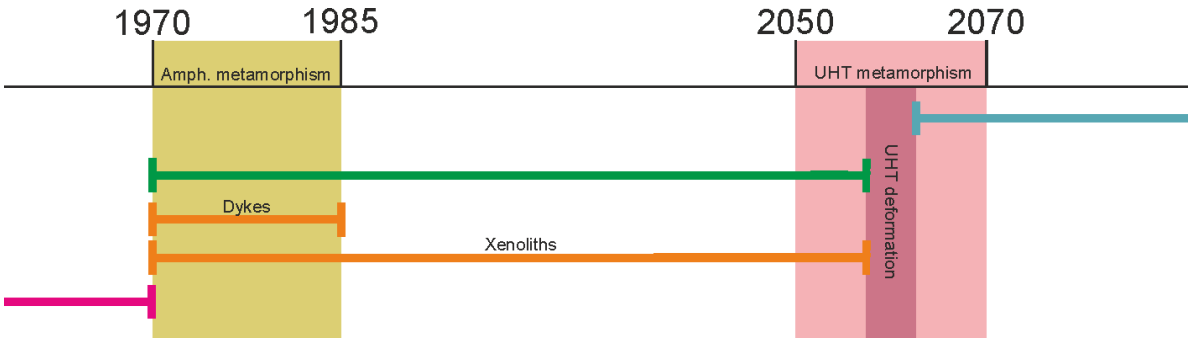

Figure 5.10. Limiting age constraints for the metadolerite and small intrusive bodies based on field relationships and thin section observations, shown on a timeline. The constraints are indicated with respect to UHT metamorphism (pink) and a theoretically shorter UHT main deformation event (hard pink), amphibolite facies metamorphism (brown), the 1990 – 1985 Ma intrusion age of the Moi-Moi metagabbro and Kabalebo charnockite and the 1970 Ma intrusion age of the Charlie gabbro. Colour coding: Blue, gabbroic granulite; green, metadolerite dykes in the granulites; orange, dykes and xenoliths in the Kabalebo Charnockite; Magenta, dykes in the Charlie gabbro.

folding could also be the result of later amphibolite facies metamorphism, in the similar phase that has affected the Moi-Moi metagabbro (Thijssen, 2015). This means that, although occurring relatively far from most Moi-Moi metagabbro bodies, they could also be related to the same magmatic event as the Moi-Moi metagabbro or possibly a new magmatic stage in between the metamorphic events. In any case, they are older than the post-metamorphic magmatic event which resulted in the Charlie gabbro.

Metadolerite dykes and xenoliths in the Charnockites

As the dykes consist of continuous segments of at least several meters long in the Kabalebo charnockites, showing minor folding, their maximum age corresponds to the intrusion age of the Kabalebo charnockites. The amphibolitic textures indicate a minimum age corresponding to the Charlie gabbro, which does not show metamorphism. The slight folding indicates that the dykes are partially deformed following crystallisation. Based on these constraints, it is likely that they belong to the Moi-Moi metagabbro event, which was related to melting of the granulites to form the Kabalebo charnockites (Klaver et al., 2015).

The xenoliths could be interpreted as either 1) pre-charnockite mafic enclaves which were taken up in the magma, indicating an older age than Kabalebo charnockite emplacement, and/or 2) fragments of syn-plutonic dykes, which were fragmented to xenoliths in later deformation. If the former scenario is true, the enclaves could be as old as late UHT metamorphism as they do not show UHT granulite metamorphism contrary to other granulitic xenoliths that show UHT metamorphism (Klaver, 2011). Similar to the dykes in the granulites, they could also reflect a new magmatic event in between the metamorphic events. If the latter scenario is true, they show a similar age ranges and they reflect the same Moi-Moi metagabbro event. In any case, the amphibolitic texture of the dykes indicates a minimum age corresponding to the intrusion age of the Charlie gabbro.

Dolerite dykes in the Charlie gabbro

Based on the primary magmatic textures and their straight, undeformed occurrence in the Charlie gabbro, the maximum age for these bodies corresponds to the intrusion age of the Charlie gabbro. While they could reflect a late phase of the Charlie gabbro, a minimum age cannot be constrained. This indicates that they could also belong to more recent dyke swarms such as the Avanevero dolerite, the Kayser dolerite or the Apatoe dolerite (de Roever et al., 2003a; Reis et al., 2013).

5.2 (Meta)dolerite geochemistry

5.2.1 Major elements

Harker diagrams have been plotted against MgO in figure 5.11. Compositions of the Charlie gabbro (grey shaded), the Moi-Moi metagabbro (vertical striped) and the anorthosite (horizontal stripes) are plotted as polygons to investigate whether there are geochemical similarities between the dykes and plutonic bodies or whether they belong to a separate generation. The variation in major elements and the overlap of the compositions with the plutonic bodies are described systematically per lithology they occur in.

Dykes in the granulites

Major element compositions for the metadolerite dykes in the granulites are plotted as green diamonds in fig. 5.11. The dykes have a relatively high magnesium content, ranging between 8–16%. Aluminium (11-15%), calcium (9-12%) and sodium (1.5-3.0%) show a gradually decreasing trend with magnesium content. Manganese (0.15-0.24%) and iron (9-12%) show no consistent trend with magnesium. Titanium (0.35-1.35%) and potassium (0.5-1.0%) show a seemingly random scatter. Silicon contents are relatively low (46.3-49.1%) and show no consistent trend.

The dykes show good overlap with the Moi-Moi metagabbro field for all elements except sodium, where 3 points plot outside the field. The dykes also show some overlap with the Charlie gabbro field, but 1- 4 samples plot outside the field for all elements. The overlap with anorthosite is good for most elements, except for sodium and titanium which show compositions consistently off the field.

Dykes and xenoliths in the Kabalebo charnockites

Major element compositions for the metadolerite dykes and xenoliths in the Kabalebo charnockites are plotted as orange diamonds in fig 5.11. The magnesium contents vary between 6-9%, where sample FN59 has a magnesium content of 13%. Aluminium (14.8-18.1%) and sodium (1.0%-3.3%) do not show a consistent trend versus magnesium. Calcium (8.1-11.7%) shows an apparent negative trend with magnesium. Iron (9.6-11.5%) and manganese (0.17-0.22%) show a narrow range in compositions with no consistent trend. The samples show a considerable range in potassium contents (0.15-1.49%), most likely reflecting contamination from the Kabalebo charnockite. Titanium (0.48-1.33%) shows scatter and silicon contents (47.9-50.4%) are relatively low, with the exception of sample FN58 (55.9%).

The xenoliths in Kabalebo charnockites show good overlap with both the Moi-Moi metagabbro and the Charlie gabbro. For aluminium and calcium, the overlap is better with the Charlie gabbro as several samples plot outside the Moi-Moi metagabbro field. For manganese and sodium, the overlap with the Moi-Moi metagabbro is better as some samples plot outside the Charlie gabbro field.

Dykes in the Charlie gabbro

The three samples analysed from dolerite dykes in the Charlie gabbro (AT04b, AT05c and AT06b) are plotted as purple diamonds in fig. 5.11. The samples plot close together, where one sample (AT05c) is enriched in iron and titanium and relatively low in silicon. Magnesium contents vary between 6.9-7.7%, making it difficult to determine a significant trend in compositions. Calcium (9.2-9.4%), aluminium (15.2-18.7%), sodium (2.3-3.0%) and potassium (0.46-0.57%) show very small variation, while silicon (46.1-51.7%), titanium (0.75-1.44%), iron (11.6-17.1%) and manganese (0.18-0.23%) show a larger spread due to deviating sample AT05c.

Two of the three samples show good compositional overlap with the Charlie gabbro they have intruded into. Sample AT05c plots outside the Charlie gabbro field for iron, silicon and titanium, but shows overlap for the other major elements.

Dyke in the Mozeskreek anorthosite

Sample BU18 from a dyke in the Mozeskreek Anorthosite is plotted as a blue diamond in fig. 5.11, the dyke shows a composition which overlaps with the range of compositions of the anorthosite it intruded in. It is relatively magnesium rich (12.0%) and silica poor (45.1%). Aluminium (14.0%), sodium (1.29%) and potassium (0.74%) contents are relatively low. Calcium (11.4%), iron (14.1%) and manganese (0.22%) contents are relatively high. The sample also overlaps with the Moi-Moi metagabbro, while significantly varying in calcium, silicon, iron, manganese and titanium content from the Charlie gabbro.

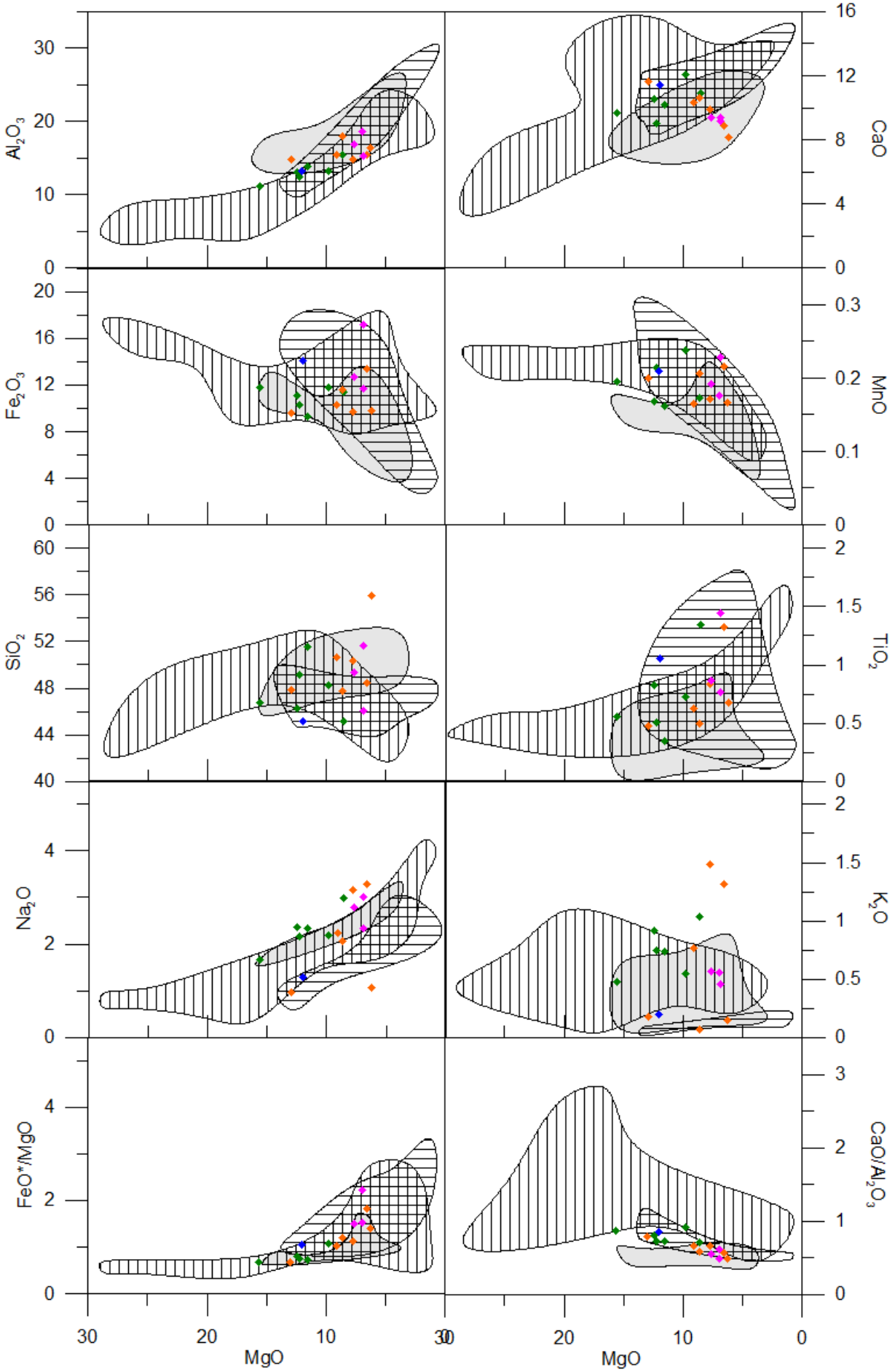

Figure 5.11 Major elements vs MgO in Harker-type diagrams for the (meta)dolerites. All values are in weight %. The grey shaded polygons indicate the range of compositions found for the Charlie gabbro, the vertically striped polygon indicates the range of compositions found for the Moi-Moi metagabbro by Thijssen (2015). The horizontally striped polygons indicate the range of compositions found for the Mozeskreek Anorthosite in this study.

5.2.2 Trace element variation

Compatible elements

Compatible element variation for nickel, vanadium, chromium and cobalt has been plotted in figure 5.12. For all dolerite bodies, nickel, chromium and cobalt show a positive trend with magnesium. Vanadium shows no systematic compositional trend with magnesium.

The metadolerite dykes in the granulites show a relatively large range in compatible element compositions. Nickel and chromium range between 140 – 330 ppm and 500 – 1500 ppm respectively, where BU09 forms an outlier of 540 ppm and 3250 ppm respectively. Vanadium ranges between 200 – 300 ppm and cobalt ranges between 45 – 75 ppm. The range in compatible elements shows good overlap with the Moi-Moi metagabbro and poor overlap with the Charlie gabbro in especially nickel, chromium and cobalt contents.

The metadolerite dykes and xenoliths in the Kabalebo charnockites also show a range in compatible element compositions. Ni and chromium range between 125 – 165 ppm and 210 – 400 ppm respectively, where FN59 forms an outlier with 370 ppm and 1100 ppm respectively. Vanadium ranges between 190 – 290 ppm and cobalt ranges between 42 – 55 ppm. The samples show good compositional overlap with the Moi-Moi metagabbro and less overlap with the Charlie gabbro in nickel and vanadium contents.

The dolerite dykes in the Charlie gabbro form a cluster of compatible element compositions. Nickel ranges between 110 – 170 ppm and chromium ranges between 88 – 105 ppm. Vanadium shows a slightly larger spread with 2 samples around 200 ppm and AT05c at 310 ppm. Cobalt contents range between 50 – 67 ppm. The sample show good overlap with both the Moi-Moi metagabbro and the Charlie gabbro.

Dolerite dyke BU18 in the Mozeskreek anorthosite has moderate nickel (250 ppm) and chromium (710 ppm) contents but high vanadium (315 ppm) and cobalt (70 ppm) contents. The composition of BU18 overlaps with the Mozeskreek anorthosite it has intruded in for all elements except chromium. It shows good overlap with the Moi-Moi metagabbro and less overlap with the Charlie gabbro in nickel and vanadium composition.

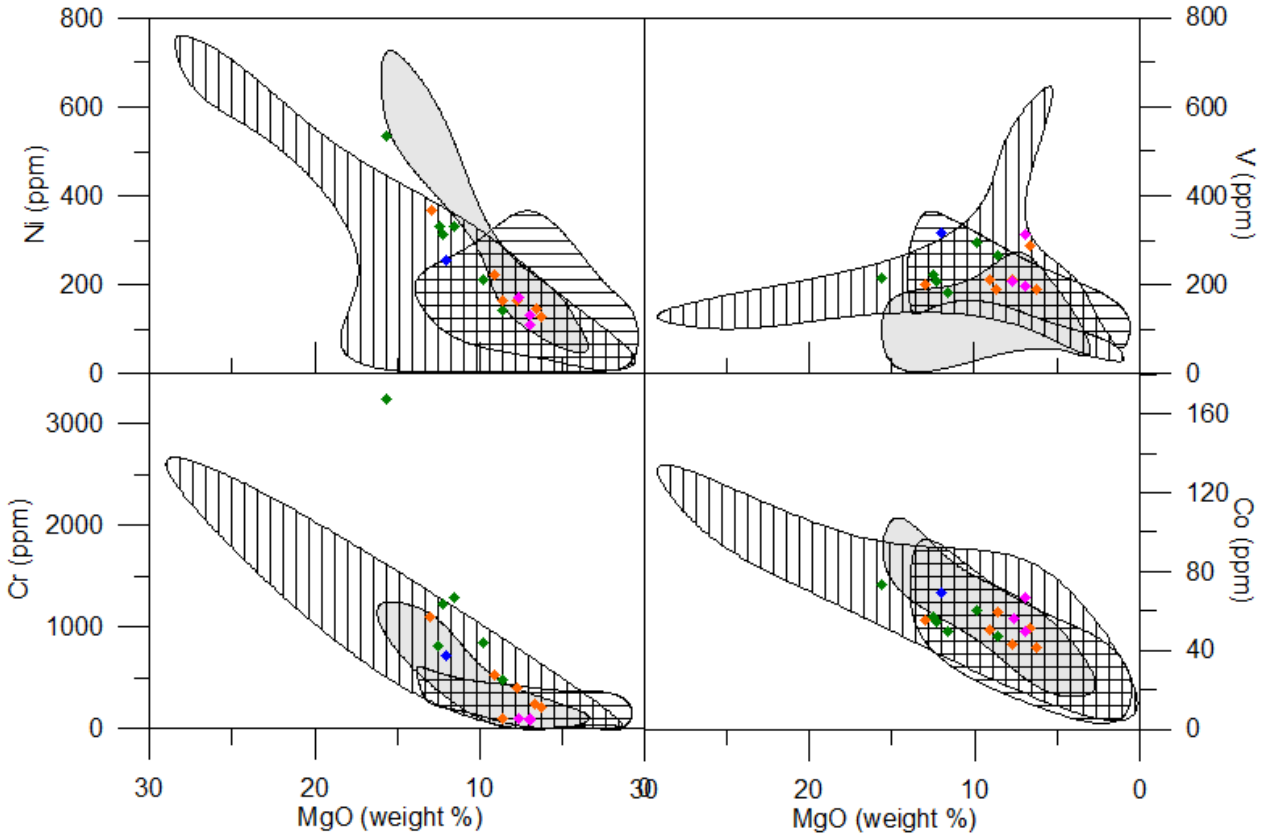

Figure 5.12 Compatible elements vs MgO in Harker-type diagrams for the (meta)dolerites. All values are in weight %. The grey shaded polygons indicate the range of compositions found for the Charlie gabbro and the vertically striped polygon indicates the range of compositions found for the Moi-Moi metagabbro by Thijssen (2015). The horizontally striped polygons indicate the range of compositions found for the Mozeskreek Anorthosite found in this study.

Incompatibles: large ion lithophile elements

Large ion lithophile element variation for rubidium, strontium and barium has been plotted in figure 5.13. The LILE contents of the dolerite bodies in the granulites and Kabalebo charnockites show considerable scatter in all plots and no consistent relationship with magnesium contents, while LILE contents of dolerite bodies in the Charlie gabbro show less variation.

The metadolerite dykes in the granulites show considerable scatter in rubidium (up to 43 ppm), barium (up to 350 ppm), and strontium (up to 1300 ppm) contents. However, as shown in figure 5.12d and e, the samples that have high contents of one of the 3 elements do not contain high concentrations of all elements. For example, BU11b has 1300 ppm strontium yet only 9 ppm rubidium and BU10a has 43 ppm rubidium yet only ~100 ppm strontium. The lack of a relationship between the elements and the fact that

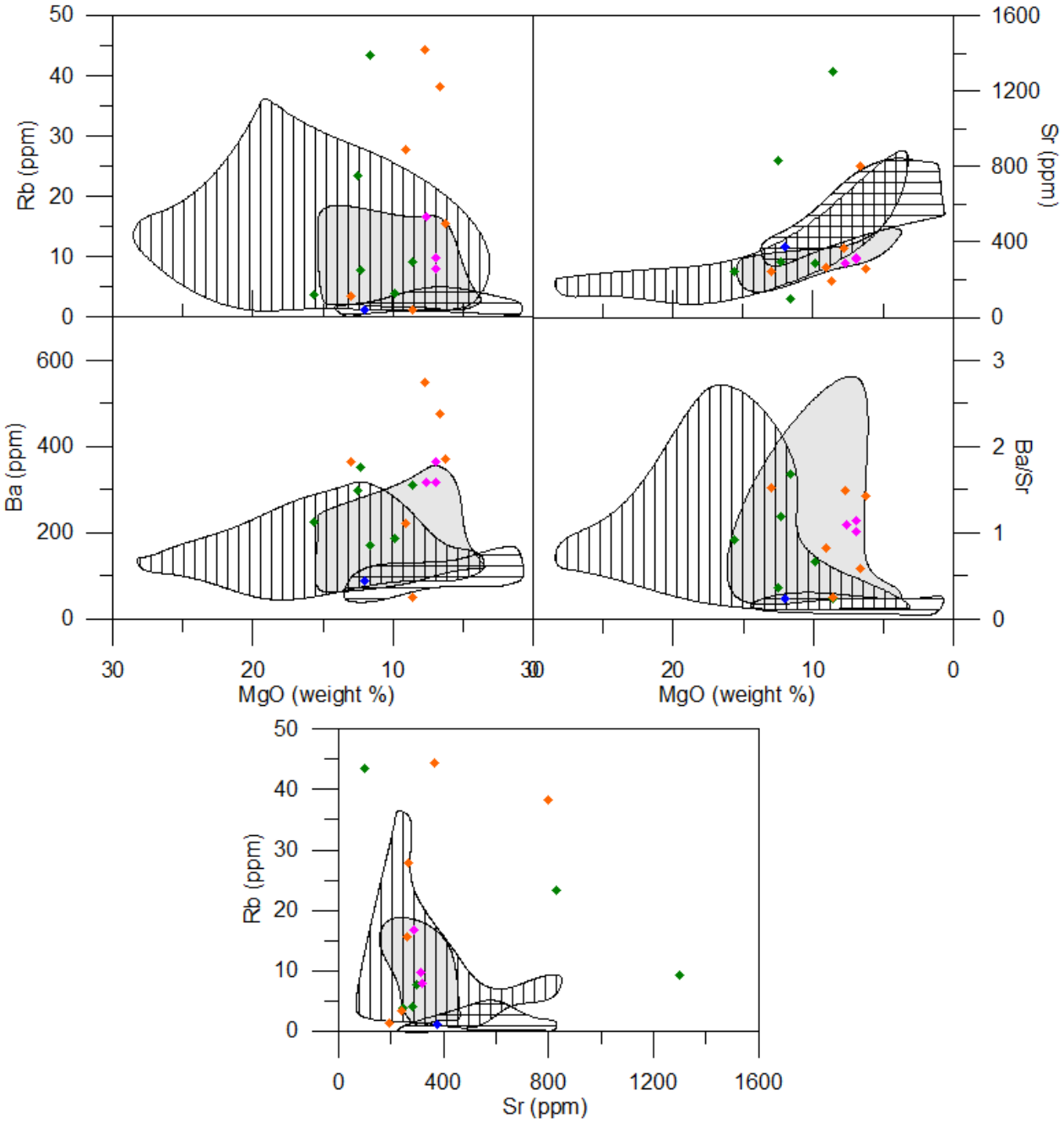

Figure 5.13 Large ion lithophile elements vs. MgO diagrams for the (meta)dolerites. All values are in weight %. The grey shaded polygons indicate the range of compositions found for the Charlie gabbro and the vertically striped polygon indicates the range of compositions found for the Moi-Moi metagabbro by Thijssen (2015). The horizontally striped polygons indicate the range of compositions found for the Mozeskreek Anorthosite found in this study.

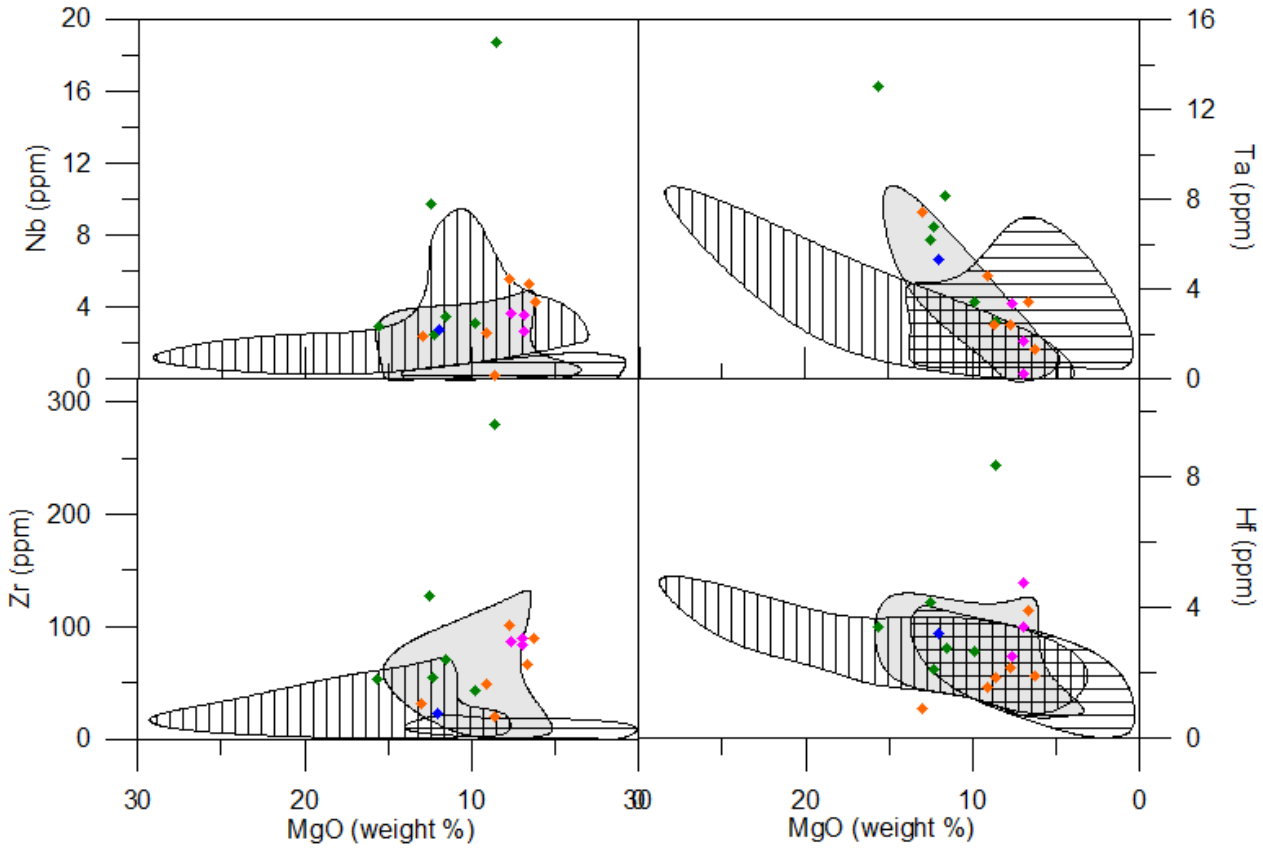

Figure 5.14 High field strength elements vs MgO diagrams for the (meta)dolerites. All values are in weight %. The grey shaded polygons indicate the range of compositions found for the Charlie gabbro and the vertically striped polygon indicates the range of compositions found for the Moi-Moi metagabbro by Thijssen (2015). The horizontally striped polygons indicate the range of compositions found for the Mozeskreek Anorthosite found in

the variation in LILE is larger than the range in compositions for (meta)gabbroic bodies, indicate a role for contaminating components of strongly varying compositions.

The metadolerite dykes and xenoliths in the Kabalebo charnockites show considerable scatter in rubidium (up to 44 ppm), barium (up to 550 ppm), and strontium (up to 800 ppm) contents. Again, there is no mutual correlation between the high rubidium and strontium contents. However, rubidium and barium contents show a better correlation than for the metadolerites in the granulites. This is probably due to contamination from alkali-feldspar from the hosting charnockites, which is consistent with the fact that the variation in LILE is larger than the variation in compositions of the gabbroic bodies.

The dolerite dykes in the Charlie gabbro show little variation in LILE contents. Strontium contents range only between 285 – 315 ppm. Barium (315 – 365 ppm) and rubidium (7 – 17 ppm) contents show a slightly larger range, indicating a varying role for alkali-feldspar. All dykes plot within compositional fields for the Charlie gabbro they intruded into.

Dolerite dyke BU18 from the Mozeskreek has relatively low rubidium (1 ppm) and barium (89 ppm) contents, while strontium (375 ppm) contents are moderate. For all LILE plots, BU18 falls within the compositional field of the Mozeskreek anorthosite it intruded into.

Incompatibles: High field strength elements

Variation for a selection of HFSE has been plotted in figure 5.14. Uranium and thorium are not included as their contents were at or below XRF detection limits and when they could be measured, the results produced a geochemically insignificant scatter. The HFSE contents of the dolerite bodies in the granulites have considerable scatter in all plots and no consistent relationship with magnesium contents, while the HFSE contents of dolerite bodies in the Kabalebo charnockites, Charlie gabbro and the Mozeskreek anorthosite show less variation.

The metadolerite dykes in the granulites show a considerably scatter in niobium (3 – 19 ppm), zirconium (40 – 280 ppm) and hafnium (2 – 9 ppm) contents. Only the variation in tantalum (3 – 13 ppm) seems to be correlated with magnesium contents. The high HFSE contents are mutually correlated yet the variation is larger than the range in metagabbroic HFSE contents, indicating contamination from a different source.

The metadolerite dykes and xenoliths in the Kabalebo charnockites show scatter in niobium (0.2 – 6 ppm), zirconium (20 – 100 ppm) and hafnium (1 – 4 ppm). Only the variation in tantalum (1 – 8 ppm) seems to be correlated with magnesium contents. Again, high HFSE are mutually correlated. The variation largely overlaps with the compositions found for the Charlie gabbro and Moi-Moi metagabbro, requiring no significant contamination from the Kabalebo charnockites
The dolerite dykes in the Charlie gabbro show little variation in HFSE contents. Niobium and zirconium cluster around ~3 ppm and ~85 ppm respectively. Hafnium (2.5 – 4.7 ppm) and tantalum (0.2 – 3.4 ppm) contents show a slightly larger range, where only tantalum is weakly correlated with magnesium. All dykes plot within compositional fields for the Charlie gabbro they intruded into.
Dolerite dyke BU18 from the Mozeskreek has relatively low niobium (2.8 ppm) and zirconium (23 ppm) contents, while tantalum (5.4 ppm) and hafnium (3.2 ppm) contents are moderate. For tantalum, zirconium and hafnium, BU18 falls within the compositional field of the Mozeskreek anorthosite it intruded into. Niobium contents are slightly enriched relative to the host anorthosite.

5.2.3 Multi element variation and rare earth elements

Based on the spread in XRF data, four samples of metadolerites in the granulites (BU09, BU10a, ER1228 and ER1232), four samples of metadolerites in the Kabalebo charnockites (BU04a, BU05, MKS32 and FN59) and one dolerite in the Charlie gabbro (AT06b) were selected to perform ICP-MS analysis for low abundance trace elements and rare earth element compositions. Rare earth and multi-element variation patterns have been plotted in figure 5.15a and b. Trace element discrimination diagrams following (Pearce, 2008) are plotted in figure 5.15c.

Rare earth elements

The REE patterns for the metadolerites in granulites show a consistent negative slope from LREE to HREE, where normalised La/Yb values range between 3.5 – 5.2. The slope is mostly present in LREE (La/Sm ~ 2.0 – 2.2), while HREE are almost completely flat (Dy/Lu ~1.1 – 1.2). BU10a forms an outlier with an even steeper slope of La/Yb ~ 18.5 and while La/Sm ~ 3.0 and Dy/Lu ~ 1.8. ER1232 is the only sample that shows a significant negative europium anomaly, where Eu/Eu* = 0.5. BU05 and AT06b show a very weak europium anomaly, at Eu/Eu* = 0.9 and 0.8 respectively. Except for sample BU10a, the patterns show good compositional overlap with the Moi-Moi metagabbro. Sample BU10a shows a stronger enrichment of LREE compared to the Moi-Moi metagabbro field.
The REE patterns for the metadolerites dykes and xenoliths in Kabalebo charnockites show a consistent negative slope for samples BU04a, BU05 and FN59 from LREE to HREE, where normalised La/Yb values range between 3.1-5.6. Slopes are mostly present in LREE (La/Sm ~ 1.8 – 2.6), while the HREE are almost completely flat (Dy/Lu ~ 1.0 – 1.2) . MKS32 shows a very weak slope of La/Yb ~ 1.5, where La/Sm ~ 1.4 and Dy/Lu ~ 1.0. None of the samples show a significant europium anomaly as Eu*/Eu > 0.88. The samples show good compositional overlap with the Moi-Moi metagabbro for all samples.
The dolerite dyke in the Charlie gabbro shows a negative slope from HREE to LREE where La/Sm = 3.6. The slope is mostly present in the LREE (La/Sm ~ 2.5), while the HREE are flat (Dy/Yb ~ 1.1). The dyke shows a weakly negative europium anomaly, where Eu/Eu* ~ 0.8. The dyke does not show compositional overlap with the Charlie gabbro it has intruded into, as all rare earth elements are significantly more enriched.

Multi element variation diagrams

The metadolerites in granulites show a general enrichment in LILE (left side of the patterns) and a weak depletion in HFSE and REE (right side of the patterns) with respect to N-MORB. Sample BU10a stands out as it is more enriched in the whole spectrum. LILE show a complex anomaly pattern, where BU09 and ER1228 have a positive barium anomaly while ER1232 shows a negative anomaly. The same two samples show a negative uranium and thorium anomaly, while ER1232 shows a positive thorium and a negative uranium anomaly. All samples show a negative niobium and tantalum anomaly, while the depth of the anomaly varies between the samples. Three of the samples show varying positive lead and potassium anomalies, while BU10a shows a weak negative anomaly for both. All samples show a negative zirconium and titanium anomaly, indicating accessory phases are not present. The fact that anomalies strongly vary between samples indicate that they might not have a homogeneous source and/or are influenced by the granulites they have intruded in.

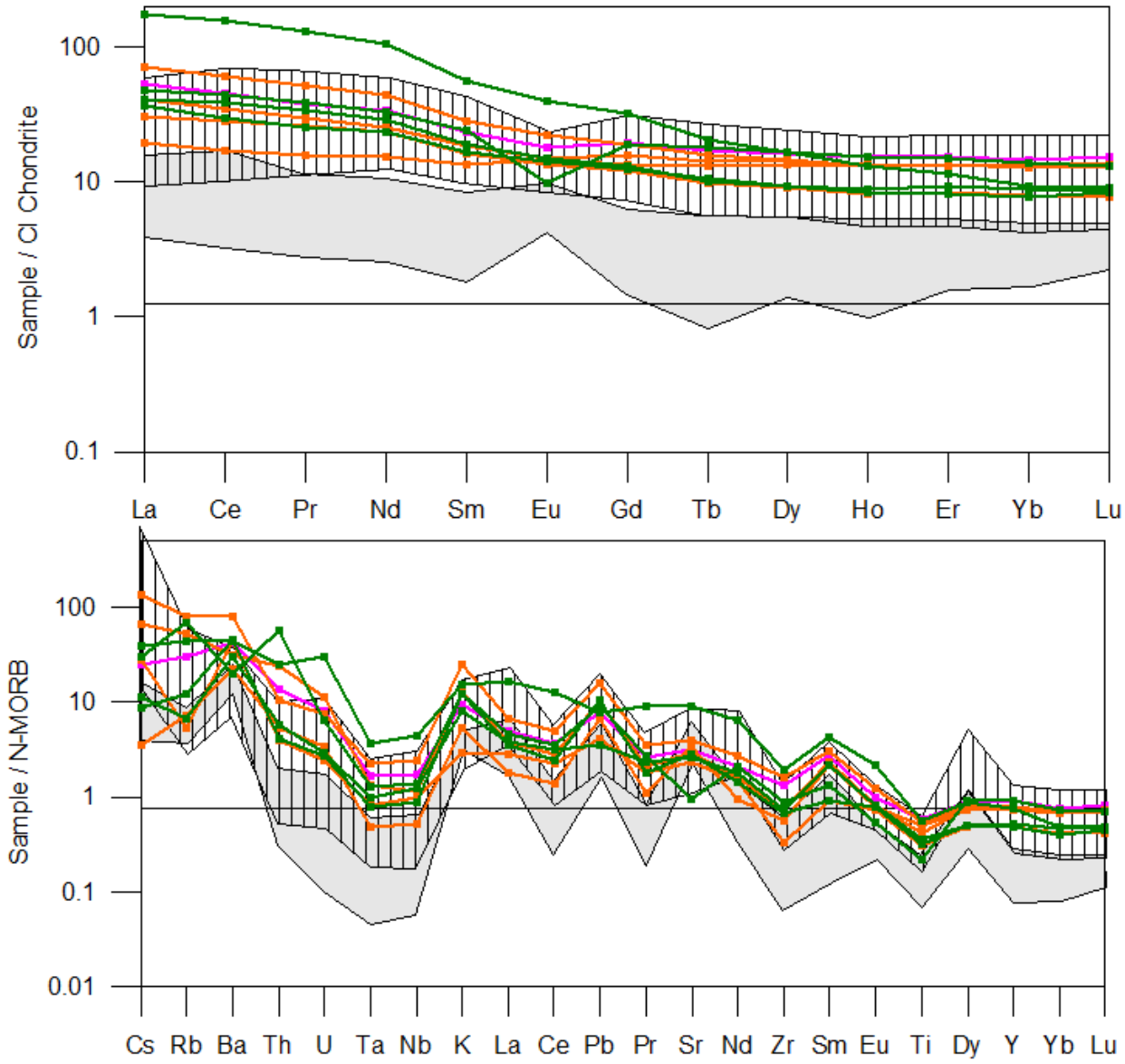

Figure 5.15. a) REE diagram with samples normalised over CI chondrite (McDonough and Sun, 1995). Lutetium is included for interpretation of radiogenic isotopes in section 4.3. b) A multi element variation diagram with values normalised over N-MORB (Sun and McDonough, 1989).

The metadolerites in charnockites show a general enrichment in LILE to a weak depletion in HFSE and REE with respect to N-MORB. BU04a and BU05 show a general enrichment for all LILE, while MKS32 and FN59 show a positive barium anomaly and lower rubidium and cesium contents. All samples except FN59 show a positive potassium anomaly, which is interpreted to reflect contamination by the hosting charnockites. All samples show a negative uranium and thorium anomaly, which coupled with a negative zirconium and titanium anomaly indicates that no significant accessory phases are present. All samples show a varying negative niobium and tantalum anomaly and a positive lead anomaly, indicating a subduction origin. MKS32 shows a strongly positive strontium anomaly, which is less developed in the other samples. All samples show a positive samarium anomaly. The samples show good compositional overlap with the Moi-Moi metagabbro, but are generally more enriched than the Charlie gabbro.

The dolerite dyke in the Charlie gabbro shows a general enrichment in LILE and a weak enrichment in HFSE to a weak depletion in REE with respect to N-MORB. All LILE are relatively high, while barium shows a weakly positive anomaly. Thorium and uranium show a weak negative anomaly, which is coupled with a weak titanium and zirconium anomaly interpreted to indicate a lack of accessory phases. The samples show a negative niobium and tantalum anomaly and a positive lead anomaly, indicating a subduction origin for the sample. Strontium and samarium show a weakly positive anomaly. The dyke does not show compositional overlap with the Charlie gabbro it has intruded into, as all rare earth elements are significantly more enriched.

5.2.4 Discussion of (meta)dolerite geochemistry

Metadolerites in granulites and Kabalebo charnockites

For most of the samples from metadolerites in the Kabalebo charnockites and granulites (except BU10a which is discussed separately below), the major and trace element variation is strongly similar to the range in compositions of the Moi-Moi metagabbro. Also, rare earth patterns and multi element variation diagrams show full overlap with the Moi-Moi metagabbro. However, both LILE and HFSE are commonly more enriched than the metagabbro. The enrichment of LILE like rubidium and barium is interpreted to be the result of contamination with the hosting granulites or charnockites, which both contain alkali-feldspar (Klaver, 2011). The enrichment of HFSE is interpreted to be the result of contamination with xenocrystic accessory phases (see also section 5.5.1 and 5.5.4). The geochemistry is consistent with a subduction zone origin, with negative niobium and tantalum anomalies and HFSE depletion and positive lead anomalies and LILE enrichment.

Compared to the Moi-Moi metagabbro, the REE patterns are relatively steep. This can indicate that they were formed by smaller amounts of partial melting of the source, which could be interpreted as that they were formed in an earlier stage compared to the Moi-Moi metagabbro plutonic bodies. Alternatively, accumulation of pyroxene can decrease the slope of a REE pattern for cumulates and raise the slope of the REE pattern for the residual magma. This is consistent with the flattening out shape of the LREE for the mafic plutonic bodies, indicating pyroxene accumulation, and the steeper slope of the metadolerite dykes, which were then derived from the residual magma.

As described in section 5.1.3 and shown in figure 5.10, the dykes in the granulites and the xenoliths in the Kabalebo charnockites could be related to late ~2.07 Ga UHT metamorphism, ~1.97 – 1.99 Ga Mafic plutonism or reflect another magmatic event in between. Based on the geochemical similarities with the Moi-Moi metagabbro, it seems more likely that both groups of metadolerites are associated with ~1.97 – 1.99 Ga mafic plutonism and this model is preferred over invoking another generation of mafic magmatism in between the two events. For the dykes in the Kabalebo charnockites, this scenario is plausible as the Moi-Moi metagabbro of the ~1.97-1.99 Ga mafic plutonic event is associated with melting of the granulites to form the Kabalebo charnockite magma (Klaver et al., 2015). For the dykes in the UHT granulites, this interpretation is problematic with the partially syn-metamorphic appearance as indicated by amphibolitic textures, folding and boudinage of the dykes (section 5.1 and de Roever et al., 2003b). If the dykes in the granulites are related to the ~1.97 – 1.99 Ga mafic plutonic event, this requires that the observed deformation and metamorphism in the dykes occurred during or after the ~1.97-1.99 Ga event. This deformation can occur

Summarizing, the scenario where all metadolerite dykes belong to the Moi-Moi metagabbro seems favourable. Alternatively, the dykes may still represent a separate generation. This possible relationship between the granulite and Kabalebo charnockite dykes with the Moi-Moi metagabbro is further investigated using radiogenic isotope variation for the dykes in section 5.3.

Sample BU10a

Sample BU10a from a metadolerite dyke in the granulites shows a slightly different pattern. Its major and trace element chemistry agrees with the rest of the metadolerite dykes and the compositional fields of the Moi-Moi metagabbro. However, the trace element and multi element variation patterns show a much stronger enrichment and less pronounced positive and negative anomalies, compared to the other dykes and the Moi-Moi metagabbro. Based on the XRF data, it can be assumed that sample BU11b would show a similar pattern, as all the trace elements have much higher concentrations compared to the other dykes.

As the same anomaly features are still present, it can be assumed that the samples originated from a similar magma source. Stronger enrichment can then either be explained by a later stage of melt extraction in the mantle with fewer percentages of partial melting. Alternatively, the stronger enrichment can also be interpreted as a stronger contamination with the host granulites. As most of the hosting intermediate granulites do not show the REE and multi element variation anomalies of the mafic bodies (Klaver, 2011), contamination with intermediate granulites would have a 'flattening' effect, which would remove the anomalies while also enriching the patterns. Contamination with hosting granulites is consistent with the interpreted presence of xenocrystic zircon in sample BU10a (see section 5.4.2 and 5.4.4).

Metadolerites in Charlie gabbro and Mozeskreek anorthosite

For the majority of major and trace elements, the dolerite dyke in the Mozeskreek anorthosite and the dykes in the Charlie gabbro geochemically overlap with the plutonic bodies they have intruded into. This indicates that they are likely to originate from the same parental magma as those bodies. However, the

rare earth and multi element variation pattern of AT06b all show a stronger enrichment than the Charlie Gabbro body it has intruded into. Since the pattern is mostly parallel to the Charlie gabbro, it could be interpreted as derived from the same parental magma, which was left more enriched after crystallisation of the Charlie gabbro plutons. However, it cannot be excluded that the dykes belong to a younger generation.
For the Mozeskreek anorthosite, this interpretation provides a good opportunity. Anorthosite geochemistry is commonly considered to reflect the accumulation process rather than the composition of the parental magma (Ashwal, 1993; Winter, 2010). Therefore, dyke BU18 is more likely to provide constraints on the composition of the (more evolved) parental magma than the anorthosites, as dykes cannot be formed by accumulation processes. No ICP-MS measurements have been performed for BU18, preventing a reliable comparison of REE and multi element variation patterns. The major and trace element geochemistry plots on the mafic end of the anorthosite spectrum in all diagrams. The dyke also shows geochemical overlap with the Moi-Moi metagabbro. This provides further indications that the Mozeskreek anorthosite body is derived from the same parental magma as the Moi-Moi metagabbro, which is also indicated by the largely overlapping geochemistry (section 4.2.3) and the similar initial values for hafnium and neodymium (section 4.3.3) for both plutonic bodies.

5.3 Radiogenic isotopes

5.3.1 Sample selection

Based on the geochemistry described in section 5.2, six (meta)dolerite samples from different locations were selected for isotope dilution. The samples were selected to represent the more mafic, primitive samples from the suites with the least signs for contamination, weathering or alteration.
Two samples (BU09 and BU10a) were selected from the metadolerite dykes in the granulites, three samples (BU04a, BU05 from this study and MKS32 of Klaver, 2011) were selected from the metadolerite dykes and xenoliths in the Kabalebo charnockites and one sample (AT06b) was selected from a dyke in the Charlie gabbro. All samples show a subduction signature in trace elements and various enrichments, especially in rubidium and barium indicating contamination with K-feldspar. Sample BU10a is a dyke from the granulites which shows a much strong enrichment in all trace elements compared to the other samples (see also section 5.2.3 and 5.2.4).

5.3.2 Results

5.3.2.1 Strontium, neodymium and hafnium isotopic variation

The variation in initial values for all isotopes of the (meta)dolerite bodies in the granulites (green diamonds), in the Kabalebo charnockites (orange diamonds) and in the Charlie gabbro (purple diamond) are plotted in figure 5.16a and b. All initial values are calculated to the 1980 Ma age of the mafic plutonic event (de Roever et al., 2003b; Klaver et al., 2015; Thijssen, 2015). Polygons of the Moi-Moi metagabbro (striped) and the Charlie gabbro (grey shaded) are added for comparison
A similar intrusion age to the mafic plutonic bodies is assumed for all metadolerite dykes, given the similarities in geochemistry to the Moi-Moi metagabbro for the dykes in the granulites and the syn-plutonic character of the dykes and xenoliths in the Kabalebo charnockites. For the metadolerite bodies that could also be older based on field relationships (BU09, BU10a, BU05 and MKS32), initial values were also calculated for their maximum 2050 Ma age corresponding to late UHT metamorphism. However, as the samples are already ~2 Ga years old, the older ages only resulted in an increase in the initial values of up to half an epsilon value for neodymium and up to 1 epsilon value for hafnium. Consequently, using 2050 Ma ages does not significantly change the patterns and possible interpretations of the (meta)dolerite initial values.
Sadly, the samarium measurement of AT06b by Triton failed to produce a good result and there was not enough material to try the measurement a second time. To be able to plot the data, the samarium concentration as measured by ICP-MS was used for the calculation. However, this gives a highly unreliable result with an error on the initial value of 17.3. This is shown by the horizontal line in figure 5.16b.

Strontium variation

Initial $^{87}Sr/^{86}Sr_{1980}$ ratios for all types of metadolerite bodies plot around the 0.702272 value for bulk silicate earth and significantly above the value of 0.70085 for the depleted mantle at 1980 Ma (DePaolo and Wasserburg, 1976), ranging between 0.701684 – 0.702479. The metadolerite bodies from the different locations show strong overlap. The metadolerites from the Kabalebo charnockites range between 0.701689 – 0.7024424, while the two dykes in the granulites yield initial values of 0.702029 and

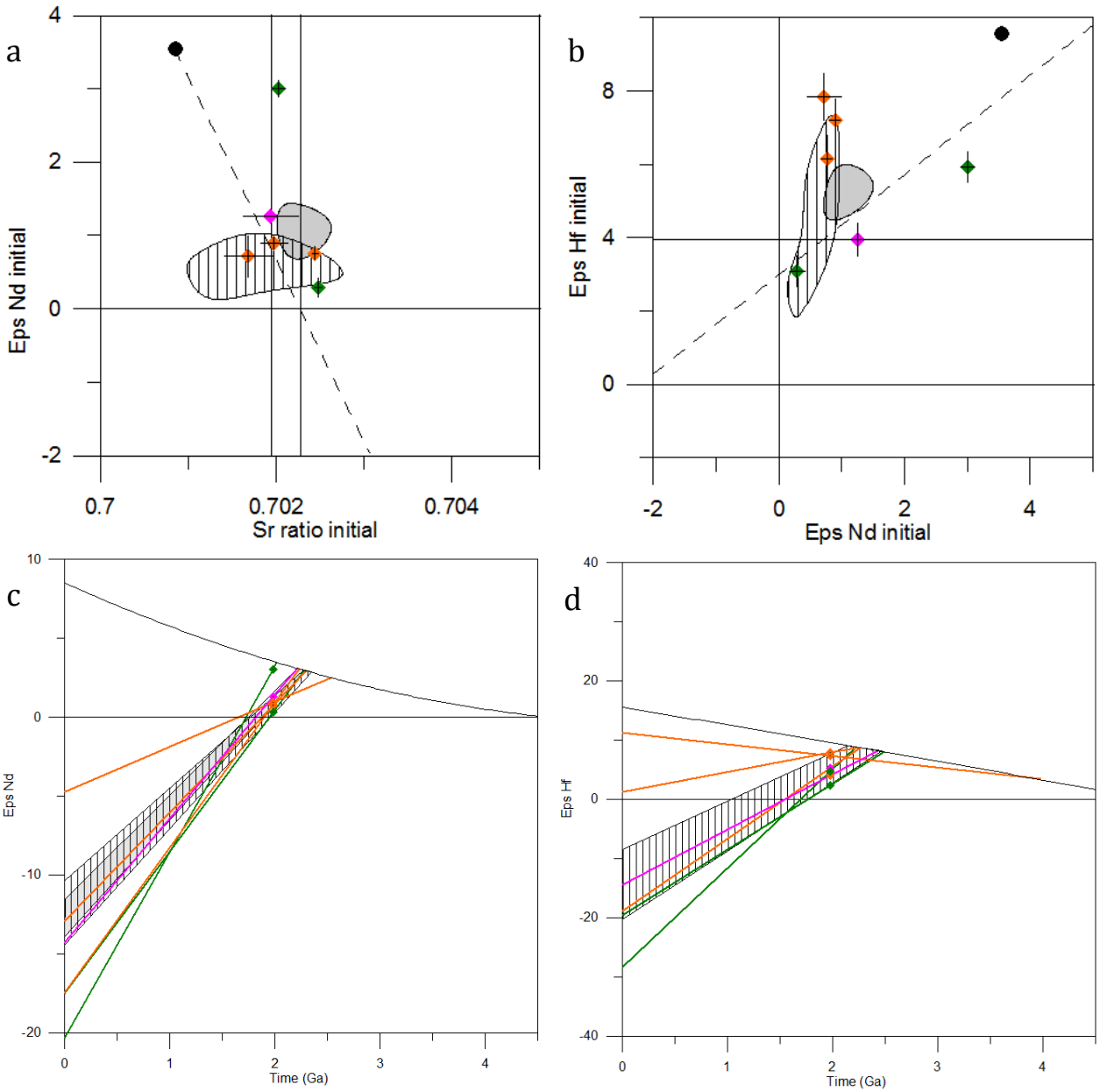

Figure 5.16. Radiogenic isotope variation for the metadolerite dykes in the granulites (green diamonds) and in the Kabalebo charnockites (orange diamonds) and the dolerite dyke in the Charlie gabbro (purple diamond). A) Initial εNd_{1980} vs initial $^{87}Sr/^{86}Sr_{1980}$ ratios. Black dot indicates composition for depleted mantle at 1980 Ma. B) Initial εHf_{1980} vs initial εNd_{1980}. Black dot indicates composition for depleted mantle at 1980 Ma. C) Neodymium evolution diagram. D) hafnium evolution diagram.

0.702479 and the dolerite dyke in the Charlie gabbro shows a value of 0.701938. The range in initial ratios also shows full overlap with the 0.701158 – 0.702620 range in initial strontium ratios found for the mafic plutonic bodies in section 4.3.

Neodymium variation

Initial εNd_{1980} value for the bulk of the metadolerite bodies plot just above the value for CHUR yet significantly below the 3.54 value for depleted mantle at 1980 Ma (DePaolo, 1981), ranging between εNd_{1980} values of 0.31 – 1.29. One sample from the metadolerites in granulites yields the lowest value of 0.31, while the metadolerites in the Kabalebo charnockites form a narrow cluster between 0.75 and 0.79. The initial value of the dolerite dyke in the Charlie gabbro is slightly higher at 1.29. This range in initial values fully overlaps with the 0.26 – 1.32 range in initial values for the mafic plutonic bodies of section 4.3. However, sample BU10a of the metadolerites in granulites has a significantly higher initial εNd_{1980} value of 3.02, much closer to the depleted mantle value.

Hafnium variation
Initial εHf_{1980} values for all metadolerite bodies show a significant range, plotting above CHUR and towards the value of 9.6 for the depleted mantle at 1980 Ma (Vervoort et al., 2000). The largest range of εHf_{1980} = 5.3 – 7.8 is recorded in the metadolerites in the Kabalebo charnockites. The metadolerite in granulites are slight lower at εHf_{1980} = 2.9 and 4.7 and the dolerite dyke in the Charlie gabbro shows a value of εHf_{1980} = 4.0. The range also shows full overlap with the 2.2 – 7.9 range in the mafic plutonic bodies.

Comparing plots of initial values
Plotting the neodymium vs. strontium ratios and the hafnium vs. neodymium ratios (fig. 5.16a and b) allows a comparison of the data with respect to depleted mantle and the mantle array (Vervoort and Blichert-Toft, 1999). The plots also allow a comparison with the polygons for the Moi-Moi metagabbro and the Charlie gabbro. While the range in strontium and neodymium (excluding the BU10a outlier) are relatively narrow, the range in hafnium is larger.
In the εNd_{1980} vs. $^{87}Sr/^{86}Sr_{1980}$ plot (fig. 5. 16a), the bulk of the data (excluding BU10a) is distributed along the dotted line between depleted mantle and the value for bulk silicate earth. Four of the samples plot on the right side of the line, while one sample (BU05) from metadolerites in the Kabalebo charnockites plots on the left side of the array. Sample BU10a is significantly above the dotted line. The three metadolerites from the Kabalebo charnockites and one metadolerite (BU09) from the granulites plot inside the field of the Moi-Moi metagabbro. Sample AT06b seems within error of the Charlie gabbro field, but the neodymium value can't really be trusted.
In the εHf_{1980} vs. εNd_{1980} plot (fig. 5.16b), the data is distributed on both sides of the mantle array (Vervoort et al., 1999). The metadolerites in Kabalebo charnockites (BU05 and MKS32) plot above the dotted line due to relatively high εHf_{1980} values around ~7.5. The metadolerite in Kabalebo charnockites and one metadolerite from the granulites (BU09) plots within error of the Moi-Moi metagabbro field. Sample AT06b plots just outside the Charlie gabbro field. Again, the neodymium value can't really be trusted.

5.3.2.2 Hafnium and neodymium model ages
Neodymium and hafnium depleted mantle model ages have been calculated. The model ages are solved for the depleted mantle evolution for neodymium of DePaolo (1981) and for hafnium of Vervoort et al. (2000). The evolution lines and model ages are plotted in figure 5.16c and d.

Neodymium evolution and model ages
The metadolerite dykes in the granulites show a strongly negative radiogenic evolution towards present day εNd_0 values of -17.5 and -20.3. The metadolerites in charnockites show a strongly varying negative radiogenic evolution towards present day εNd_0 values ranging between -17.4 and -4.7. The dolerite dyke from the Charlie gabbro shows a negative radiogenic evolution to a εNd_0 value of -14.3, which overlaps with the range of radiogenic evolutions in the mafic plutonic rocks. Sample BU05 is the only other sample that shows a similar radiogenic evolution to the mafic plutonic rocks. The strong range in neodymium radiogenic evolutions is consistent with the strong variation in LREE slope for the metadolerite dykes (see also section 5.2.3 and 5.2.4) causing various Sm/Nd ratios.
From all the metadolerite bodies, 4 samples result in neodymium T_{DM} ages ranging between 2.21 and 2.29 Ga, consistent with the 2.22 – 2.31 Ga range in most mafic plutonic samples. Sample BU10a resulted in a relatively young T_{DM} age of 2.02 Ga due to its higher initial εNd_{1980} value and sample MKS32 resulted in an older age of 2.53 Ga. However, given its anomalously flat neodymium evolutions the error is very big, and the older age can also be an artefact of a flat evolution.

Hafnium evolution and model ages
The metadolerite dykes in the granulites show a strongly negative radiogenic evolution towards present day εHf_0 values of -19.6 and -28.3. The metadolerites in charnockites show a strongly varying negative to positive radiogenic evolution towards present day εHf_0 values ranging from -18.9 to 11.2. The dolerite dyke in the Charlie gabbro displays a negative radiogenic evolution towards an εHf_0 of -14.4, which overlaps with the hafnium evolutions for the bulk of the Moi-Moi metagabbro samples. Samples BU09 of the metadolerites in granulites and BU04a of the metadolerites in Kabalebo charnockites also show evolutions overlapping with the Moi-Moi metagabbro. While sample BU10a is the only sample that shows an anomalously negative evolution, the other deviations are all positive. The strongly varying hafnium

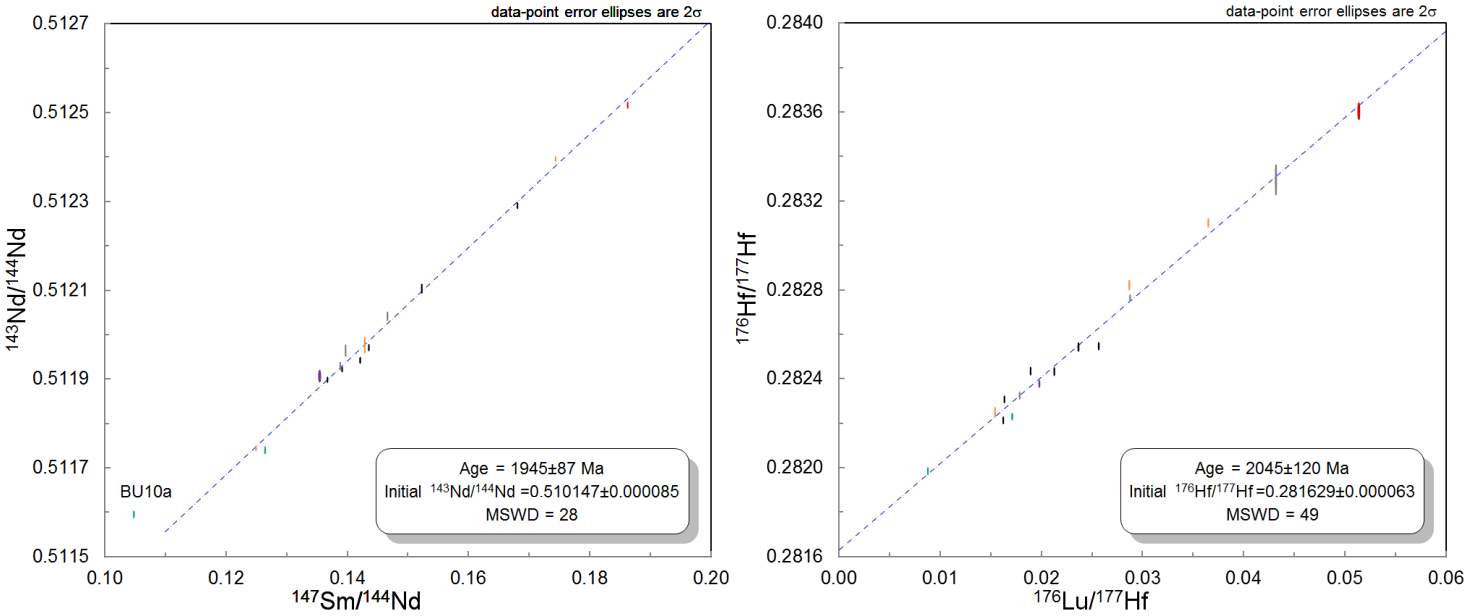

Figure 5.17. Sm/Nd and Lu/Hf isochron results, calculated with IsoPlot 4.15. Samples are plotted as error ellipses. Black ellipses are samples of the Moi-Moi metagabbro, gray ellipses are the samples of the Charlie gabbro and the red ellipse indicates the sample from the Mozeskreek anorthosite.

evolution is consistent with the variation in HFSE and HREE elements as described in section 5.2.3 and 5.2.4, leading up to varying Lu/Hf ratios.
Despite the strong range in Lu/Hf ratios, the range in hafnium T_{DM} ages for the bulk of the samples of 2.22 – 2.48 Ga is in full overlap with the 2.12 – 2.49 Ga range in the mafic plutonic rocks. However, given its positive radiogenic evolution almost parallel to evolution of depleted mantle, sample MKS 32 has a strongly anomalous T_{DM} of 4.0 Ga.

5.3.2.3 Hafnium and neodymium isochrons

As only up to three samples were analysed for the different metadolerite bodies, a reliable isochron age could not be calculated for the different bodies. An isochron of all metadolerites could be calculated, but given the fact that BU10a strongly deviates from the other samples, only 4 samples would be left which would not produce a reliable isochron either. Alternatively, an isochron age is calculated for all mafic igneous bodies together, where BU10a is excluded for the calculation of the Sm-Nd isochron as it forms an outlier (fig. 5.17a and b).
The Sm-Nd data result in an errorchron age of 1945 ± 87 Ma as the MSWD = 28. The Lu-Hf data results in an errorchron age of 2045 ± 120 Ma as the MSWD 49.

5.3.3 Interpretation and discussion

Metadolerites in Kabalebo charnockites
The metadolerite bodies in the Kabalebo charnockites all plot near the Moi-Moi metagabbro end-member of the mixing curve in fig. 5.16b, indicating they are derived from the same parental magma as the Moi-Moi metagabbro and did not experience significant magma mixing with the hosting Kabalebo charnockites. Their common origin with the Moi-Moi metagabbro is consistent with interpretations of Klaver et al. (2015) that the Moi-Moi metagabbro event provided the heat source for melting of the granulites to form the Kabalebo charnockites. The fact that they do not show mixing is surprising. Apparently, the bodies were not exactly contemporaneous and either of the bodies was already sufficiently crystallised at the time they came in contact, preventing magma mixing. For the metadolerite dykes and xenoliths in the Kabalebo charnockites, the overlap with the end-member Moi-Moi composition rules out the possibility that the dykes belong to late UHT metamorphic dykes, as well as the possibility that they represent a separate magmatic phase, which were considered as options in section 4.1.3.

Metadolerites in granulites
The dyke of sample BU10a shows overlapping hafnium and strontium values, yet higher neodymium values. This would indicate a different, more depleted mantle source for the sample compared to the other analysed samples. However, considering the strongly enriched REE patterns and the weaker anomalies in

the multi element variation diagrams compared to the other metadolerites in the granulites as discussed in section 5.2.4, it is highly likely that the sample was influenced by contamination. This is consistent with the indications for xenocrystic zircon in the dyke as described in section 5.4.4. This is also indicated by the apparent disagreement in the errorchrons, where for the sample plots on the errorchron while the sample plots significantly off the Sm-Nd errorchron. Consequently, a geologic significance cannot be attributed to the values.

The other metadolerite dyke in the Blanche Marie granulite (BU09) plots on the range of Moi-Moi metagabbro compositions, corresponding to about 7% charnockite mixing if the same mixing model for the Kabelebo charnockites and Moi-Moi metagabbro is applied. This interpretation seems attractive, but cannot simply be applied since there are no known nearby occurrences of charnockites and the larger charnockite bodies occur ~50 km away. Consequently, the value would be interpreted as reflecting a different magmatic generation, which happens to fall on the same mixing ling.
However, hypothetically it could also be interpreted that the dyke is contaminated by either a charnockite body in the subsurface or the hosting granulites. As granulite melting is the interpreted source for the charnockite magma, it is possible that the initial values for the Kabalebo charnockites are directly inherited from the granulites. While no hafnium data is available for the granulites, the similar initial neodymium values clustering around ~ 0 for the granulites are in support of this hypothesis (Klaver et al., 2015). As already discussed for BU10a, at least some of the dykes have experienced mixing with the granulites.
The concentrations for hafnium and neodymium would be different in the granulites then the Kabalebo charnockites, so a mixing model following DePaolo and Wasserburg (1979) would probably have a different parabolic shape, but still lead to the same point. However, since there are no available hafnium values for the granulites, a mixing model to validate this idea cannot be calculated.

Consequently, both dykes cannot be used as direct evidence for either a similar parental magma origin with the Moi-Moi metagabbro or a different origin. However, the dykes show more similarities to the Moi-Moi metagabbro event than to UHT metamorphism. A rough age of the dykes has been established based on field relationships in 5.1.3 as between 1970 – 2050 Ma, and the dykes show a clear subduction zone signature as described in 5.2.4. Although they may be derived from a slightly different mantle source, they indicate the same tectonic regime in a similar time period, so the consequences of an interpreted different mantle source would have no significant geodynamic implications and could simply reflect mantle heterogeneity. Given the subduction zone signature, a relationship with the ~1.97-1.99 Ga magmatic event is preferred over a relationship with UHT metamorphism, which is interpreted to occur in a regime of crustal stretching (Delor et al., 2003b). If an age would be obtained for the dykes, they could provide constraints the exact timing of the subduction event leading up to the ~1.97-1.99 Ga magmatic event.

Dolerite in Charlie gabbro
In figure 5.16 a, sample AT06b plots close to, but outside the field for the Charlie gabbro it has intruded in. This provides no direct indication that the dyke represents a late phase of the same parental magma. Alternatively, the dyke could also reflect either of three younger generations of dyke swarms: 1) Avanevero dolerite, 2) Kayser dolerite or 3) Apatoe dolerites (de Roever et al., 2003a; Reis et al., 2013).
Given that the sample plots relatively close to the Sm-Nd and Lu-Hf errorchrons for all analysed samples, it is unlikely that the dyke is much younger than 1.98 Ga. This means the Apatoe dolerites can be excluded, which yields a Mesozoic age of 227 ± 10 Ma (Priem et al., 1968). Also, the alkaline Kayser dolerites can be excluded based on the tholeiitic geochemistry of the dolerite dykes in the Charlie gabbro (de Roever et al., 2003a).
For the Avanevero dolerite as the remaining candidate, the geochemistry for major and trace elements is strongly overlapping with the geochemistry of the dolerite dykes in the Charlie gabbro (Reis et al., 2013). Sadly, no strontium, neodymium or hafnium isotopic data is available for the Avanevero dolerite. However, sample AT06b contains large porphyritic hornblende crystals and the pyroxene-hornblende rich matrix shows recrystallization by metamorphism. This has not been described for the post-metamorphic Avanevero dolerite. Additionally, the Avanavero has been described to form dykes between 50 – 1000 m thickness (Bosma et al., 1984). While ~1 m dykes should be possible for the Avanavero dykes, their common occurrence in the Charlie gabbro (four dykes were found in an exposure of ~1 km long) compared to the rarity of similar-sized Avanavero dykes in all other Bakhuis lithologies would be difficult to explain. Consequently, the dykes are instead interpreted as reflecting a late phase from the parental magma of the Charlie gabbro.

Neodymium and hafnium evolution and model ages
For some of the samples, neodymium and hafnium depleted mantle model ages show a range between 2.21 – 2.48 Ga which overlaps with what is found for the mafic plutonic bodies. However, especially for the εNd values, the metadolerite dykes show significantly more variation in evolution towards present day εNd_0 values than the mafic plutonic bodies.

Three samples show a more negative radiogenic evolution than the range in the mafic plutonic bodies, indicating lower Sm/Nd ratios. One sample shows a more positive radiogenic evolution compared to the mafic plutonic bodies, indicating they have comparatively elevated Sm/Nd ratios. For the Mozeskreek anorthosite, a similar variation was interpreted to be the effect of variation in accumulation processes (see section 4.3.3). However, as shown in figure 5.15a, for the metadolerite dykes there is a significant variation in the slope of the diagrams. While they share a common enrichment in HREE, the LREE are very variably enriched. The steepness of a REE slope is a function of the degree of partial melting. The elevated Sm/Nd ratios and the deviating neodymium evolution are thus interpreted to reflect heterogeneities in the degree of partial melting for formation of the magma's the dykes are derived from.

For the variation in the hafnium evolution, three sample from the metadolerites in the granulites and Kabalebo charnockites also deviate as more negative (BU10a) to more positive (BU05 and MKS32) compared to the range in the mafic plutonic bodies. Similar to the deviating samples in the mafic plutonic bodies (see section 4.3.3), this is interpreted to the be effect of varying roles for zircons. For the metadolerites in the granulites, the lutetium enrichment is comparable for most of the samples (see fig. 5.15a) indicating that the variation occurs in the hafnium content. For BU10a, which shows a more negative radiogenic evolution, it is interpreted that xenocrystic zircon is present (see also section 5.4.4). As hafnium is strongly incorporated in zircon, the sample will have excess hafnium, lowering the Lu/Hf ratio. For the metadolerites in the Kabalebo charnockites, the enrichment is also similar between the samples (fig. 5.15a). Inversely, the deviating positive hafnium evolution is thus interpreted to reflect extraction of zircon out of the samples, increasing the Lu/Hf ratio.

5.4 U-Pb zircon dating

5.4.1 Sample selection
Most dykes are too fine-grained and mafic to expect good quality zircons large enough to be separated or analysed by LA-ICP-MS for U-Pb dating. However, (de Roever et al., 2003b) managed to separate zircon from two metadolerite dykes at the Blanche Marie falls. Pb-Pb evaporation analysis resulted in 2056 ± 4 Ma and 2060 ± 4 Ma ages, which were interpreted as 'the age of dyke crystallisation'. However, in section 5.2 and 5.3 the metadolerite dykes and xenoliths in the granulites and Kabalebo charnockites are interpreted to belong to the same magmatic event as the Moi-Moi metagabbro, for which an age of ~1980 Ma is established (Klaver et al., 2015; Thijssen, 2015). A probable explanation could be that the zircon in the samples of (de Roever et al., 2003b) was not formed by crystallisation of the dolerite but taken up as xenocrysts from the host granulites. Although no size for the separated zircon crystals is reported by (de Roever et al., 2003b), it seems unlikely zircon crystals large enough for mineral separation would have grown in a fine-grained metadolerite. In an attempt to check the interpretation of (de Roever et al., 2003b), the internal and external textures in zircon of metadolerite dyke sample BU10a were analysed with EMP in both thin section and in zircon concentrate loaded into an epoxy resin mount.
The other sample that was selected for zircon analysis is BU13, taken from the high grade gabbroic granulite body at the Blanche Marie falls. The body was first sampled and described by Klaver (2011), who interpreted the body to be part of the same mafic granulites exposed further upstream of the Nickerie river. To investigate its geologic significance and possible relationship to UHT metamorphism, zircon was separated and analysed for textures and morphology to interpret a metamorphic or igneous origin, and the U-Pb age was measured by LA-ICP-MS.

5.4.2 Zircon textures and morphology
BSE images of zircon in thin section and separated in mounds are shown in figure 5.19.

BU10a
An automatic (overnight) EMP scan on the typically high BSE signal of zirconium phases (both zircon and baddeleyite) resulted in a bimodal population of zircon grains and no baddeleyite.
The first population is coarse grained, consisting of 300-500 µm long and 100-150 µm wide subhedral to anhedral zircon grains which show complex, fragmented zonation patterns (fig. 5.19a and b). Resorption

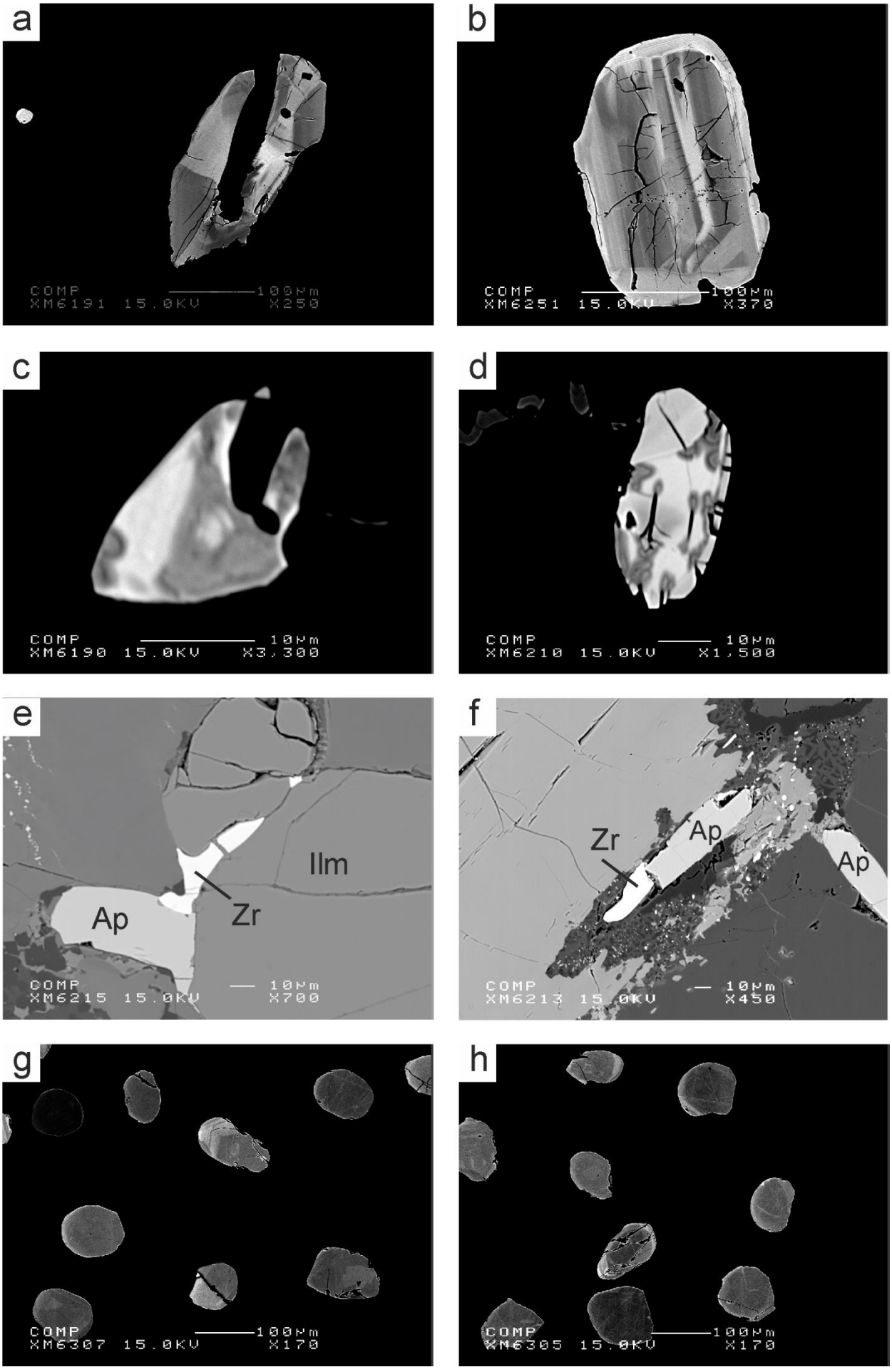
a
COMP
XM6191 15.0KV
100µm
X250
b
COMP
XM6251 15.0KV
100µm
X370
c
COMP
XM6190 15.0KV
10µm
X3,300
d
COMP
XM6210 15.0KV
10µm
X1,500
e
Ilm
Zr
Ap
COMP
XM6215 15.0KV
10µm
X700
f
Zr
Ap
Ap
COMP
XM6213 15.0KV
10µm
X450
g
COMP
XM6307 15.0KV
100µm
X170
h
COMP
XM6305 15.0KV
100µm
X170

Figure 5.19 (previous page). BSE images of zircon from samples BU10a and BU13 in thin section and concentrates in mounds. A) Resorption of the core of a coarse xenocrystic zircon in BU10a. B) Thin neocrystallised rim around a coarse xenocrystic fractured core in BU10a. Fractures do not propagate in the rim. C) Fine-grained skeletal zircon in BU10a. D) Fine-grained zircon in BU10a showing alteration at the ends of cracks. E and F) Zircon in BU13 crystallising in between ilmenite and apatite, indicating a primary magmatic origin. G and H) Rounded zircon crystals while most crystal show no internal textures, some crystals show faint compositional zoning.

along the boundaries is common and resorption of a zircon core is well visible in one in-situ grain (fig. 5.19a). Grains commonly only show zonation patterns parallel to their present length direction (fig 5.19a) and only rarely include pyramidal tips in growth zonation, indicating they represent fragments of larger relatively acicular crystals. Grains are commonly fractured, where one grain shows fractures in the core of zircon that do not propagate in a neocrystallised rim (fig. 5.19b)
The second, fine-grained population is an order of magnitude smaller, ranging from moderately equigranular habits, at ~30 µm length and ~10 µm width, to acicular habits, at ~100 µm length and ~10 µm width. The crystals are commonly anhedral and/or skeletal (fig. 5.19c). No clear internal textures could be observed, and some crystals show strong alteration along cracks (fig. 5.19d).

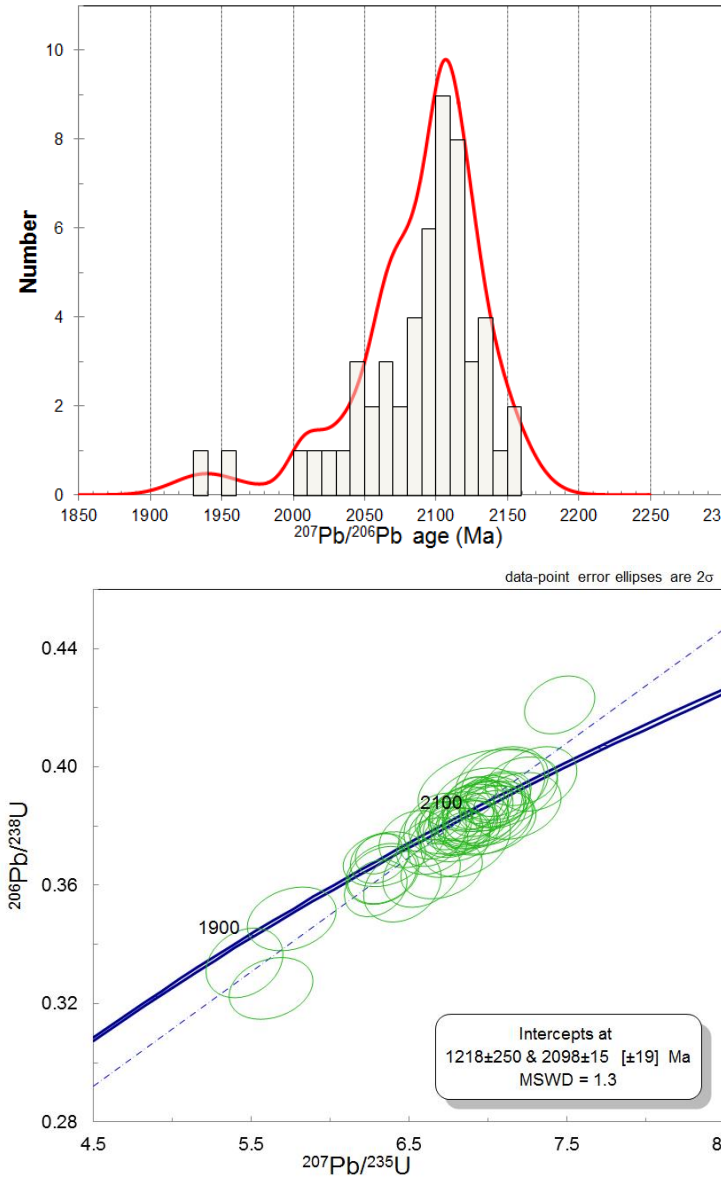

Figure 5.20. Above: Probability density plot and histogram for the $^{207}Pb/^{206}Pb$ results. Below: Concordia diagram with error ellipses of all results.

BU13
The automatic scan resulted in a single zircon population and no baddeleyite. Zircons from BU13 are generally brighter in BSE images than zircons from sample BU10a. In thin section, zircon is associated with other accessory minerals such as apatite and titanite which indicates a primary magmatic origin from locally enriched melt (fig. 5.19e and f). The habit is generally subhedral to rounded, with crystal sizes up to ~150 µm in length and 50 – 100 µm (fig. 5.19g and h). The zircons are characterized by very little internal structure or zoning, as BSE images yield strongly homogeneous grains and only some crystals show faint zones which could indicate compositional zoning (fig. 5.19g and h). Most crystals are intact, while a small fraction of the separated zircon shows extensive fracturing. No resorption boundaries are visible as crystal faces are commonly straight.

5.4.3 U-Pb age results

U-Pb zircon age results have been plotted in figure 5.20.
The Pb-Pb ages show an almost perfect normal distribution with a peak at 2107 Ma. The younger side of the distribution shows a slightly more gradual decrease, indicating the presence of 2050-2070 ages.
The U-Pb concordia shows very little discordance, as most analyses are within error of the Concordia line. Three analyses form a normal

discordant cluster and one analysis is reverse discordant. The discordance age of 2098 ± 15 Ma with an MSWD of 1.3 is in good agreement with the Pb-Pb age peak.

5.4.4 Discussion

The age of metadolerite dykes in the UHT granulites

Given the resorption textures and fragmented zonation pattern textures in the coarse grained zircon population of sample BU10a, they are interpreted to reflect xenocrysts, rather than indicating primary crystallisation of the dyke or its amphibolite facies metamorphism. A primary crystallisation origin for zircon of this size in a dyke is highly unlikely and requires strong enrichment in zirconium, equivalent of a more felsic magma such as the Kabalebo charnockites in the south of the Bakhuis belt. This is inconsistent with the multi element variation patterns of BU10a, where HFSE are relatively depleted with respect to patterns of the Kabalebo charnockites (Klaver et al., 2015). However, addition of xenocrystic zircon due to contamination with hosting granulites is consistent with the slightly elevated REE and multi element variation patterns of dyke BU10a compared to the other metadolerite dykes. Additionally, the CIPW norm of BU10a (see section 5.2) contains about ~25% olivine, indicating silica poor conditions and baddeleyite is expected to crystallise instead of zircon. This indicates that the second, fine-grained (tens of microns) population zircon is not primary but could be formed as the result of breakdown of xenocrystic zircon. Consequently, this generation could yield an age similar to the intrusion of the dyke. However, it seems more likely that (Roever et al., 2003) separated the coarse grained xenocrystic zircon as the fine-grained population is too small to pick up in conventional mineral separation techniques. Their 2056 ± 4 Ma and 2060 ± 4 Ma ages are thus re-interpreted to reflect UHT metamorphism in the hosting granulites, which are the likely source for xenocrystic zircon. This is consistent with what is suggested in (Klaver et al., 2015). Although there are no absolute ages for the metadolerite dykes, a probable estimation of their age can be made. Based on their geochemical with the Moi-Moi metagabbro, indicating a subduction origin, there are most likely an early phase of ~1.97-1.99 Ga mafic plutonism.

The age and significance of the gabbroic granulite

The euhedral to subhedral equigranular habit of the zircon and especially its association with other accessory phases such as apatite and ilmenite, indicate that the zircon is of a primary origin. Weak oscillatory zoning, typical for a magmatic origin, is preserved in some of the grains but has most likely been obscured by metamorphism for the bulk of the grains. A primary origin for zircon is consistent with the occurrence of zircon in MORB-type magmas described for other settings (Grimes et al., 2007; Stepanova et al., 2014).

The 2098 ± 15 Ma U-Pb age is thus interpreted as a magmatic age. The tendency of the Pb-Pb distribution towards younger ages, if not a statistical artefact, could be interpreted as the effect of minor resetting during subsequent UHT granulite metamorphism. The 2098 ± 15 Ma for the gabbroic granulite body is significantly older than, yet relatively close to the 2060-2075 Ma range in ages for peak metamorphism recorded in the associated UHT granulites (Nanne, 2013). This is another argument against a metamorphic age, as UHT metamorphism has been temporally homogeneous over the Bakhuis belt at ~2070 Ma.

Previously obtained U-Pb zircon granulite protolith ages of 2130 ± 11 Ma have been interpreted as detrital grains from the surrounding TTG-Greenstone belt (Nanne, 2013). With a magmatic protolith age predating UHT granulite metamorphism by only about ~20 Ma, the gabbroic granulite provides a unique opportunity to determine the conditions leading up to UHT metamorphism in the Bakhuis Belt. Regretfully, no geochemistry or isotope dilution was performed for samples of the body in this study. However, sample MKS 42 was taken from the same body by Martijn Klaver in 2010 and analysed for major and trace element geochemistry, as well as strontium and neodymium isotopic variation although not by isotope dilution. Some of the results are presented in plots in his thesis (Klaver, 2011) but the data is hardly described or discussed. The next section briefly describes and discusses the results of MKS42, based on data from the appendices to Klaver (2011). Initial neodymium and strontium ratios have been recalculated to an intrusion age of 2098 Ma. The geodynamic significance of the gabbroic granulite and its relationship to UHT metamorphism is discussed in section 6.1.

Geochemistry and interpretation of MKS42

Major elements indicate a mafic chemistry with low silica contents (47.7%), yet comparatively low magnesium (6.5%) and high iron (15.37%) and manganese (0.22%) contents, resulting in a low Mg# (45.6). Potassium (0.44%) and aluminium (14.05%) contents are low while titanium (1.66%), calcium (10.96%) and sodium (2.44%) are relatively high.

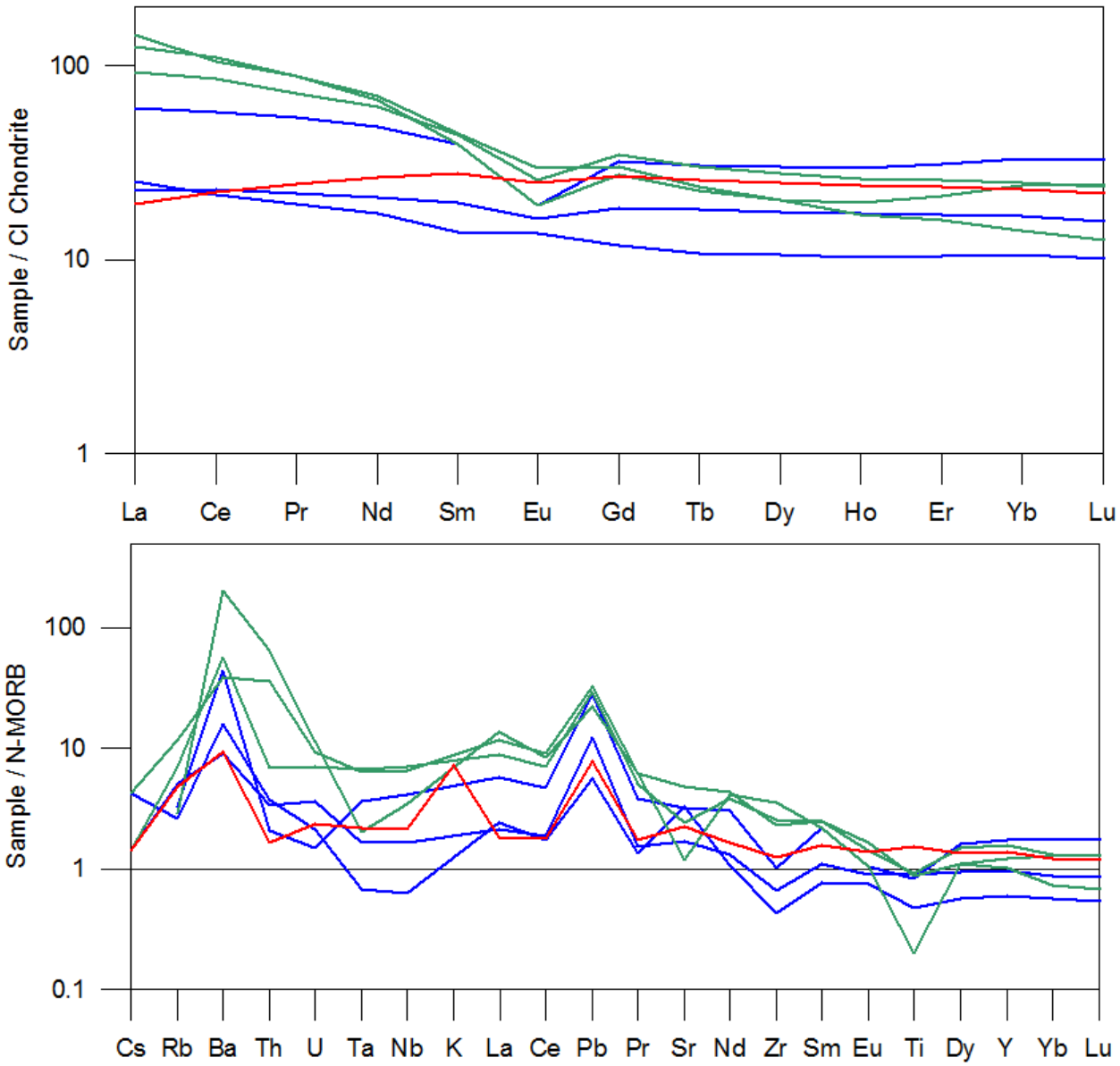

Figure 5.21. Trace element and REE geochemistry for MKS 42 and the other granulites. Data is taken from the appendices to Klaver (2011). Blue patterns for the mafic granulites, green patterns for the intermediate granulites. Sample MKS42 is the red pattern. Above: REE diagram normalised over CI chondrite (McDonough and Sun, 1995). Below: A multi element variation diagram with values normalised over N-MORB (Sun and McDonough, 1989).

Compatible trace elements are comparatively low, except for vanadium (~400 ppm), which is consistent with the high titanium content. LILE concentrations are very low. However, these concentrations can easily be influenced by metamorphism or migmatisation. HFSE are high, especially hafnium (4.87 ppm) and zirconium (73.36 ppm).

The REE and multi element variation patterns are plotted in figure 5.21. The REE pattern is weakly positive (La/Yb ~ 0.83). The positive pattern is expressed in a positive slope for the LREE (La/Sm ~ 0.69), while HREE show a weakly negative slope (Dy/Lu ~ 1.14). No europium anomaly is visible. The positive slope separates the gabbroic granulite from the other mafic granulites, which all show a negative slope and are generally more enriched (Klaver, 2011). The flat enriched pattern is typical for MORB-type magmas. The MORB pattern is also expressed in the multi element variation pattern normalised to N-MORB. Weak positive lead, strontium and rubidium-barium anomalies form the exception to an otherwise completely flat pattern, close to normalised values of 1. No niobium or tantalum anomaly is observed, which is common for the other mafic granulites (fig. 5.21).

Initial value for neodymium for MKS42 is slightly higher than the mafic granulites (fig. 5.22), while the initial strontium values overlap with the mafic granulites. The evolution from initial εNd_{2098} value (2.13 ±

2) towards the present day εNd_0 value (4.33) is positive, consistent with the positive LREE slope which shows a superchondritic Sm/Nd ratio. The positive Sm/Nd ratio generates no intersect with the depleted mantle evolution line of DePaolo (1981). However, the initial εNd_{2098} value of 2.13 is relatively close to his depleted mantle value at 2098 Ma of 3.21. The low initial $^{87}Sr/^{86}Sr$ ratio (0.7019182) and the negative evolution of the ratio also indicate a depleted mantle origin. However, this could be an artefact of an altered Rb/Sr ratio during UHT metamorphism and migmatisation.

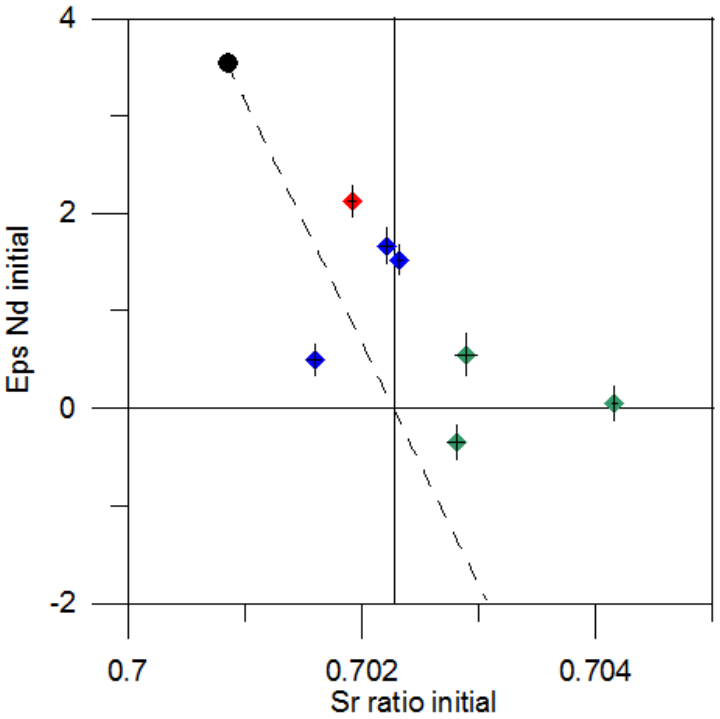

Figure 5.22. Plot of initial εNd_{2098} vs $^{87}Sr/^{86}Sr_{2098}$ ratios for sample MKS42 (red diamond) compared to other mafic granulites (blue diamonds) and intermediate granulites (green diamonds). All data taken from Klaver (2011), initial values have been recalculated to a 2098 Ma age.

6. Discussion

6.1 Relationships of the mafic igneous intrusions

6.1.1 Mafic plutonic bodies

Significance of hornblende in the Moi-Moi metagabbro

The petrographic and mineral chemical data presented in section 4.1 show that the poikilitic hornblende occurring in the Moi-Moi metagabbro is formed by both primary crystallisation as an intercumulus phase (group 1 textures) or as late primary phase, as the result of a reaction between olivine and pyroxenes and an evolved hydrous liquid to form hornblende (group 2 textures). The two different processes for hornblende formation indicate that the different occurrences reflect samples from varied parts of magmatic evolution of the Moi-Moi metagabbro. This provides further evidence for the strong fractionation and accumulation processes that have affected the suite, as described by Thijssen (2015).

To crystallise hornblende as a primary phase, the magma must contain significant amounts of water. The presence of significant amounts of water in the magma is consistent with the interpretation of Thijssen (2015), that the suite belongs to an Alaskan-type complex which is commonly associated with the root zones of volcanic arcs (e.g. Beard, 1986).

The relationship between Mozeskreek anorthosite and other mafic bodies

Several indications are interpreted to reflect a common parental magma for the Mozeskreek Anorthosite with the Moi-Moi metagabbro: 1) Overlapping or closely approximating geochemistry in most major and compatible elements, including a common subduction signature. 2) The granular metamorphic texture. 3) The presence of water in the magma as indicated by intercumulus and poikilitic hornblende. 4) The common U-Pb zircon age around 1980 Ma for both types of bodies (de Roever et al., 2003b; Thijssen, 2015). Geochemical differences with the Moi-Moi metagabbro, such as low contents for rubidium and barium are interpreted to reflect plagioclase accumulation processes. The hafnium and neodymium data neither confirms nor denies a relationship with the Moi-Moi metagabbro, as only one sample was analysed. While, the single data point plots off of a hypothetical range in Moi-Moi metagabbro ranges corrected for mixing with the Kabalebo charnockites, that range is still within the relatively large hafnium error of the single data point.

The introduction of water to form intercumulus and poikilitic hornblende is interpreted to occur in a late stage of anorthosite crystallisation, given the magmatic breccia shown in figure 4.5c, where anorthosite clasts occur in a gabbroic matrix which locally contains cm-sized hornblende crystals. Based on these relationships, the Mozeskreek anorthosite can be interpreted to reflect an early, anhydrous phase of the Moi-Moi metagabbro parental magma.

The formation of the Mozeskreek anorthosite is interpreted following the model for Proterozoic massif-type anorthosites of Ashwal (1993), where lower density plagioclase-rich crystal mushes rise up in the crust and further crystallise as a pluton. Although the presence of other bauxite caps nearby in the belt could indicate other occurrences of anorthosites, the relative scarcity of anorthosite bodies in the Bakhuis belt is interpreted to be the result of high water contents in the parental magma, which suppressed plagioclase crystallisation (Sisson and Grove, 1993). The presence of the anorthosite bodies further indicates that the ~1.97-1.99 magmatic event is associated with a major event of magmatic differentiation. It is commonly assumed that formation of Proterozoic massif-type complexes occurs in a relatively stabilised tectonic regime void of large scale continued lower crustal deformation such as a post-collisional setting, where a parental magma has the time to fractionate (Ashwal, 1993; Ashwal, 2010; McLelland et al., 2010).

Relationship between the Charlie gabbro and Moi-Moi metagabbro events

While the Charlie gabbro and Moi-Moi metagabbro U-Pb baddeleyite and zircon dating results in ages that are mutually within error, Thijssen (2015) argues based on field relationships, petrography and geochemistry that they reflect two separate magmatic events. The hydrous Moi-Moi metagabbro is interpreted to reflect an Alaskan-type cumulate complex, which are commonly interpreted as the root zones of volcanic arcs (Batanova et al., 2005; Dhuime et al., 2009; Irvine, 1974; Jagoutz and Schmidt, 2013; Spandler et al., 2003). The anhydrous Charlie gabbro displays the geochemistry of a high alumina basalt (HAB) magma and is interpreted as a tholeiitic event which is correlated in age to three dyke swarms in

central Venezuela. The latter dykes were suggested by Ibanez-Mejia (pers. comm.) to be part of a Large Igneous Province, formed by asthenospheric upwelling or a mantle plume (Thijssen, 2015).
The interpretation of two separate events is consistent with the radiogenic isotope study in this thesis. The hafnium and neodymium data for the Moi-Moi metagabbro show a steep positive trend, which is interpreted to reflect various amounts of magma mixing with the Kabalebo charnockites. Calculating a mixing model following DePaolo and Wasserburg (1979) resulted in mixing percentages of up to 11-12%. Magma mixing is consistent with geochemical and petrographic indications of Klaver et al. (2015) and the hypothesis that zircon crystals could be transferred from the Kabalebo charnockites to the Moi-Moi metagabbro (Klaver et al., *in press*). When the data is corrected for mixing, Moi-Moi metagabbro forms a cluster around $\varepsilon Nd_{1980} \sim 1$ and $\varepsilon Hf_{1980} \sim 8$. The Charlie gabbro does not show a mixing trend and cluster around slightly higher εNd_{1980} of ~ 1.2 and lower εHf_{1980} of ~ 5. The difference in unmixed initial values provides evidence for a differences mantle source and magmatic evolution for both magmatic events.
While field and petrographic evidence shows that the Charlie gabbro is younger than the Moi-Moi metagabbro, the U-Pb zircon and baddeleyite ages are mutually within error (Thijssen, 2015), indicating the magmatic events closely followed each other. Therefore, evidence that the two magmatic bodies have a different mantle origin has important implications for the ~1.97-1.99 Ga magmatic event. The significance of this observation is discussed in section 6.2.2.

6.1.2 Metadolerite dykes and small intrusive bodies

Metadolerite dykes in granulites and Kabalebo charnockites
Based on the similar amphibolitic petrography, overlapping geochemistry and an overlapping range in hafnium and neodymium isotope compositions, the metadolerites in the Kabalebo charnockites are interpreted to be derived from the same parental magma as the Moi-Moi metagabbro. The metadolerites show a stronger enrichment in REE than the Moi-Moi metagabbro, which is interpreted as indicating the dykes are derived from a more evolved parental magma after crystallisation of the Moi-Moi metagabbro. The initial values of the metadolerites in the Kabalebo charnockites all plot around the Moi-Moi metagabbro end member values of $\varepsilon Nd_{1980} \sim 1$ and $\varepsilon Hf_{1980} \sim 8$, without variation between dykes and xenoliths in the charnockites.
While the dykes in the granulites also have a similar amphibolitic petrography and a largely overlapping geochemistry, the neodymium and hafnium isotopes do not provide conclusive evidence for a similar or different origin with the Moi-Moi metagabbro.
One sample (BU10a) shows overlapping neodymium and strontium values, but strongly deviating neodymium values. Given the indications for contamination in REE and multi element variation patterns and the evidence for xenocrystic zircon in the sample, the deviating values cannot be interpreted as evidence for either a similar or a different origin for the dyke. The other sample (BU09) plots on the mixing line between the Moi-Moi metagabbro and the Kabalebo charnockites, which is odd as there are no known nearby occurrence of charnockites. Consequently, the values could indicate a different source and identity for the dykes. Alternatively, the sample could also have been contaminated by charnockites in the subsurface or by the hosting granulites. The hosting granulites have similar initial neodymium values of ~-1 – 0 as the charnockites (Klaver et al., 2015), and possibly have similar hafnium initial values, as the values for the charnockites could be directly inherited from the granulites during melting. Consequently, a definitive relationship or difference between the dykes and the Moi-Moi metagabbro cannot be determined.
Re-examination of zircon habit and textures in sample BU10a indicated that the zircon must be xenocrystic, derived from the hosting granulites. This indicates the 2056 ± 4 Ma and 2060 ± 4 Ma ages found by de Roever et al. (2003b) do not reflect primary crystallisation in the metadolerite but more likely UHT metamorphism in the hosting granulites. Consequently, the field relationships provide the only constraints on their possible age, which should be younger than UHT metamorphism (2050 Ma) and older than intrusion of the Charlie gabbro (1970 Ma). As they show a similar subduction signature in geochemistry, their age is most likely closer to the age of the Moi-Moi metagabbro (1980 Ma) than the age of UHT metamorphism, which is interpreted to have occurred in a regime of crustal stretching (Delor et al., 2003b). Consequently, there is no evidence for a generation of dykes which can be related to UHT metamorphism.

Dolerite dykes in the Charlie gabbro
Based on the overlapping geochemistry and the dolerite dykes in the Charlie gabbro are interpreted to be derived from the same parental magma body as the hosting Charlie gabbro, reflecting a later magmatic pulse.

Dyke in the Mozeskreek anorthosite
Based on the overlapping geochemistry, the single analysed dyke in the Mozeskreek anorthosite is interpreted to belong to the same parental magma as its hosting body. As the Mozeskreek anorthosite is dominantly a cumulate body, the dyke provides better constraints on the parental magma composition than the anorthosite. Given that this dyke is also in good geochemical overlap with the Moi-Moi metagabbro, this provides further indications that the dyke and the Mozeskreek anorthosites are derived from the same parental magma as the Moi-Moi metagabbro.

Gabbroic granulite
Given the 2098 ± 15 Ma U-Pb zircon age for the gabbroic granulite, it is interpreted as a pre-metamorphic rather than syn-metamorphic mafic magmatic body. The geochemistry of the body as described by (Klaver, 2011) is consistent with a typical MORB-magma, with minor enrichments for barium, rubidium, potassium and lead, indicating a role for K-feldspar. Additionally, the strontium and neodymium data indicate a depleted mantle origin. The significance of primitive mafic magmatism in the granulites ~25 Ma before UHT metamorphism is discussed in section 6.2.1.

6.2 Geodynamic implications

In this section, the geodynamic implications of the data are placed in a regional framework. The data is discussed chronologically, starting with ~2.07 Ga UHT metamorphism followed by ~1.97-1.99 Ga mafic magmatism.

6.2.1 ~2.07 Ga UHT metamorphism

Significance of the gabbroic granulite
The 2098 ± 15 Ma age for a MORB-type mafic granulite provides new constraints on the protolith for UHT metamorphism and the conditions leading up to UHT metamorphism. A similar age of 2092 Ma +- 32 Ma was found for the core of an inherited crystal in the Moi-Moi metagabbro by Thijssen (2015), showing a similar U-Pb discordance as BU13. Due to the large errors on the data, the inherited CL-bright cores were interpreted to reflect UHT metamorphism in the granulites. In the light of the age of BU13, it is possible that the cores represent a similar ~2.1 Ga magmatic protolith age.
The protolith of the Bakhuis belt is interpreted as a supracrustal suite of metasedimentary to metavolcanic igneous rocks, with Nd model ages ranging between 2.19 – 2.40 Ga (de Roever et al., 2003b). Previously obtained U-Pb monazite and zircon Bakhuis granulite protolith ages or inherited grains in magmatic rocks range between 2110 – 2150 and have been interpreted as detrital crystals from the surrounding TTG-Greenstone belt (Klaver et al., 2015; Nanne, 2013). The 2098 ± 15 Ma provides the first absolute constraint on the age of formation of the protolith. Additionally, the MORB-type composition and strongly depleted initial neodymium value indicate a primitive, oceanic affinity of the protolith.
Formation of oceanic crust below the TTG-greenstone belt is constrained to 2.26 – 2.20 Ga, which is significantly older than the age of the gabbroic granulite. The formation of the TTG-greenstone belts surrounding the Bakhuis belt is considered as between 2.18 – 2.12 Ga (Delor et al., 2003b). The youngest age for the TTG-greenstone belt is obtained by Norcross et al. (2000), who dated metavolcanics in Guyana to a U-Pb zircon age of 2120 ± 2 Ma. It is unlikely that the gabbroic granulite reflects a younger metavolcanic rock formed in the same period of TTG-greenstone formation, as after 2120 Ma the tectonic setting is considered to change dramatically. The interval between 2.11 – 2.08 Ga is considered to be a period of major granitic plutonism coeval with sinistral 'sliding' and the formation of pull-apart basins, eventually leading to asthenospheric upwelling and UHT metamorphism in the Bakhuis belt (Delor et al., 2003b). The extensive granitic plutonism is considered to be the result of melting of the TTG-greenstones, and presently no primitive, MORB-type plutonism is presently documented around ~2100 Ma elsewhere in the shield. Consequently, it is interpreted that the Bakhuis belt constituted a separate tectonic entity since at least ~2100 Ma. The primitive MORB-type magma is interpreted to reflect formation of a narrow rift or even a narrow oceanic basin in between the TTG-greenstones belts.

UHT Metamorphism
Initially, it was thought that the UHT metamorphism saw considerable coeval magmatism. In the first paper on UHT metamorphism in the Bakhuis belt, de Roever et al. (2003b) assumed both the Kabalebo charnockites in the southwest and the widespread occurring metadolerite dykes were coeval to UHT metamorphism. As it was recently shown, the Kabalebo charnockites are considerably younger and belong to the ~1.97-1.99 Ga plutonic event (Klaver, 2011; Klaver et al., 2015). All presently described and

analysed mafic bodies in Thijssen (2015) and this thesis are also interpreted to belong to the same ~1.97-1.99 Ma magmatic event and thus are considered to be unrelated to UHT metamorphism. Although it is possible that there are undiscovered syn-metamorphic magmatic bodies hidden in the dense jungle of the Bakhuis belt, the scenario that the UHT metamorphic event did not see coeval mafic magmatism becomes quite plausible.
In the model of Delor et al. (2003b), UHT metamorphism is proposed to be the result of sinistral crustal stretching, which causes upwelling of the asthenosphere in the Bakhuis belt, forming a narrow zone in between two continental-scale TTG-greenstone boudins. The intrusion of the gabbroic granulite at 2.10 possibly indicates the crustal thinning process already started in an early phase of sinistral stretching. While this model seems the most likely of the models presented in section 1.2.4, there is no direct supporting evidence and the exact tectonic setting and the heat source for UHT metamorphism remain unconstrained.

6.2.2 ~1.97-1.99 Ga magmatic event

The ~1.97-1.99 Ga magmatic event in the Bakhuis belt has been shown to be very complex and consist of at least 2 generations of mafic magmatism with associated (meta)dolerite dykes, one of which resulted in melting of UHT granulites to form charnockites and a phase of amphibolite facies metamorphism. (Klaver, 2011; Klaver et al., 2015; Klaver et al., in press; Thijssen, 2015). This phase was interpreted as a second 'UHT-like' event by Klaver et al. (2015). In this thesis, the event is referred to as the ~1.97-1.99 Ga magmatic event as there is no evidence for UHT metamorphic conditions.

First phase: Moi-Moi metagabbro, charnockite formation and the Mozeskreek anorthosite

The first phase of mafic magmatism consists of intrusion of the Moi-Moi metagabbro, which are interpreted as an Alaskan-type cumulate complex which is commonly associated with the root zones of arcs. Abundant primary magmatic hornblende crystals provide evidence for significant amounts of water in the magma, which is interpreted as the result of melting of a hydrous, subduction-metasomatised mantle. As shown in this thesis, associated metadolerite dykes of up to ~1 m thick are common in the granulites. The heat from this magmatic phase is interpreted as the heat source for melting of the granulites to form the Kabalebo charnockites in the southwest of the Bakhuis belt (Klaver et al., 2015), which is evidenced in this thesis by a magma mixing trend between the Moi-Moi metagabbro and the Kabalebo charnockite. Lastly, the Mozeskreek anorthosite is interpreted to be part of this magmatic phase and represents a plagioclase-rich crystal mush derived from the same parental magma. The wealth of magmatic activity and melting processes indicates this phase constitutes a period of major magmatic underplating associated with considerable heat production.
Numerous (poikilitic and intercumulus) hornblende-bearing mafic-ultramafic bodies similar to the Moi-Moi metagabbro have been described for western Suriname, indicating the Moi-Moi metagabbro extends over a significant portion of the CSID-belt. Within the CSID-belt, these bodies are coeval with widespread felsic volcanism and subvolcanic granitoid intrusions (de Roever et al., 2010; Delor et al., 2003b; Nadeau et al., 2013; Reis et al., 2000). The metavolcanic series show open folding, indicating Transamazonian orogeny was still active. More importantly, amphibolite to granulite facies metamorphism in the Cauarane-Coeroeni Belt to the south has recently also been constrained to 2.01 – 1.98 Ga (Fraga et al., 2009a). The association of metamorphism and magmatic activity is interpreted to reflect initiation of northward subduction to the south of the greenstone belt, suggesting that convergence and collision in the Transamazonian orogeny continued until at least 1.98 Ga (Fraga et al., 2009a; Fraga et al., 2009b; Klaver et al., 2015). The petrographical and geochemical evidence for Alaskan-type complexes in Thijssen (2015) and the evidence for a hydrous magmatic phase as indicated by primary hornblende in this thesis provide the first direct indications for the inferred subduction setting during the ~1.97-1.99 Ga magmatic phase.

Second phase: HAB-type Charlie gabbro

The second phase of magmatism constitutes the intrusion of the anhydrous Charlie gabbro in the Bakhuis belt, which shows a HAB-type geochemistry (Thijssen, 2015). As shown in this thesis, the Charlie gabbro is derived from a different mantle source than the Moi-Moi metagabbro. Additionally, the Charlie gabbro bodies are cut by dolerite dykes, which are interpreted to represent a later stage of the same magmatic event. The different mantle source for temporally very close magmatic events provides the first evidence for a radical change in tectonic regime during the ~1.97-1.99 plutonic event.
In Thijssen (2015), this event is interpreted to reflect the transition from subduction to slab detachment, resulting in upwelling of the asthenosphere through the downgoing slab. The interpretation of upwelling of the asthenosphere is used to explain the transition of hydrous melting to dry melting and is consistent

with the contrasting neodymium and hafnium values for the Charlie gabbro and the Moi-Moi metagabbro found in this thesis.
The HAB-type magma of the Charlie gabbro has presently only been discovered in the Bakhuis belt. In the surrounding CSID-belt, the period after 1.98 Ga is characterised by intrusion of e.g., muscovite-biotite granite around 1.97 Ga and biotite granites around 1.95 Ga (Kroonenberg and de Roever, 2010), which probably represents the lateral equivalents of 1.97-1.96 Ga collisional I-type and S-type granites in Roraima, Brazil (Almeida et al., 2007; Reis et al., 2000). Southward in the Cauarane–Coeroeni belt, a second pulse of high grade metamorphism and migmatisation is recorded at 1.99 – 1.97 (Fraga et al., 2009b; Kroonenberg and de Roever, 2010; Nadeau et al., 2013). Additionally, abundant post-collisional <1.90 Ga granitoids occur south of the belt (Fraga et al., 2008). All of these constraints indicate a major phase of collision south of the Bakhuis belt starting at ~1.97 Ga and are consistent with a model of slab detachment as the origin for the HAB-magmas of the Charlie gabbro in the Bakhuis belt.

Amphibolite facies metamorphism
A puzzling component of the ~1.97-1.99 Ga plutonic event is amphibolite facies metamorphism, which is only shown by the first generation of ~1.97-1.99 magmatic rocks (Moi-Moi metagabbro, Mozeskreek anorthosite and metadolerite dykes). The absence of amphibolite facies metamorphism in the Charlie gabbro provides a limiting constraint on the age of ~1970 ± 17 Ma. A late phase of static amphibolite facies metamorphism forming granoblastic recrystallization is widely present in the granulites (as for example shown for BU12 and BU13 in section 5.1.1), but dating of the phase is difficult. It is possible that this phase occurred at 1.98 Ga and represents the same phase that has influenced the Moi-Moi metagabbro.
There are several indications for a regional character of this phase of metamorphism. The CSID-belt surrounding the Bakhuis contains a folded (low-grade) metavolcanic sequence of 1.98 – 1.99 Ga (de Roever et al., 2010). Additionally, the Cauarane – Coeroeni belt to the south records amphibolite to granulite facies metamorphism in the interval of 2.01 – 1.98 Ga, which is split in a first phase of granulite metamorphism at 2.01 – 1.99 Ga showing intense folding and migmatisation and a second phase of 1.99 – 1.97 Ga static metamorphism (Fraga et al., 2009b), where the letter is very similar to the static metamorphism in the Bakhuis belt. The Cauarane – Coeroeni belt is also intruded by unmetamorphosed granites around 1.98-1.97 Ga. As sample EG1665 is taken from the Coeroeni gneiss, that belt was also intruded by Moi-Moi-type metagabbro in its late evolution. All these indications are interpreted to reflect a regional phase of static amphibolite facies metamorphism in the entire CSID-belt and surroundings closely following major collision as recorded by metamorphism in the Cauarane – Coeroeni belt. The static character of this amphibolite facies and the wealth of magmatism recorded in- and outside the Bakhuis belt are interpreted to reflect a period of major magmatic underplating in the interval of 1.99 – 1.97 Ga.

7. Concluding remarks

7.1 Conclusions

Poikilitic hornblende crystals in the Moi-Moi metagabbro are petrographically grouped in two categories: 1) Poikilitic hornblende with inclusions of olivine, pyroxene and plagioclase which are interpreted to reflect primary, intercumulus hornblende and 2) poikilitic hornblende with inclusions of plagioclase and no or only fragmented, embayed crystals of pyroxene and olivine. The latter group is interpreted to have formed by a late primary reaction between olivine and pyroxenes and an evolved hydrous melt. Both groups show an Al^{IV}/Al^{VI} partitioning typical of a primary magmatic origin. Hornblendes in samples from the Bakhuis belt have consistently lower Ti contents, which is interpreted as the effect of exsolution in observable Ti-Fe oxides during amphibolite facies metamorphism. The presence of primary hornblende in the Moi-Moi metagabbro provides evidence for a hydrous magmatic origin, which is consistent with the subduction signature shown for the samples (Thijssen, 2015).
The Mozeskreek anorthosite is a 3 x 4 km body of layered anorthosites to (leuco)gabbros and shows several indications for a similar origin to the Moi-Moi metagabbro: 1) Overlapping or closely approximating geochemistry in most major and compatible elements, including a common subduction signature. 2) A granoblastic metamorphic texture. 3) The presence of water in the magma as indicated by intercumulus and poikilitic hornblende. 4) The common U-Pb zircon age around 1980 Ma for both types of bodies. Geochemical differences with the Moi-Moi metagabbro, such as low contents for rubidium and barium are interpreted to reflect plagioclase accumulation processes. Strontium, neodymium and hafnium isotope compositions for one sample did not confirm or deny a common mantle source with the Moi-Moi metagabbro. The anorthosite is interpreted to have formed following the model the for Proterozoic massif-type complexes, where the relative scarcity of anorthosites in the Bakhuis belt is interpreted as the result of the presence of water, which suppressed plagioclase crystallisation, in the parental magma.
In neodymium and hafnium isotopes the Moi-Moi metagabbro shows a steeply positive trend which can be explained by magma mixing with the Kabalebo charnockites. A mixing model resulted in mixing factors of up to ~11-12%. When the data of the Moi-Moi metagabbro is corrected for mixing, the data forms a cluster around $\varepsilon Nd_{1980} \sim 1$ and $\varepsilon Hf_{1980} \sim 8$, which differs significantly from the cluster for the Charlie gabbro at εNd_{1980} of ~ 1.2 and εHf_{1980} of ~ 5. This indicates a different mantle source for the two bodies, despite the relatively close U-Pb zircon ages of 1984 ± 4 and 1970 ± 17 Ma for the Moi-Moi metagabbro and the Charlie gabbro respectively (Thijssen, 2015). The close temporal association of the bodies that show a different source and magmatic evolution indicates a change in tectonic regime during the ~1.97 – 1.99 Ga magmatic event.

Metadolerites in the Kabalebo charnockites are pyroxene-amphibolites and occur as thin (dm-scale), continuous segments of several meters in length and as dm-sized xenoliths. The metadolerites show a typical geochemistry of subduction zone, overlapping with the chemistry and the cluster of unmixed strontium, neodymium and hafnium values of the Moi-Moi metagabbro. This indicates a common mantle source, which is consistent with the interpretation that the Moi-Moi magmatic event provided the heat source for melting of the granulites to produce the Kabalebo charnockites (Klaver et al., 2015; Klaver et al., *in press*).
Metadolerites in the UHT granulites occur as foliated and weakly folded pyroxene-amphibolite dykes of up to ~1 m thickness. Dyke geochemistry shows a typical subduction zone signature, similar to the Moi-Moi metagabbro. Due to contamination with the hosting granulites, the strontium, neodymium and hafnium isotopes could not be used to infer a different or similar mantle source as the Moi-Moi metagabbro. Zircon for one of the dykes was interpreted to be xenocrystic, derived from the hosting granulites, indicating the 2070 Ma age obtained by de Roever et al. (2003b) reflects UHT metamorphism in the hosting granulites rather than the age of dyke crystallization. Given the subduction zone geochemistry, an age and relationship close to the ~1.97 – 1.99 is considered to be more likely
(Meta)dolerite dykes in the Charlie gabbro and the Mozeskreek anorthosite show a similar geochemistry to their hosting mafic bodies. The strontium, neodymium and hafnium values for one dolerite dyke in the Charlie gabbro plot close to, but outside the range of the Charlie gabbro. Based on the lack of petrographic and geochemical similarities, the dyke could not be correlated to one of the later dyke swarms and is interpreted as a late phase of the Charlie gabbro parental magma.
A U-Pb zircon age of 2098 ± 15 Ma was obtained for a gabbroic granulite body at Blanche Marie falls, which was interpreted as a primary crystallisation protolith age, based on the association of zircon with other accessory phases. The body shows a typical MORB-type geochemistry and radiogenic isotopes indicate a depleted mantle origin. At present, no other ~2.10 Ga MORB-type bodies have been described

for the Bakhuis belt or the TTG-greenstones of the Guiana shield. The body is interpreted to indicate the Bakhuis belt formed a separated tectonic entity since at least 2.10, possible a narrow rift basin or a narrow developing oceanic basin.

None of the presently analyzed magmatic bodies in the Bakhuis belt show evidence for a relationship with UHT metamorphism. Although it is possible that there are undiscovered syn-metamorphic magmatic bodies hidden in the dense jungle of the Bakhuis belt, the scenario that the UHT metamorphic event did not see coeval mafic magmatism becomes quite plausible. Consequently, the exact tectonic setting and the heat source for UHT metamorphism remain unconstrained.
Together, Thijssen (2015) and this thesis form a comprehensive study of magmatism during the 1.97 – 1.99 Ga magmatic event in the Bakhuis belt. The event is separated in two phases. The first phase constitutes a period of major hydrous magmatic underplating, resulting in the intrusion of the hydrous Moi-Moi metagabbro, the Mozeskreek anorthosite and melting of intermediate granulites to form the Kabalebo charnockites. The Moi-Moi metagabbro is interpreted to reflect an Alaskan-type cumulate complex, commonly associated with the root zone of an arc. The first phase is associated with regional amphibolite facies metamorphism in the Bakhuis belt and the surrounding CSID and Cauarane – Coeroeni belts, which provide further indications for the regional scale of the first magmatic phase. The second phase of magmatism is formed by the intrusion of the anhydrous Charlie gabbro, which shows a HAB-type geochemistry. The body is presently only discovered in the Bakhuis belt, but can be correlated to collisional I-type and S-type granitic plutons in the CSID-belt to the south. Consequently, the transition to anhydrous melting below the Bakhuis belt is interpreted to reflect slab detachment and associated asthenospheric upwelling, as the result of collision to the south.

7.2 Recommendations for further research

As the possibilities for investigating possible syn-metamorphic intrusive bodies seem to be exhausted, further research into UHT metamorphism in the Bakhuis belt require different pursuits.

- Firstly, more information could be derived on the protolith to UHT metamorphism. As shown in this thesis, at least part of the protolith is significantly different from the surrounding TTG-greenstone belts and a thorough investigation into the age, geochemistry and provenance of the protolith could provide important information about the conditions leading up to UHT metamorphism and the role of the Bakhuis belt in the Guiana shield in general.

- Secondly, more work could be done on determining the P-T path of metamorphism. While the extent and conditions of metamorphism have been thoroughly investigated by Nanne (2013), much less is known about the exact shape of the P-T path. Modelling mineral reactions which occur in the granulites the conditions should put more points on the P-T path which would provide important clues into the tectonic setting where UHT metamorphism has occurred.

The conditions and tectonic setting of the ~1.97-1.99 Ga magmatic event is still not well enough understood. Especially the geologically quick transition from hydrous arc-type complexes with anorthosites to anhydrous HAB-type magmatism is puzzling. The proposed model for slab detachment should be confirmed or denied by further investigating the age, geochemistry and isotope compositions of various magmatic bodies in the surrounding CSID-belt.

8. Acknowledgements

Firstly, I owe gratitude to my supervisors. First supervisor Emond de Roever is thanked for offering me this project and providing committed assistance throughout, either in organising logistics for the fieldwork, motivating me to perform my labwork, assisting me in forming interpretations of the data or acting as a walking encyclopaedic resource on the geology of the Guiana shield in general and the Bakhuis belt in particular. Fraukje Brouwer and Gareth Davies are sincerely thanked for finding time in their busy schedules to act as a VU supervisor and second assessor, respectively. Fraukje is additionally thanked for helping to smooth out communication in this project. Gareth is additionally thanked for a thorough discussion of the isotope dilution data. Martijn Klaver is thanked for coming up with the idea of performing isotope dilution to establish magma mixing. Also, Martijn is thanked for providing criticism on a first version of my interpretation of the isotope data and assistance in the lab, despite being very busy with his own PhD at the VU.

Several people have been instrumental in providing the logistics and lodging that were required for us to be able to perform fieldwork in the remote jungle of the Bakhuis belt. For the Kabalebo Nature Resort, Karel and Joyce Dawson are thanked for facilitating our special logistical wishes in the Kabalebo area and generously providing a discount on our stay because of their interest in science. Armida is thanked for organising the logistics and providing the information we need to set up the excursions into the jungle. In the field, Mr. Harderwijk and especially Mr. Jozef Jogi are thanked for acting as experienced guides and, when necessary, opening new pathways in the dense jungle to get us where we wanted to go. Norman Mac-Intosh is thanked for preparing and facilitating our 4-WD journey to the center of the Bakhuis. By setting up camp, cooking for us and taking general good care of us, he allowed us to put our full attention to performing the fieldwork itself. Also, the GMD of Suriname and especially M. Autar is thanked for providing permission to export the samples and allowing us to use some of the samples in the archives of the GMD.

For assisting me in my labwork, I owe gratitude to a large number of people. Bouk Lacet and Wynanda Koot are thanked for, removing weathered surfaces from the samples and preparing thin sections and mineral mounts. Sergej Matveev is thanked for helping me with the EMP hornblende and zircon analysis, instructing me how to make beads and pellets and taking care of the XRF analyses. Richard Smeets is thanked for instructions in the clean lab and on the chromatographic separations. Bas van der Wagt is thanked for performing ICP-MS analyses of the samples and helping me with the lutetium and hafnium analyses on Neptune. Matthijs van der Ven and Suzette Timmerman are thanked for help with making filaments and performing strontium, neodymium and hafnium TIMS analyses on both the old 262 machine and the Triton. Jasper Berndt is thanked for assistance with U-Pb analyses in Muenster, and for calculating and checking the data. However, I owe the most gratitude to Roel van Elsas, for performing zircon separation for the two samples in my project, while I was very busy on things he felt were more important to the earth science department.

This project would not have been possible without financial support from the Stichting Dr. Schürmann fund, the Stichting Molengraaff fund and the Faculty of Earth and Life Sciences (FALW), who covered the majority of the costs for performing fieldwork in Suriname and the costs for LA-ICP-MS analysis in Muenster.

Lastly, I want to thank my field buddy and tireless project fellow Inja Thijssen, for all the fun times during the fieldwork in Suriname and afterwards in the lab and during writing. Inja has been to a lot more trouble than necessary to get her project finished. I hope that in spite of this, she too will be able to look back at a satisfying master thesis.

9. References

Almeida, M.E., Macambira, M.J.B., Oliveira, E.C., 2007. Geochemistry and zircon geochronology of the I-type high-K calc-alkaline and S-type granitoid rocks from southeastern Roraima, Brazil: Orosirian collisional magmatism evidence (1.97–1.96 Ga) in central portion of Guyana Shield. Precambrian Research, 155(1–2): 69-97.

Andreoli, M.A.G., Hart, R.J., Ashwal, L.D., Coetzee, H., 2006. Correlations between U, Th Content and Metamorphic Grade in the Western Namaqualand Belt, South Africa, with Implications for Radioactive Heating of the Crust. Journal of Petrology, 47(6): 1095-1118.

Ashwal, L.D., 1993. Anorthosites. Springer-verlag, Berlin.

Ashwal, L.D., 2010. The temporality of anorthosites. The Canadian Mineralogist, 48(4): 711-728.

Avelar, V.G.d., Lafon, J.M., Delor, C., Guerrot, C., Lahondère, D., 2003. Archean crustal remnants in the easternmost part of the Guiana Shield: Pb-Pb and Sm-Nd geochronological evidence for Mesoarchean versus Neoarchean signatures. Géologie de la France, 2-3-4: 83-99.

Baier, J., Audétat, A., Keppler, H., 2008. The origin of the negative niobium tantalum anomaly in subduction zone magmas. Earth and Planetary Science Letters, 267(1–2): 290-300.

Batanova, V.G. et al., 2005. Crustal Evolution of Island-Arc Ultramafic Magma: Galmoenan Pyroxenite–Dunite Plutonic Complex, Koryak Highland (Far East Russia). Journal of Petrology, 46(7): 1345-1366.

Bea, F., 2012. The sources of energy for crustal melting and the geochemistry of heat-producing elements. Lithos, 153: 278-291.

Beard, J., Borgia, A., 1989. Temporal variation of mineralogy and petrology in cognate gabbroic enclaves at Arenal volcano, Costa Rica. Contributions to Mineralogy and Petrology, 103(1): 110-122.

Beard, J.S., 1986. Characteristic mineralogy of arc-related cumulate gabbros: Implications for the tectonic setting of gabbroic plutons and for andesite genesis. Geology, 14(10): 848-851.

Blichert-Toft, J., Chauvel, C., Albarède, F., 1997. Separation of Hf and Lu for high-precision isotope analysis of rock samples by magnetic sector-multiple collector ICP-MS. Contributions to Mineralogy and Petrology, 127(3): 248-260.

Bohlen, S.R., 1987. Pressure-Temperature-Time Paths and a Tectonic Model for the Evolution of Granulites. The Journal of Geology, 95(5): 617-632.

Bohlen, S.R., 1991. On the formation of granulites. Journal of Metamorphic Geology, 9(3): 223-229.

Bohlen, S.R., Mezger, K., 1989. Origin of Granulite Terranes and the Formation of the Lowermost Continental Crust. Science, 244(4902): 326-329.

Bosma, W., Kroonenberg, S.B., van Lissa, R.V., Maas, K., de Roever, E.W.F., 1984. An explanation to the geology of Suriname. Geol. Mijnb. Dienst Suriname, 27: 31-82.

Brandt, S., Will, T.M., Klemd, R., 2007. Magmatic loading in the proterozoic Epupa Complex, NW Namibia, as evidenced by ultrahigh-temperature sapphirine-bearing orthopyroxene–sillimanite–quartz granulites. Precambrian Research, 153(3–4): 143-178.

Brown, M., 1993. P–T–t evolution of orogenic belts and the causes of regional metamorphism. Journal of the Geological Society, 150(2): 227-241.

Brown, M., 1998a. Ridge-trench interactions and high-T-low-P metamorphism, with particular reference to the Cretaceous evolution of the Japanese Islands. Geological Society, London, Special Publications, 138(1): 137-169.

Brown, M., 1998b. Unpairing metamorphic belts: P–T paths and a tectonic model for the Ryoke Belt, southwest Japan. Journal of Metamorphic Geology, 16(1): 3-22.

Brown, M., 2006. Duality of thermal regimes is the distinctive characteristic of plate tectonics since the Neoarchean. Geology, 34(11): 961-964.

Brown, M., 2007. Metamorphic Conditions in Orogenic Belts: A Record of Secular Change. International Geology Review, 49(3): 193-234.

Chamberlain, C.P., Sonder, L.J., 1990. Heat-Producing Elements and the Thermal and Baric Patterns of Metamorphic Belts. Science, 250(4982): 763-769.

Clark, C., Fitzsimons, I.C.W., Healy, D., Harley, S.L., 2011. How Does the Continental Crust Get Really Hot? Elements, 7(4): 235-240.

Collins, W.J., 2002. Hot orogens, tectonic switching, and creation of continental crust. Geology, 30(6): 535-538.

Conrad, W.K., Kay, R.W., 1984. Ultramafic and Mafic Inclusions from Adak Island: Crystallization History, and Implications for the Nature of Primary Magmas and Crustal Evolution in the Aleutian Arc. Journal of Petrology, 25(1): 88-125.

Cordani, U.G., Fraga, L.M., Reis, N., Tassinari, C.C.G., Brito-Neves, B.B., 2010. On the origin and tectonic significance of the intra-plate events of Grenvillian-type age in South America: A discussion. Journal of South American Earth Sciences, 29(1): 143-159.
Costa, F., Dungan, M.A., Singer, B.S., 2002. Hornblende- and Phlogopite-Bearing Gabbroic Xenoliths from Volcán San Pedro (36°S), Chilean Andes: Evidence for Melt and Fluid Migration and Reactions in Subduction-Related Plutons. Journal of Petrology, 43(2): 219-241.
Currie, C.A., Hyndman, R.D., 2006. The thermal structure of subduction zone back arcs. Journal of Geophysical Research: Solid Earth, 111(B8): n/a-n/a.
da Rosa-Costa, L.T., Lafon, J.-M., Cocherie, A., Delor, C., 2008. Electron microprobe U–Th–Pb monazite dating of the Transamazonian metamorphic overprint on Archean rocks from the Amapá Block, southeastern Guiana Shield, Northern Brazil. Journal of South American Earth Sciences, 26(4): 445-462.
da Rosa-Costa, L.T., Lafon, J.M., Delor, C., 2006. Zircon geochronology and Sm–Nd isotopic study: Further constraints for the Archean and Paleoproterozoic geodynamical evolution of the southeastern Guiana Shield, north of Amazonian Craton, Brazil. Gondwana Research, 10(3–4): 277-300.
da Rosa-Costa, L.T., Monié, P., Lafon, J.-M., Arnaud, N.O., 2009. 40Ar–39Ar geochronology across Archean and Paleoproterozoic terranes from southeastern Guiana Shield (north of Amazonian Craton, Brazil): Evidence for contrasting cooling histories. Journal of South American Earth Sciences, 27(2–3): 113-128.
da Rosa-Costa, L.T. et al., 2003. Geology and geochronology of Archean and Paleoproterozoic domains of southwestern Amapá and northwestern Pará, Brazil, southeastern Guiana shield. Géologie de la France, 2-3-4: 101-120.
Dasgupta, S., Bose, S., Das, K., 2013. Tectonic evolution of the Eastern Ghats Belt, India. Precambrian Research, 227: 247-258.
Day, W.C. et al., 1997. Geology of the Lo Increible Mining District and U-Pb Age of the Early Proterozoic Yuruari Formation of the Pastora Supergroup, Guayana Shield, Venezuela US Geol. Surv. Open file Rep., 2124: E1-E13.
de Groot, K., 2008. Geothermo(baro)metry of ultrahightemperature metamorphism in the Bakhuis Mountain, Surinam., VU University Amsterdam.
de Roever, E.W.F., Kroonenberg, S.B., Delor, C., Phillips, D., 2003a. The Käyser dolerite, a Mesoproterozoic alkaline dyke suite from Suriname. Géologie de la France, 2-3-4: 161-174.
de Roever, E.W.F. et al., 2003b. The Bakhuis ultrahigh-temperature granulite belt (Suriname): I. petrological and geochronological evidence for a counterclockwise P-T path at 2.07-2.05 Ga. Géologie de la France, 2-3-4: 175-205.
de Roever, E.W.F., Lafon, J.M., Delor, C., Guerrot, C., 2010. Orosirian magmatism and metamorphism in Surinam: new geochronological constraints, 46th Congresso Brasileiro de Geologia, Belem, Brasil.
Deckart, K., Féraud, G., Bertrand, H., 1997. Age of Jurassic continental tholeiites of French Guyana, Surinam and Guinea: Implications for the initial opening of the Central Atlantic Ocean. Earth and Planetary Science Letters, 150(3–4): 205-220.
Deer, W.A., Howie, R.A., Zussman, J., 1992. An introduction to the rock-forming minerals. Longman Scientific & Technical.
Delor, C. et al., 2003a. Transamazonian crustal growth and reworking as revealed by the 1:500,000-scale geological map of French Guiana (2nd edition). Géologie de la France, 2-3-4: 5-57.
Delor, C. et al., 2003b. The Bakhuis ultrahigh-temperature granulite belt (Suriname): II. implications for late Transamazonian crustal stretching in a revised Guiana Shield framework. Géologie de la France, 2-3-4: 207-230.
DePaolo, D.J., 1981. Neodymium isotopes in the Colorado Front Range and crust-mantle evolution in the Proterozoic. Nature, 291(5812): 193-196.
DePaolo, D.J., Wasserburg, G.J., 1976. Inferences about magma sources and mantle structure from variations of 143Nd/144Nd. Geophysical Research Letters, 3(12): 743-746.
DePaolo, D.J., Wasserburg, G.J., 1979. Petrogenetic mixing models and Nd-Sr isotopic patterns. Geochimica et Cosmochimica Acta, 43(4): 615-627.
Dhuime, B. et al., 2009. Geochemical Architecture of the Lower- to Middle-crustal Section of a Paleo-island Arc (Kohistan Complex, Jijal–Kamila Area, Northern Pakistan): Implications for the Evolution of an Oceanic Subduction Zone. Journal of Petrology.
Elburg, M., Vroon, P., van der Wagt, B., Tchalikian, A., 2005. Sr and Pb isotopic composition of five USGS glasses (BHVO-2G, BIR-1G, BCR-2G, TB-1G, NKT-1G). Chemical Geology, 223(4): 196-207.

Ellis, D.J., 1980. Osumilite-sapphirine-quartz granulites from Enderby Land, Antarctica: P-T conditions of metamorphism, implications for garnet-cordierite equilibria and the evolution of the deep crust. Contributions to Mineralogy and Petrology, 74(2): 201-210.
Ellis, D.J., 1987. Origin and evolution of granulites in normal and thickened crusts. Geology, 15(2): 167-170.
England, P.C., Thompson, A.B., 1984. Pressure—Temperature—Time Paths of Regional Metamorphism I. Heat Transfer during the Evolution of Regions of Thickened Continental Crust. Journal of Petrology, 25(4): 894-928.
Fleet, M.E., Barnett, R.L., 1978. Al iv /Al vi partitioning in calciferous amphiboles from the Frood Mine, Sudbury, Ontario. The Canadian Mineralogist, 16(4): 527-532.
Fraga, L.M., Macambira, M.J.B., Dall'Agnol, R., Costa, J.B.S., 2009a. 1.94–1.93 Ga charnockitic magmatism from the central part of the Guyana Shield, Roraima, Brazil: Single-zircon evaporation data and tectonic implications. Journal of South American Earth Sciences, 27(4): 247-257.
Fraga, L.M., Reis, N.J., Dall'Agnol, R., 2009b. Cauarne-Coeroeni Belt – the main tectonic feature of the Central Guyana Shield, Northern Amazonian Craton. In: Norte, S.-N. (Editor), Simpósio de Geologia da Amazônia, Manaus.
Fraga, L.M., Reis, N.J., Dall'Agnol, R., Armstrong, R., 2008. The Cauarane-Coeroene belt, the tectonic southern limit of the preserved Rhyacian crustal domain in the Guyana Shield, northern Amazonian Craton., 33rd Internation Geologic Congress, Oslo, Norway.
Gorczyk, W., Smithies, H., Korhonen, F., Howard, H., Quentin De Gromard, R., 2015. Ultra-hot Mesoproterozoic evolution of intracontinental central Australia. Geoscience Frontiers, 6(1): 23-37.
Grimes, C.B. et al., 2007. Trace element chemistry of zircons from oceanic crust: A method for distinguishing detrital zircon provenance. Geology, 35(7): 643-646.
Hacker, B.R. et al., 2000. Hot and Dry Deep Crustal Xenoliths from Tibet. Science, 287(5462): 2463-2466.
Hammarstrom, J.M., Zen, E.-a., 1986. Aluminum in hornblende; an empirical igneous geobarometer. American Mineralogist, 71(11-12): 1297-1313.
Harley, S.L., 1989. The origins of granulites: a metamorphic perspective. Geological Magazine, 126(03): 215-247.
Harley, S.L., 1998. On the occurrence and characterization of ultrahigh-temperature crustal metamorphism. Geological Society, London, Special Publications, 138(1): 81-107.
Harley, S.L., 2008. Refining the P–T records of UHT crustal metamorphism. Journal of Metamorphic Geology, 26(2): 125-154.
Hawkesworth, C.J., O'Nions, R.K., Arculus, R.J., 1979. Nd and Sr isotope geochemistry of island arc volcanics, Grenada, Lesser Antilles. Earth and Planetary Science Letters, 45(2): 237-248.
Holland, T., Blundy, J., 1994. Non-ideal interactions in calcic amphiboles and their bearing on amphibole-plagioclase thermometry. Contributions to Mineralogy and Petrology, 116(4): 433-447.
Houseman, G.A., McKenzie, D.P., Molnar, P., 1981. Convective instability of a thickened boundary layer and its relevance for the thermal evolution of continental convergent belts. Journal of Geophysical Research: Solid Earth, 86(B7): 6115-6132.
Hyndman, R.D., Currie, C.A., Mazzotti, S.P., 2005. Subduction zone backarcs, mobile belts, and orogenic heat. GSA Today, 15(2): 4-10.
Irvine, T.N., 1974. Petrology of the Duke Island Ultramafic Complex Southeastern Alaska. Geological Society of America Memoirs, 138: 1-244.
Irvine, T.N., Baragar, W.R.A., 1971. A Guide to the Chemical Classification of the Common Volcanic Rocks. Canadian Journal of Earth Sciences, 8(5): 523-548.
Jagoutz, O., Schmidt, M.W., 2013. The composition of the foundered complement to the continental crust and a re-evaluation of fluxes in arcs. Earth and Planetary Science Letters, 371–372: 177-190.
Johnson, M.C., Rutherford, M.J., 1989. Experimental calibration of the aluminum-in-hornblende geobarometer with application to Long Valley caldera (California) volcanic rocks. Geology, 17(9): 837-841.
Kelsey, D.E., 2008. On ultrahigh-temperature crustal metamorphism. Gondwana Research, 13(1): 1-29.
Kelsey, D.E., Hand, M., 2015. On ultrahigh temperature crustal metamorphism: Phase equilibria, trace element thermometry, bulk composition, heat sources, timescales and tectonic settings. Geoscience Frontiers(0).
Kemp, A.I.S., Shimura, T., Hawkesworth, C.J., EIMF, 2007. Linking granulites, silicic magmatism, and crustal growth in arcs: Ion microprobe (zircon) U-Pb ages from the Hidaka metamorphic belt, Japan. Geology, 35(9): 807-810.

Klaver, M., 2011. The relationship between dry granitoid magmatism and UHT-metamorphism, Bakhuys granulite belt, Western Suriname, VU University Amsterdam.
Klaver, M., de Roever, E.W.F., Nanne, J.A.M., Mason, P.R.D., Davies, G.R., 2015. Charnockites and UHT metamorphism in the Bakhuis Granulite Belt, western Suriname: Evidence for two separate UHT events. Precambrian Research, 262(0): 1-19.
Klaver, M. et al., *in press*. Mafic magmatism in the Bakhuis Granulite Belt (western Suriname): relationship with charnockite magmatism and UHT metamorphism. Journal of the Geological Society of Sweden.
Kramers, J.D., Kreissig, K., Jones, M.Q.W., 2001. Crustal heat production and style of metamorphism: a comparison between two Archean high grade provinces in the Limpopo Belt, southern Africa. Precambrian Research, 112(1–2): 149-163.
Kroonenberg, S.B., de Roever, E.W.F., 2010. Geological Evolution of the Amazonian Craton, Amazonia: Landscape and Species Evolution. Wiley-Blackwell Publishing Ltd., pp. 7-28.
Lafrance, J., Bardoux, M., Voicu, G., Stevenson, R., Machado, N., 1999. Geological and metallogenic environments of gold deposits of the Guiana Shield; a comparative study between St-Elie (French Guiana) and Omai (Guyana). Exploration and Mining Geology, 8(1-2): 117-135.
Le Maitre, R.W., 2002. Igneous rocks: A Classification and Glossary of Terms. Recommendations of the International Union of Geological Sciences. Cambridge University Press, Cambridge.
Leake, B.E. et al., 1997. Nomenclature of amphiboles; Report of the Subcommittee on Amphiboles of the International Mineralogical Association, Commission on New Minerals and Mineral Names. American Mineralogist, 82(9-10): 1019-1037.
Lindsley, D.H., Frost, B.R., Frost, C.D., Scoates, J.S., 2010. Petrology, geochemisty and structure of the Chugwater Anorthosite, Laramie Anorthosite Complex, southeastern Wyoming. The Canadian Mineralogist, 48(4): 887-923.
Mahlen, N.J., Beard, B.L., Johnson, C.M., Lapen, T.J., 2008. An investigation of dissolution methods for Lu-Hf and Sm-Nd isotope studies in zircon- and garnet-bearing whole-rock samples. Geochemistry, Geophysics, Geosystems, 9(1): n/a-n/a.
Maidment, D.W., Hand, M., Williams, I.S., 2013. High grade metamorphism of sedimentary rocks during Palaeozoic rift basin formation in central Australia. Gondwana Research, 24(3–4): 865-885.
Martin, R.F., 2007. Amphiboles in the Igneous Environment. Reviews in Mineralogy and Geochemistry, 67(1): 323-358.
McDonough, W.F., Sun, S.s., 1995. The composition of the Earth. Chemical Geology, 120(3–4): 223-253.
McLelland, J.M., Selleck, B.W., Hamilton, M.A., Bickford, M.E., 2010. Late- to post-tectonic setting of some major Proterozoic Anorthosite - Mangerite - Charnockite - Granite (AMCG) suites. The Canadian Mineralogist, 48(4): 729-750.
Milesi, J.P. et al., 1995. Les minéralisations du Nord de la Guyane française dans leur cadre géologique. Chronique de la Recherche Minière, 518: 5-58.
Minter, W.E.L., 2006. The sedimentary setting of Witwatersrand placer mineral deposits in an Archean atmosphere. Geological Society of America Memoirs, 198: 105-119.
Montgomery, C.W., Hurley, P.M., 1978. Total-rock UPb and RbSr systematics in the Imataca Series, Guayana Shield, Venezuela. Earth and Planetary Science Letters, 39(2): 281-290.
Münker, C., Weyer, S., Scherer, E., Mezger, K., 2001. Separation of high field strength elements (Nb, Ta, Zr, Hf) and Lu from rock samples for MC-ICPMS measurements. Geochemistry, Geophysics, Geosystems, 2(12): n/a-n/a.
Nadeau, S. et al., 2013. Guyana: the Lost Hadean crust of South America? Brazilian Journal of Geology, 43: 601-606.
Nanne, J.A.M., 2013. The regional extent of ultrahigh-temperature metamorphism in the Bakhuis Granulite Belt, W Surinam, VU University Amsterdam.
Nogueira, S.A.A., Bettencourt, J.S., Tassinari, C.C.G., 2000. Geochronology of the granitoid hosted Salamangone gold deposit, Lourenqo District Amapá, Brazil. Revista Brasileira de Geociências, 30(2): 261-264.
Norcross, C., Davis, D.W., Spooner, E.T.C., Rust, A., 2000. U-Pb and Pb-Pb age constraints on Paleoproterozoic magmatism, deformation and gold mineralization in the Omai area, Guyana Shield. Precambrian Research, 102(1–2): 69-86.
Nowell, G.M. et al., 1998. High precision Hf isotope measurements of MORB and OIB by thermal ionisation mass spectrometry: insights into the depleted mantle. Chemical Geology, 149(3–4): 211-233.
Pearce, J.A., 2008. Geochemical fingerprinting of oceanic basalts with applications to ophiolite classification and the search for Archean oceanic crust. Lithos, 100(1–4): 14-48.

Pearce, J.A., Cann, J.R., 1973. Tectonic setting of basic volcanic rocks determined using trace element analyses. Earth and Planetary Science Letters, 19(2): 290-300.
Platt, J.P., England, P.C., 1994. Convective removal of lithosphere beneath mountain belts; thermal and mechanical consequences. American Journal of Science, 294(3): 307-336.
Pownall, J.M., Hall, R., Armstrong, R.A., Forster, M.A., 2014. Earth's youngest known ultrahigh-temperature granulites discovered on Seram, eastern Indonesia. Geology.
Priem, H.N.A., Boelrijk, N.A.I.M., Hebeda, E.H., Th. Verdurmen, E.A., Verschure, R.H., 1971. Isotopic Ages of the Trans-Amazonian Acidic Magmatism and the Nickerie Metamorphic Episode in the Precambrian Basement of Suriname, South America. Geological Society of America Bulletin, 82(6): 1667-1680.
Priem, H.N.A., Hebeda, E.H., Boelrijk, N.A.I.M., Verschure, R.H., 1968. Isotope age determinations on Surinam Rocks, 3. Proterozoic and Permo-Triassic basalt magmatism in the Guiana Shield. Geol. Mijnb. Dienst Suriname, 47: 17-20.
Prouteau, G., Scaillet, B., Pichavant, M., Maury, R., 2001. Evidence for mantle metasomatism by hydrous silicic melts derived from subducted oceanic crust. Nature, 410(6825): 197-200.
Raase, P., 1974. Al and Ti contents of hornblende, indicators of pressure and temperature of regional metamorphism. Contributions to Mineralogy and Petrology, 45(3): 231-236.
Raczek, I., Jochum, K.P., Hofmann, A.W., 2003. Neodymium and Strontium Isotope Data for USGS Reference Materials BCR-1, BCR-2, BHVO-1, BHVO-2, AGV-1, AGV-2, GSP-1, GSP-2 and Eight MPI-DING Reference Glasses. Geostandards Newsletter, 27(2): 173-179.
Raczek, I., Stoll, B., Hofmann, A.W., Peter Jochum, K., 2001. High-Precision Trace Element Data for the USGS Reference Materials BCR-1, BCR-2, BHVO-1, BHVO-2, AGV-1, AGV-2, DTS-1, DTS-2, GSP-1 and GSP-2 by ID-TIMS and MIC-SSMS. Geostandards Newsletter, 25(1): 77-86.
Reis, N.J., De Faria, M.S.G., Fraga, L.M., Haddad, R.C., 2000. Orosirian calc-alkaline volcanism and the Orocaima event in the northern Amazonian Craton, eastern Roraima state, Brazil. Revista Brasileira de Geociências, 30(3): 380-383.
Reis, N.J. et al., 2013. Avanavero mafic magmatism, a late Paleoproterozoic LIP in the Guiana Shield, Amazonian Craton: U–Pb ID-TIMS baddeleyite, geochemical and paleomagnetic evidence. Lithos, 174: 175-195.
Rutter, M.J., Van der Laan, S.R., Wyllie, P.J., 1989. Experimental data for a proposed empirical igneous geobarometer: Aluminum in hornblende at 10 kbar pressure. Geology, 17(10): 897-900.
Sandiford, M., 1985. The metamorphic evolution of granulites at Fyfe Hills; implications for Archaean crustal thickness in Enderby Land, Antarctica. Journal of Metamorphic Geology, 3(2): 155-178.
Sandiford, M., 1989. Horizontal structures in granulite terrains: A record of mountain building or mountain collapse? Geology, 17(5): 449-452.
Sandiford, M., Powell, R., 1986. Deep crustal metamorphism during continental extension: modern and ancient examples. Earth and Planetary Science Letters, 79(1–2): 151-158.
Santos, J.O.S. et al., 2003. Age, source, and regional stratigraphy of the Roraima Supergroup and Roraima-like outliers in northern South America based on U-Pb geochronology. Geological Society of America Bulletin, 115(3): 331-348.
Santosh, M., Kusky, T., 2010. Origin of paired high pressure–ultrahigh-temperature orogens: a ridge subduction and slab window model. Terra Nova, 22(1): 35-42.
Santosh, M., Kusky, T., Wang, L., 2011. Supercontinent cycles, extreme metamorphic processes, and changing fluid regimes. International Geology Review, 53(11-12): 1403-1423.
Santosh, M., Omori, S., 2008. CO2 windows from mantle to atmosphere: Models on ultrahigh-temperature metamorphism and speculations on the link with melting of snowball Earth. Gondwana Research, 14(1–2): 82-96.
Sisson, T.W., Grove, T.L., 1993. Experimental investigations of the role of H2O in calc-alkaline differentiation and subduction zone magmatism. Contributions to Mineralogy and Petrology, 113(2): 143-166.
Smithies, R.H. et al., 2011. High-Temperature Granite Magmatism, Crust–Mantle Interaction and the Mesoproterozoic Intracontinental Evolution of the Musgrave Province, Central Australia. Journal of Petrology, 52(5): 931-958.
Spandler, C. et al., 2003. Petrogenesis of the Greenhills Complex, Southland, New Zealand: magmatic differentiation and cumulate formation at the roots of a Permian island-arc volcano. Contributions to Mineralogy and Petrology, 144(6): 703-721.
Spear, F.S., 1981. An experimental study of hornblende stability and compositional variability in amphibolite. American Journal of Science, 281(6): 697-734.

Stepanova, A.V. et al., 2014. Palaeoproterozoic Continental MORB-type Tholeiites in the Karelian Craton: Petrology, Geochronology, and Tectonic Setting. Journal of Petrology, 55(9): 1719-1751.
Sun, S.-s., McDonough, W.F., 1989. Chemical and isotopic systematics of oceanic basalts: implications for mantle composition and processes. Geological Society, London, Special Publications, 42(1): 313-345.
Tassinari, C.C.G. et al., 2004. The Imataca Complex, NW Amazonian Craton, Venezuela: Crustal evolution and integration of geochronological and petrological cooling histories. Episodes, 27(1): 3-12.
Théveniaut, H. et al., 2006. Paleoproterozoic (2155–1970 Ma) evolution of the Guiana Shield (Transamazonian event) in the light of new paleomagnetic data from French Guiana. Precambrian Research, 150(3–4): 221-256.
Thijssen, A.C.D., 2015. The age and geochemistry of the mafic-ultramafic intrusions and their relation to UHT metamorphism in the Bakhuis Granulite Belt, Western Suriname, VU University Amsterdam.
Thirlwall, M.F., 1991. Long-term reproducibility of multicollector Sr and Nd isotope ratio analysis. Chemical Geology: Isotope Geoscience section, 94(2): 85-104.
Vanderhaeghe, O. et al., 1998. Contrasting mechanism of crustal growth: Geodynamic evolution of the Paleoproterozoic granite–greenstone belts of French Guiana. Precambrian Research, 92(2): 165-193.
Vervoort, J.D., Blichert-Toft, J., 1999. Evolution of the depleted mantle: Hf isotope evidence from juvenile rocks through time. Geochimica et Cosmochimica Acta, 63(3–4): 533-556.
Vervoort, J.D. et al., 2000. Hf–Nd isotopic evolution of the lower crust. Earth and Planetary Science Letters, 181(1–2): 115-129.
Vervoort, J.D., Patchett, P.J., Blichert-Toft, J., Albarède, F., 1999. Relationships between Lu–Hf and Sm–Nd isotopic systems in the global sedimentary system. Earth and Planetary Science Letters, 168(1–2): 79-99.
Walsh, A.K. et al., 2015. P–T–t evolution of a large, long-lived, ultrahigh-temperature Grenvillian belt in central Australia. Gondwana Research, 28(2): 531-564.
Wan, B., Xiao, W., Windley, B.F., Yuan, C., 2013a. Permian hornblende gabbros in the Chinese Altai from a subduction-related hydrous parent magma, not from the Tarim mantle plume. Lithosphere, 5(3): 290-299.
Wan, Y. et al., 2013b. Episodic Paleoproterozoic (~2.45, ~1.95 and ~1.85 Ga) mafic magmatism and associated high temperature metamorphism in the Daqingshan area, North China Craton: SHRIMP zircon U–Pb dating and whole-rock geochemistry. Precambrian Research, 224: 71-93.
Weis, D. et al., 2006. High-precision isotopic characterization of USGS reference materials by TIMS and MC-ICP-MS. Geochemistry, Geophysics, Geosystems, 7(8): n/a-n/a.
Weis, D., Kieffer, B., Maerschalk, C., Pretorius, W., Barling, J., 2005. High-precision Pb-Sr-Nd-Hf isotopic characterization of USGS BHVO-1 and BHVO-2 reference materials. Geochemistry, Geophysics, Geosystems, 6(2): n/a-n/a.
Wells, P.R.A., 1980. Thermal models for the magmatic accretion and subsequent metamorphism of continental crust. Earth and Planetary Science Letters, 46(2): 253-265.
Wetherill, G.W., 1956. Discordant uranium-lead ages, I. Transactions, American Geophysical Union, 37(3): 320-326.
Whitney, D.L., Evans, B.W., 2010. Abbreviations for names of rock-forming minerals. American Mineralogist, 95(1): 185-187.
Winter, J.D.N., 2010. An Introduction to Igneous and Metamorphic Petrology. Prentice Hall.
Yan, S. et al., 2015. Petrology and geochemistry of late Carboniferous hornblende gabbro from the Awulale Mountains, western Tianshan (NW China): Implication for an arc–nascent back-arc environment. Journal of Asian Earth Sciences(0).